Crystal growth and characterization of doped perovskite titanates $A\mathrm{TiO}_3$ and single-layered manganites $R_{1-x}A_{1+x}\mathrm{MnO}_4$

Johannes Engelmayer

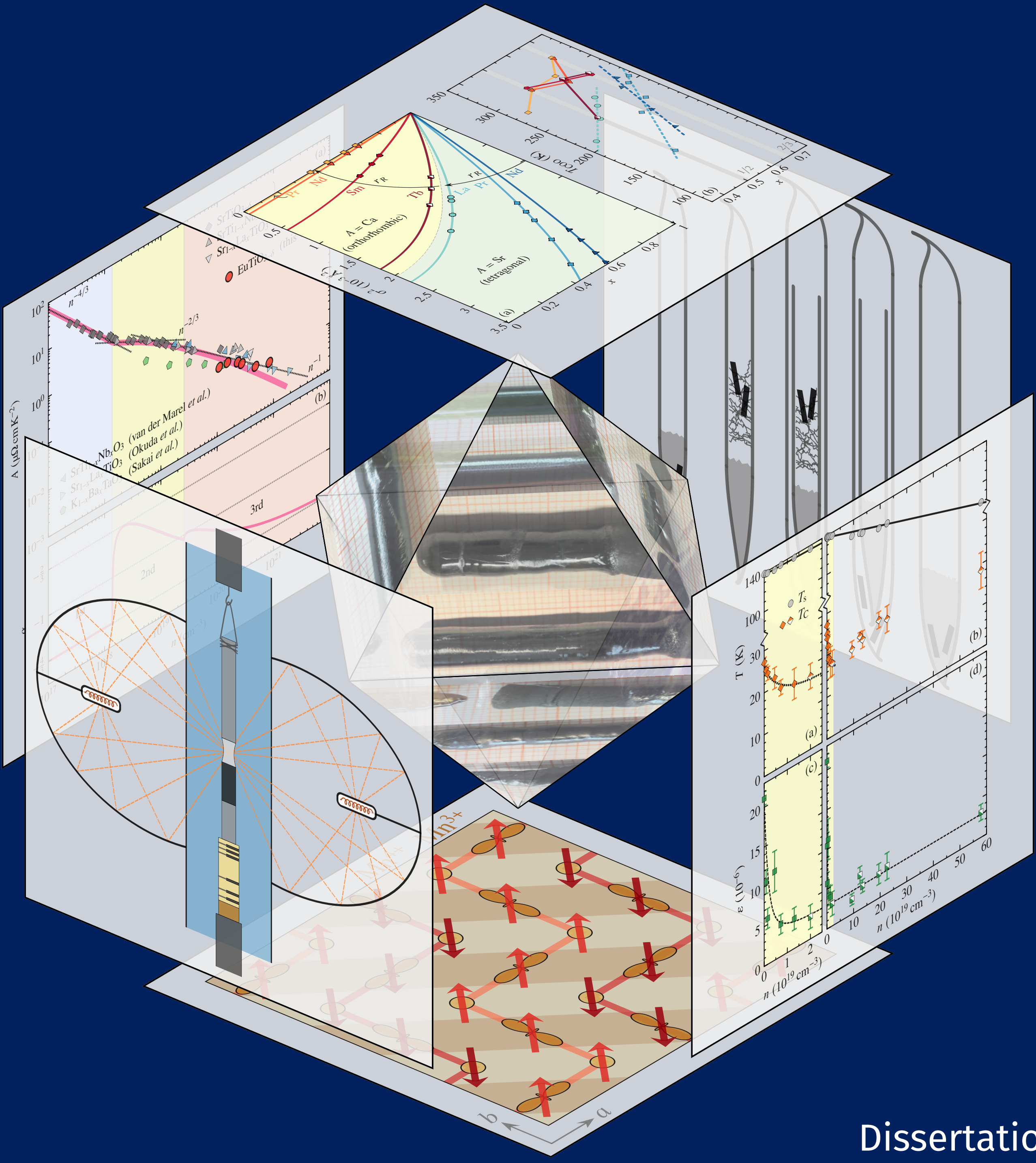

Dissertation

Crystal growth and characterization of doped perovskite titanates $A\mathrm{TiO}_3$ and single-layered manganites $R_{1-x}A_{1+x}\mathrm{MnO}_4$

Inaugural-Dissertation

zur

Erlangung des Doktorgrades
der Mathematisch-Naturwissenschaftlichen Fakultät
der Universität zu Köln

vorgelegt von
Johannes Engelmayer
aus Köln

Köln, 2020

Berichterstatter:	Prof. Dr. Thomas Lorenz Prof. Dr. Markus Braden
Vorsitzender der Prüfungskommission:	Prof. Dr. Simon Trebst
Tag der mündlichen Prüfung:	03.02.2020

Contents

Introduction

Oxygen is the most abundant element in the bulk composition of Venus, Earth, and Mars [1–5], but its presence as free gas in the atmosphere is a unique characteristic of planet Earth [6]. This oxidizing environment offers ideal conditions for the emergence and stability of oxidic materials and their investigation (not to mention the emergence and stability of the investigator). After fluorine, oxygen has the highest electronegativity of all elements [7]. Its strong tendency to gain two electrons allows it to form chemical compositions with almost all other elements. Thus, it is no surprise that the vast majority of all minerals in the Earth's crust are compositions with oxygen [8].

Oxides with perovskite structure are the predominant solid phase on Earth—$MgSiO_3$ is the most abundant natural compound [9]—and are likewise ubiquitous in science and technology. Their relevance for solid-state physics and chemistry is based on both their uncomplex crystal structure, simplifying theoretical approaches, as well as their tolerance to chemical substitutions [10]. The latter renders oxides with perovskite structure and its descendants to be a most versatile playground for the investigation of many-body physics, interactions, and ordering phenomena. Perovskite-type oxides appear as hosts of diverse physical phenomena such as high-T_c superconductivity ($La_{2-x}A_xCuO_4$ with A = Ca, Sr, Ba) [11, 12], large magnetoresistances ($La_{0.67}Ba_{0.33}MnO_x$) [13], ferroelectricity (ATiO$_3$ with A = Ba, Pb, Cd) [14–18], and quantum paraelectricity (ATiO$_3$ with A = Ca, Sr, Eu and $KTaO_3$) [19–22].

The observation of these phenomena in their pristine entity—to the greatest possible extent—requires high-purity materials, which are hardly found in nature. Sophisticated techniques of crystal growth allow the synthesis of high-quality samples under reproducible conditions even beyond the scope of naturally occurring materials and, furthermore, the creation of systems with tailored physical properties. Prime examples for this approach are $BaTiO_3$ and $SrTiO_3$ that were synthesized and studied decades before their discovery in nature [23, 24], while most other significant perovskite materials are still only obtained artificially.

One of the most common phenomena in solid-state physics is the metal–insulator transition (MIT) [25]. Often, it is generated by aliovalent chemical substitutions in an originally insulating material. One can distinguish MIT by the insulator type of the pristine parent compound. Typically, insulators are systems with completely filled or empty bands, but systems with partially filled bands can be insulating as well if the electron–electron repulsion prevents electronic delocalization. The first type is known as band insulator, whereas the second type is referred to as Mott insulator. In this thesis, doped perovskite titanates ATiO$_3$ and single-layered manganites $R_{1-x}A_{1+x}MnO_4$ are studied, representing examples of band insulators and Mott insulators, respectively.

Perovskite titanates are either ferroelectrics or quantum paraelectrics, for which a ferroelectric long-range order is suppressed by quantum fluctuations. While both $SrTiO_3$ and $CaTiO_3$ are quantum paraelectrics, the solid solution $Sr_{1-x}Ca_xTiO_3$ with an A-site sharing of strontium and calcium hosts a ferroelectric phase for $0.0018 \leq x < 0.12$ [26]. Furthermore, pristine $SrTiO_3$ is a large-gap band insulator that becomes metallic upon reduction ($SrTiO_{3-\delta}$) [27] and even superconducting at extremely dilute charge-carrier concentrations of $n \simeq 5 \times 10^{17}\,\mathrm{cm}^{-3}$ [28]. Systems with combined calcium substitution and reduction ($Sr_{1-x}Ca_xTiO_{3-\delta}$) exhibit a competition of dilute metallicity and ferroelectricity [29, 30]. Characteristic anomalies signaling the ferroelectric transition at T_C of the insulating parent compound $Sr_{1-x}Ca_xTiO_3$ persist in $Sr_{1-x}Ca_xTiO_{3-\delta}$ upon increasing charge-carrier concentration n and shift to lower temperatures. The anomalies vanish at a critical carrier density n_c that depends on the calcium content x in a way being typical for quantum phase transitions [30]. These findings are primarily based on minima in the resistivity and demand a confirmation by a thermodynamic probe. In this work, $Sr_{1-x}Ca_xTiO_{3-\delta}$ with a fixed calcium content $x = 0.009$ and charge-carrier density n tuned from the insulating parent up to $n \simeq 60 \times 10^{19}\,\mathrm{cm}^{-3}$ is investigated by thermal-expansion measurements. The evolution of the T_C-related anomalies with n is discussed and a phase diagram for $Sr_{1-x}Ca_xTiO_{3-\delta}$ is derived.

The extremely dilute metallicity in doped $SrTiO_3$ is enabled by its huge permittivity peaking at $\varepsilon \simeq 20\,000$ in the low-temperature regime [20]. Because ε determines the effective Bohr radius a_B^* of the donor atoms, it is a measure of the overlap of the electronic wave functions. Surprisingly, the resistivity of $SrTiO_{3-\delta}$ shows an AT^2 behavior being typically considered as a fingerprint of electron–electron scattering [31]. Conventional theories of interelectronic scattering are challenged in view of the low charge-carrier densities in $SrTiO_{3-\delta}$ and the origin of the T^2 behavior remains an open question to date. The related compound $EuTiO_3$ shares the quantum paraelectric behavior and the crystal structure with $SrTiO_3$, but, in contrast to the latter, it contains a magnetic Eu^{2+} ion. Its magnetic moments order antiferromagnetically below $T_N = 5.5\,\mathrm{K}$. Moreover, the band gap of $EuTiO_3$ is much smaller than that of its sister compound resulting in a measurable resistivity below room temperature. Analogous to $SrTiO_{3-\delta}$, a metal–insulator transition can be induced in $EuTiO_3$ by a removal of oxygen. A T^2 resistivity in doped $EuTiO_3$ has not been described previously. Because in contrast to $SrTiO_3$ and $Sr_{1-x}Ca_xTiO_3$, crystals of $EuTiO_3$ are not commercially available, single-crystals of $EuTiO_3$ are grown within the scope of this thesis. Oxygen-deficient metallic $EuTiO_{3-\delta}$ is obtained via annealing. The induced metal–insulator transition is investigated by resistivity and Hall-effect measurements and a possible T^2 behavior is discussed. The results draw a comprehensive picture of dilute metallicity in perovskite oxides with a quantum paraelectric parent.

Doped Mott insulators develop complex real-space patterns of charges, orbitals, and magnetic moments [32–34]. One of the most thoroughly studied compounds in this field is $La_{1-x}Sr_{1+x}MnO_4$ whose crystal structure is identical to that of high-T_c cuprates and can be considered as layered perovskite. The material hosts Mn^{3+} and Mn^{4+} ions in a ratio controlled by the doping level x. A simultaneous charge and orbital order (COO) emerges at a transition temperature T_{COO} and an additional magnetic order arises at T_{N}, where the manganese spins arrange in ferromagnetic zig-zag chains with antiferromagnetic interchain coupling. The ordering patterns of charges and orbitals as well as the step length of the zig-zag chains both depend on x. Commensurate doping levels $x = 1/2, 2/3, 3/4, \ldots$ are of special interest since they imply the number of Mn^{3+} ions to be an integer multiple of the number of Mn^{4+} ions. Half-doped compounds are described by the so-called Goodenough model that predicts alternating stripes of Mn^{3+} and Mn^{4+} ions, where adjacent Mn^{3+} stripes have alternating d_{z^2}-orbital orientations. The zig-zag chains below T_{N} consist of three-spin steps. Upon increasing x, the compound $\mathrm{La}_{1-x}\mathrm{Sr}_{1+x}\mathrm{MnO}_4$ is prone to chemical phase separation, which is why high-quality single crystals are not available beyond $x \simeq 0.6$. A substitution of La and/or Sr opens the door to higher doping levels and moves commensurate doping levels besides $x = 1/2$ within reach. Indeed, the compounds $\mathrm{Pr}_{1-x}\mathrm{Ca}_{1+x}\mathrm{MnO}_4$ and $\mathrm{Nd}_{1-x}\mathrm{Sr}_{1+x}\mathrm{MnO}_4$ with $x = 2/3$ can be synthesized and show alternating Mn^{3+} single stripes and Mn^{4+} double stripes in the COO phase and four-spin zig-zag chains below T_{N} [35]. Hitherto, a systematic survey of the evolution of T_{COO} with x for different element combinations $R_{1-x}A_{1+x}\mathrm{MnO}_4$ is lacking. Within the scope of this thesis, centimeter-sized single crystals of $R_{1-x}\mathrm{Ca}_{1+x}\mathrm{MnO}_4$ (R = Pr, Nd, Sm, Tb) and $R_{1-x}\mathrm{Sr}_{1+x}\mathrm{MnO}_4$ (R = Pr, Nd) are grown, covering a doping range $0.5 \leq x \leq 0.73$. As known from $\mathrm{La}_{1-x}\mathrm{Sr}_{1+x}\mathrm{MnO}_4$, the COO transition produces characteristic signatures in resistivity, magnetization, and heat capacity [36, 37]. Hence, these three quantities are used to detect COO anomalies in all synthesized crystals. A common $T_{\mathrm{COO}}(x)$ phase diagram for all $R_{1-x}A_{1+x}\mathrm{MnO}_4$ compounds is established and discussed in the context of structural disorder created by the ion-size mismatch of R and A.

This thesis is structured as follows. Chapter 1 is dedicated to the growth of single crystals, which is one of the pillars of this thesis. A general introduction to the applied floating-zone method is followed by a detailed synthesis description for EuTiO_3, where special attention is paid to the reduction of the as-grown crystals. Chapter 2 begins with a general introduction to perovskite titanates and highlights common properties of both $\mathrm{Sr}_{1-x}\mathrm{Ca}_x\mathrm{TiO}_3$ and EuTiO_3. The main part of this chapter covers the thermal-expansion study on $\mathrm{Sr}_{1-x}\mathrm{Ca}_x\mathrm{TiO}_{3-\delta}$. Chapter 3 has two parts: The first covers the characterization of the as-grown pristine EuTiO_3 crystal by resistivity, magnetization, heat capacity, and permittivity. The second part contains the study on reduced, metallic $\mathrm{EuTiO}_{3-\delta}$. Chapter 4 deals with the crystal growth of single-layered manganites $R_{1-x}A_{1+x}\mathrm{MnO}_4$ and the COO transition studied by resistivity, magnetization, and heat-capacity measurements.

1 Preparation of single crystals

The synthesis of single crystals by the so-called floating-zone technique is a central part of this thesis. The first part of this chapter contains a general description of this method including all preparatory steps. Because two different furnace models were used for the growth processes, special attention is paid to the different characteristics of both furnace designs. The second part of this chapter covers the growth of $EuTiO_3$ crystals and different variants of electron doping in this material, in particular the annealing of as-grown $EuTiO_3$ as well as the crystal growth of $Eu_{1-x}La_xTiO_3$ and $EuTi_{1-x}Nb_xO_3$. The preparation of single-layered manganites is subject to Ch. 4.

Contents

1.1 Introduction

Research in solid-state physics requires solids, at least from an experimental point of view. Solids can be amorphous or crystalline, where the latter are subdivided into polycrystalline and single-crystalline solids. The need for single crystals is based on the fact that most characteristics of crystalline solids are anisotropic, and measurements on polycrystalline samples cannot distinguish between different crystallographic orientations. Anisotropic behavior is then averaged out. To investigate a physical property in a well-defined crystallographic direction, the availability of single crystals is mandatory.

Although the Earth's crust offers plenty of minerals in single-crystalline form, their varying chemical purity, phase purity, and defect concentration complicates investigations of physical phenomena in their pure and unbiased nature, and hinders reproducible results (each sample is unique), not to mention the difficulties of exploration and the limitation to naturally existing and accessible compounds. Thus, the investigation of natural minerals in solid-state research is present[1] but rather an exception. Instead, solid-state researchers prefer uniform crystals of high purity, synthesized under well-defined and reproducible conditions in a laboratory. Nevertheless, it is worth to mention that some of the most prominent materials in solid-state research are not artificial but actually found in nature, e.g., $CaTiO_3$ as perovskite [39–41], $SrTiO_3$ as mineral tausonite [23], $BaTiO_3$ as barioperovskite [24], and $PbTiO_3$ as macedonite [42]. A comprehensive overview of minerals with perovskite structure can be found in Ref. [43].

Prerequisite of high-purity crystals are high-purity starting materials, usually polycrystalline powders. Many techniques are suited to transform a polycrystalline material into a single crystal; a process that is referred to as crystal growth. The preferred method used within this thesis is the floating-zone technique. An overview of other techniques can be found in Refs. [44, 45].

1.2 The floating-zone method

1.2.1 Scope

The floating-zone technique has significant advantages over other growth methods, especially compared to crucible-based techniques. It allows the growth of centimeter-sized[2,3], uniform single crystals in a comparably large accessible temperature range up to 2200 °C with halogen lamps and up to 3000 °C with xenon arc lamps [46]. Since no crucible is needed, no limitations caused by the crucible material can occur like contaminations of the sample with crucible material, chemical reactions between sample and crucible, or a limited accessible temperature range due to the melting point of the crucible.

Like all growth methods, the floating-zone technique has also limitations. It is not suitable for materials with high vapor pressure (evaporation during the growth process), low surface

---

[1] One example is the mineral aegirine $NaFeSi_2O_6$, a member of the pyroxene family, where a specific sample was found to be actually $Na_{1.04}Fe_{0.83}Ca_{0.04}Mn_{0.02}Al_{0.01}Ti_{0.08}Si_2O_6$ [38].

[2] Typical values are 5 mm in diameter and up to 10 cm in length. The actual size depends on the size of the chemical test tube (and rubber tube) that is used to shape the polycrystalline rod beforehand [see Sec. 1.2.2]. Apart from that, the size is limited only by the characteristics of the mirror furnace, in particular, by the width of the focus (concerning the diameter) and by the travel way of the shafts (concerning the length).

[3] This is rather large compared to crystals obtained from vapor transport but small compared to silicon crystals produced by Czochralski method. Therefore, the floating-zone technique is predominantly used for research purposes but not for industrial production.

tension (the material becomes too liquid), high viscosity (the material becomes not liquid enough), or structural phase transition(s) between melting point and room temperature (the crystal cracks upon cooling). Some of these limitations can be diminished or circumvented, e.g., the evaporation can be compensated by using excessive material as is done for the growth of manganites and molybdates [see Secs. 4.4.2 and A.1.2, respectively].

1.2.2 Preparatory steps

The procedure of single-crystal synthesis using the floating-zone technique usually requires the following preparatory steps. Not all of them are needed in any case (bracketed are optional) and most of them are not exclusive to the floating-zone technique but also necessary for other methods, e.g., for other growth-from-melt techniques or growth-from-solution techniques.

- Examination of the availability and processability of chemicals.
- Setting up and balancing the chemical equation.
- Calculating the required amount of powder for each reactant.
- Weighing of the powder.
- Mixing and grinding the powder.
- [Heating the powder to induce a solid state reaction.]
- Shaping and pressing of the powder to form a rod.
- [Sintering of the rod.]

Each of these steps and its relevance for the synthesized materials is described in the following.

Availability and processability Usually, the desired chemical product is not commercially available, neither as powder, nor as single crystal (one exception is $SrTiO_3$). Thus, it has to be made from materials that are commercially available, in most cases oxide powders (metal oxides, carbonates, or hydroxides), but also pure elements. Often, there is more than one oxide for a certain element, e.g., TiO, Ti_2O_3, and TiO_2 for titanium, EuO, Eu_3O_4, and Eu_2O_3 for europium. Oxides of the same element can differ in their properties quite a lot. Although it might be possible to find a proper chemical equation for each oxide of the same element, often only one viable alternative remains after considering all relevant aspects: oxidation state, stability under air and humidity, vapor pressure, melting point, production of surplus oxygen, available purity and quantity, etc. have to be considered here. In many cases, the oxide with the highest oxidation state is preferable since it is the most stable compound. An extensive discussion for the case of europium and titanium is given in Sec. 1.4.1.

Chemical equation and calculation of powder mass Once the reactants are chosen, the chemical equation has to be set up. The balancing is done by setting up and solving a system of linear equations. The mass ratio of powders that have to be weighed in requires knowledge of the molar masses of the reactants, which is simply the sum of the molar masses of their constituents multiplied with their number. The atomic weights of the elements can be found in the biennial review "Atomic weights of the elements (IUPAC Technical Report)"[4] [48]. The absolute powder masses depend on the desired total mass for the mixture, which itself depends on the powder density and the intended size of the rod that has to be formed later on. Within this work, a bit more total mass was weighed in than actually needed for one rod because after each production step, a small amount of powder was kept for possible investigations later on (usually powder diffraction measurements or EDX analyses).

It might be necessary either to weigh in an excess of a certain reactant in order to compensate evaporation (e.g., for manganites [see Sec. 4.4.2]) or to weigh in an oxygen deficiency to compensate oxygen capture (e.g., for $EuTiO_3$ [see Sec. 1.4.1]).

Weighing, mixing, and grinding For weighing the powders, a Sartorius ED224S analytical balance was used that has an accuracy of 0.1 mg [49]. A homogeneous mixture is substantial for the solid-state reaction. It ensures that all reaction partners find each other and no residual reactants survive the chemical reaction process. The consistency of reactants ranges from finely granulated to lumped. Therefore, a simple mixing with a spoon or spatula is not sufficient. An additional grinding is needed to crush the lumps. Mixing and grinding can be done manually by using an agate[5] pestle and mortar or by using a planetary ball mill (Fritsch Pulverisette). It consists of a lockable agate mortar with three agate balls, covered with a lid of the same material, which is installed into a rotator with adjustable rotation speed and milling time.

The usual procedure begins with a manual mixing with a spoon (and a manual grinding with a pestle if the powder is lumped) followed by 30 min to 60 min milling. An interlude of manual mixing avoids that some material eludes the intermixing by sticking at the mortar walls, the lid, and the balls. The sticky powder is removed from the agate parts and reunited with the rest using a piece of overhead transparency. Scratching with a spoon or spatula implies the risk of swarf contamination, while overhead transparencies are made of flexible organic material that does not chip but adapt to the shape of the mortar and balls. The mixing and grinding procedure is completed by another milling for 30 min to 60 min. In the first run, a high rotation speed is used to set the focus on grinding, while in the second run a slower speed is used to emphasize the mixing.

The degree of intermixing can be judged easily if all powders have different colors, e.g., for $Nd_{1-x}Ca_{1+x}MnO_4$, where the reactants are blue (Nd_2O_3), white ($CaCO_3$), and brown-black (MnO_2), and for $LiFe(WO_4)_2$, where the reactants are white (Li_2CO_3), red (Fe_2O_3), and black ($WO_{2.9}$). If all reactants have the same color, a visual inspection does not help, e.g., for $SrTiO_3$, where the reactants $SrCO_3$ and TiO_2 are both white[6]. Since 2×30 min

---

[4] Standard atomic weights depend on isotopic abundances that are found in natural materials of the Earth's crust. Due to natural variation, the isotopic composition can be different for a specific piece of material [47]. However, this effect is small and negligible for our purpose.

[5] A natural variety of quartz (SiO_2).

[6] Although the color shade is slightly different (TiO_2 appears yellowish compared to $SrCO_3$), the mixing is not accompanied by a visible color change.

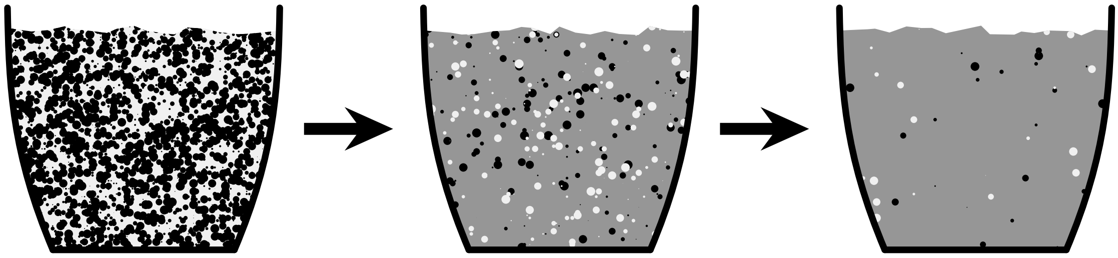

Figure 1.1: Illustration of powder reactions. Left: Mixture of two reactants (black and light gray) in a crucible. Center: Residual reactants embedded in a matrix of their product (dark gray) after first heating. Right: Repeated mixing and heating minimizes unreacted residuals and increases homogeneity. Since the average distance of reaction partners becomes larger after each step, the temperature should be increased as well, to increase the diffusion length.

milling—together with the described interlude—is sufficient for the multicolored powders, one can assume the same for the unicolored powders.

If no powder reaction is done before the floating-zone procedure (e.g., like in the synthesis of $EuTiO_3$), or if the volume of one reactant is extremely small compared to the other reactants (e.g., the amount of lanthanum for $Eu_{1-x}La_xTiO_3$ with $x \leq 0.1\,\%$), then mixing and grinding is even more crucial. In these cases, longer milling times (e.g., 3×60 min) and an additional manual interlude has been used.

Powder reactions For most materials, it is appropriate to separate the chemical reaction from the crystal growth procedure. This yields the most homogeneous, thoroughly reacted materials because after each heating, the material is ground and mixed again. The heating induces a solid state reaction, which is permitted by particle diffusion processes. The diffusion length is proportional to the temperature. Due to the finite diffusion length, one can assume that not all reaction partners found each other during the first heating [see Fig. 1.1]. As a result, dilute residuals of the reactants remain present, embedded in the chemical product. By a subsequent grinding and mixing, these residuals are homogeneously distributed over the entire product. The average distance between reaction partners is now larger compared to the unreacted mixture. To increase the diffusion length, a higher temperature is used in the second run. This procedure can be repeated as often as necessary to increase the homogeneity up to a sufficient level. Powder diffraction is a proper tool to judge the effect of time and temperature on the powder's homogeneity and the usefulness of further heating processes. Therefore, small amounts of powder are kept after each heating.

There might be good reasons to skip powder reactions completely. The main advantage of the floating-zone technique to be a crucible-free method is partially foiled by powder reactions because they require crucibles. Chemical reactions between powder and crucible, or contamination with crucible material can be an issue already far below the melting point. In some cases, this problem can be circumvented by using other crucible materials (e.g., platinum, alumina, zirconia, magnesia) or at least attenuated by using a pressed pellet of powder to minimize the contact area. This method has been used for the preparation of molybdates [see Sec. A.1.2]. If loose powder of the same material is put between pellet and crucible, the contact area can be reduced even to zero.

Another reason to skip powder reactions is oxygen capture. If the intended oxidation states are below the maximum possible, the presence of oxygen during the heating procedure will result in further oxidation and has to be prevented. Possible sources of oxygen are residual amounts of air after flushing the furnace, leakages in the furnace system, oxygen contaminations of the used inert gas, and release of oxygen from the furnace itself upon heating. None of these oxygen sources can be eliminated completely. This becomes increasingly problematic with each heating procedure. Therefore, the number of preliminary reactions should be kept as small as possible, which is counterproductive concerning the goal of a maximum homogeneity; a typical optimization problem. If preliminary powder reactions are skipped, chemical reaction and crystal growth take place during the floating-zone procedure. A prime example of this approach is the growth of $EuTiO_3$ [see Sec. 1.4.1 for a detailed description].

Shaping and pressing of the rod The characteristics of a floating-zone furnace require samples with cylindrical symmetry. Therefore, the powder has to be formed as cylindrical rod. This is done using a flexible rubber tube (a so-called Penrose drain[7]) that shrinks upon compression and a test tube for shaping the rubber tube. One end of the rubber is sealed by a knot, the other end is kept open. The rubber is inserted into a test tube of sufficient length and diameter, the open end is everted and put over the rim of the test tube. Talc[8] between rubber and test tube makes the removal afterwards easier. To shape the rubber, the test tube is pumped through a hole at the bottom. Thus, the rubber adapts the test tube's shape. A crumpled piece of paper at the bottom of the test tube avoids a suction of the rubber into the pump line.

A high densification is of essential importance for a successful crystal growth to minimize capillary effects during the melting process [see Sec. 4.4]. Because bulk density and tap density of a powder can diverge a lot, the powder is filled into the rubber and densified by vibrations via hitting the test tube. To obtain a homogeneous density, filling and hitting are alternated frequently. When the rubber is filled completely, it is sealed with a silicone plug by putting the everted part of the rubber over the plug. Air residuals are removed by pumping the rubber. This is done by puncturing the plug with a cannula that is connected to the pump line. A crumpled piece of paper, stuffed into the plug beforehand, avoids a suction of powder. Due to its elasticity, the silicone plug is self-sealing after removal of the cannula and can be reused many times. A bending of the rod can be anticipated by softly rolling the rod over a flat surface. Any initial bending will be magnified by the subsequent pressing as well as by a potential sintering later on and should be avoided from the beginning. The rod

---

[7] A Penrose drain is intended for medical applications, in particular as surgical drain. It is named after the American surgeon Charles Bingham Penrose (1862–1925) [50].

[8] Magnesium silicate monohydrate ($3\,MgO \cdot 4\,SiO_2 \cdot H_2O$)

is pressed using a manual hydraulic press. Typical values are 15 to 20 tons weight on an area of $\pi(32\,\mathrm{mm})^2$, which corresponds to a pressure between approximately 45 MPa and 60 MPa. After releasing the pressure slowly, the rod is taken out of the water and uncaged carefully from its rubber shell using nail scissors.

Sintering Sintering is a “temperature-induced coalescence and densification of porous solid particles below the melting points of their major components” [51]. As already pointed out, densification is important to prevent capillary action during melting. For many materials, sintering is crucial for a stable floating-zone procedure. Prime example is the growth of manganites [see Sec. 4.4]. In principle, sintering can be done either in a muffle furnace or tube furnace—this demands the usage of a crucible or boat, with all its already discussed shortcomings—or in the floating-zone image furnace. The latter variant requires a fixation of the rod with a wire. Depending on the rod material, this can be impractical because the softness of the rod may hinder a fixation and will break in the attempt. In this case, an additional preliminary sintering in a muffle furnace or tube furnace is needed to harden the rod. This approach is necessary for the growth of manganites [see Sec. 4.4] while for titanates, the stability of the merely pressed rod is sufficient to fix a wire [see preparation of $EuTiO_3$ and $YTiO_3$ in Secs. 1.4.2 and A.3, respectively].

1.3 Growth procedure

Principle Principle of the floating-zone technique is the punctual melting of a polycrystalline sample while traveling the melting zone through the sample. Below the melting zone, the material recrystallizes to larger grains. Progressively, the grains with favorable orientation grow faster at the expense of unfavorable oriented ones; a process that is referred to as nucleation. In the end, ideally, one single crystallite survives.

Mirror-furnace setup The punctual melting is achieved with light emitted by a halogen lamp and focused by a concave mirror. The geometrical shape of the mirror needs to have two focal points; a requirement, that is implemented by the ellipsoid. The light source is located in one focal point, the light destination (i.e., the sample to be melted) in the other one. Floating-zone systems can utilize a single lamp–mirror combination [46, 52–54] [see Fig. 1.2 (a)] or multiple lamp–mirror modules in order to increase the accessible power at the destination and to improve the homogeneity of heat distribution. Most commercial systems have either two or four lamp–mirror modules with ellipsoidal mirrors arranged such that their target focal points coincide in the center [see Figs. 1.2 (b) and 1.2 (c)].

Figure 1.2 (d) shows a front-view cross section of a two-mirror furnace. Two cylindrical steel shafts with vertical travel way through the central focus allow a mounting of the sample. The sample to be melted—the so-called feed rod—is attached to the upper shaft using a

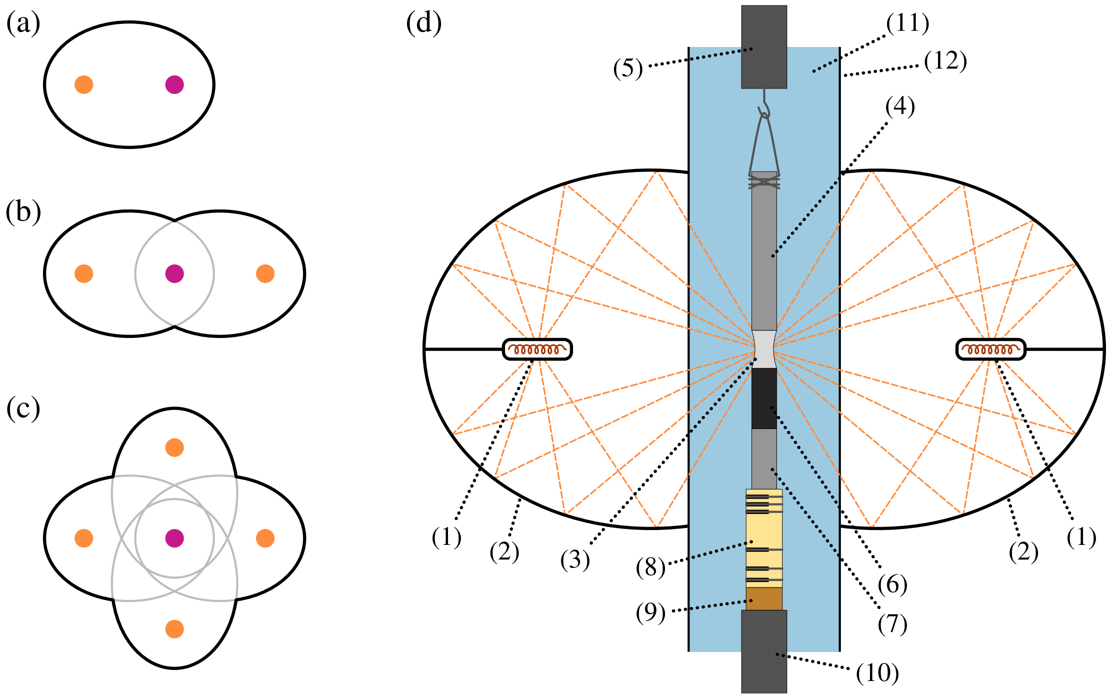

Figure 1.2: Floating-zone furnace layout. Top-view cross sections of different furnace layouts with lamps (●) and common focal points (●): (a) single-mirror layout, (b) two-mirror layout, (c) four-mirror layout. (d) Front-view cross section of a two-mirror furnace: Light emitted by halogen lamps (1) is collected by ellipsoidal mirrors (2) and focused in the center, where the melting zone is established (3). It travels upwards through the feed rod (4) that is fixed by a wire to the upper shaft (5). Below the melting zone, the crystal (6) grows on top of the seed rod (7) that is fixed to a corundum tube (8), which itself is connected by a metal socket (9) to the lower shaft (10). The sample space contains a defined atmosphere (11) that is confined by a quartz tube (12).

high-melting wire[9] for fixation. A so-called seed rod is fixed on the lower shaft. It allows an independent control of the two solid parts above and below the melting zone. Both shafts can rotate with individual rates and senses of rotation. In addition to the overall pulling rate, also a relative travel speed of the shafts can be set. The sample chamber is surrounded by a quartz tube allowing the crystal growth to take place in a defined atmosphere with pressures up to nearly 10 bar.

In our institute, two floating-zone furnaces are available: the four-mirror system FZ-T-10000-H-VI-VP by Crystal Systems Inc. (CSI)[10] built in August 2000 and the two-mirror system SC1-MDH by Canon Machinery Inc. (CMI) built in March 2012. The focus travel through the feed rod is achieved either by moving the mirror stage upwards and keeping

---

[9] A nickel–chromium alloy (90 % Ni, 10 % Cr), melting point 1430 °C [55], trade name Chromel or Chromega, originally intended as thermocouple wire.

[10] Now Crystal Systems Corporation (CSC).

the shafts fixed (CSI) or by moving both shafts downwards while keeping the mirror stage fixed (CMI). An overview of the properties of both furnaces is given in Tab. 1.1.

Growth direction A crystal can be forced to grow into a specific crystallographic direction by using an oriented single-crystal as seed. The material grown on top adapts the crystallographic orientation even if the seed crystal is not of the same material as the feed rod but has similar lattice parameters. This allows to skip the nucleation process (which usually costs some millimeters/hours) and to start directly with the single-crystal growth. Disadvantage of this method is, that an existing single crystal has to be sacrificed with the risk of destruction upon melting. Furthermore, even a small misalignment of the seed crystal will result into an inclined growth direction and the crystal will gradually grow out of the focus. Apart from that, it might be desirable to allow a crystal starting its growth from scratch, e.g., to determine the natural growth direction later on. Within this work, only polycrystalline seed rods were used.

1.3.1 Parameters

Crystal growth can be optimized by several parameters. Parameters of the preparatory production steps are already discussed in the previous sections. Nevertheless, they are part of the total parameter space for floating-zone crystal growth and have to be considered in the optimization process.

Furnace model If different furnace models are available, the furnace design is an important additional parameter to choose from. Two- and four-mirror furnaces have different properties apart from the number of mirrors. A four-mirror furnace has a more homogeneous heat distribution, which is desirable in-plane but unwanted vertically where a large temperature gradient is advantageous. Thus, a two-mirror furnace usually produces a smaller melting zone [56, 57] than the four-mirror version. If the single-lamp power is the same, a four-mirror furnace has a higher total power compared to a two-mirror model. At the same time, the ellipsoidal surface per mirror is smaller because four mirrors have to share the 360° of the mirror-stage plane around the center. This means the ellipsoids are more truncated at the edges, while the mirrors of the other system even exceed the ellipsoidal vertices. Therefore, in the four-mirror layout, a single mirror collects less light than one of the two-mirror system. This is seen in the comparison of both systems given in Tab. 1.1: although the maximum total power differs by 2000 W, the highest accessible temperature differs by 100 °C only. Furthermore, the effective power at the sample location strongly depends on a precise adjustment of the lamps, which is more difficult the more lamps are to be adjusted. Thus, the advantage of having two more mirrors is partially foiled.

Another difference is the cold trap, which is available for the two-mirror furnace only[11].

---

[11] This is a difference of these two specific furnace models but not of two- and four-mirror furnaces in general. There can be four-mirror furnaces with a cold-trap option and two-mirror furnaces without.

Parameter	CSI	CMI
Built	August 2000	March 2012
Number of lamps and mirrors	4	2
Single-lamp power (W)	150, 300, 500, 1000, 1500	1500, 2000
Max. total power (W)	6000	4000
Max. temperature (°C)	2200	2100 †
Max. pressure (bar)	9.5	9.7
Max. growing length (mm)	150	200
Automatic growth speed ($\mathrm{mm\,h^{-1}}$)	0.05–27	0.5–50
Manual growth speed ($\mathrm{mm\,min^{-1}}$)	50–700	300
Max. rotation speed (rpm)	5–60	5–60
Mirror stage	movable	fixed
Upper shaft	movable	movable
Lower shaft	fixed	movable
Cold trap	no	optional
Cooling of mirrors/lamps	air	water
Cooling of sample-space sockets	water	water
Remote control	no	yes

Table 1.1: Properties of floating-zone image furnaces. Comparison between CRYSTAL SYSTEMS INC. (CSI) model FZ-T-10000-H-VI-VP [58] and CANON MACHINERY INC. (CMI) model SC1-MDH [59]. † Estimated value.

If a material evaporates upon melting, the vapor deposits on comparatively cold parts of the sample chamber, which are typically the water cooled metal sockets of the quartz tube but also the quartz itself. Over time, the quartz tube is covered with deposit, which dims out the light arriving at the sample location. The result is an effective power decline that has to be compensated by a power raise, which again fuels the evaporation. To counteract this problem, a colder part can be supplied that catches the vapor instead of the quartz tube. This so-called cold trap is a water-cooled metal cylinder that is located close to the central focus. For materials with high vapor pressure (e.g., ruthenates), the usage of a cold trap is mandatory, but also for less evaporating materials (e.g., manganites, molybdates) it is helpful. For non-evaporating materials (e.g., titanates, zirconates), a cold trap makes no difference.

Lamp power Apart from the furnace model, the floating-zone procedure itself has a bunch of parameters that can be adjusted. The most prominent one is the lamp power, which is directly related to the temperature at the central focus. A list of all lamps available in our institute is given in Tab. 1.2. One can choose between lamps with different maximum powers ranging from 150 W to 1500 W for the four-mirror furnace (CSI), or 1500 W to 2000 W for

ID	Furnace	Power (W)	Filament	Lamp item number	Growths
	CSI	150	flat	JIH-100V-150WG-CS	0
L1	CSI	300	flat	JIH-100V-300WG-CS	3
	CSI	500	flat	JIH-100V-500WG-CS	0
L2	CSI	1000	flat	JIH-100V-1000WCG-CS	42
L3	CSI	1500	flat	JIH-100V-1500WCG-CS	1
L4	CSI	1000	helixlike	JCD-100V-1000WC	1
	CMI	1500	flat	JIH-100V-150WG-CS	0
L5	CMI	2000	flat	JIH-100V-150WG-CS	73

Table 1.2: Halogen lamps for floating-zone systems. Overview of single-end halogen lamps from Ushio Lighting, Inc. available in our institute for both floating-zone furnace models FZ-T-10000-H-VI-VP (CSI) and SC1-MDH (CMI). Lamps L1, L2, L3, L4, and L5 were used within the scope of this thesis.

the two-mirror furnace (CMI). Naturally, lamps with the largest maximum power have the broadest accessible temperature range but also the largest filaments. Since the focused light is an image of the lamp filament, a larger maximum power usually comes at the price of a larger lamp filament resulting in a broader spot and a reduced effective temperature at the sample location. Thus, a lamp with double maximum power does not provide twice as large temperatures. Furthermore, lamps with smaller maximum power allow a finer graduation of the power adjustment. To get the sharpest spot, it is advantageous to choose from all lamps that allow a melting of the respective material, the lamps with the lowest maximum power.

Most of the lamps [see Tab. 1.2] are designed with a flat filament that produces an image that is flat likewise resulting in a rather homogeneous heat distribution within the filament plane and a steep temperature gradient perpendicular to that plane[12]. In contrast, the filaments of the JCD lamp model (L4) are helixlike and produce a more circular spot resulting in an (usually unwanted) smoother vertical temperature gradient [see also Sec. 4.4]. Within the scope of this thesis, for all growths carried out in the CMI furnace, the 2000 W lamps (L5) were used. For growths in the CSI furnace, 1500 W lamps (L2) and helix-filament lamps (L4) were used only once [see Sec. 4.4]. The 300 W lamps (L1) were used for three attempts to grow $LiFe(WO_4)_2$ [see Sec. A.5]. All other growths in the CSI furnace were performed with 1000 W flat-filament lamps (L2).

One should note that the actual temperature of a sample located at the focus depends not only on the lamp power but also on the sample's characteristics like reflectivity, emissivity, and thermal conductivity.

Atmosphere A quartz tube confines the sample space and allows the crystal growth to take place in a defined atmosphere. One can choose between reducing (forming gas H_2 + Ar

---

[12] Therefore, the lamps are installed with filaments perpendicular to the growth direction.

or H_2 + N_2), oxidizing (O_2), or inert gases (Ar, N_2). Pressures up to nearly 10 bar can be established [see Tab. 1.1] either static or with gas flow. Vapor deposition on the quartz tube can be minimized not only by a cold trap but also by using a gas flow which carries the vapor out of the sample chamber. Increasing the gas pressure can help to diminish evaporation but also requires a temperature increase to keep the sample liquid.

Pulling speed and shaft rotation The pulling speed is the relative speed of sample and mirror plane. With this speed, the solid phase melts at the upper boundary of the melting zone and recrystallizes at its lower boundary. For example, in $EuTiO_3$ (lattice parameter $a \approx 3.8$ Å), a pulling speed of $10\,\mathrm{mm\,h^{-1}}$ ($\approx 28\,000$ Å $\mathrm{s^{-1}}$) corresponds to a crystallization rate of approximately 7100 unit cells per second. Typically, low pulling speeds enhance the melting and minimize the emergence of impurity phases in the recrystallized part. Therefore, the speed is usually chosen as small as possible. However, in order to minimize evaporation, the pulling speed should be as fast as possible; another optimization problem. The upper shaft is controllable independently. Its relative speed to the lower shaft controls the thickness of the crystal. It can move either downwards, to enlarge the crystal's diameter, or upwards to shorten it. Shaft rotation has an influence on the convection flows inside the liquid phase and, in consequence, on the shape of the liquid–solid phase boundary.

1.3.2 How to find the right parameters

Many aspects of the floating-zone process can be described with theoretical models (e.g., Ref. [60]) that provide the ideal growth parameters for a certain material. However, such a model has to be fed with a bunch of material-specific properties. It requires knowledge about the surface tension, wetting angle, and viscosity of the liquid phase, the density, optical properties (e.g., emissivity, absorption), and thermal conductivity of both liquid and solid phase as well as the temperature and pressure dependence of all of these properties. Thus, despite the existence of theoretical models for the floating-zone process, a principal dilemma remains: Researchers are mostly interested in materials with new, unknown characteristics, so the information needed to predict the growth parameters is not available. Contrariwise, if a material is known in such detail that the ideal growth parameters are predictable, there is no need to grow it because everything is already known[13]. Therefore, crystal growth in solid state research is performed using an empirical approach, i.e., observing the system's improvement or impairment when one parameter is changed while all others stay fixed. Hence, finding the right parameters for a certain material is usually a time-consuming and exhausting procedure. Literature recipes (often not available, or not reliable) or one's own experience with similar materials can be used as a starting point.

---

[13] This is the perspective of fundamental research. Of course, for industrial production, such models can be useful. A prime example for that is silicon.

Reactants	Powder/SC	Atmosphere	Temp.	Dwell	Ref.
Eu_2O_3, TiO_2	Powder	H_2	1200 °C	2 h	[61]
Eu_2O_3, TiO_2	Powder	H_2	1200 °C	unknown	[62]
Eu_2O_3, TiO_2	Powder	Ar + 5 % H_2 flow	1000 °C	2 × 10 h	[63]
Eu_2O_3, TiO_2	Powder	H_2 flow	1150 °C	20 h	[64]
EuO, TiO_2	Powder	"non-oxidizing"	unknown	unknown	[65]
EuO, TiO_2	Powder	Vacuum	1000 °C	8 h	[62]
Eu_2O_3, Ti_2O_3	Powder	Vacuum	1150 °C	72 h	[62]
Eu_2O_3, Ti_2O_3	Powder	Ar	1400 °C	4 d	[66, 67]
Eu_2O_3, Ti_2O_3	Powder	Ar	1753 °C	2 d + 3 d	[68]
Eu_2O_3, Ti_2O_3	Powder	Ar + 10 % H_2	1500 °C	unknown	[69]
Eu_2O_3, Ti, TiO_2	Single crystal	Ar	(no powder reaction)		[70]

Table 1.3: Preparation of $EuTiO_3$ in literature. The single crystals grown in Ref. [70] were also used in Refs. [68, 71–73] as described in Ref. [68].

1.4 Growth of $EuTiO_3$

1.4.1 Chemical aspects

Compared to $SrTiO_3$ [see Sec. A.2], the synthesis of $EuTiO_3$ is more complicated. The preparation recipes for $EuTiO_3$ described in literature differ a lot from each other, not only regarding the heating parameters (temperature, duration, atmosphere) but also the used reactants. An overview of literature recipes is given in Tab. 1.3. Like most transition metals, titanium appears in many different oxidation states ranging from elemental titanium metal, over TiO and Ti_2O_3 to the fully oxidized TiO_2. Furthermore, one should be aware of the fact that not all of these oxides have the well-defined stoichiometry that its formula suggests, but they rather show a certain phase width, which is seen in Ti–TiO_2 phase diagrams, e.g., in Refs. [74–78]. Europium can be divalent or trivalent [see Sec. 3.2.2] and appears as metal, EuO, the mixed-valent Eu_3O_4, and fully oxidized Eu_2O_3 [79].

Due to this large number of potential reactants, the number of combinations that can produce $EuTiO_3$ is manifold. By looking at literature recipes, one finds no one using metallic Eu or mixed-valent Eu_3O_4, two groups use EuO [62, 65], all others use Eu_2O_3 [61–64, 69–71, 80, 81]. Since europium is divalent in the desired product [see also Sec. 3.2.2], it seems obvious to start with an oxide containing Eu^{2+} as well, which is EuO. The chemical equation would be simply $EuO + TiO_2 \longrightarrow EuTiO_3$, which is actually used in Refs. [62, 65]. However, EuO is not easy to handle due to its sensitivity to humidity and air. Therefore, it is reasonable to follow the majority of publications and use the most stable oxide Eu_2O_3. It is clear that this choice requires a charge transfer during the chemical reaction to get Eu^{2+}.

For titanium, it is less obvious which reactants to choose. The following four paths are possible: The reaction

$$\frac{1}{2}\,\mathrm{Eu_2O_3} + \mathrm{TiO_2} \longrightarrow \mathrm{EuTiO_3} + \frac{1}{4}\,\mathrm{O_2}\uparrow \tag{1.1}$$

requires the usage of a reducing atmosphere, otherwise the surplus oxygen will provide the formation of Eu^{3+} and produce the pyrochlore $\mathrm{Eu_2Ti_2O_7}$ via $\mathrm{Eu_2O_3} + 2\,\mathrm{TiO_2} \longrightarrow \mathrm{Eu_2Ti_2O_7}$. Reaction path (1.1) is used in Refs. [61–64]. A usage of $\mathrm{TiO_2}$ together with $\mathrm{Eu_2O_3}$ without the requirement of a reducing atmosphere is only possible in combination with a second titanium reactant. One example is

$$\frac{1}{2}\,\mathrm{Eu_2O_3} + \frac{1}{4}\,\mathrm{Ti} + \frac{3}{4}\,\mathrm{TiO_2} \longrightarrow \mathrm{EuTiO_3} \tag{1.2}$$

which is used in Refs. [70, 71, 75]. Another example is

$$\frac{1}{2}\,\mathrm{Eu_2O_3} + \frac{1}{2}\,\mathrm{TiO} + \frac{1}{2}\,\mathrm{TiO_2} \longrightarrow \mathrm{EuTiO_3} \tag{1.3}$$

which seems to be unattempted in literature. However, the most straightforward reaction with $\mathrm{Eu_2O_3}$ is

$$\frac{1}{2}\,\mathrm{Eu_2O_3} + \frac{1}{2}\,\mathrm{Ti_2O_3} \longrightarrow \mathrm{EuTiO_3} \tag{1.4}$$

because it does not produce surplus oxygen, it requires only two reactants, and no reducing atmosphere is needed. It is used in Refs. [62, 66, 69, 81]. Drawback of $\mathrm{Ti_2O_3}$ is its finite phase width that is considerably larger than that of $\mathrm{TiO_2}$ [75]; an issue also pointed out in Ref. [82]. While the first method (1.1) requires a reducing atmosphere, for the other three paths at least an inert atmosphere is needed to avoid the emergence of the pyrochlore phase by captured oxygen.

Apart from these stoichiometric variants, it can be necessary to compensate oxygen capture by starting with an oxygen-deficient composition. This is only possible with two different titanium oxides $\mathrm{Ti}_a\mathrm{O}_b$ and $\mathrm{Ti}_c\mathrm{O}_d$ adjusted in the desired ratio. The general chemical equation for that is

$$\frac{1}{2}\,\mathrm{Eu_2O_3} + m\,\mathrm{Ti}_a\mathrm{O}_b + n\,\mathrm{Ti}_c\mathrm{O}_d \longrightarrow \mathrm{EuTiO}_y \tag{1.5}$$

with prefactors

$$m = \frac{c}{bc - ad}\left(y - \frac{3}{2} - \frac{d}{c}\right), \qquad n = \frac{a}{ad - bc}\left(y - \frac{3}{2} - \frac{b}{a}\right) = \frac{1 - ma}{c}, \tag{1.6}$$

in which $a, c \in \{1, 2\}$ and $b, d \in \{0, 1, 2, 3\}$ with $bc \neq ad$. The amount of oxygen y is usually expressed as deviation from the stoichiometric value $y = 3 - \delta$. For TiO and $\mathrm{TiO_2}$, Eq. (1.5) reduces to

$$\frac{1}{2}\,\mathrm{Eu_2O_3} + \left(\frac{7}{2} - y\right)\mathrm{TiO} + \left(y - \frac{5}{2}\right)\mathrm{TiO_2} \longrightarrow \mathrm{EuTiO}_y\,. \tag{1.7}$$

	Ti	TiO	Ti_2O_3	TiO_2
Ti	–			
TiO	$[1.5, 2.5]$	–		
Ti_2O_3	$[1.5, 3.0]$	$[2.5, 3.0]$	3	
TiO_2	$[1.5, 3.5]$	$[2.5, 3.5]$	$[3.0, 3.5]$	3

Table 1.4: Combinations of titanium-oxide reactants. Accessible ranges of oxygen content y in the reaction (1.5) for all combinations of titanium oxides.

Reactants	Eq.
Eu_2O_3, Ti, TiO_2	(1.2)
Eu_2O_3, Ti_2O_3	(1.4)
Eu_2O_3, TiO, Ti_2O_3	(1.8)
Eu_2O_3, TiO, TiO_2	(1.7)

Table 1.5: Reactant combinations for $EuTiO_3$. All tested combinations and their respective chemical equation.

Name	Formula	Appearance	Purity
Europium(III) oxide	Eu_2O_3	white	99.99 %
Lanthanum(III) oxide	La_2O_3	white	99.99 %
Titanium	Ti	metallic	99.99 %
Titanium(II) oxide	TiO	brown	99.5 %
Titanium(III) oxide	Ti_2O_3	dark violet	99.8 %
Titanium(IV) oxide	TiO_2	white	99.99 %
Niobium(V) oxide †	Nb_2O_5	white	99.9 %

Table 1.6: Reactants for ABO_3. Polycrystalline powders used as reactants for the synthesis of ABO_3 (A = Eu, $Eu_{1-x}La_x$, B = Ti, $Ti_{1-x}Nb_x$). † from CHEMPUR, other powders from ALFA AESAR.

This choice of reactants limits the (nominally) accessible oxygen content to $2.5 \leq y \leq 3.5$ or $-0.5 \leq \delta \leq 0.5$. For TiO and Ti_2O_3, Eq. (1.5) reduces to

$$\frac{1}{2}\, Eu_2O_3 + (6 - 2y)\, TiO + \left(y - \frac{5}{2}\right) Ti_2O_3 \longrightarrow EuTiO_y\,. \tag{1.8}$$

Here, the nominal oxygen content is limited to $2.5 \leq y \leq 3$ or $0 \leq \delta \leq 0.5$. An overview of all possible combinations of titanium-oxide reactants is given in Tab. 1.4 including the accessible ranges of oxygen content y. All combinations of reactants, tested within the scope of this thesis, are listed in Tab. 1.5.

1.4.2 Preparation

Polycrystalline powders of Eu_2O_3, Ti, TiO, Ti_2O_3, and TiO_2 were used as starting materials [see Tab. 1.6 for details]. Within this work, all three stoichiometric variants with inert atmosphere were carried out, i.e., reaction path (1.2) using the reactants Eu_2O_3, Ti, TiO_2 (sample JE87), path (1.4) using Eu_2O_3, Ti_2O_3 (sample JE88), and path (1.3) using Eu_2O_3,

Sample		R	Floating-zone furnace parameters								SC
ID	y		M/L	Gas	Sintering		Growth				
					U V	v mm/h	U V	v mm/h	r rpm	p bar	
JE87	3	(1.2)	CMI/L5	Ar	-	-	78	10	34	3–7	-
JE88	3	(1.4)	CMI/L5	Ar	-	-	80	10	38–47	2.5	-
JE90	2.95	(1.8)	CMI/L5	Ar	72	20	80	10	30	2	-
JE91	3	(1.3)	CMI/L5	Ar	-	-	70	10	30	3	-
JE93	3	(1.3)	CMI/L5	Ar	60	15	69	10	22–30	3	✓
JE95	3	(1.3)	CMI/L5	Ar	70	15	-	-	-	-	-
JE102	3	(1.3)	CMI/L5	Ar	55	20	55	10	34	7.5	-
JE107	2.95	(1.7)	CMI/L5	Ar	-	-	83	30	36	1.4	-
JE108	3	(1.3)	CMI/L5	Ar	-	-	55	10	24–34	1.1	-
JE109	3	(1.3)	CMI/L5	Ar	-	-	70	8	28	1.3	-
JE110	2.99	(1.7)	CMI/L5	Ar	-	-	72	8	28	1.2	-
JE111	2.98	(1.7)	CMI/L5	Ar	-	-	75	8	28	1.4	✓✓

Table 1.7: Synthesis of $EuTiO_3$: Parameters. All attempts to synthesize $EuTiO_3$ with sample identifier, nominal oxygen content y, chemical reaction R, furnace model M and halogen lamps L [see Tab. 1.2], gas, lamp voltage U in V and pulling speed v in mm h^{-1} used for sintering and growth, relative rotation of the rods r in rpm, gas pressure p in bar, and success of single-crystal growth SC [see Tab. 1.8].

TiO, TiO_2 (samples JE91, JE93, JE95, JE102, JE108, JE109). Details of the growth parameters are summarized in Tab. 1.7. Although only small crystals could be obtained, the reactant combination with Eu_2O_3, TiO, and TiO_2 was the best working one and was used from sample JE91 onwards. All $EuTiO_3$ samples were prepared without any preliminary powder reaction, similar to Ref. [70], i.e., the powders were mixed, directly pressed to a rod, and installed into the floating-zone furnace. As already explained in Sec. 1.2.2, skipping the powder reactions is an appropriate way to minimize the risk of oxygen capture. However, the main issue of $EuTiO_3$ growth was a sudden change of the feed rod's melting point after a few millimeters growth. This might be a hint for leakages in the gas system of the mirror furnace causing an increasing oxygen contamination during the growth process.

In order to compensate oxygen capture, several off-stoichiometric mixtures with oxygen deficiencies $0.01 \leq \delta \leq 0.05$ were weighed in (samples JE90, JE107, JE110, JE111). One, using reaction (1.8) with $\delta = 0.05$ (sample JE90) and three, using (1.7) with $\delta = 0.01, 0.02,$ and 0.05 (samples JE110, JE111, and JE107, respectively). The most successful growth attempt is JE111 having a nominal oxygen deficiency of $\delta = 0.02$. A single crystal of approximately 1.5 cm in length has been achieved. Apart from one small piece from JE93, all investigated $EuTiO_3$ samples are cut from this JE111 crystal.

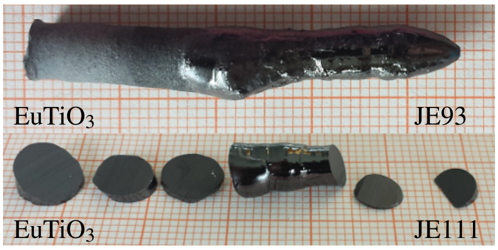

Figure 1.3: Single crystals of $EuTiO_3$. Only small single-crystalline pieces were obtained from JE93, whereas JE111 contains a larger piece of ≃ 1.5 cm.

Symb.	Single-crystal size
-	No single crystal
✓	Millimeter size
✓✓	≃ 1 cm
✓✓✓	Numerous centimeters

Table 1.8: Symbols for single-crystal sizes.

Ion	Wyckoff symbol	Site symmetry	Coordinates
Eu	$1b$	$m\bar{3}m$	1/2, 1/2, 1/2
Ti	$1a$	$m\bar{3}m$	0, 0, 0
O	$1d$	$4/mm.m$	1/2, 0, 0

Table 1.9: Atomic positions of $EuTiO_3$. Standard setting of the cubic perovskite structure with space group $Pm\bar{3}m$ (No. 221), where Ti is placed at the origin and Eu at the center of the unit cell [84] [for an illustration see Fig. 2.3]. The atomic positions have no free parameter.

1.4.3 Properties of the as-grown $EuTiO_3$ crystals

$EuTiO_3$ crystals show neither facets nor an appreciable cleavage. They are opaque with black color, in agreement with Ref. [82]. The color can be explained by band structure calculations that suggest a band gap of 1 eV between the Eu 4f band and the Ti 3d band, and a Fermi level at the upper boundary of the Eu 4f states [83].

Figure 1.4 shows an x-ray powder diffraction pattern measured with a BRUKER D5000-MATIC diffractometer with Bragg–Brentano geometry and Cu x-ray tube. The software JANA2006 [85] was used for structure refinement. The powder diffraction pattern is well-described by a single-phase Rietveld analysis using the cubic space group $Pm\bar{3}m$ (No. 221) and the atomic positions given in Tab. 1.9, with the exception of one single peak at $2\theta = 29.2°$ that cannot be described within this model. The refined lattice parameter is $a = 3.902\,00(15)$ Å, which is significantly smaller than most of the literature values $a > 3.904$ Å [64, 71]. As shown in Ref. [86], the lattice parameter of $EuTiO_{3-\delta}$ is sensitive to the exact oxygen content since the change $Ti^{4+} \longrightarrow Ti^{3+}$ ($\delta > 0$) increases the unit-cell volume, whereas a change $Eu^{2+} \longrightarrow Eu^{3+}$ ($\delta < 0$) decreases it. Thus, a smaller lattice parameter might point to the presence of a certain amount of Eu^{3+}.

$EuTiO_3$ hosts divalent europium [see also Sec. 3.2.2] with an electronic configuration of [Xe]4f^7 that implies a rather large magnetic moment of $7\mu_B$. In contrast, Eu^{3+} has no magnetic moment because its configuration [Xe]4f^6 leads to $J = 0$ [see also Tab. 3.3]. Thus, for a pure Eu^{2+} system, one expects a saturation magnetization $M_{sat} = g_J J = 7\,\mu_B$.

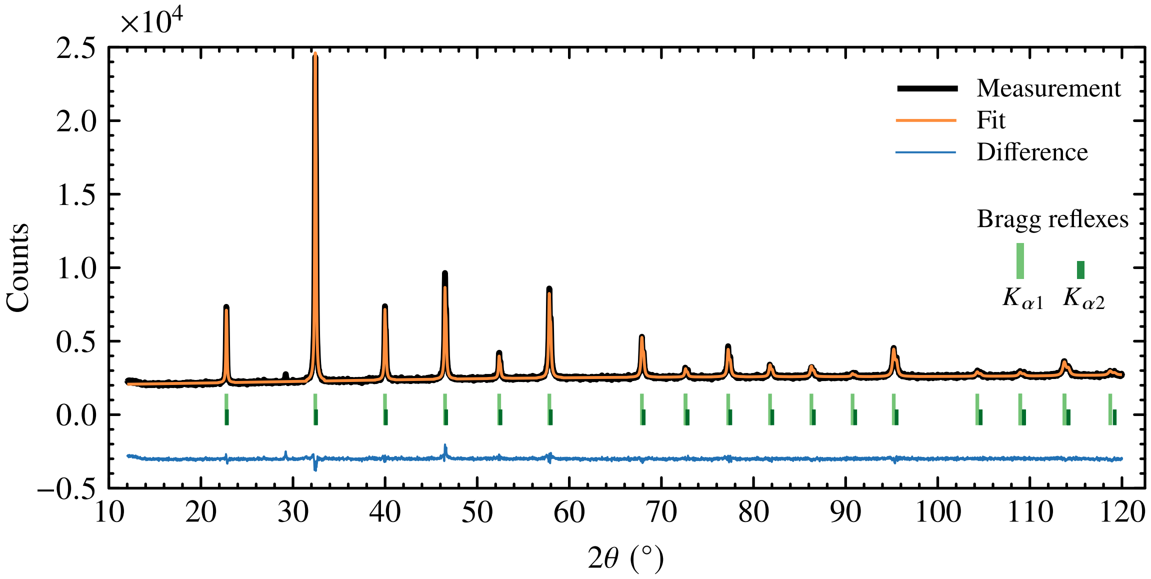

Figure 1.4: XRD powder pattern of $EuTiO_3$ and Rietveld fit. Powder x-ray diffraction pattern of pristine $EuTiO_3$ with Rietveld fit using space group $Pm\bar{3}m$ (No. 221) [see Tab. 1.9]. The difference curve is shifted by -0.3×10^4 for clarity. Locations of Bragg reflexes are indicated by bars.

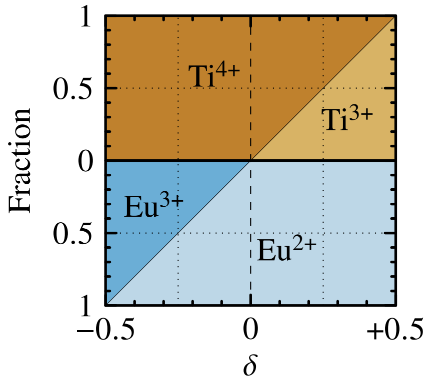

Figure 1.5: Oxidation states in $EuTiO_{3-\delta}$. Area plot of the nominal relative amounts of Ti^{4+} (🟫) and Ti^{3+} (🟨) as well as Eu^{3+} (🟦) and Eu^{2+} (⬜) as a function of oxygen deficiency δ. For $\delta \leq 0$ one finds $Eu^{2+}_{1+2\delta}Eu^{3+}_{-2\delta}Ti^{4+}O^{2-}_{3-\delta}$, whereas for $\delta \geq 0$ it is $Eu^{2+}Ti^{3+}_{2\delta}Ti^{4+}_{1-2\delta}O^{2-}_{3-\delta}$.

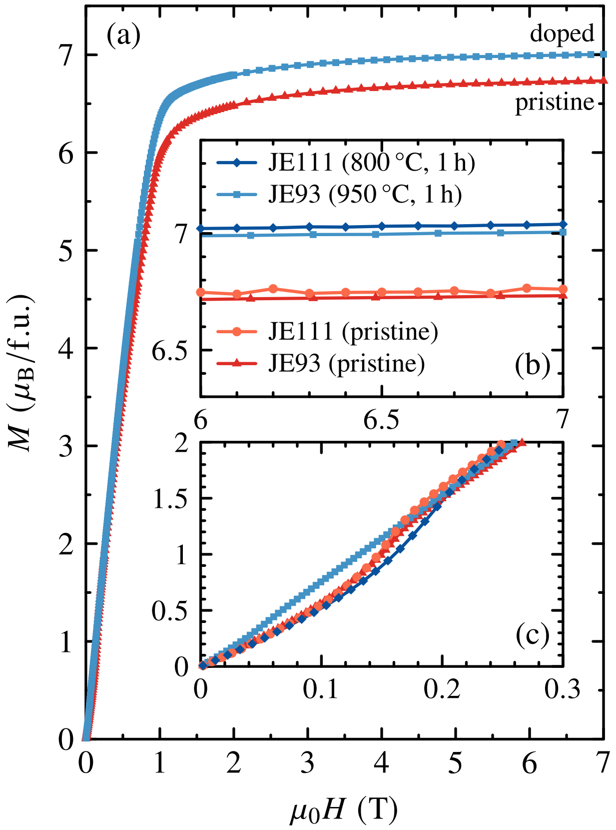

Figure 1.6: Saturation magnetization of pristine and doped EuTiO$_3$. (a) Magnetization as a function of magnetic field at $T = 2$ K comparing a pristine and a metallic sample originating from the same EuTiO$_3$ crystal. The orientation was $\boldsymbol{H} \parallel$ [100] except for JE93 (950 °C), where the field was parallel to [110]. (b) Detail view of the saturation values of two pairs of pristine and insulating samples, where each pair originates from different crystals JE93 and JE111. (c) Detail view of the small-field range. The spin-flop-related anomaly appears for all samples except JE93 (950 °C), which was measured with a different field orientation $\boldsymbol{H} \parallel$ [110].

A measurement of the magnetization as a function of magnetic field yields a saturation value $M_{\mathrm{sat}} = 6.7\,\mu_B$, which is 96 % of the theoretically expected value. Therefore, one can assume a fraction of 4 % Eu^{3+} in the as-grown EuTiO$_3$ crystal, which corresponds to an oxygen excess of $\delta = -0.02$ and a nominal composition EuTiO$_{3.02}$ [see Fig. 1.5]. This value is found to be reproducible since two crystals (JE93 and JE111) from different growths of EuTiO$_3$ show the same values for M_{sat} [see Fig. 1.6]. In view of the fact that for JE111, a nominal oxygen deficiency of $\delta = 0.02$ ($y = 2.98$) was weighed in, this could be a hint for leakages in the furnace system. Detailed measurements on as-grown EuTiO$_3$ are subject to Sec. 3.4.

1.5 Doping of EuTiO$_3$

While pure EuTiO$_3$ is a semiconductor, the material becomes metallic—analogous to SrTiO$_3$ [see Sec. 2.1]—either via reduction (EuTiO$_{3-\delta}$) [64], by substitution of Eu^{2+} with a trivalent ion like La^{3+} (Eu$_{1-x}$La$_x$TiO$_3$) [70, 87], or by a substitution of Ti^{4+} with a pentavalent ion like Nb^{5+} (EuTi$_{1-x}$Nb$_x$O$_3$) [88]. All three variants were carried out within this thesis while the emphasis was on reduction.

ID	d (mm)	A	Ti	S	PC	B	TT	QW	HG	Furn.	#	Expl.	Fig. 1.7
A1	9	-	old	-	-	✓	-	-	-	tube	11	2	(a)
A2	9	-	old	-	-	✓	-	-	✓	muffle	1	1	(a)
A3	9	-	new	-	-	✓	-	-	-	tube	2	2	(a)
A4	9	-	new	✓	-	✓	-	-	-	tube	7	0	(a)
A5	9	✓	new	✓	✓	✓	-	-	✓	tube	1	0	(a)
A6	9	✓	new	-	✓	✓	-	-	-	tube	1	1	(a)
A7	9	✓	new	-	✓	-	✓	-	-	tube	4	2	(b)
A8	9	✓	new	-	✓	-	✓	✓	✓	tube	1	1	(c)
A9	6	✓	new	-	✓	-	-	✓	-	tube	5	0	(d)
A10	6	✓	new	-	✓	✓	-	-	✓	tube	1	0	(e)

Table 1.10: Annealing methods. Quartz tube diameter d, tube cleaning with acetone (A), Ti powder batch, usage of straw (S) and pipe cleaner (PC), samples buried in Ti powder (B), tube-in-tube method (TT), separation of samples and Ti by quartz wool (QW), quartz tube heating with heatgun (HG), furnace type (Furn.), uses (#), explosions (Expl.), and illustrating figure.

1.5.1 $EuTiO_{3-\delta}$

Reduction is performed via annealing, i.e., heating the samples under vacuum with nearby titanium metal powder (chemical purity 99.99 %) acting as oxygen catcher. For that, sample and titanium powder are placed in a half-open fused-quartz tube that is triply flushed with argon, then pumped with a turbo molecular pump down to $\lesssim 10^{-5}$ mbar, and afterwards fused and sealed using an oxyhydrogen torch.

Similar annealing times and temperatures as for reduced $SrTiO_3$ were used as starting point. Spinelli *et al.* [89] use temperatures ranging from 650 °C to 1100 °C and dwell times of 0.5 h to 2 h.

Instable quartz tubes A serious issue arose in the scope of sample annealing. Some of the quartz tubes were destroyed when heated at temperatures $T_{\mathrm{ann}} \geq 800$ °C. The event occurred occasionally and was not reproducible but its probability increased with increasing temperature and it never appeared below 800 °C. Usually, the annealing procedures ran overnight such that in most cases, the exact time of the destruction event was unknown. Only one single explosion was directly observed and occurred after reaching the plateau temperature right at the beginning of the dwell time. In each case, the result was a broken quartz tube with fragments spread over the entire corundum tube of the furnace and the lab floor. The remains of titanium metal powder inside the furnace turned white indicating a complete oxidization to TiO_2, whereas the shot-out titanium powder remained pristine. Similarly, the condition of the $EuTiO_3$ samples depended on whether they remained inside the furnace or were shot out. In the latter case, they were intact and could be used for a retry,

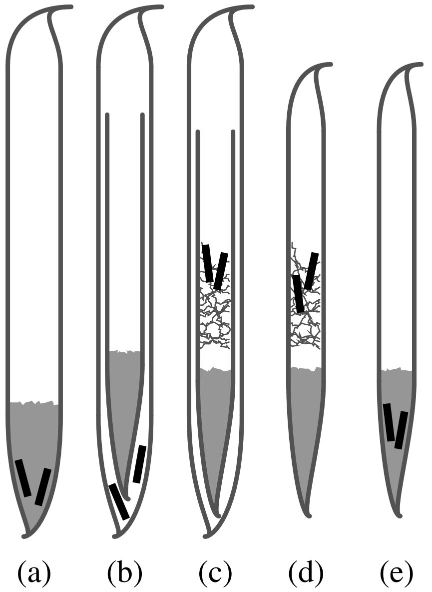

Figure 1.7: Annealing methods. Basic methods listed in Tab. 1.10: (a) 9 mm quartz tube with samples buried in Ti powder (Methods A1–A6). (b) Tube-in-tube method: Ti powder in 6 mm half-open quartz tube inside a 9 mm quartz tube with samples (Method A7). (c) Tube-in-tube method with quartz wool separating samples and Ti (Method A8). (d) 6 mm quartz tube with quartz wool separating samples and Ti (Method A9). (e) 6 mm quartz tube with samples buried in Ti (Method A10).

while in the former case they showed a white coating and were discarded.

The possible reasons for the explosions are manifold. A pressure increase due to residual gas inside the quartz tube can be excluded because the titanium powder jumps slightly when the valve to the pump line is opened during the flushing procedure. Furthermore, the quartz tube shrinks upon melting, indicating at least an underpressure inside the tube. Water residues inside the quartz tube are unlikely. Cleaning the quartz tube with acetone beforehand and heating the tube with a heat gun while pumping could not avoid the explosions.

Chemical reactions between titanium and quartz are known. McCarthy *et al.* report that “TiO, Ti and EuO attack silica and noble metals” at 1400 °C [75]. Although the highest applied annealing temperature is 450 °C lower than that, a reaction might still be possible. In order to exclude a weakening of the tube by chemical reactions, a tube-in-tube technique is developed: The titanium powder is placed inside a smaller half-open quartz tube which itself is placed inside the larger tube that is sealed [see Fig. 1.7 (b)]. Thus, the titanium powder has no contact to the outer tube.

Another potential origin is the thermal expansion of titanium particles that are embedded inside the twisted quartz after sealing. When filling titanium powder into the quartz tube, tiny amounts remain across the entire tube. This cannot be avoided completely. The usage of a tight-fitting straw prevents a contact of titanium with the largest part of the tube during filling and guides the powder directly to the bottom. Unfortunately, the powder is spread over the entire tube when removing the straw. Therefore, instead of using a straw, the powder was simply filled with a spatula and the tube was cleaned afterwards using a pipe cleaner and acetone. A mechanical instability of the quartz might also result from residual stress caused by improper sealing. Therefore, the twisted end of the sealed tube was heated for a longer time to allow a release of any potential stress. Production errors of the quartz tubes

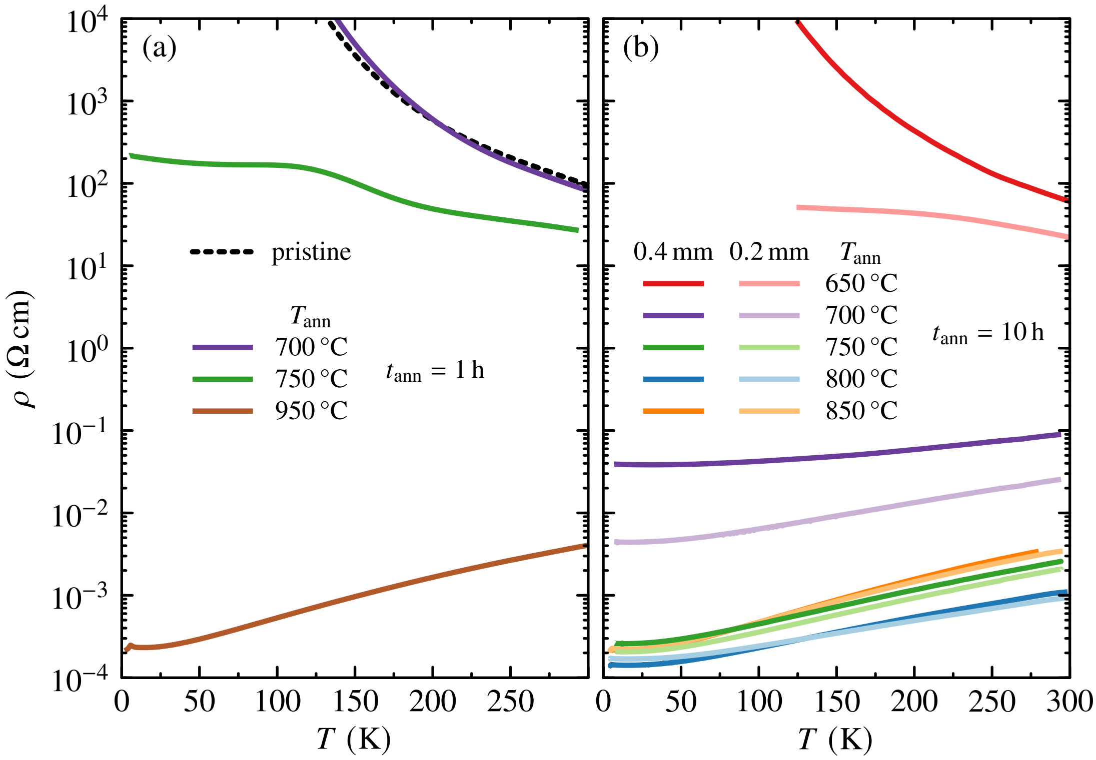

Figure 1.8: Effect of annealing time and temperature on the resistivity of $EuTiO_{3-\delta}$. (a) Resistivity $\rho(T)$ of samples annealed for $t_{ann} = 1$ h at different temperatures T_{ann} in comparison to $\rho(T)$ of pristine $EuTiO_3$ (dashed curve). (b) Increasing t_{ann} to 10 h yields much smaller resistivities for the same annealing temperatures T_{ann} as indicated by dotted arrows. Samples of 0.4 mm and 0.2 mm thickness are annealed simultaneously in the same quartz tube and show highly unequal $\rho(T)$ curves for $T_{ann} < 750$ °C.

or transport damages are another potential source of mechanical instabilities. Although a visual inspection of the tubes gave no evidence for that, invisible imperfections like residual stress or hairline cracks cannot be excluded completely.

The described circumventions were applied without any effect on the occurrence of explosions. The only reliable way to avoid this issue was the application of lower temperatures and the use of quartz tubes with smaller diameter which appear to be mechanically more robust [see Fig. 1.7 (e)]. Table 1.10 summarizes all tested annealing methods.

Temperature limit Samples annealed for 10 h at temperatures above 800 °C agglomerated with the surrounding titanium powder. Therefore, annealing methods were tested where samples and titanium powder are separate. This is realized either by a separate quartz tube for the titanium or by using quartz wool as spacer. When using the tube-in-tube method as described above, the titanium powder is placed in a separate tube anyway, while the samples are located between outer and inner tube [see Fig. 1.7 (b)]. Quartz wool allows a closer

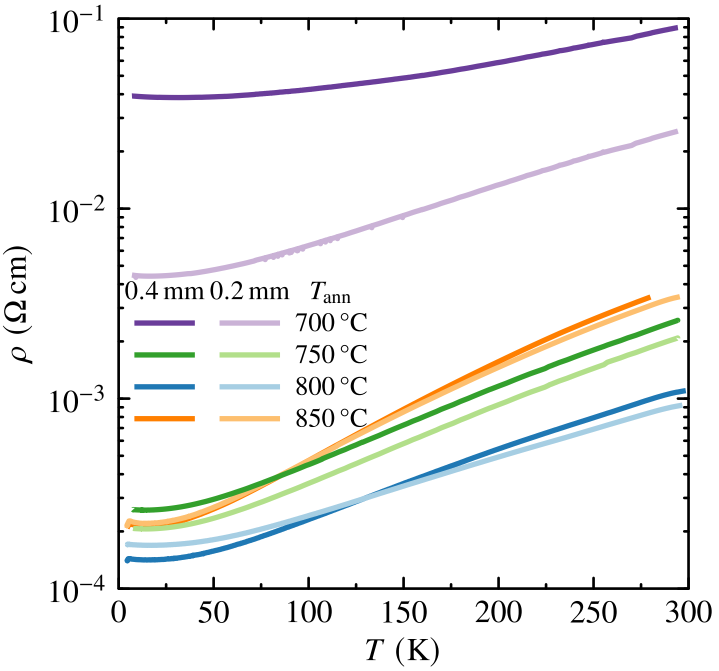

Figure 1.9: Homogeneity of EuTiO$_{3-\delta}$. Samples with $T_{\text{ann}} \geq 750$ °C show almost no thickness dependence in $\rho(T)$. The same annealing method is used for sample pairs with T_{ann}/°C = 700, 750, 800 (samples buried in Ti), whereas the sample pair with $T_{\text{ann}} = 850$ °C was separated from Ti.

distance between samples and titanium while keeping both separate [see Figs. 1.7 (c, d)]. Both methods successfully avoid the described agglomeration but they result in a less effective annealing as is discussed in the following paragraph.

Homogeneity To judge the effect of annealing time and temperature, resistivity measurements were performed using a standard four-probe method and a home-built dipstick setup for wet cryostats (SCHNELLMESSSTAB). The first approach to obtain metallic EuTiO$_3$ was a heating at 950 °C for 1 h which already brought a fairly metallic sample [see Fig. 1.8 (a)]. In order to cover the range between this metallic sample and the pristine semiconducting material, different annealing temperatures were tested while keeping the time of 1 h fixed. A sample annealed at 700 °C has an almost identical resistivity as the pristine sample. Annealing at 750 °C yields a sample with an intermediate $\rho(T)$. If the annealing time is increased to 10 h, the samples become much more metallic at a given temperature. A sample annealed for 10 h at 750 °C is as metallic as a sample annealed for 1 h at 950 °C [see Fig. 1.8 (b)]. If one considers the temperature to be responsible for the carrier concentration, while the annealing time determines the homogeneity, this result has to be interpreted as a hint that the samples are not homogeneous after 1 h.

In order to have an indicator for homogeneity, in each run two samples with different thicknesses (0.2 mm and 0.4 mm) were annealed simultaneously in the same quartz tube. As is seen in Fig. 1.8, sample pairs of different thickness annealed at the same temperature show highly unequal resistivity curves if $T_{\text{ann}} < 750$ °C, whereas the samples with higher annealing temperatures show almost no thickness dependence. Figure 1.9 depicts a detail

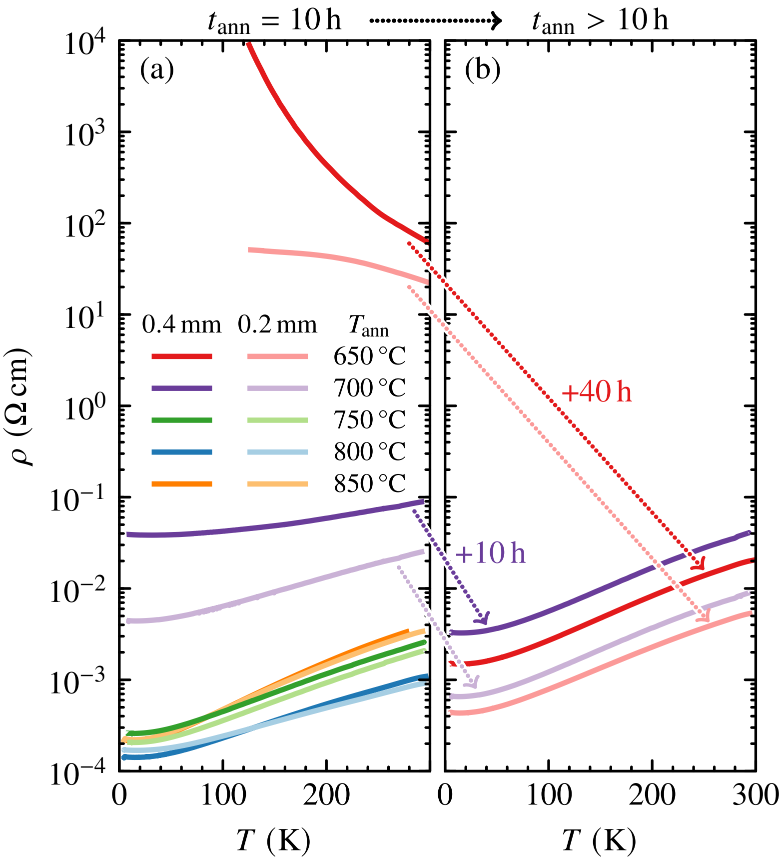

Figure 1.10: Low-temperature and long-time annealing of EuTiO$_3$. By increasing the annealing time t_{ann} = 10 h (a) to t_{ann} > 10 h (b) while keeping T_{ann} fixed, the resistivities of both sample pairs with T_{ann} = 650 °C and T_{ann} = 700 °C approach that of the metallic samples with T_{ann} = 750 °C. However, the difference in $\rho(T)$ of simultaneously annealed samples does not shrink, i.e., the thickness dependence persists upon increasing t_{ann}.

view of the most metallic samples of Fig. 1.8 (b). The remaining differences in $\rho(T)$ for samples pairs annealed at $T_{ann} \geq 750$ °C are tiny compared to the highly unequal samples with $T_{ann} < 750$ °C. Samples with T_{ann}/°C = 700, 750, 800 are annealed while buried in titanium powder [see Figs. 1.7 (a, e)] and their respective $\rho(T)$ curves are ordered by T_{ann}. In contrast, the sample pair with T_{ann} = 850 °C is annealed using the tube-in-tube method, where titanium and samples are separate [see Fig. 1.7 (b)]. Therefore, these samples are less metallic. Only the six homogeneous samples are considered in the discussion of the metal–insulator transition in Ch. 3.

Low-temperature annealing In order to obtain homogeneous samples with resistivities between the pristine semiconducting and the most metallic ones, the sample pairs with T_{ann}/°C = 650, 700 were annealed again for a longer time while keeping the annealing temperature fixed. The sample pair with T_{ann} = 650 °C was annealed for another 40 h and the sample pair with T_{ann} = 700 °C was annealed for another 10 h. Figure 1.10 shows the result of this efforts. Both sample pairs are much more metallic after the additional annealing procedures and approach the resistivity range of the most homogeneous samples. Nevertheless, the two samples of each pair do not approach each other and keep the thickness dependence.

Sample				Floating-zone furnace parameters							SC
ID	Sub.	x	y	M/L	Sintering		Growth				
					U V	v mm/h	U V	v mm/h	r rpm	p bar	
JE120	La	0.001	2.97	CMI/L5	70	9	85	8	34	2	-
JE121	La	0.001	2.97	CMI/L5	60	2	59–84	5	32	3.1	-
JE122	La	0.001	2.96	CMI/L5	60	2	68	8	32	2.2	✓
JE124	La	0.01	2.96	CMI/L5	60	1	65–75	8–10	32	2	✓✓
JE125	La	0.05	2.98	CMI/L5	50	1.5	60	10	32	5	✓
JE126	Nb	0.01	2.98	CMI/L5	54	1.3	61	10	32	5.7	✓✓
JE127	Nb	0.05	2.99	CMI/L5	57	3.5	62	10	32	5.8	✓✓✓
JE128	Nb	0.03	2.99	CMI/L5	57	3.5	61	5	36	6	-
JE129	Nb	0.02	3	CMI/L5	57	2.2	61	5	36	6	✓

Table 1.11: Synthesis of $Eu_{1-x}La_xTiO_y$ and $EuTi_{1-x}Nb_xO_y$: Parameters. All attempts to synthesize $Eu_{1-x}La_xTiO_y$ and $EuTi_{1-x}Nb_xO_y$ with sample identifier, nominal substitution x (La or Nb), nominal oxygen content y, furnace model M and halogen lamps L [see Tab. 1.2], gas, lamp voltage U in V and pulling speed v in mm h^{-1} used for sintering and growth, relative rotation of the rods r in rpm, gas pressure p in bar, and success of single-crystal growth SC [see Tab. 1.8]. A pure Ar atmosphere is used throughout.

1.5.2 $Eu_{1-x}La_xTiO_3$ and $EuTi_{1-x}Nb_xO_3$

Oxygen-defect gradients are naturally expected in post-annealed single crystals. To precisely determine the metal–insulator transition, it is necessary to have homogeneously doped $EuTiO_3$ samples. Chemical substitution appears to be an appropriate alternative to post annealing of crystals, since the doping is inherent to the relative amounts of the reactants. Apart from reduction, electron doping can be achieved by substituting europium with lanthanum [70, 87] or by a substitution of titanium by niobium ($EuTi_{1-x}Nb_xO_3$) [88].

The recipes used for $Eu_{1-x}La_xTiO_3$ and $EuTi_{1-x}Nb_xO_3$ are based on that of the most successful growth of $EuTiO_3$ (sample JE111). For both materials, a nominal oxygen deficiency is weighed in by adjusting the two titanium oxides TiO and TiO_2. The general chemical equation for $Eu_{1-x}La_xTiO_y$ using Eu_2O_3, La_2O_3, TiO, and TiO_2 is

$$\frac{1-x}{2}\,\mathrm{Eu_2O_3} + \frac{x}{2}\,\mathrm{La_2O_3} + \left(\frac{7}{2} - y\right)\mathrm{TiO} + \left(y - \frac{5}{2}\right)\mathrm{TiO_2} \longrightarrow \mathrm{EuTiO}_y \tag{1.9}$$

with $0 \leq x \leq 1$ and $2.5 \leq y \leq 3.5$. The equation for $EuTi_{1-x}Nb_xO_3$ using Eu_2O_3, Nb_2O_5, TiO, and TiO_2 is

$$\frac{1}{2}\,\mathrm{Eu_2O_3} + m\,\mathrm{TiO} + n\,\mathrm{TiO_2} + \frac{x}{2}\,\mathrm{Nb_2O_5} \longrightarrow \mathrm{EuTi}_{1-x}\mathrm{Nb}_x\mathrm{O}_y \tag{1.10}$$

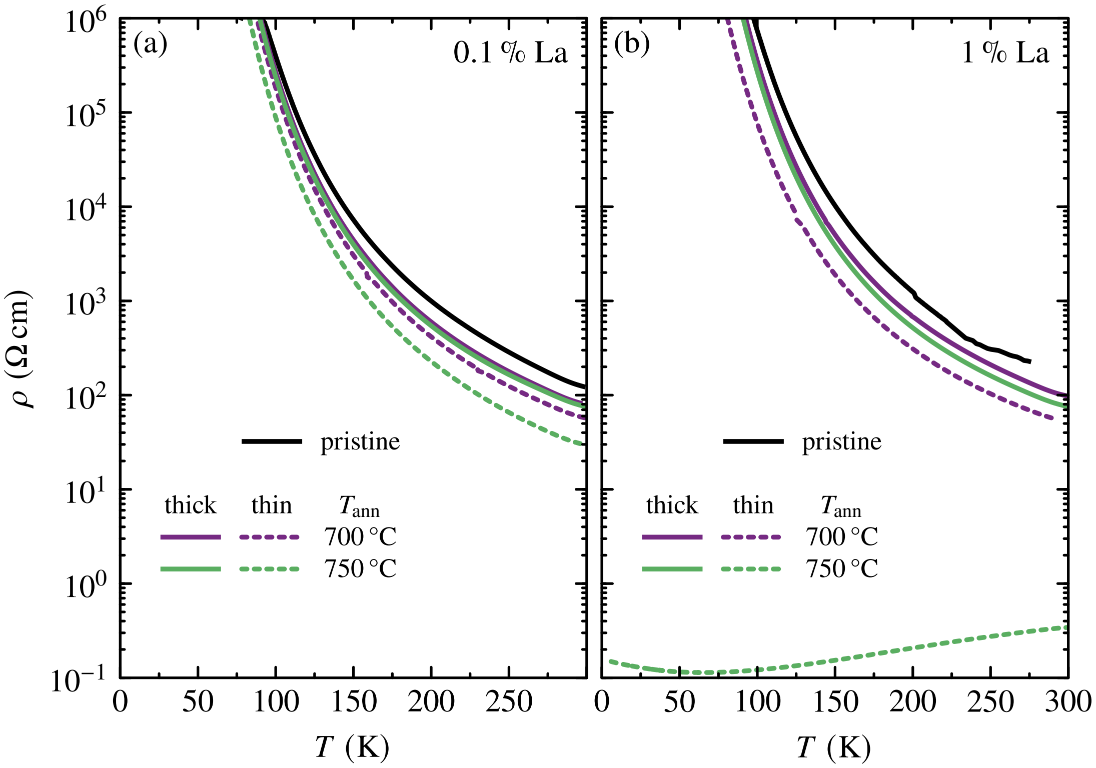

Figure 1.11: Resistivity of $Eu_{1-x}La_xTiO_{3-\delta}$ (x = 0.001, 0.01). Resistivity of $Eu_{1-x}La_xTiO_{3-\delta}$ with lanthanum contents of 0.1 % (a) and 1 % (b). For both compounds, $\rho(T)$ of the pristine material (black solid lines) is compared to that of samples annealed at 700 °C and 750 °C. Pairs of thick (≈ 0.5 mm, solid lines) and thin samples (≈ 0.3 mm, dashed lines) were annealed simultaneously in the same quartz tube.

with prefactors

$$m = \frac{7}{2} - y + \frac{3}{2}x \qquad n = y - \frac{5}{2} - \frac{3}{2}x\,. \tag{1.11}$$

Three compounds of $Eu_{1-x}La_xTiO_3$ with x = 0.001, 0.01, and 0.05, as well as four crystals of $EuTi_{1-x}Nb_xO_3$ with x = 0.01, 0.02, 0.03, and 0.05 were grown. Details of the growth parameters are summarized in Tab. 1.11. The resistivity of pristine $Eu_{1-x}La_xTiO_3$ is very similar to that of pristine $EuTiO_3$. Neither a lanthanum content of 0.1 % nor of 1 % appears to have any effect on the conductivity [see Fig. 1.11]. Therefore, annealing is applied in addition. Also for $Eu_{1-x}La_xTiO_3$, two samples of different thickness are annealed simultaneously in order to have an indicator for homogeneity. As is seen from Fig. 1.11, an annealing temperature T_{ann} = 700 K has almost no influence on $\rho(T)$ independent of x. Thus, the partial substitution of europium by lanthanum gave no advantage compared to the merely annealed $EuTiO_{3-\delta}$.

2 $Sr_{1-x}Ca_xTiO_3$

The competition between ferroelectric order and dilute metallicity in $Sr_{1-x}Ca_xTiO_{3-\delta}$ has been hitherto investigated primarily by resistivity measurements. Here, thermal-expansion measurements are used as thermodynamic probe to elucidate the nature of the ferroelectric-like transition in metallic $Sr_{1-x}Ca_xTiO_{3-\delta}$. The evolution of both the structural transition temperature T_s and the Curie temperature T_C as a function of charge-carrier density n is studied ranging from the insulating parent compound up to $n \approx 6 \times 10^{20}\,\text{cm}^{-3}$ while keeping a fixed calcium content of $x = 0.009$. Signatures of the ferroelectric transition of the insulating parent remain present in thermal-expansion measurements over the entire doping range but change in character at a threshold carrier density n^*. Parts of this chapter are based on data already published in J. Engelmayer *et al.*, Phys. Rev. B **100**, 195121 (2019) [90] and C. W. Rischau *et al.*, Nat. Phys. **13**, 643 (2017) [30].

Contents

2.1 Introduction

Solids with completely filled or empty bands are insulators, but systems with partially filled bands can be insulating as well if electron–electron repulsion prevents delocalization. Such systems are called Mott insulators[1]. Hence, perovskite titanates (ATiO$_3$) can be subdivided into two classes: Mott insulators and band insulators. If A is trivalent, titanium is trivalent as well ($A^{3+}Ti^{3+}O_3$) with one single electron in the 3d band [see Tab. 3.3]. These materials like $LaTiO_3$ or $YTiO_3$ [see also Sec. A.3] are typical Mott insulators [91–93]. If perovskite titanates have a divalent ion on the A site (e.g., Ca^{2+}, Sr^{2+}, Ba^{2+}, Cd^{2+}, Pb^{2+}, Eu^{2+}), titanium is

---

[1] A detailed description is subject to the manganites chapter [see Sec. 4.3.1].

tetravalent and the material is a band insulator. In this $A^{2+}\mathrm{Ti}^{4+}\mathrm{O}_3$ class, various ferroelectric systems are known, e.g., BaTiO_3 [14, 15], PbTiO_3 [16], CdTiO_3 [17, 18], while others like CaTiO_3 [19, 94, 95], SrTiO_3 [20], and EuTiO_3 [21, 69] are quantum paraelectrics, i.e., a ferroelectric long-range order is suppressed by quantum fluctuations.

SrTiO_3 attracts attention primarily by its huge low-temperature permittivity and by the striking absence of physical (ordering) effects like electric polarization, magnetism, and metallicity while showing multiple instabilities toward different ground states, e.g., ferroelectric, antiferroelectric, and superconducting phases [see Fig. 2.1]. Using SrTiO_3 as origin, rich physics can be obtained by isovalent A-site substitution to induce ferroelectricity (e.g., $\mathrm{Sr}_{1-x}\mathrm{Ca}_x\mathrm{TiO}_3$), by aliovalent A-site or B-site substitution to induce conductivity (e.g., $\mathrm{SrTi}_{1-x}\mathrm{Nb}_x\mathrm{O}_3$, $\mathrm{Sr}_{1-x}\mathrm{La}_x\mathrm{TiO}_3$, $\mathrm{SrTiO}_{3-\delta}$)[2], or by magnetic substitution ($\mathrm{Sr}_{1-x}\mathrm{Eu}_x\mathrm{TiO}_3$). Furthermore, different effects can be combined, e.g., in $\mathrm{Sr}_{1-x}\mathrm{Ca}_x\mathrm{TiO}_{3-\delta}$, where a ferroelectric phase competes with a metallic phase. In this thesis, examples for both A- and B-site-substituted perovskite titanates from the band-insulator class $A^{2+}\mathrm{Ti}^{4+}\mathrm{O}_3$ are studied. Section 2.2 gives an overview of quantum paraelectrics in general and summarizes the knowledge about the parent compound SrTiO_3. It sets the basis for the discussion of $\mathrm{Sr}_{1-x}\mathrm{Ca}_x\mathrm{TiO}_3$ in Sec. 2.3 and for EuTiO_3 that is subject of the following Ch. 3, since both materials share many characteristics with SrTiO_3. Section 2.3 deals with the competition between ferroelectric and metallic states in $\mathrm{Sr}_{1-x}\mathrm{Ca}_x\mathrm{TiO}_{3-\delta}$.

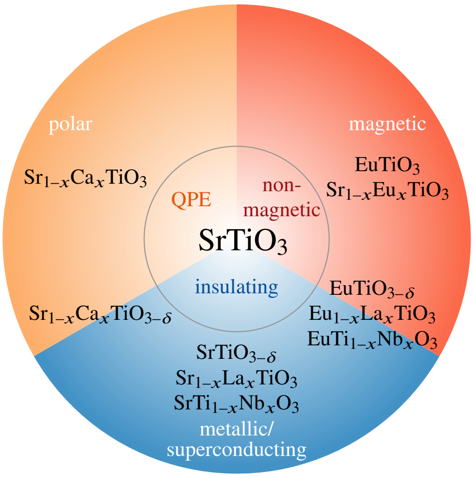

Figure 2.1: Overview of phenomena in SrTiO_3-related materials.

2.2 Properties of SrTiO_3

2.2.1 Dielectric properties

Dielectric properties of titanium oxides are investigated since the early 20th century. Initially, TiO_2 and its various modifications were in focus [97–99], but in the 1940s the interest moved to titanates with high dielectric constants, in particular perovskite titanates $A\mathrm{TiO}_3$ with an alkaline ion on the A site (Ca, Sr, Ba) [100–102]. Because the at that time novel ferroelectric effect was only known from materials with rather complicated structures like Rochelle salt $\mathrm{NaKC_4H_4O_6 \cdot 4\,H_2O}$ [103–105] and potassium dihydrogen phosphate $\mathrm{KH_2PO_4}$ [106, 107] the discovery of ferroelectricity in BaTiO_3 attracted the primary attention [14, 108–

---

[2] An oxygen deficiency can be seen as B-site substitution since it is formally a partial substitution of Ti^{4+} by Ti^{3+} ions. This can be written as $A\mathrm{Ti}^{3+}_{2\delta}\mathrm{Ti}^{4+}_{1-2\delta}\mathrm{O}_{3-\delta}$. However, this is an oversimplification because the d-shell electrons of titanium are delocalized and, therefore, a strict ionic picture is improper.

Figure 2.2: Permittivity of quantum paraelectrics. Compilation of literature data of the perovskite materials $SrTiO_3$ [20], $KTaO_3$ [22], $EuTiO_3$ [21], and $CaTiO_3$ [19], together with TiO_2 (rutile) [96]. Except for $CaTiO_3$, all measurements are performed on single crystals.

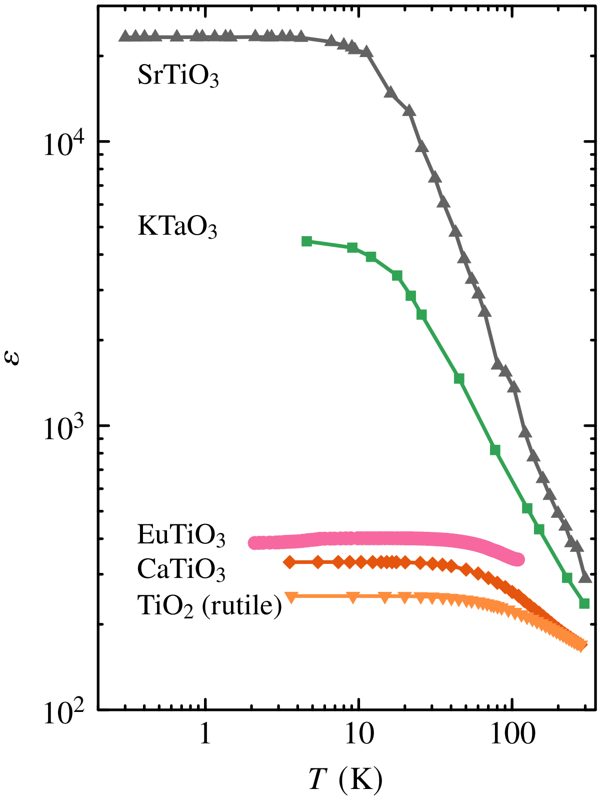

118]. Even though nowadays many ferroelectric transition-metal oxides are known such as $LiTaO_3$, $LiNbO_3$ [119–121][3], $KNbO_3$ [123–125][3], and $PbTiO_3$ [16, 126], $BaTiO_3$ became prototypical being the first hydrogen-free ferroelectric [108].

In parallel, the absence of a ferroelectric transition in $SrTiO_3$ became clear in 1950 by first low-temperature measurements of the permittivity down to 1.3 K on polycrystalline samples [127] and was later confirmed on single crystals [128]. The high-temperature behavior of the permittivity $\varepsilon(T)$ follows essentially a Curie–Weiss law in both $SrTiO_3$ and $BaTiO_3$. However, in $SrTiO_3$ the Curie–Weiss dependence turns into a plateau that continues down to lowest temperatures [see Fig. 2.2]. This behavior can only be understood by taking quantum effects into account. By extending purely classical descriptions of $BaTiO_3$ [129–131], J. H. Barrett developed a quantum mechanical treatment of this behavior [132] that nowadays is called quantum paraelectricity or incipient ferroelectricity. The same behavior was found in the perovskite oxide $KTaO_3$ [22] and, decades later, also in further perovskite titanates $CaTiO_3$ [19, 94, 95] and $EuTiO_3$ [21]. Yet, it is worth to mention that quantum-paraelectric behavior is not restricted to perovskites but also appears in materials with other crystal structures, e.g., in rutile TiO_2 [96, 133–135] and the hexaferrites $BaFe_{12}O_{19}$ and $SrFe_{12}O_{19}$ [136–138]. Figure 2.2 compares literature data of the temperature-dependent

---

[3] In the first half of the 20th century, niobium (Nb) was also called columbium (Cb) [122]. Hence, in some publications, $LiNbO_3$ and $KNbO_3$ are written as $LiCbO_3$ and $KCbO_3$, e.g., in Refs. [119, 123].

Material class	Ferroelectrics	Quantum paraelectrics
Perovskite titanates	$BaTiO_3$, $PbTiO_3$, $CdTiO_3$, $Sr_{1-x}Ca_xTiO_3$, $Ca_{1-x}Pb_xTiO_3$	$CaTiO_3$, $SrTiO_3$, $EuTiO_3$
Non-titanate perovskites	$KNbO_3$, $KTa_{1-x}Nb_xO_3$	$KTaO_3$
Non-perovskites	$LiNbO_3$, $LiTaO_3$, KH_2PO_4, $NaKC_4H_4O_6 \cdot 4\,H_2O$	TiO_2 (rutile), $BaFe_{12}O_{19}$, $SrFe_{12}O_{19}$

Table 2.1: Ferroelectric and quantum-paraelectric materials. Selected examples from different material classes. See text for references.

permittivities of different quantum paraelectrics. An overview of ferroelectric and quantum-paraelectric materials is given in Tab. 2.1.

There are several ways to induce a ferroelectric phase transition in quantum-paraelectric materials. In $SrTiO_3$, this can be done by stress [139, 140], with an electric field [141–143], or by chemical substitution $Sr_{1-x}Ca_xTiO_3$. The latter variant is discussed in detail in Sec. 2.3. Analogous instabilities are known from the non-titanate quantum paraelectric $KTaO_3$ that becomes ferroelectric under stress [144, 145] or by chemical substitution $KTa_{1-x}Nb_xO_3$ [146–148].

2.2.2 Crystal structure

$SrTiO_3$ is an ideal perovskite at room temperature with cubic space group $Pm\bar{3}m$ (No. 227) [see Fig. 2.3]. Upon cooling, the material undergoes a structural phase transition to tetragonal. First indications for this transition were obtained from electron paramagnetic resonance (EPR) studies of $SrTiO_3$ with diverse magnetic impurities like Mn^{4+} [149], Fe^{3+} [150], Gd^{3+} [151]. While first publications in 1959 [149, 150] just report a difference in the crystal structure between room temperature and liquid-nitrogen temperature the actual transition temperature $T_s \approx 110\,K$ was determined with EPR in 1962 [151]. This was confirmed by x-ray diffraction measurements two years later [152] suggesting also further structural phase transitions at lower temperatures that could not be verified later on. The space group in the tetragonal phase was determined in 1967 to be $I4/mcm$ (No. 140) [153]. Today it is well-established that $SrTiO_3$ remains tetragonal down to lowest temperatures [154], at least at ambient pressure. Theoretical predictions of high-pressure tetragonal, orthorhombic, and lower-symmetric phases at room temperature exist [155]. Furthermore, there is experimental evidence for stress-induced ferroelectricity in $SrTiO_3$ at liquid-helium temperature [139, 140], which necessarily implies the loss of inversion symmetry. Therefore, the centrosymmetric space group $I4/mcm$ cannot represent the symmetry in this ferroelectric state [see also Tab. C.1].

The transition $Pm\bar{3}m \rightarrow I4/mcm$ is antiferrodistortive with a tilting of the TiO_6 octahedra around the c axis [153, 156–158] as illustrated in Fig. 2.4. In the classification of octahedra tilts in perovskites developed by A. M. Glazer [159, 160] this is written as $(a^0a^0c^-)$, where

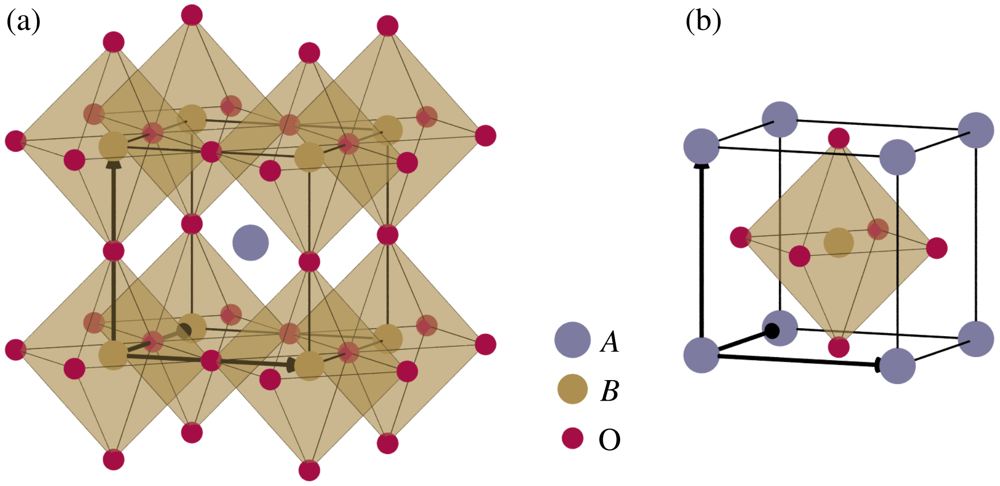

Figure 2.3: Perovskite structure. Unit cell of an ideal perovskite oxide ABO_3 with space group $Pm\bar{3}m$ (No. 221) in orthographic projection. Ion radii are scaled down for clarity. For realistic relative sizes see Fig. 3.2. (a) Unit cell with origin set to the B atom. Oxygen atoms outside the unit cell are added to complete the octahedra. (b) Unit cell with origin set to the A atom.

a^0 indicates the absence of tilting around the a axis and c^- represents an antiphase tilting around the c axis. In the notation of K. S. Aleksandrov [161] this is written as (00ϕ). The transition $Pm\bar{3}m \longrightarrow I4/mcm$ adheres a group–subgroup relation.

Group–subgroup relation A common method to illustrate group–subgroup relations is the Bärnighausen tree [162–164]. Setting up a Bärnighausen tree is instructive to understand structural transitions, evaluate the emergence of twin domains, and helps to prepare structure refinements. The higher symmetric space group $\mathcal{G}$ and its subgroup $\mathcal{H}$ are written in a top-down manner and connected by an arrow that indicates the symmetry reduction. The arrow is labeled with subgroup type, subgroup index, basis transformation, and origin shift. If the subgroup $\mathcal{H}$ is a maximal subgroup of $\mathcal{G}$, then $\mathcal{H}$ is either a translationengleiche (t) or klassengleiche (k) subgroup. If $\mathcal{H}$ is not a maximal subgroup of $\mathcal{G}$, the symmetry reduction from $\mathcal{G}$ to $\mathcal{H}$ is written as a sequence of maximal subgroups. The index i of a subgroup $\mathcal{H}$ is the number of cosets of $\mathcal{H}$ in $\mathcal{G}$ (in a finite group, this would imply a reduction of the number of symmetry elements in $\mathcal{H}$ by $1/i$ compared to $\mathcal{G}$). This is important in the context of transformation twinning: for a translationengleiche subgroup, the subgroup index i is equal to the number of possible twin domains [165, p. 414]. In contrast, no twin domains arise for klassengleiche subgroups, but so-called antiphase domains (or translation domains) appear [162, 165, 166].

The Bärnighausen tree for the structural transition in $ATiO_3$ (A = Sr, Eu, $Sr_{1-x}Ca_x$) is shown in Fig. 2.5. For the tree setup, the guidelines given in Ref. [167, p. 135] are used. Because $I4/mcm$ is not a maximal subgroup of $Pm\bar{3}m$, the transition $Pm\bar{3}m \longrightarrow I4/mcm$

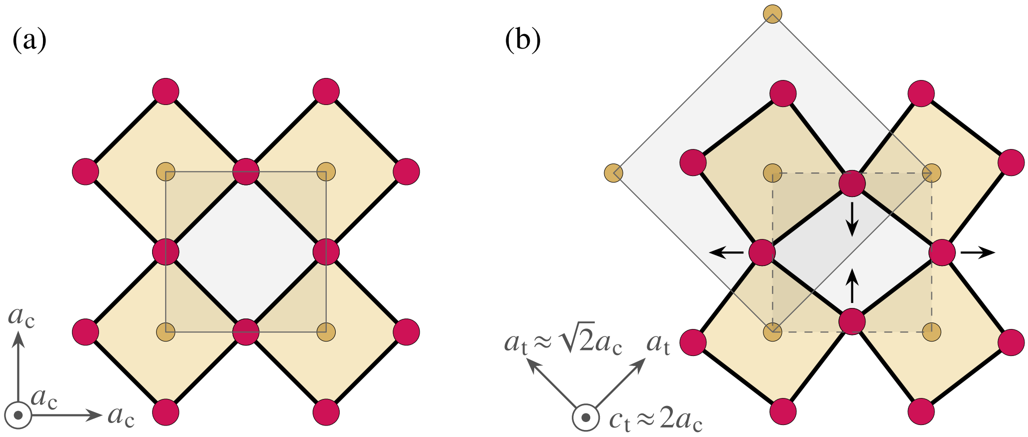

$Pm\bar{3}m$ (221) $I4/mcm$ (140)

Figure 2.4: Illustration of the cubic-to-tetragonal transition in ATiO$_3$. View of the perovskite structure along a 4-fold rotation axis. Titanium ions (●) define the corners of the unit cell (□) and are surrounded by oxygen ions (●) forming octahedra (▣). (a) Ideal cubic perovskite realized in the high-temperature phases of ATiO$_3$ with A = Sr, Eu, Ca, Ba [see Fig. 2.3 for a three-dimensional view]. (b) At the cubic-to-tetragonal transition, the oxygen ions move as indicated by black arrows. Along c_t, the octahedra tilt in an antiphase manner. The tetragonal unit cell volume (□) is four times larger than the pseudo-cubic one (⬚).

requires an intermediate step using the translationengleiche subgroup $P4/mmm$ (No. 123) with index 3. Here, no basis transformation or origin shift is needed. The space group $I4/mcm$ of the low-temperature phase is a klassengleiche subgroup of $P4/mmm$ with index 2 and basis transformation $\boldsymbol{a}+\boldsymbol{b}$, $-\boldsymbol{a}+\boldsymbol{b}$, $2\boldsymbol{c}$. The number of possible twin domains for the transition $Pm\bar{3}m \rightarrow I4/mcm$, which is relevant for the later-discussed thermal-expansion data on $Sr_{1-x}Ca_xTiO_3$ [see Sec. 2.3.2], appears as index $i = 3$ of the translationengleiche subgroup. The Bärnighausen tree is complemented by boxes [right half of Fig. 2.5] showing the atomic positions in the respective space group including element symbol, Wyckoff position and multiplicity, site symmetry, and atomic coordinates. The coordinate transformation given as arrow label corresponds to the basis transformation on the left. Wyckoff positions, site symmetries, atomic coordinates and their transformation are taken from the *International Tables for Crystallography Vol. A* and *Vol. A1* [84, 168]. The $I4/mcm$ phase has one single free parameter x that is related to the octahedron rotation angle φ via $x = (1 - \tan\varphi)/4$. Starting from $\varphi = 0°$ ($x = 0.25$) at $T_s \approx 110\,\mathrm{K}$, the angle reaches its maximum value of $\varphi \approx 2°$ ($x \approx 0.24$) at lowest temperature [71, 154, 169][4].

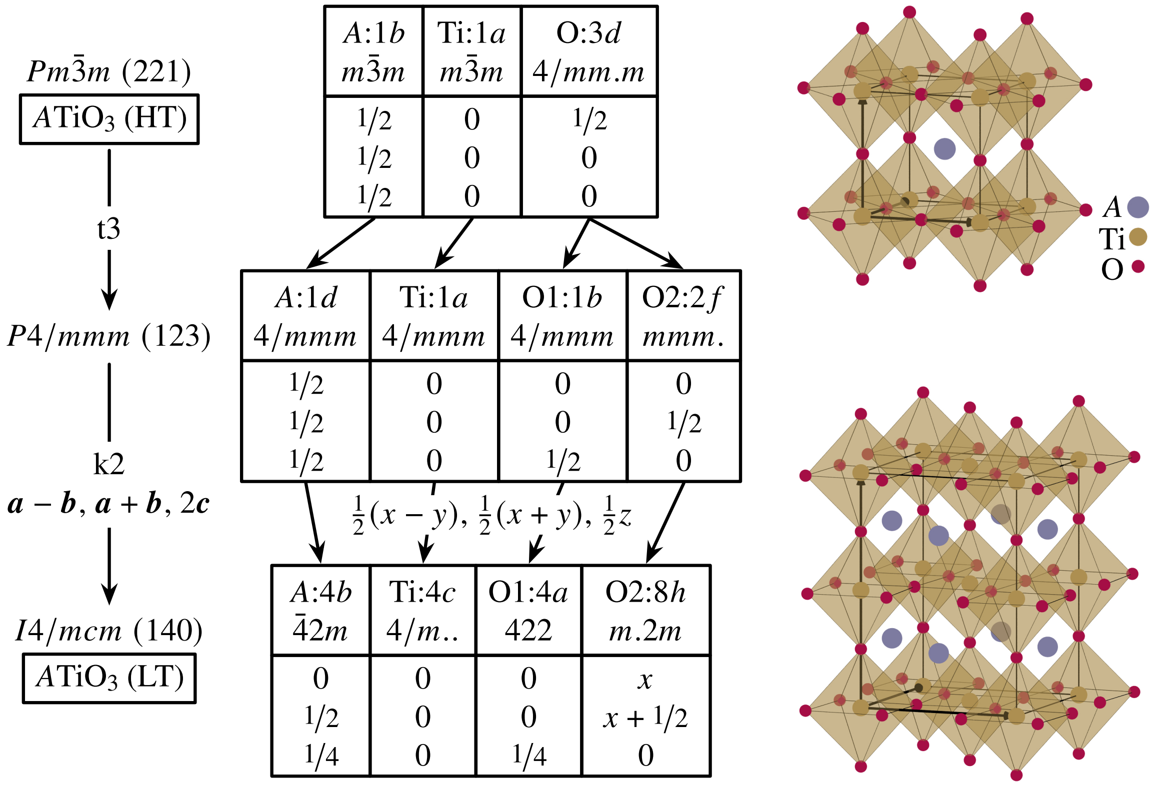

Figure 2.5: Group–subgroup relation for the structural phase transition in ATiO$_3$. The space groups $Pm\bar{3}m$ of ideal perovskites and $I4/mcm$ of the low-temperature phase of ATiO$_3$ (A = Sr, Eu, $Sr_{1-x}Ca_x$) are linked via a group–subgroup relation represented as Bärnighausen tree. For a sequence of maximal subgroups, $P4/mmm$ is needed as intermediate step. Tables show element symbols, Wyckoff positions, site symmetries, and atomic coordinates. The origin is set to the titanium ion. The free parameter is $x \approx 0.24$ [71, 154, 169][4].

2.3 $Sr_{1-x}Ca_xTiO_3$

Solid solutions of BaTiO$_3$, SrTiO$_3$, and CaTiO$_3$ are investigated since the 1940s [173–179]. Complete solid solutions over the entire composition range are possible for $Sr_{1-x}Ca_xTiO_3$ and $Sr_{1-x}Ba_xTiO_3$ [174, 176, 177, 180], whereas the $Ba_{1-x}Ca_xTiO_3$ system exhibits a certain insolubility range [176, 179, 180]. Phase diagrams of $Sr_{1-x}Ca_xTiO_3$ in literature differ partially from each other. Essentially two variants exist, both shown in Fig. 2.6. The more recent phase diagram by Carpenter *et al.* [172] basically reinforces an earlier phase diagram by Mitsui and Westphal [181] showing a broad tetragonal $I4/mcm$ phase over the entire range of x, separating the high-temperature cubic $Pm\bar{3}m$ phase from the low-

---

[4] The structure refinement in Ref. [154] has wrong Wyckoff positions and the multiplicities conflict with the chemical formula. Correct Wyckoff positions are given, e.g., in Refs. [71, 169].

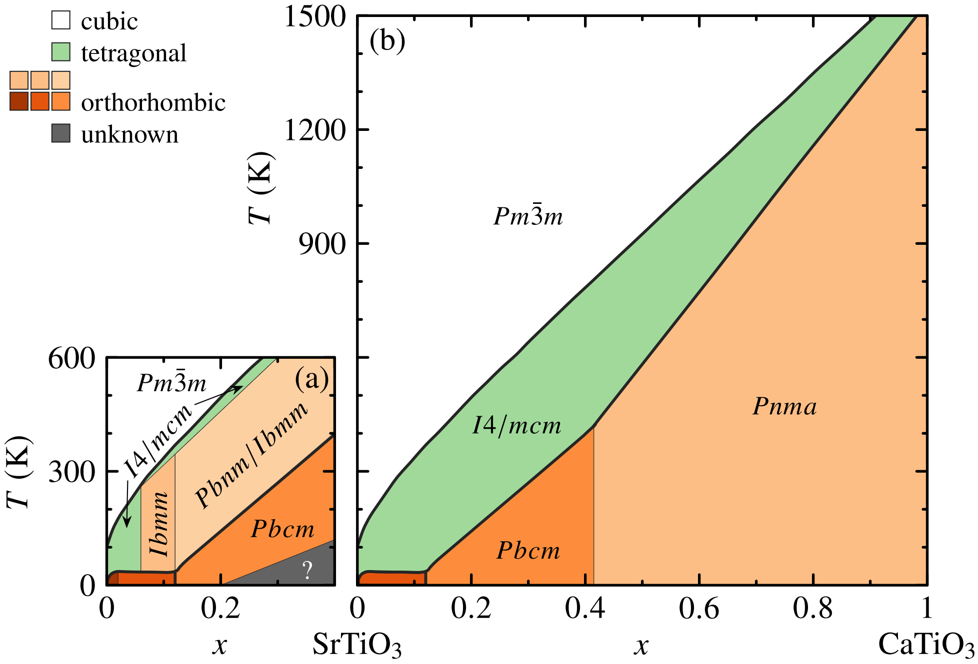

Figure 2.6: Literature phase diagrams of $Sr_{1-x}Ca_xTiO_3$. (a) Phase diagram adapted from Ranjan *et al.* [170, 171]. (b) Phase diagram adapted from Carpenter *et al.* [172]. Thick black lines represent phase boundaries that are identical in both diagrams. The ferroelectric phase (🟧) in (b) is in (a) further subdivided into a quantum ferroelectric (🟫) and a relaxor-ferroelectric phase (🟧).

temperature orthorhombic phases [see Fig. 2.6 (b)]. In contrast, in the phase diagram by Ranjan *et al.* [170], which is reproduced almost unchanged in Refs. [171, 182, 183], further orthorhombic phases appear, while the tetragonal phase remains in a narrow range only [see Fig. 2.6 (a)]. However, both phase diagrams essentially agree within the strontium-rich range $x \leq 0.06$ that is relevant for this thesis.

Although a ferroelectric transition is absent in both end members $SrTiO_3$ and $CaTiO_3$ [95, 127], mixing Sr and Ca on the *A* site ($Sr_{1-x}Ca_xTiO_3$) induces ferroelectricity already for tiny calcium substitutions $0.0018 \leq x < 0.12$ [26], whereas for larger calcium contents $x \gtrsim 0.12$ the material becomes antiferroelectric [170, 171, 184, 185]. In the ferroelectric phase one can distinguish two regimes: The first one shows an increasing $T_C(x)$ for $0.0018 \leq x < 0.02$ and is referred to as quantum ferroelectric phase [26, 29, 30, 171, 182, 183] resembling a $T_C \propto (x - x_c)^{1/2}$ behavior known from $KTa_{1-x}Nb_xO_3$ [148]. The second regime $0.02 \leq x < 0.12$ shows a constant T_C [26] and is labeled as relaxor-ferroelectric phase [170, 171, 182–184].

In addition to the cubic-to-tetragonal transition $Pm\bar{3}m \rightarrow I4/mcm$ at higher temperatures, the transition to the ferroelectric state implies a further structural transition. As already pointed out in the context of stress-induced ferroelectricity in $SrTiO_3$, the finite polarization

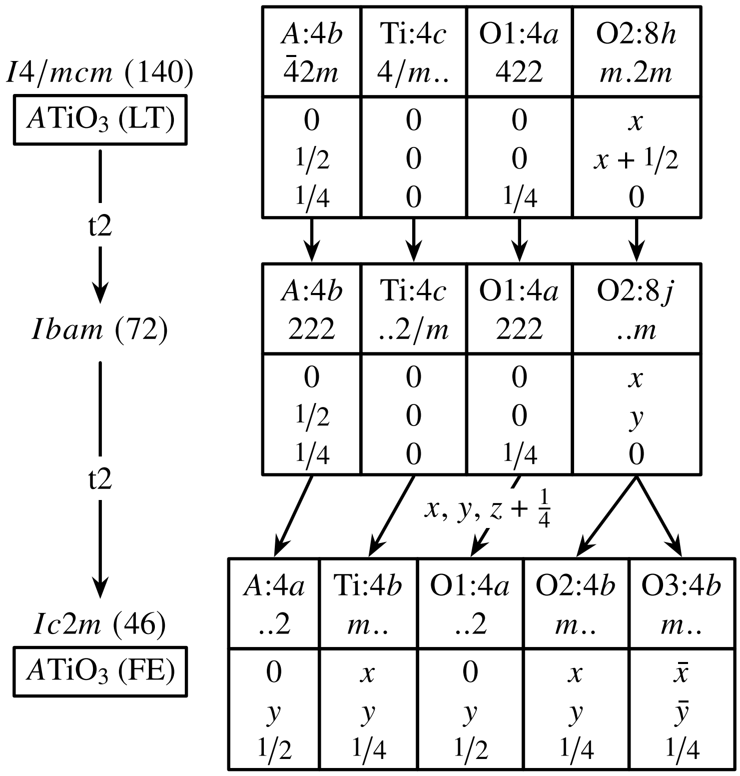

Figure 2.7: Group–subgroup relation for the ferroelectric phase transition in ATiO$_3$. Space groups $I4/mcm$ and $Ic2m$ are linked by a group–subgroup relation, where $Ibam$ is needed as intermediate step for a sequence of maximal subgroups. Wyckoff positions, site symmetries, atomic coordinates and their transformation are taken from the *International Tables for Crystallography Vol. A* and *Vol. A1* [84, 168].

in the ferroelectric state requires the absence of an inversion center. Because the space group $I4/mcm$ is centrosymmetric, the transition at T_C necessarily involves a symmetry reduction. The crystal structure in the ferroelectric phase was found to have the orthorhombic point group $mm2$ [172, 186, 187]. The actual space group was specified for $x = 0.02, 0.04$ by x-ray diffraction measurements to be $Ic2m$ (No. 46) [188]. Figure 2.7 shows the group–subgroup relation for the transition $I4/mcm \rightarrow Ic2m$ as Bärnighausen tree, where $Ibam$ (No. 72) is needed as intermediate group since $Ic2m$ is not a maximal subgroup of $I4/mcm$. Space group $Ibam$ is a translationengleiche subgroup of $I4/mcm$ with index 2 and $Ic2m$ is likewise a translationengleiche subgroup of $Ibam$ with index 2. Hence, in the transition $I4/mcm \rightarrow Ic2m$ the number of possible twin domains increases by a factor of 4: the symmetry reduction $I4/mcm \rightarrow Ibam$ doubles the number of twin domains because a and b axis become unequal; another factor of 2 is obtained from the loss of inversion symmetry in $Ibam \rightarrow Ic2m$ [see also Tab. C.1].

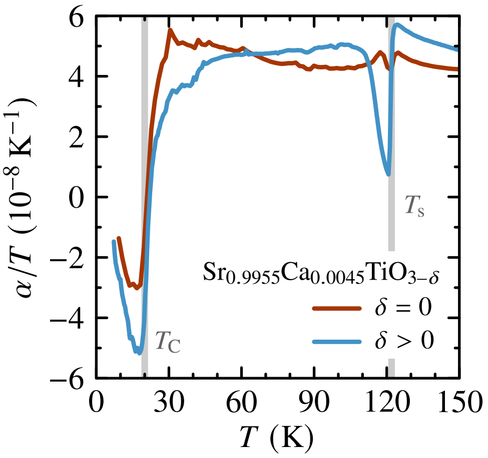

Figure 2.8: Thermal expansion of $Sr_{0.9955}Ca_{0.0045}TiO_{3-\delta}$. Comparison of $\alpha(T)/T$ of pristine insulating $Sr_{0.9955}Ca_{0.0045}TiO_3$ and metallic $Sr_{0.9955}Ca_{0.0045}TiO_{3-\delta}$ with a charge-carrier density of $n = 6.6 \times 10^{17}\,cm^{-3}$ [30], both showing a very similar anomaly at 20 K.

2.3.1 Ferroelectric order versus metallicity

Pristine $SrTiO_3$ is a band-gap insulator ($\Delta \approx 3.2$ eV) [189, 190] that becomes metallic[5] upon n-type doping either via reduction ($SrTiO_{3-\delta}$) [27, 89, 191, 193, 197, 201], via substitution of Ti^{4+} by pentavalent ions like Nb^{5+} ($SrTi_{1-x}Nb_xO_3$) [89, 194, 202, 203], or via substitution of Sr^{2+} by trivalent ions like La^{3+} ($Sr_{1-x}La_xTiO_3$) [201, 203–207]. In all three n-doped variants of $SrTiO_3$ an additional superconducting phase is found in a carrier-concentration range $5 \times 10^{17}\,cm^{-3} \lesssim n \lesssim 10^{21}\,cm^{-3}$ with a maximum critical temperature $T_c \approx 0.4$ K [28, 191, 194, 206].

In crystals with both calcium substitution and electron doping ($Sr_{1-x}Ca_xTiO_{3-\delta}$) the T_C-related anomalies of the ferroelectric insulating parent compound persist within the metallic and superconducting phase [29, 30]. This is seen for $Sr_{1-x}Ca_xTiO_{3-\delta}$ with $x = 0.0045$ by Raman measurements of the TO_1 soft mode [30] as well as by thermal-expansion measurements. Figure 2.8 shows α/T of pristine $Sr_{0.9955}Ca_{0.0045}TiO_3$ and metallic $Sr_{0.9955}Ca_{0.0045}TiO_{3-\delta}$ with a charge-carrier density of $n = 6.6 \times 10^{17}\,cm^{-3}$. Both crystals show a very similar anomaly at $T_C \approx 20$ K of the insulating parent. In contrast, the anomalies at the structural transition $T_s \approx 122$ K look very different. The weakly pronounced anomaly of the pristine crystal indicates a comparably homogeneous distribution of twin domains, whereas the doped sample with its distinct anomaly is closer to a monodomain.

For $x = 0.0022$ and $x = 0.009$, this ferroelectriclike transition has been investigated as a function of charge-carrier concentration n by Rischau *et al.* [30]. In that report, the T_C-related minima in resistivity data $\rho(T)$ shift to lower temperatures upon increasing n and disappear above a critical, x-dependent charge-carrier density n_c, where the sample with larger x shows a higher n_c [see Fig. 2.9]. Although the origin of this behavior remained unresolved, Rischau *et al.* suggested a mechanism where the ferroelectriclike phase is destroyed by destructively interfering Friedel oscillations of neighboring dipoles [30]. A

---

[5] In early publications, in particular in the 1960s and 1970s, the metallic behavior in n-doped $SrTiO_3$ is called "semiconducting", e.g., in Refs. [27, 191–200].

Figure 2.9: Phase diagram of $Sr_{1-x}Ca_xTiO_{3-\delta}$ ($x = 0.0022, 0.009$) as seen by resistivity. Lines are guides to the eye. Adapted from Ref. [30].

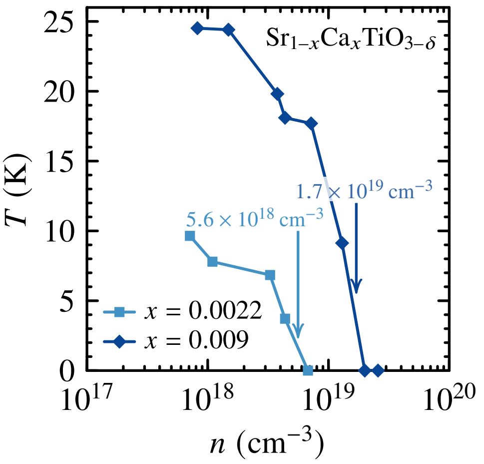

theoretical treatment of such a mechanism was given by Glinchuk *et al.* already much earlier [208, 209].

The appearance of ferroelectric order in insulating quantum paraelectrics like $SrTiO_3$ and $KTaO_3$ is discussed by Rowley *et al.* in the context of quantum criticality [210]. For $SrTiO_3$, the quantum control parameter can be tuned either by stress [140], by chemical substitution like in $Sr_{1-x}Ca_xTiO_3$, or by oxygen isotope exchange $SrTi(^{16}O_{1-x}{}^{18}O_x)_3$ [211]. In such a scenario, the charge-carrier concentration n acts as an additional control parameter toward a metallic ground state. The presence of a quantum phase transition is intrinsically tied to a divergence of the Grüneisen parameter [212]. If the quantum phase transition is pressure-driven, this holds for the Grüneisen ratio $\Gamma = \alpha/c_p$, where α is the thermal-expansion coefficient and c_p is the molar specific heat at constant pressure. Furthermore, Γ exhibits a sign change in the vicinity of a quantum critical point [213]. Because c_p is always positive, a sign change of Γ is the result of a sign change in α. Experimental evidence for such sign changes in α exists for diverse materials where the quantum control parameter is either a magnetic field [214–221], a chemical and hydrostatic pressure [222], or the charge-carrier concentration [223]. Hence, thermal expansion is a proper tool to investigate phase transitions in general and quantum phase transitions in particular.

2.3.2 Measurements on $Sr_{1-x}Ca_xTiO_{3-\delta}$ ($x = 0.009$)

Methods

A commercial $Sr_{1-x}Ca_xTiO_3$ single crystal with a calcium substitution of $x = 0.009$ was used for this study. The nominal calcium content was confirmed by secondary ion mass spectrometry (SIMS) analysis as described in Ref. [29]. The crystal was cut into cuboid pieces with all faces being cubic {100} planes and dimensions optimized for Hall-effect measurements, typically $0.5 \times 2.5 \times 5$ mm. In the following sections, the sample's edges L_1, L_2, and L_3 correspond to the sample's long, medium, and short directions, respectively. In order to induce electron doping, the samples were annealed under vacuum ($\lesssim 10^{-5}$ mbar)

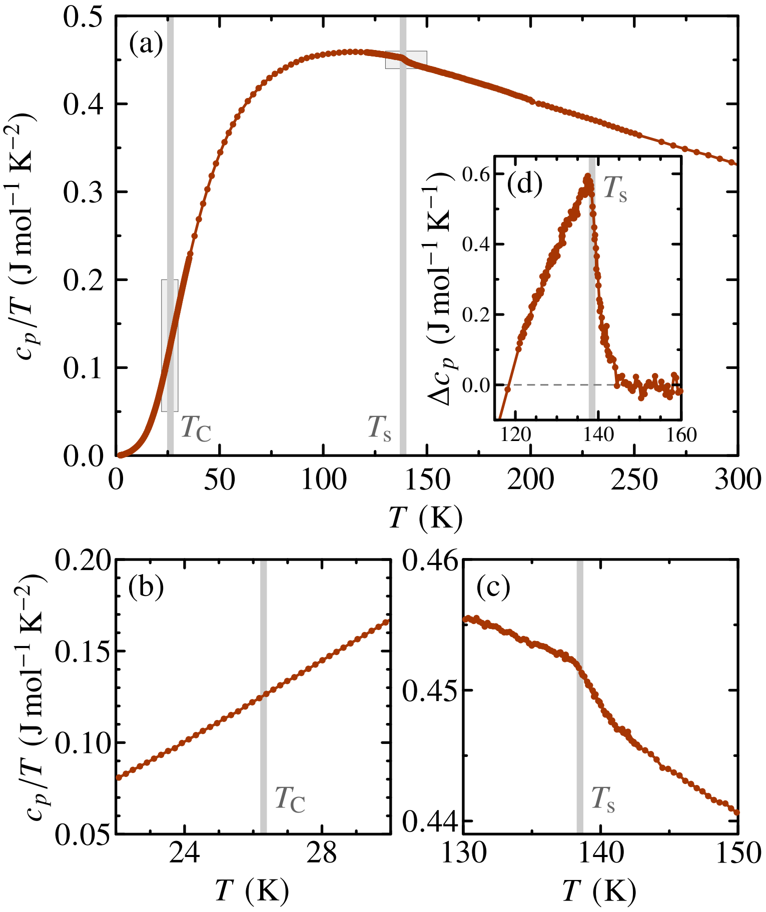

Figure 2.10: Specific heat of pristine $Sr_{0.991}Ca_{0.009}TiO_3$. (a) Complete temperature range of c_p/T. Vertical lines indicate transition temperatures T_C and T_s as determined from thermal-expansion measurements. Boxes indicate positions of detail views. (b, c) Detail views of c_p/T around T_C and T_s, respectively. (d) Jump Δc_p at T_s with subtracted background (dashed line).

for 1 to 2 hours at temperatures between 700 °C and 1000 °C, depending on the intended charge-carrier concentration. Hall-effect measurements were carried out via a standard six-probe method using a commercial cryostat (PPMS by QUANTUM DESIGN) with resistivity option. This preliminary work, including crystal orientation, cutting, annealing, and Hall measurements on $Sr_{0.991}Ca_{0.009}TiO_{3-\delta}$ samples, was performed by Carl Willem Rischau, Xiao Lin, and Benoît Fauqué [30].

The uniaxial length change $\Delta L(T)$ was measured with a home-built capacitance dilatometer [224] while heating the sample continuously from liquid-helium temperature to 180 K at a rate of about 0.1 K min^{-1}. The thermal-expansion coefficient $\alpha = (1/L_0)(\partial \Delta L/\partial T)$ is determined numerically, i.e., by piecewise linear fits of $\Delta L(T)/L_0$. The heat-capacity measurement was performed using a microcalorimeter option of the PPMS.

Pristine $Sr_{0.991}Ca_{0.009}TiO_3$

Figure 2.10 shows the specific heat $c_p(T)/T$ of pristine $Sr_{0.991}Ca_{0.009}TiO_3$. Vertical lines indicate transition temperatures T_s and T_C obtained from thermal-expansion measurements

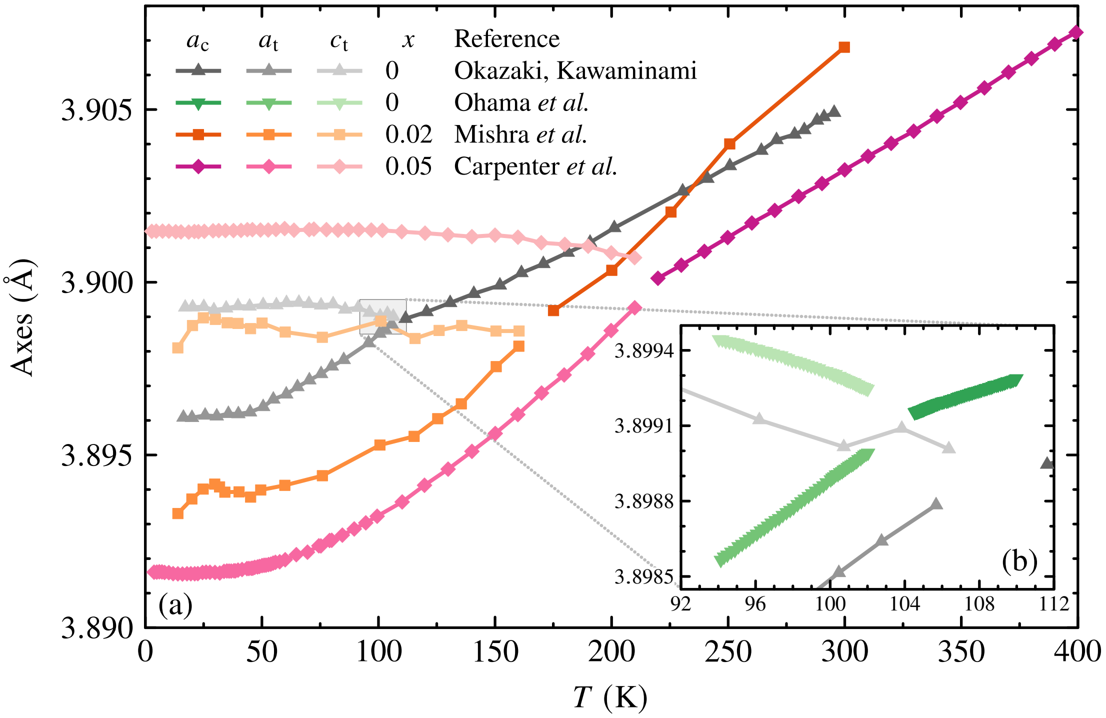

Figure 2.11: Lattice parameters of $Sr_{1-x}Ca_xTiO_3$ ($x = 0, 0.02, 0.05$). (a) Literature data of the lattice parameters from x-ray powder diffraction measurements of $SrTiO_3$ by Okazaki and Kawaminami [227], as well as $Sr_{0.98}Ca_{0.02}TiO_3$ by Mishra *et al.* [228] and $Sr_{0.95}Ca_{0.05}TiO_3$ by Carpenter *et al.* [172]. (b) Enlarged view of the $SrTiO_3$ data around T_s in comparison to data of Ohama *et al.* [229] revealing the different resolutions.

[see Fig. 2.12]. Detail views of the temperature ranges around T_C and T_s [Fig. 2.10 (b) and (c)] show a distinct anomaly at T_s in agreement with previous reports [29, 225], whereas no anomaly can be resolved around T_C. Figure 2.10 (d) shows the specific-heat jump Δc_p at T_s obtained by subtracting a polynomial fit, similar to that in Refs. [29, 226]. To fit the background signal, the function $c_p(T) = aT^2 + bT + c$ is used in the range $145\,\mathrm{K} \leq T \leq 180\,\mathrm{K}$ with fit parameters $a = -8.96 \times 10^{-4}\,\mathrm{J\,mol^{-1}\,K^{-3}}$, $b = 0.613\,\mathrm{J\,mol^{-1}\,K^{-2}}$, and $c = -5.65\,\mathrm{J\,mol^{-1}\,K^{-1}}$. The jump's magnitude is similar to that reported in Ref. [29] measured on the same compound.

Figure 2.12 (a) shows thermal-expansion coefficients α_i/T of pristine $Sr_{0.991}Ca_{0.009}TiO_3$ measured along the cubic $\langle 100 \rangle$ directions (solid lines) that are parallel to the sample's edges L_i. Figure 2.12 (b) displays the corresponding uniaxial length change $\Delta L_i/L_0$ adjusted to the cubic lattice parameter at 150 K, which is estimated from the available x-ray data of $SrTiO_3$ and $Sr_{0.98}Ca_{0.02}TiO_3$ [227, 228] to be $a_c = 3.899$ Å [see Fig. 2.11]. In practical terms, this means that the temperature dependence of the lattice parameter $a(T)$ is calculated from uniaxial length change $\Delta L(T)/L_0$ via

$$a(T) = \left(\frac{\Delta L(T)}{L_0} + 1\right) a(T_0)\,, \tag{2.1}$$

where $T_0 = 150\,\mathrm{K}$ is the normalization temperature and $a(T_0) = 3.899\,\text{Å}$ is the lattice parameter at T_0.

At high temperatures the α_i are identical and show pronounced anomalies around 139 K and 27 K. The upper temperature can be identified with the cubic-to-tetragonal transition temperature T_s. While pure $SrTiO_3$ becomes tetragonal around $T_s \simeq 105\,\mathrm{K}$ [151, 152, 229, 230], the transition temperature in $Sr_{1-x}Ca_xTiO_3$ increases with increasing x [29, 171, 172, 181, 228] up to $T_s \gtrsim 1500\,\mathrm{K}$ in pure $CaTiO_3$ [231–233]. This corresponds to the topmost phase boundary in Fig. 2.6. The transition temperature $T_s \simeq 139\,\mathrm{K}$ of our pristine sample with $x = 0.009$ is in agreement with findings in Refs. [29, 234]. The symmetry reduction involved in this transition is $Pm\bar{3}m \longrightarrow I4/mcm$ which is the same for the entire composition range of $Sr_{1-x}Ca_xTiO_3$ and already discussed in detail in Sec. 2.2.2. As can be seen from the illustration of this transition in Fig. 2.4, the cubic axes a_c and the tetragonal axes a_t, c_t are related via $a_t \approx \sqrt{2}a_c$ and $c_t \approx 2a_c$. It is evident, that the sample's edges L_i, which are parallel to the cubic $\langle 100\rangle_c$ directions, point along $\langle 110\rangle_t$ with respect to the tetragonal axes a_t. The lower anomaly at 27 K signals the transition to the ferroelectric phase that was detected by $P(E)$ hysteresis loops [30]. While the structural transition at T_s is seen mainly in the α component along L_3, the T_C-related anomaly predominantly appears in the components measured along L_2 and L_1, respectively.

Twinning In general, structural phase transitions involve transformation twinning [235], [165, p. 414]. For a cubic-to-tetragonal transition one expects the emergence of at least three twin domains, since each of the cubic $\langle 100\rangle_c$ axes can be transformed into the tetragonal $[001]_t$ axis [see Sec. 2.2.2]. The appearance of twin domains allows different α_i to (partially) compensate each other, i.e., a completely twinned sample should exhibit an isotropic uniaxial thermal expansion $\bar{\alpha}$, that is related to the volume expansion $\beta = 3\bar{\alpha}$. In general, the volume expansion is determined by $\beta = \sum_i \alpha_i$, where α_i are the uniaxial expansion coefficients along a set of three pairwise orthogonal directions. In a tetragonal crystal, this means $\beta = 2\alpha_{a_t} + \alpha_{c_t}$ with the (generally anisotropic) main-axis expansion coefficients α_{a_t} and α_{c_t} along the tetragonal axes a_t and c_t, respectively. In our crystal, the transition at T_s is almost volume-conserving as can be seen by $\bar{\alpha} = \beta/3$ [black dashed line in Fig. 2.12 (a)], i.e., the spontaneous expansion along L_1 and L_2 is roughly compensated by the contraction along L_3. Also the parent compound $SrTiO_3$ shows a nearly volume-conserving behavior around T_s, as seen in the temperature-dependent lattice parameters determined from high-resolution x-ray diffractometry measurements [229]. In our crystal, the anisotropic α_i and the nearly volume conservation indicate highly unequal twinning fractions. Using a capacitance dilatometer naturally implies the application of a certain uniaxial stress that, in some cases, can be sufficient to provoke a (partial) detwinning of the

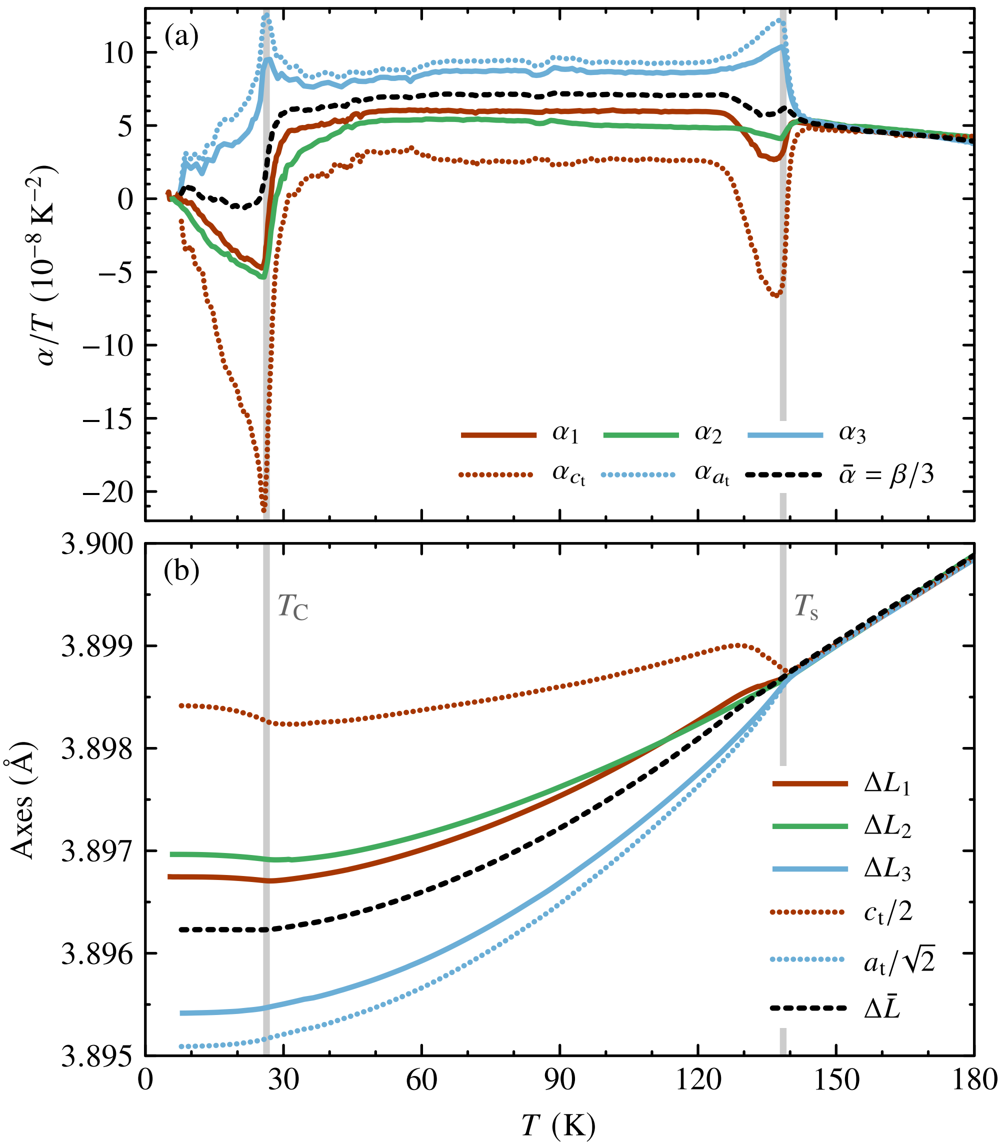

Figure 2.12: Thermal expansion of pristine $Sr_{0.991}Ca_{0.009}TiO_3$. (a) Thermal-expansion coefficients α_i/T (solid lines) measured along the sample's edges L_i, which are parallel to the cubic axes $\langle 100\rangle_c$, together with the reconstructed α_i/T of the tetragonal axes $c_t/2$ and $a_t/\sqrt{2}$ (dotted lines) and average linear expansion $\bar{\alpha} = \beta/3$ (dashed line). (b) Corresponding uniaxial length changes ΔL_i (solid lines) and average length change $\Delta\bar{L}$ (dashed line) each adjusted to the cubic lattice parameter $a(150\,\mathrm{K}) = 3.899$ Å. Vertical lines indicate transition temperatures T_s and T_C.

crystal [220, 236, 237]. This is apparently not the case in our sample, where the appearance of a dominating twin is not triggered by external conditions but rather predetermined by intrinsic crystal defects. This is supported by the fact, that we observe an expansion along L_1 and a compression along L_3 when cooling across T_s, although the force applied via the dilatometer acts on the smallest cross-sectional area of our sample and consequently produces the largest pressure when measuring along L_1, whereas along L_3 the force acts on the largest cross section producing the smallest pressure.

The fraction of the tetragonal axes a_t and c_t parallel to the sample's edges L_i can be estimated by comparing the thermal-expansion coefficients of our measurements with the slope changes of the temperature-dependent lattice parameters around T_s from x-ray powder diffraction measurements, which are inherently blind to twinning. Such data exist for $Sr_{1-x}Ca_xTiO_3$ with $x \geq 0.02$ [172, 228] only and in comparably low resolution [see Fig. 2.11 (a)]. Hence, for the slope comparison we use data of $SrTiO_3$ [229] measured by high-angle double-crystal x-ray diffractometry (HADOX) [238, 239], which have a much higher resolution [see Fig. 2.11 (b)]. At T_s, these data show an a_t-axis contraction upon cooling that corresponds to a change $\Delta\alpha_a \simeq 8 \times 10^{-6}\,\mathrm{K}^{-1}$ and a c_t-axis expansion corresponding to $\Delta\alpha_c \simeq -16 \times 10^{-6}\,\mathrm{K}^{-1}$. By comparing these values to our thermal-expansion anomalies $\Delta\alpha_i$ at T_s [see Fig. 2.12 (a)] and taking

$$\sum_i \Delta\alpha_i = 2\Delta\alpha_a + \Delta\alpha_c$$

into account, we estimate that along L_3, the crystal contains approximately $0.9a_t$ and $0.1c_t$, whereas L_1 contains $0.5a_t$ and $0.5c_t$, and L_2 contains $0.6a_t$ and $0.4c_t$. Thus, we obtain the following system of linear equations:

$$\Delta\alpha_1 = 0.5\Delta\alpha_a + 0.5\Delta\alpha_c \tag{2.2}$$

$$\Delta\alpha_2 = 0.6\Delta\alpha_a + 0.4\Delta\alpha_c \tag{2.3}$$

$$\Delta\alpha_3 = 0.9\Delta\alpha_a + 0.1\Delta\alpha_c \tag{2.4}$$

One can determine $\Delta\alpha_a$ and $\Delta\alpha_c$ from any subset of two equations, in particular

$$\text{from (2.2), (2.3):}\quad \Delta\alpha_a = 5\Delta\alpha_2 - 7\Delta\alpha_1, \qquad \Delta\alpha_c = 9\Delta\alpha_1 - 5\Delta\alpha_2 \tag{2.5}$$

$$\text{from (2.2), (2.4):}\quad \Delta\alpha_a = 1.25\Delta\alpha_3 - 0.25\Delta\alpha_1, \qquad \Delta\alpha_c = 2.25\Delta\alpha_1 - 1.25\Delta\alpha_3 \tag{2.6}$$

$$\text{from (2.3), (2.4):}\quad \Delta\alpha_a = 1.33\Delta\alpha_3 - 0.33\Delta\alpha_2, \qquad \Delta\alpha_c = 3\Delta\alpha_2 - 2\Delta\alpha_3\,. \tag{2.7}$$

Equation (2.4) has the largest coefficient for $\Delta\alpha_a$ and Eq. (2.2) has the largest coefficient for $\Delta\alpha_c$, i.e., $\Delta\alpha_1$ and $\Delta\alpha_3$ are closest to the pure tetragonal axes. Therefore, solution (2.6) is preferable, since it has the smallest relative uncertainties. Using this solution, we obtain the dotted lines in Figures 2.12 (b) representing the temperature-dependent behavior of the tetragonal axes $a_t/\sqrt{2}$ and $c_t/2$. Dotted lines in 2.12 (a) show the corresponding thermal-expansion coefficients. The derived anomalies $\Delta\alpha_a$ and $\Delta\alpha_c$ around T_s are by construction identical to those in the temperature-dependent x-ray data of the $SrTiO_3$ lattice

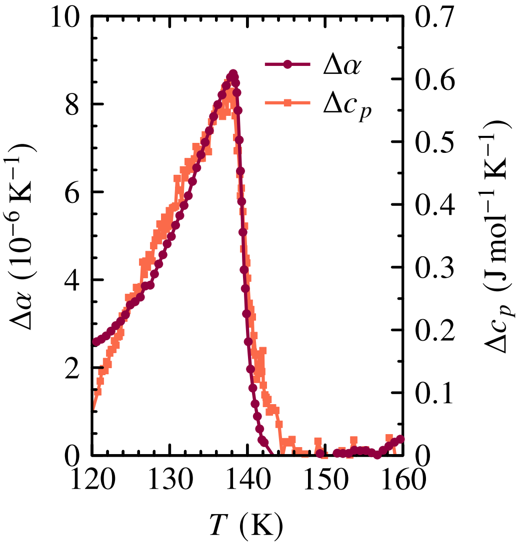

Figure 2.13: Comparison of $\Delta\alpha_{a_t}$ and Δc_p of pristine $Sr_{0.991}Ca_{0.009}TiO_3$ at T_s. Jumps of the thermal-expansion coefficient α (left axis) and the molar specific heat c_p (right axis) at the structural phase transition.

parameters [229], but the relation $2\Delta\alpha_a \approx -\Delta\alpha_c$ is independent from this reconstruction since it follows directly from the (almost) absent anomaly in the volume expansion β and the tetragonal symmetry. In contrast to the cubic-to-tetragonal transition, the ferroelectric transition at T_C is not volume conserving as is seen in the pronounced anomaly of the averaged uniaxial expansion $\bar{\alpha}$ [see black dashed line in Fig. 2.12 (a)]. Furthermore, the reconstructed tetragonal axes anomalies at T_C suggest that the volume-expansion anomaly essentially arises from a c-axis expansion upon cooling, while the transition is roughly area-conserving regarding the ab plane. The latter is naturally expected for a tetragonal-to-orthorhombic transition with opposite expansion anomalies of similar magnitudes along the orthorhombic a and b axes. The ferroelectric polarization is expected to be aligned along one of these axes [26, 188, 240]. As discussed in Sec. 2.3, a tetragonal-to-orthorhombic transition increases the number of possible twin domains at least by a factor of 2. The simultaneous loss of an inversion center creates another factor of 2, yielding a total number of 4 twin domains, when starting from a tetragonal monodomain. Thus, a threefold-twinned tetragonal crystal develops up to 12 twin domains in the orthorhombic phase. As already mentioned, the sample's edges are parallel to the cubic $\langle 100\rangle_c$ axes. This implies that the uniaxial length change is measured along $\langle 110\rangle_o$ in the orthorhombic phase and is blind to any in-plane anisotropy because $\alpha_{[110]_o} = (\alpha_a + \alpha_b)/2$. Furthermore, the twin domains created by the loss of inversion symmetry cannot be distinguished by thermal expansion.

Figure 2.13 compares the jumps in $\alpha_{a_t}(T)$ and $c_p(T)$ at $T_s \approx 139\,\mathrm{K}$. To obtain the jump Δc_p, the background is fitted above T_s using a polynomial fit function as already explained in the context of Fig. 2.10 (d). For $\Delta\alpha_{a_t}$, the data is fitted in the range $143\,\mathrm{K} \leq T \leq 155\,\mathrm{K}$ using the fit function $\alpha_{a_t}(T) = aT^2 + bT + c$ with parameters $a \simeq -8.1\times10^{-10}\,\mathrm{K}^{-4}$,

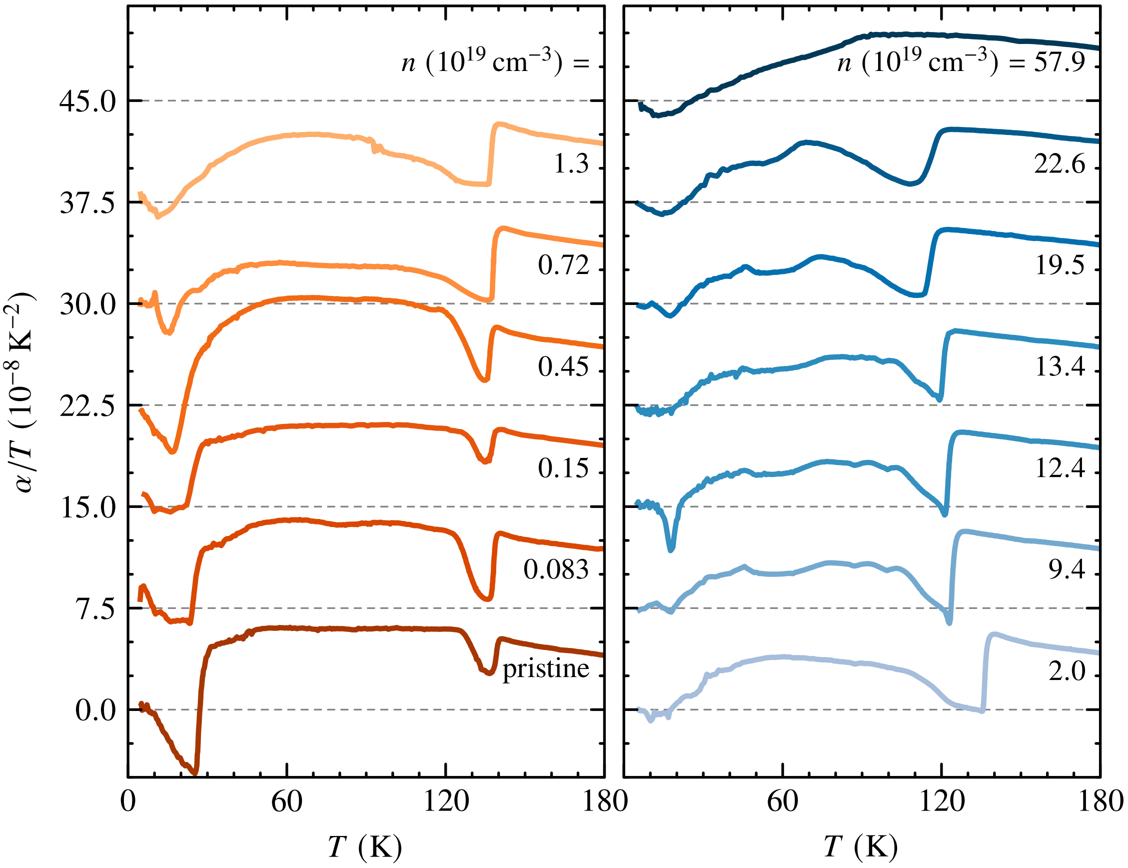

Figure 2.14: Thermal expansion of $Sr_{0.991}Ca_{0.009}TiO_{3-\delta}$. Thermal-expansion coefficient α/T versus T of $Sr_{0.991}Ca_{0.009}TiO_{3-\delta}$ with different carrier densities n. For clarity, the curves are shifted by $7.5 \times 10^{-8}\,K^{-2}$ with respect to each other.

$b \simeq 1.8 \times 10^{-7}\,K^{-3}$, and $c \simeq -1.7 \times 10^{-6}\,K^{-2}$. By using the Ehrenfest relation

$$\frac{dT_s}{dp_{a_t}} = V_{mol} T_s \frac{\Delta\alpha_{a_t}}{\Delta c_p} \tag{2.8}$$

one can estimate the uniaxial pressure dependence of the transition temperature T_s. The molar volume is $V_{mol} = N_A V_{uc}/N_{uc} = N_A a^3 \simeq 3.57 \times 10^{-5}\,m^3\,mol^{-1}$ with unit-cell volume $V_{uc} = a^3 \simeq (3.9\,Å)^3$ and the number of formula units per unit cell $N_{uc} = 1$. From Fig. 2.13 (a), one extracts $\Delta\alpha_{a_t} \simeq 8.6 \times 10^{-6}\,K^{-1}$ and $\Delta c_p \simeq 0.6\,J\,mol^{-1}\,K^{-1}$ resulting in $dT_s/dp_{a_t} \approx 72\,K\,GPa^{-1}$.

Electron-doped $Sr_{0.991}Ca_{0.009}TiO_{3-\delta}$

Oxygen-deficient crystals $Sr_{0.991}Ca_{0.009}TiO_{3-\delta}$ are obtained by annealing and their charge-carrier densities are determined by Hall-effect measurements as described in Sec. 2.3.2.

On each sample, the uniaxial thermal expansion was measured along L_1. Figure 2.14 shows the thermal-expansion coefficients α/T versus T of $Sr_{0.991}Ca_{0.009}TiO_{3-\delta}$ crystals with different charge-carrier concentrations up to $n \leq 57.9 \times 10^{19}\,\mathrm{cm}^{-3}$. The α/T curve of the pristine sample, already shown in Fig. 2.12, is included for comparison. For clarity, the curves are shifted by $7.5 \times 10^{-8}\,\mathrm{K}^{-2}$ with respect to each other. It is reasonable to assume only minor variations in the twin-domain distribution between individual samples because all samples were obtained by parallel cuts from the original single crystal of pristine $Sr_{0.991}Ca_{0.009}TiO_3$. This assumption is supported by the fact that all samples, apart from that with highest n, show clear anomalies of the same sign and similar shape indicating the cubic-to-tetragonal transition at T_S. With increasing n the transition temperature linearly decreases from $T_S \simeq 139$ K in the pristine sample down to $\simeq 116$ K for $n = 22.6 \times 10^{19}\,\mathrm{cm}^{-3}$ [see Fig. 2.15 (a)]. Such a linear decrease of $T_S(n)$ is analogously found in reduced $SrTiO_3$ crystals without calcium [198, 199, 241]. A decreased T_S is also seen in reduced samples of the related compound $EuTiO_{3-\delta}$ [242] as discussed in Ch. 3. This suggests that this systematic decrease of T_S upon reduction is a generic trend in perovskite titanates. In contrast, an n-type doping by chemical substitution like in $SrTi_{1-x}Nb_xO_3$ increases T_S [241].

An extrapolation of the linear $T_S(n)$ dependence to the highest doping $n = 57.9 \times 10^{19}\,\mathrm{cm}^{-3}$ matches the kink of the α/T curve of the corresponding sample. This suggests that the structural transition remains present across all doping levels, but is hardly seen in the sample with highest doping. It is reasonable to attribute this weakly pronounced anomaly to the presence of more homogeneously distributed twin domains in this specific sample, i.e., the averaged uniaxial expansion $\bar{\alpha}$ is measured which hardly shows any anomaly, since the transition is almost volume conserving as discussed above. This resembles the behavior of the earlier discussed $Sr_{0.9955}Ca_{0.0045}TiO_{3-\delta}$, where the anomaly at T_S is much weaker compared to that of pristine $Sr_{0.9955}Ca_{0.0045}TiO_3$ [see Fig. 2.8].

The transition at $T_C \simeq 27$ K manifests itself as sharp anomaly in α/T of pristine $Sr_{0.991}Ca_{0.009}TiO_3$. It remains clearly identifiable for the lower-doped samples [see left panel of Fig. 2.14] and shifts down to 18 K for $n = 1.3 \times 10^{19}\,\mathrm{cm}^{-3}$. In contrast, the higher-doped samples [see right panel of Fig. 2.14] show anomalies that are much less pronounced (except for the sample with $n = 12.4 \times 10^{19}\,\mathrm{cm}^{-3}$). Nevertheless, a signature of the transition remains present in the α/T curves of all samples. Even the more homogeneously twinned, highest-doped sample with $n = 5.79 \times 10^{19}\,\mathrm{cm}^{-3}$ shows a minimum in α/T around 17 K, signaling the spontaneous volume expansion, while the volume-conserving transition at T_S only produces a kink. This is similar to the earlier discussed $Sr_{0.9955}Ca_{0.0045}TiO_{3-\delta}$, where the anomalies at T_C are very similar between doped and insulating crystals, while the T_S-related anomalies are very different indicating unequally distributed twin domains [see Fig. 2.8].

Figure 2.15 (b) shows both transition temperatures T_S and T_C as a function of charge-carrier density n in linear scales. Figure 2.15 (a) is a detail view of the low-n regime. The cubic-to-tetragonal transition is shown with a linear fit of $T_S(n)$ (solid line). Both the linear $T_S(n)$ behavior and the essentially absent weakening of the associated anomalies indicate a rather homogeneous distribution of oxygen vacancies and resulting charge-carriers. Despite

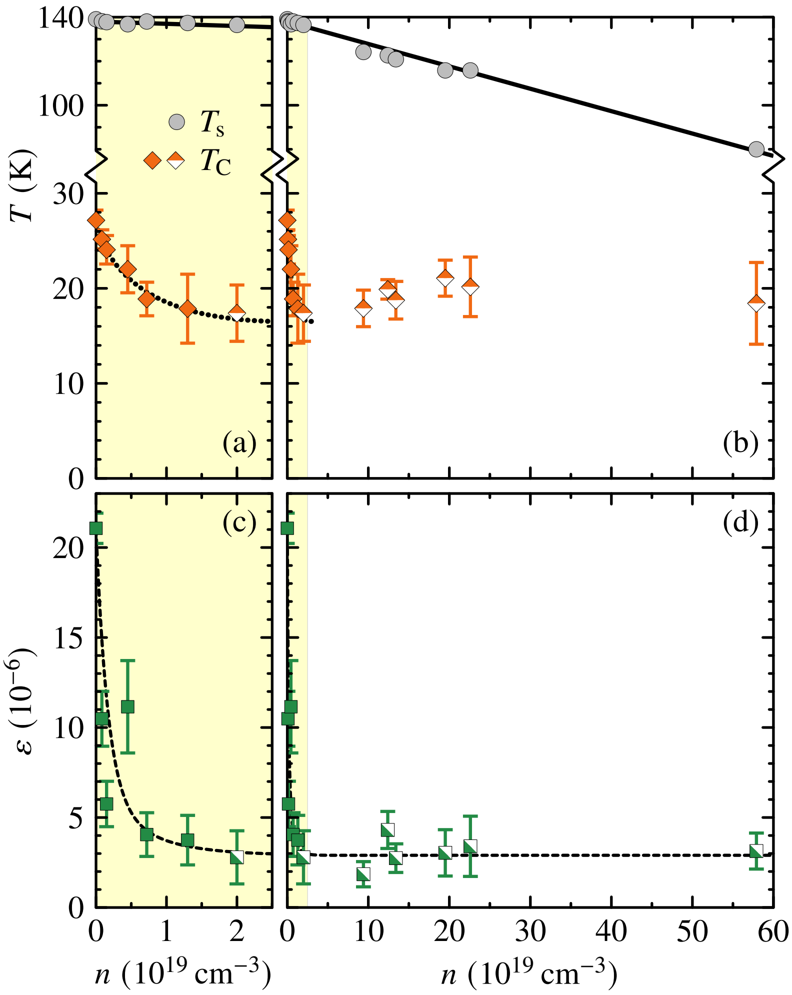

Figure 2.15: Phase diagram of $Sr_{0.991}Ca_{0.009}TiO_{3-\delta}$. (a, b) Transition temperatures T_s and T_C as a function of charge-carrier density n with linear fit of $T_s(n)$ (solid line) and guide to the eye for $T_C(n)$ (dotted curve). Note the scale breaks in both panels. Half-filled symbols refer to broad anomalies. (c, d) Spontaneous strain $\varepsilon(n)$ with guide to the eye (dotted curve). (a) and (c) show a detail view of the low-n regime.

the linearity of $T_s(n)$, the transition at T_C shows a more complex behavior as a function of n. While the ferroelectric transition of pristine $Sr_{0.991}Ca_{0.009}TiO_{3-\delta}$ produces a distinct anomaly in α/T, the broadening for the low-doped samples requires an appropriate criterion to define T_C and, furthermore, the inclusion of error bars. Hence, the maximum slope is taken to define T_C, while its temperature difference to the minimum in α/T is used as a measure of the transition width, that is shown as error bars in Figs. 2.15 (a) and (b). In the low-n regime ($n \leq 1.3 \times 10^{19}$ cm^{-3}), the corresponding $T_C(n)$ curve is concave as indicated by the dotted curve in Fig. 2.15 (a). For larger carrier densities, $T_C(n)$ basically saturates at a slightly elevated temperature and simultaneously increased error bars.

In order to quantify the up to now more qualitative distinction of sharp and broad anomalies, we use the spontaneous strain ε as a further measure for the T_C-related transition. By using a smooth background $\alpha_{bg}(T)$, the spontaneous strain is calculated via $\varepsilon = \int (\alpha - \alpha_{bg})\, dT$. The thermal expansion of $SrTiO_3$ is generally suited to serve as background because the material remains tetragonal down to lowest temperatures [154]. Indeed,

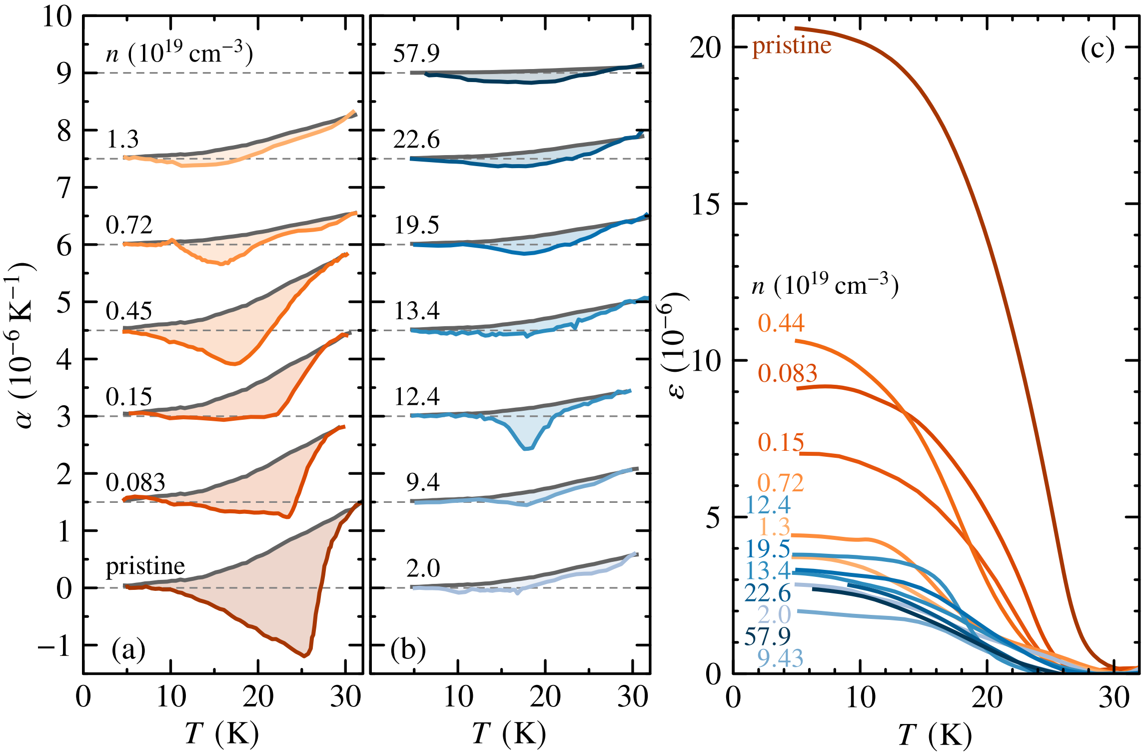

Figure 2.16: Determination of spontaneous strain ε in $Sr_{0.991}Ca_{0.009}TiO_{3-\delta}$. (a, b) Thermal-expansion coefficient $\alpha(T)$ of $Sr_{0.991}Ca_{0.009}TiO_{3-\delta}$ in the temperature range around T_C. Curves are shifted with respect to each other by 1.5×10^{-6} K^{-1} for clarity; zeros are indicated by dashed lines. Each curve is shown with a scaled $\alpha(T)$ of $SrTiO_3$ matching the data of the respective $Sr_{0.991}Ca_{0.009}TiO_{3-\delta}$ above the anomaly. Shaded areas are proportional to ε. (c) Spontaneous strain ε as a function of temperature.

by measuring the uniaxial length change of $SrTiO_3$ we obtain a smooth $\alpha_{STO}(T)$ behavior at low temperatures. This is different from thermal-expansion data measured under high uniaxial compressive stress [243] that show a minimum between 20 K and 30 K. There, a single-domain $SrTiO_3$ crystal is measured, resulting from stress-induced detwinning. Furthermore, $SrTiO_3$ is known to develop a stress-induced ferroelectric state [139, 140], as discussed in Sec. 2.1, what might explain the observed anomaly in that report. This assumption is supported by the similarity of this anomaly to that in our calcium-substituted, ferroelectric sample.

To serve as a background, the measured $\alpha_{STO}(T)$ curve was scaled to match the $\alpha(T)$ data of the respective $Sr_{0.991}Ca_{0.009}TiO_{3-\delta}$ sample above the T_C-related transition [see Figs. 2.16 (a) and (b)]. The scaling depends on the exact temperature where both curves shall merge. Especially the broad anomalies allow a certain freedom for this scaling. Therefore, the merge temperature was varied between 25 K and 35 K and the respective

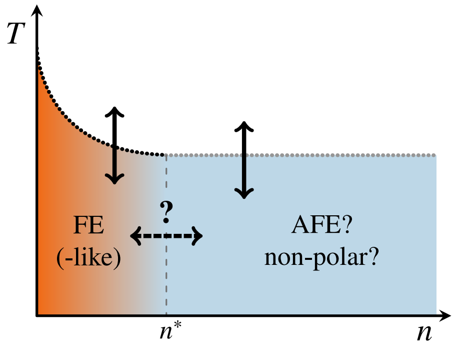

Figure 2.17: Generic phase diagram of $Sr_{1-x}Ca_xTiO_{3-\delta}$. A possible phase diagram of doped $Sr_{1-x}Ca_xTiO_3$ with a ferroelectric(-like) phase in the dilute regime and a transition to an unknown phase upon crossing a threshold carrier density n^*. Measurements as a function of temperature at fixed n (solid arrows) like $\alpha(T)$ are sensitive to the $T_C(n)$ phase boundary (dotted) but blind to a vertical phase boundary at n^* (dashed).

values for ε were used to define error bars. Figure 2.16 (c) shows the resulting $\varepsilon(T)$ curves, whereas the evolution of $\varepsilon(T = 4.2\,\mathrm{K})$ with charge-carrier density is seen in Fig. 2.15 (d). Figure 2.15 (c) displays a detail view of the low-n regime. It is seen, that $\varepsilon(T = 4.2\,\mathrm{K}, n)$ decreases rapidly below a threshold carrier density $n^* \approx 1.3 \times 10^{19}\,\mathrm{cm}^{-3}$ and levels off for higher carrier densities at a small value of $\simeq 15\,\%$ of the initial spontaneous strain of the pristine sample. Qualitatively, $T_C(n)$ shows a similar behavior [see Fig. 2.15 (a)] but saturates at a much higher level of $\simeq 60\,\%$ relative to T_C of pristine $Sr_{0.991}Ca_{0.009}TiO_3$. Half-filled symbols in Fig. 2.15 refer to data points in the saturated range of $\varepsilon(T = 4.2\,\mathrm{K}, n)$ indicating broad anomalies in $\alpha(T)$.

2.3.3 Conclusion

Rischau *et al.* observed that characteristic features of the ferroelectric phase transition in insulating pristine $Sr_{1-x}Ca_xTiO_3$ persist upon weak charge-carrier doping and vanish toward higher carrier concentrations n in a way being typical for quantum phase transitions [30]. Because this observation is based on minima in resistivity data $\rho(T, n)$, it necessitated a study via a thermodynamic probe. The main findings of this study are as follows: First, the persistence of a ferroelectriclike transition in the metallic phase is clearly confirmed by pronounced α/T anomalies in samples where n is below a threshold carrier density $n^* \approx 1.3 \times 10^{19}\,\mathrm{cm}^{-3}$. It should be emphasized, that the metallic conductivity in these samples is a real bulk property and not just a surface effect, as shown by Shubnikov–de Haas oscillations [30]. Furthermore, all these samples become superconducting at lower temperatures. Second, in contrast to the resistivity results of Rischau *et al.*, the anomalies in α/T do not vanish completely upon a further increase of charge-carrier concentration. Even though the features become very broad, a signature remains present in all samples of the entire studied doping range. Third, the thermal-expansion data do not give any indication for a sign change of the T_C-related anomalies as a function of n.

On the one hand, this could be the hint for a continuously disappearing ferroelectric order with increasing n. On the other hand, sharpness and shape of the α/T anomalies change qualitatively when crossing a certain carrier density around $n^* \approx 1.3 \times 10^{19}\,\mathrm{cm}^{-3}$ which may point to different crystal symmetries on both sides of n^*. Indeed, the requirement for a non-centrosymmetric space group is obsolete in the presence of mobile charge carriers.

However, it is plausible that this requirement is not destroyed immediately for very dilute charge carriers, but needs a certain threshold concentration. This resembles the situation of the low-temperature phase in insulating $Sr_{1-x}Ca_xTiO_3$, where, starting from the strontium-rich end, the non-centrosymmetric ferroelectric phase ($Ic2m$) changes to centrosymmetric antiferroelectric ($Pbcm$) as a function of calcium content x, as discussed in Sec. 2.3 [see also Fig. 2.6]. Moreover, the existence of ferroelectric metals has been discussed for a long time [244–246] and is, indeed, considered as a structural transition in a metal with loss of inversion symmetry.

Figure 2.17 shows a possible phase diagram for $Sr_{1-x}Ca_xTiO_{3-\delta}$, where the ferroelectric phase of the pristine insulating parent is extended toward a threshold carrier density n^* where the detected anomalies in $\alpha(T)$ change qualitatively. The phase above n^* is unknown. One possibility would be an antiferroelectric phase analogous to the case of insulating $Sr_{1-x}Ca_xTiO_3$ above $x = 0.12$ [170, 171, 184, 185]. Furthermore, a structural phase transition to a centrosymmetric space group can be involved. If the phase boundary at n^* is (almost) vertical, it can hardly be detected by temperature-dependent measurements like $\alpha(T)$. A structural analysis of $Sr_{1-x}Ca_xTiO_{3-\delta}$ crystals with different n is needed to unveil the nature of this unknown phase.

3 $EuTiO_3$

The as-grown $EuTiO_{3-\delta}$ is characterized and found to be oxygen-excessive with $\delta = -0.02$. Key figures like Néel temperature and Weiss temperature are in agreement with literature data. The metal–insulator transition (MIT) in oxygen-deficient $EuTiO_{3-\delta}$ is investigated by resistivity and Hall-effect measurements. The critical carrier density n_c for the MIT is compared with that of other doped perovskite materials with an insulating, quantum-paraelectric parent in the context of the so-called Mott criterion. An AT^2 resistivity is observed whose prefactor A scales with n. Using a simple model with three parabolic bands, an $A(n)$ function is derived that universally describes the experimental $A(n)$ behavior for diverse doped perovskite titanates. Parts of this chapter are based on data already published in J. Engelmayer *et al.*, Phys. Rev. Materials **3**, 051401(R) (2019) [242].

Contents

3.1 Introduction

Isovalent A-site substitutions in $SrTiO_3$ usually distort the lattice and destroy the cubic symmetry (i.e., the transition to the cubic phase is shifted to higher temperatures) as is seen for $Sr_{1-x}Ca_xTiO_3$ in Fig. 2.6. Europium offers the opportunity for an isovalent A-site substitution without severely affecting the crystal structure—Sr^{2+} and Eu^{2+} have a very similar ionic radius [see Tab. 3.1]—and simultaneously introducing magnetic effects into the system since Eu^{2+} has a magnetic moment of $7\mu_B$. Just like for $Sr_{1-x}Ca_xTiO_3$ and $Sr_{1-x}Ba_xTiO_3$, the solid solution $Sr_{1-x}Eu_xTiO_3$ exists over the entire composition range, but in contrast to the former, it remains cubic at room temperature for all x [247, 248]. This is not surprising because both end members $SrTiO_3$ and $EuTiO_3$ are cubic, whereas $CaTiO_3$ is orthorhombic [233] and $BaTiO_3$ is tetragonal [249] at room temperature. However, the lattice

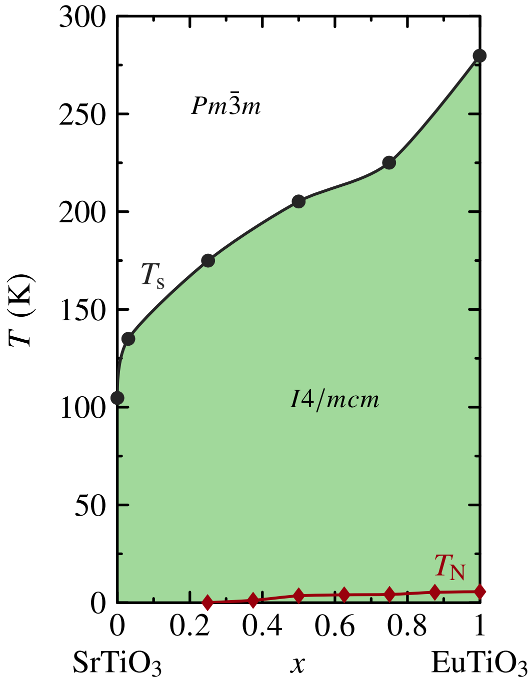

Figure 3.1: Phase diagram of Sr$_{1-x}$Eu$_x$TiO$_3$. Compiled from literature data of the structural transition temperature T_s [248] and the Néel temperature T_N [250]. Lines are guides to the eye.

is not completely unaffected by a replacement of strontium with europium. The transition temperature T_s of the cubic-to-tetragonal transition increases for SrTiO$_3$ → EuTiO$_3$ by a factor of ≈ 2.5 [see Fig. 3.1] but this change is much smaller than for SrTiO$_3$ → CaTiO$_3$, where the transition temperature becomes larger by a factor of ≈ 15 [see Fig. 2.6].

Hence, both end members SrTiO$_3$ and EuTiO$_3$ are structurally much more similar than any other pair of perovskite titanates. They share not only the same room-temperature crystal symmetry and the $Pm\bar{3}m \rightarrow I4/mcm$ transition, but both materials are believed to remain tetragonal down to lowest temperatures and both show quantum paraelectric behavior [20, 21, 69]. Despite these commonalities, they have also clear differences, where the macroscopic appearance of the crystals is the most obvious one: stoichiometric SrTiO$_3$ crystals are transparent, whereas EuTiO$_3$ is opaque with black color [see Sec. 1.4.3]. The latter has a band gap of 1 eV [83] and shows a measurable resistivity below room temperature [70], whereas SrTiO$_3$ is highly insulating with a gap of 3.2 eV [189]. While SrTiO$_3$ is nonmagnetic, the magnetic moments in EuTiO$_3$ order antiferromagnetically below $T_N = 5.5$ K [see Sec. 3.2.2].

In the previous chapter 2, charge-carrier doping is discussed in the context of the competition between a ferroelectric and metallic phase in Sr$_{1-x}$Ca$_x$TiO$_{3-\delta}$. Here, the focus is on the metal–insulator transition (MIT) itself and the electronic properties of weakly doped perovskite titanates in general. As already mentioned in Sec. 2.3.1, the highly insulating parent compound SrTiO$_3$ turns metallic[1] by diverse variants of n-type doping, in particular reduction (SrTiO$_{3-\delta}$) [27, 89, 191, 193, 197, 201], aliovalent B-site substitution

---

[1] See also footnote 5 on page 40.

($SrTi_{1-x}Nb_xO_3$) [89, 194, 202, 203], or aliovalent A-site substitution ($Sr_{1-x}La_xTiO_3$) [201, 203–207]. Independent of the doping method, a superconducting phase appears in a charge-carrier density regime $5 \times 10^{17}\,\mathrm{cm}^{-3} \lesssim n \lesssim 10^{21}\,\mathrm{cm}^{-3}$, where the maximum critical temperature is $T_c \approx 0.4\,\mathrm{K}$ [28, 191, 194, 206]. These remarkably low carrier concentrations identified $SrTiO_3$ as the most dilute superconductor[2] [252, 253]. In the metallic phase, a T^2 behavior of the resistivity is found in all three compounds $SrTiO_{3-\delta}$ [31], $SrTi_{1-x}Nb_xO_3$ [254], and $Sr_{1-x}La_xTiO_3$ [255].

Conventional theoretical explanations for the appearance of a T^2 resistivity are challenged in view of the extremely dilute charge carriers in metallic $SrTiO_3$ [31]. While electron–phonon scattering creates a T^5 resistivity at low temperatures which can be described within the Bloch–Grüneisen theory, a T^2 resistivity is known to arise from electron–electron scattering. W. G. Baber derived a T^2 behavior for systems with two bands and different band masses, where scattering is dominated by collisions between localized s electrons and delocalized d electrons [256]. This theory appropriately described the earlier observed T^2 low-temperature resistivity in transition metals like platinum [257]. The presence of Umklapp scattering has been shown to be another source for a T^2 behavior of the resistivity [258, 259]. Neither applies to the situation of doped $SrTiO_3$ since the system has a single-component Fermi surface and appropriate Fermi wave vectors for Umklapp scattering are not available for $n \lesssim 2 \times 10^{20}\,\mathrm{cm}^{-3}$ [31]. Thus, the origin of the T^2 resistivity in doped $SrTiO_3$ remains an open question. For many materials—especially heavy-fermion systems—the prefactor A of $\rho(T) = \rho_0 + AT^2$ is related to the electronic specific heat coefficient γ, because both depend on the Fermi energy E_F, as is expressed in the Kadowaki–Woods ratio A/γ^2 [260]. Because E_F itself depends on the carrier density n one may expect a particular scaling behavior in $A(n)$. Indeed, such a scaling behavior is observed for metallic $SrTiO_{3-\delta}$ [31].

The already discussed similarities to $SrTiO_3$ designate $EuTiO_3$ as a prime candidate to investigate these characteristics in another system. The following Sec. 3.2 briefly sums up the knowledge about $EuTiO_3$, in particular the crystal structure and the magnetic properties. Section 3.4 covers the characterization of the as-grown pristine $EuTiO_3$ crystals. The magnetic phase diagram is explored using temperature- and field-dependent measurements of resistivity, magnetization, uniaxial length change, heat capacity, and permittivity. The findings are compared to literature data. Section 3.5 deals with the properties of reduced $EuTiO_{3-\delta}$. The metal–insulator transition is studied by resistivity and Hall-effect measurements. Using these results, the critical charge-carrier density n_c for the MIT is estimated and compared with the Bohr radius in the context of the so-called Mott criterion. The temperature-dependent behavior of the mobility of $EuTiO_{3-\delta}$ is compared to that of $SrTiO_{3-\delta}$. The resistivity is found to obey a $\rho \propto AT^2$ behavior, where the prefactor A depends on the charge-carrier density n. A simple three-band model is used that describes the

---

[2] Pure bismuth has an even lower charge-carrier density $n = 3 \times 10^{17}\,\mathrm{cm}^{-3}$ and becomes superconducting at $T_c \approx 0.5\,\mathrm{mK}$ [251]. Doped $SrTiO_3$ with $n_c < 4 \times 10^{17}\,\mathrm{cm}^{-3}$ does not show superconductivity down to 60 mK [28]. However, a possible superconducting phase at temperatures comparable to the T_c of bismuth cannot be ruled out.

Site	Ion	Coordination	Eff. ion radius (Å)
X	O^{2-}	6 ‡	1.40
A	Ba^{2+}	12	1.61
A	Sr^{2+}	12	1.44
A	Ca^{2+}	12	1.34
A	Eu^{2+}	12	1.43 †
A	Eu^{3+}	12	1.23 †
A	La^{3+}	12	1.36
B	Nb^{5+}	6	0.64
B	Ti^{3+}	6	0.670
B	Ti^{4+}	6	0.605

Table 3.1: Ionic radii in perovskite titanates. Values are taken from Shannon [261] except † which are estimated values [see also Tab. 3.2]. ‡ As pointed out in Ref. [263, p. 54], the coordination of O^{2-} in perovskite materials is debatable. Often, it is assumed to be 6 (see, e.g., Refs. [264, 265] or [266, Suppl.]).

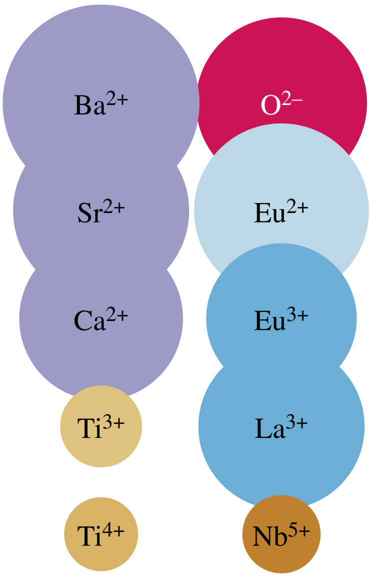

Figure 3.2: Illustration of ionic radii in perovskite titanates. Ionic radii for the respective coordinations in Tab. 3.1 drawn to scale.

$A(n)$ behavior of doped perovskite titanates including $EuTiO_{3-\delta}$, $SrTiO_{3-\delta}$, $SrTi_{1-x}Nb_xO_3$, and $Sr_{1-x}La_xTiO_3$.

3.2 Properties of $EuTiO_3$

3.2.1 Crystal structure

At room temperature, $EuTiO_3$ is isostructural to $SrTiO_3$, i.e., it has the same cubic space group $Pm\bar{3}m$ (No. 221) and the same lattice parameter $a \approx 3.9\,Å$ [61], which is not surprising, since the ionic radii of Eu^{2+} and Sr^{2+} are of similar size [261] [see Tabs. 3.1, 3.2, and Fig. 3.2]. Although the crystal structure of $EuTiO_3$ was determined already in 1953 [61], a first indication for a structural phase transition was found only in 2011 [66], the actual low-temperature tetragonal structure one year later [67, 71, 262] having the same space group $I4/mcm$ (No. 140) like $SrTiO_3$ in the tetragonal phase [see Sec. 2.2.2]. Because $EuTiO_3$ and $SrTiO_3$ have the same crystal symmetries in the cubic and tetragonal phase, the discussion of the structural phase transition [see Sec. 2.2.2] including the Bärnighausen tree [see Fig. 2.5] applies to both materials.

Unlike $SrTiO_3$, which has its cubic-to-tetragonal transition at $T_s = 110\,K$ [151], $EuTiO_3$

Table 3.2: Ionic radii of Sr^{2+} and Eu^{2+} for different coordinations. Values taken from Shannon [261] except ‡, which is an estimated value assuming that Eu^{2+} is constantly smaller by 0.01 Å compared to Sr^{2+} with the same coordination number.

	Effective ion radius (Å)	
Coordination	Sr^{2+}	Eu^{2+}
6	1.18	1.17
7	1.21	1.20
8	1.26	1.25
9	1.31	1.30
10	1.36	1.35
12	1.44	1.43 ‡

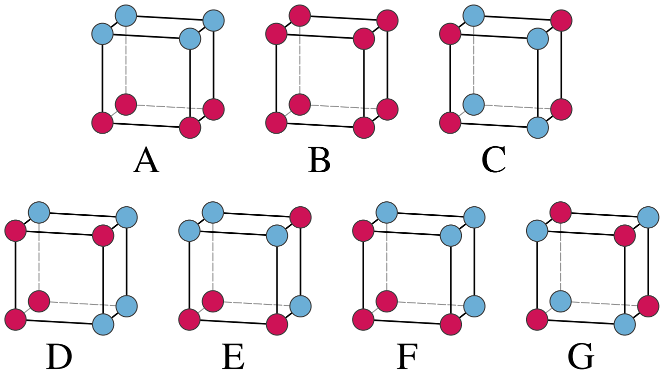

Figure 3.3: Nomenclature for magnetic structures. Adapted from Wollan and Koehler [268]. Circles illustrate magnetic moments. Same colors represent parallel moments, different colors represent antiparallel moments.

becomes tetragonal at much higher temperatures. However, the exact transition temperature is still under debate. Bussmann-Holder *et al.* [66] attribute a tiny specific-heat anomaly at 282 K to a structural phase transition, what roughly matches their own theoretical prediction of $T_s \approx 298$ K. This is supported by the findings in Refs. [72] and [267], where the specific heat shows a kink at 283 K and 281 K, respectively. In contrast, temperature-dependent synchrotron x-ray powder-diffraction data show distinct transitions at 235 K [71], as well as 245 K and 260 K [64], depending on the individual sample. These differences in T_s of different crystals are attributed to a strong impact of defect concentration [64]. However, the large discrepancies of the observed T_s signatures between thermodynamic and x-ray measurements are assumed to arise from a mismatch of long range and short range structural order [72]. An x-ray study suggests the lattice of $EuTiO_3$ in the tetragonal phase to be intrinsically disordered [71].

3.2.2 Magnetic structure

Europium is one of only two rare-earth elements (the other one is ytterbium) where a stable divalent oxidation state is known[3]. Divalent europium is actualized not only in

---

[3] Metastable YO exists as epitaxial thin film [269]. An obvious approach to get divalent ions is the synthesis of monoxides, since oxygen has a strong tendency to gain two electrons. Although significant efforts were made to obtain other rare-earth monoxides $R^{2+}O^{2-}$ [270–272], EuO is the only one that can be synthesized

Ion	Configuration	S	L	J	Symbol	g_J	μ_J/μ_B
O^{2-}	[Ne]	0	0	0	$^1S_0$	0	0
Ba^{2+}	[Xe]	0	0	0	$^1S_0$	0	0
Sr^{2+}	[Kr]	0	0	0	$^1S_0$	0	0
Ca^{2+}	[Ar]	0	0	0	$^1S_0$	0	0
La^{3+}	[Xe]	0	0	0	$^1S_0$	0	0
Eu^{2+}	$[Xe]4f^7$	7/2	0	7/2	$^8S_{7/2}$	2	7
Eu^{3+}	$[Xe]4f^6$	3	3	0	$^7F_0$	0	0
Nb^{5+}	[Kr]	0	0	0	$^1S_0$	0	0
Ti^{4+}	[Ar]	0	0	0	$^1S_0$	0	0
Ti^{3+}	$[Ar]3d^1$	1/2	2	3/2	$^2D_{3/2}$	4/5	1.2
Ti^{3+}	$[Ar]3d^1$	1/2	0	1/2	$^2S_{1/2}$	2	1

Table 3.3: Electronic configuration of ions in perovskite titanates. Spin quantum number S, orbital angular momentum quantum number L, total angular momentum quantum number J, term symbol $^{2S+1}L_J$, Landé factor g_J, and total magnetic moment μ_J according to Hund's rules. The last line shows values for $L = 0$, since the angular momentum is suppressed in 3d ions.

$EuTiO_3$ but also in $EuZrO_3$ [65, 276], $EuHfO_3$ [276], in europium chalcogenides EuO, EuS, EuSe, EuTe [277], and various others [278, 279]. The electronic configuration of Eu^{2+} is $[Xe]4f^7$ which implies a rather large magnetic moment of $7\mu_B$, whereas Eu^{3+} has no magnetic moment, since its configuration $[Xe]4f^6$ leads to $J = 0$ [see Tab. 3.3]. While $EuTiO_3$ is a paramagnet at high temperatures, the magnetic moments of Eu^{2+} order antiferromagnetically at $T_N \approx 5.5\,K$[4]. Early neutron scattering studies from 1966 suggest a G-type configuration [280], as is defined in the nomenclature introduced by Wollan and Koehler [268] [see Fig. 3.3]. This configuration has been confirmed by more recent neutron experiments from 2012 [63] which also provide evidence for the magnetic moments to point along tetragonal $\langle 110 \rangle_t$ directions.

The G-type configuration is the only one, in which nearest neighbors are always antiparallel [see Fig. 3.3]. To be more precise: for each spin, all 6 nearest neighbors are antiparallel,

---

under ambient pressure; a finding supported by calculations of the Gibbs energy change for the reaction $R + R_2O_3 \longrightarrow 3\,R^{2+}O^{2-}$ [273]. However, a high-pressure synthesis is possible for RO with R = La, Ce, Pr, Nd, Sm, Yb. Nevertheless, EuO and YbO are the only ones with divalent rare-earth ions. The others are metallic with trivalent rare-earth ions, what can be written as $R^{3+}(e^-)O^{2-}$ (the purely ionic picture breaks down here) [273]. The electronic configuration is then rather $[Xe]4f^{n-1}3d^1$ than $[Xe]4f^n$ [274]. This is also known from (non-oxide) ytterbium chalcogenides YbS, YbSe, and YbTe [275].

[4] The numbers given in literature vary between 5.3 K [280, 281], 5.4 K [80], 5.5 K [21, 282], 5.6 K [72], and 5.7 K [283]. A T_N of 6 K in Ref. [70] is either rounded or wrongly cited from Ref. [282]. The 5.7 K mentioned in Ref. [284] and the 5.6 K in Refs. [81, 88] are both wrongly taken from Ref. [21], where a T_N of 5.5 K is found, confirming the result of Ref. [282]. A T_N of 5.2 K in Ref. [82] is wrongly cited from Ref. [280], where 5.3 K is given.

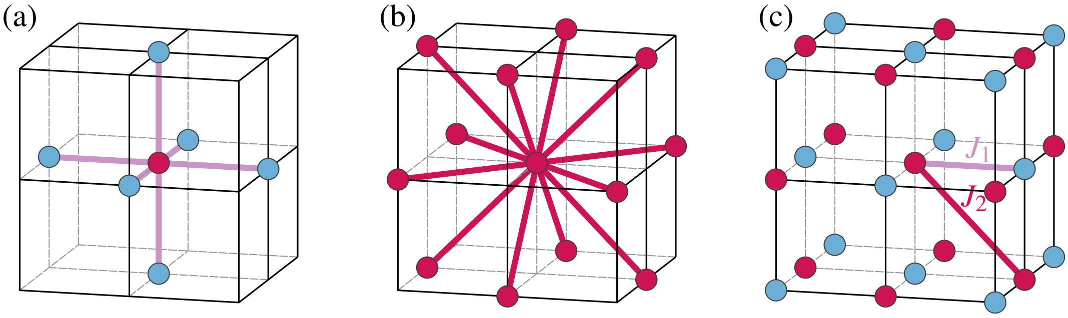

Figure 3.4: G-type unit cell and coupling constants. Each magnetic moment has 6 nearest neighbors aligned antiparallel (a) and 12 next-nearest neighbors aligned parallel (b). (c) Coupling constants J_1 (nearest-neighbor interaction) and J_2 (next-nearest-neighbor interaction).

all 12 next-nearest neighbors are parallel. Thus, one can define two different coupling constants: J_1 for nearest neighbor interaction and J_2 for next-nearest neighbor interaction [see Fig. 3.4]. If the antiferromagnetic lattice is considered to consist of two interpenetrating ferromagnetic sublattices, J_1 represents the intersublattice coupling and J_2 describes the intrasublattice coupling. Within molecular field theory[5], the following relations hold for the Weiss temperature θ_W and the Néel temperature T_N [286]:

$$\frac{3k_B}{2S(S+1)}\theta_W = Z_1J_1 + Z_2J_2 \tag{3.1}$$

$$\frac{3k_B}{2S(S+1)}T_N = -Z_1J_1 + Z_2J_2\,, \tag{3.2}$$

where Z_1 is the number of nearest neighbors and Z_2 the number of next-nearest neighbors. An overview of experimental literature values for T_N and θ_W is given in Tab. 3.4 and discussed in Sec. 3.4. Using average values $T_N = 5.5\,\mathrm{K}$ and $\theta_W = 3.6\,\mathrm{K}$ as well as $Z_1 = 6$ and $Z_2 = 12$, one obtains the coupling constants $J_1/k_B = -15\,\mathrm{mK}$ and $J_2/k_B = 36\,\mathrm{mK}$. Of course, there are theoretical models beyond the mean-field approach of Eqs. (3.1) and (3.1), e.g., in Refs. [267, 280]. Both yield larger absolute values for J_1 and J_2 but all models agree concerning the signs ($J_1 < 0$, $J_2 > 0$) and relative magnitudes ($J_2 \approx -2J_1$) of the coupling constants [see Tab. 3.4].

Thus, $EuTiO_3$ is an example for an antiferromagnet with positive Weiss temperature [250, 280]. This is not overly surprising, because a cubic G-type antiferromagnet naturally has twice as much next-nearest neighbors than nearest neighbors [see Fig. 3.4]. To produce a negative Weiss temperature within the model of (3.1), the absolute value of the nearest-neighbor interaction needs to be more than twice as large as the next-nearest-neighbor interaction, i.e., $\theta_W < 0 \Leftrightarrow 2J_2 < -J_1$ if $Z_2 = 2Z_1$. The related antiferromagnetic

---

[5] One should note that different sign conventions for coupling constants are used in literature [285, pp. 76, 79]. Here, we follow the convention used in Refs. [82, 250, 276, 280, 282], where $J > 0$ ($J < 0$) corresponds to ferromagnetic (antiferromagnetic) coupling.

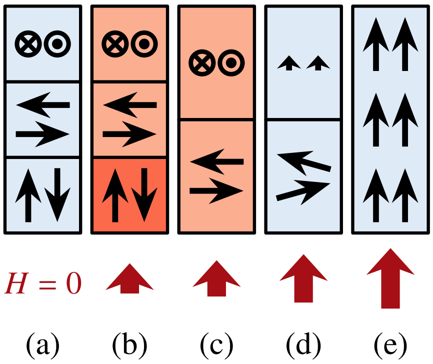

Figure 3.5: Spin-flop transition in cubic antiferromagnets. (a) The zero-field configuration consists of three perpendicular antiferromagnetic domains. (b) In an external magnetic field, the domain with antiparallel moments is unfavorable and will shrink. (c) With increasing field strength, this domain finally vanishes. (d) In the remaining domains, the moments will start to cant. (e) At sufficiently large fields, a field-polarized single domain is created.

compounds EuZrO$_3$ and EuHfO$_3$ also show positive Weiss temperatures [276] which are, however, much smaller than that of EuTiO$_3$.[6]

This magnetic configuration in EuTiO$_3$ is supported by density-functional theory using a local density approximation (LDA+U) [287], by a first-principles study using the generalized gradient approximation (GGA+U) [288], as well as by band-structure calculations using a hybrid Hartree–Fock density-functional approach [83]. The LDA+U approach found the system to be critically balanced between ferromagnetism and antiferromagnetism [287]. The Hartree–Fock density-functional calculations show, that the antiferromagnetic superexchange between neighboring Eu^{2+} moments, that is mediated by the Ti 3d states, competes with the indirect ferromagnetic exchange between Eu 5d states [83]. Furthermore, these theoretical approaches find a switchover from AFM to FM upon increasing unit-cell volume [83, 287, 288].

Because the structural phase transition of EuTiO$_3$ was found only in 2011 [66], all earlier theoretical treatments of the magnetism in this material, e.g., Refs. [83, 281, 287], assumed a cubic symmetry. Independent of the above described ambiguities regarding the exact transition temperature T_s of the cubic-to-tetragonal transition, it is doubtless that $T_N \ll T_s$, i.e., EuTiO$_3$ is definitely tetragonal in the magnetically ordered state. The consequences of a tetragonal symmetry for the G-type magnetic structure, the possible emergence of twin domains, and the implications concerning a spin-flop transition have been addressed in Refs. [63, 72].

For a cubic G-type antiferromagnet without external magnetic field one expects the emergence of three perpendicular antiferromagnetic domains [see Fig. 3.5 (a)]. When a magnetic field is applied, the domain with moments (anti-)parallel to the external field becomes energetically unfavorable [Fig. 3.5 (b)]. This domain will finally vanish, whereas the perpendicular domains grow [Fig. 3.5 (c)], a process that is referred to as spin-flop transition. Upon increasing field, the magnetic moments increase their in-field component by canting [Fig. 3.5 (d)] and ultimately align parallel to the field [Fig. 3.5 (e)].

In a tetragonal G-type antiferromagnet like EuTiO$_3$, one might expect structural twin

---

[6] Positive Weiss temperatures in antiferromagnets are not restricted to G-type configurations but are also found for other magnetic structures, e.g., in the A-type antiferromagnet LaMnO$_3$ [268].

domains in addition to antiferromagnetic domains. As shown in Ref. [63], the magnetic moments in $\mathrm{EuTiO_3}$ point along tetragonal $\langle 110\rangle_\mathrm{t}$ directions. A magnetic field applied along a cubic $[100]_\mathrm{c}$ direction is parallel to a $[110]_\mathrm{t}$ direction in the tetragonal phase. Thus, the relative orientations of spins and external field illustrated in Fig. 3.5 is still correct, but each structural twin domain contains only two antiferromagnetic domains as is discussed in Ref. [72].

3.3 Methods

The $\mathrm{EuTiO_3}$ crystals were synthesized as described in Sec. 1.4.2. The as-grown crystal was oriented using a Laue camera and cut into cuboid pieces with all faces being $\{100\}$ planes. Few samples with faces (110), (111), $(1\bar{2}1)$ were cut. Resistivity and Hall-effect measurements were carried out by a standard four-probe and six-probe method, respectively. For temperatures $5\,\mathrm{K} \leq T \leq 300\,\mathrm{K}$, different home-built dipstick setups for wet cryostats were used, whereas the low-temperature range $250\,\mathrm{mK} \leq T \leq 1.8\,\mathrm{K}$ was covered using a commercial ^{3}He dipstick insert system (Heliox by Oxford Instruments). Specific heat in the low-temperature range was measured using the Heliox system with a home-built calorimeter option, while a commercial cryostat (PPMS by Quantum Design) with calorimeter option was used for measurements up to room temperature. Magnetization was measured with a commercial SQUID cryostat (MPMS by Quantum Design). Thermal expansion and magnetostriction were measured with a home-built capacitance dilatometer option for the Heliox system. Dielectric measurements were performed by Christoph P. Grams using a PPMS cryostat in combination with a high-impedance frequency-response analyzer (Novocontrol) and a vector network analyzer (ZNB8 by Rohde & Schwarz) covering a joint frequency range of $1\,\mathrm{Hz} \leq \nu \leq 100\,\mathrm{MHz}$.

3.4 Measurements on pristine $\mathrm{EuTiO_3}$

Magnetization Figure 3.6 shows the magnetization $M(T)$ of pristine $\mathrm{EuTiO_3}$ for selected magnetic fields $\mu_0 H$ applied parallel to the cubic $[100]_\mathrm{c}$ direction. Because zero-field-cooled (zfc) and field-cooled (fc) data are on top of each other, only the latter is shown. All curves show an anomaly at the Néel temperature $T_\mathrm{N} = 5.5\,\mathrm{K}$. Above T_N, the magnetization of $\mathrm{EuTiO_3}$ is that of a typical paramagnet. Thus, the inverse magnetic susceptibility $\chi^{-1} = \mu_0 H/M$ [see Fig. 3.6 (b)] shows a perfectly linear temperature dependence. A Curie–Weiss fit in the range $T \geq 20\,\mathrm{K}$ using the function $\chi^{-1} = aT + b$ yields the fit parameters $a = 0.735\,\mathrm{T\,f.u.}\,\mu_\mathrm{B}^{-1}\,\mathrm{K}^{-1}$ and $b = -0.261\,\mathrm{T\,f.u.}\,\mu_\mathrm{B}^{-1}$. Using the Curie–Weiss law

$$\chi = \frac{C}{T - \theta_\mathrm{W}} \tag{3.3}$$

yields a Curie–Weiss constant $C_\mathrm{exp} = 1/a = 13.6\,\mu_\mathrm{B}\,\mathrm{f.u.}^{-1}\,\mathrm{T}^{-1} = 95.5 \times 10^{-6}\,\mathrm{m^3\,K\,mol^{-1}}$ and a Weiss temperature $\theta_\mathrm{W} = -b/a = 3.55\,\mathrm{K}$. This value is in agreement with most of

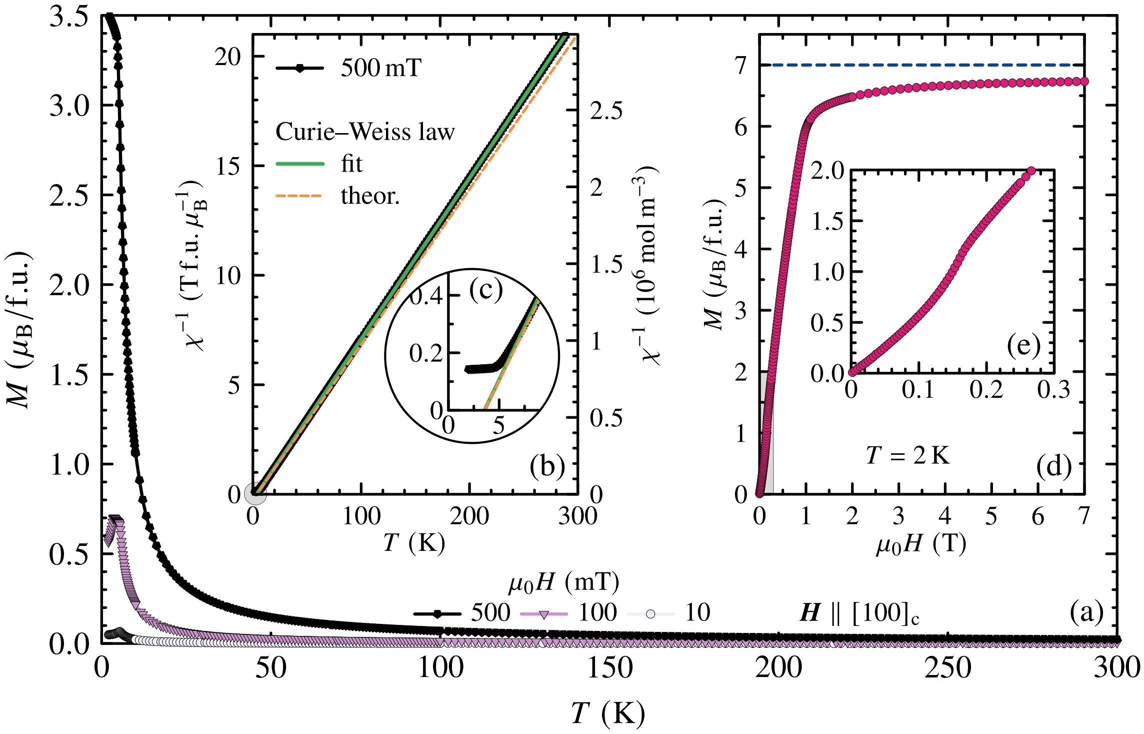

Figure 3.6: Magnetization $M(T,H)$ of pristine EuTiO$_3$. (a) Magnetization as a function of temperature for different magnetic fields applied parallel to the cubic $[100]_c$ direction. (b) Inverse susceptibility $\chi^{-1} = \mu_0 H/M$ at 500 mT with Curie–Weiss fit (green solid line) for $T \geq 20$ K and theoretical Curie–Weiss law (orange dashed line) expected for a spin-7/2 system. (c) Detail view of the low-temperature regime, revealing the Weiss temperature $\theta_W = 3.55$ K. (d) Magnetization at 2 K as a function of magnetic field. Saturation magnetization of $7\mu_B$ is shown as blue dashed line. (e) Detail view of the small-field range of $M(H)$.

the literature data, where the Weiss temperature is in the range $3.1\,\mathrm{K} \leq \theta_W \leq 3.8\,\mathrm{K}$, with the exception of Ref. [250], where a much larger $\theta_W = 4.5$ K is reported. A comparison of literature values for T_N and θ_W is given in Tab. 3.4.

The theoretically expected Curie–Weiss function is shown as dashed line in Figs. 3.6 (b) and 3.6 (c). It is calculated using the Curie constant in units of $\mu_B\,\mathrm{f.u.}^{-1}\mathrm{T}^{-1}$ given by

$$C = \frac{\mu_B g_J^2 J(J+1)}{3k_B}, \tag{3.4}$$

with Bohr magneton μ_B, electron g factor $g_J = 2$, total angular momentum quantum number J, and Boltzmann constant k_B. With $J = 7/2$, one obtains a value of $C_{\mathrm{theor}} = 14.1\,\mu_B\,\mathrm{f.u.}^{-1}\,\mathrm{T}^{-1} = 99 \times 10^{-6}\,\mathrm{m}^3\,\mathrm{K}\,\mathrm{mol}^{-1}$. By comparing experimental and theoretical values for the Curie–Weiss constant one finds $C_{\mathrm{exp}}/C_{\mathrm{theor}} = 0.965$, i.e., the experimental value is only 96.5 % of the value for a pure 7/2 system. In reverse, the experimental value

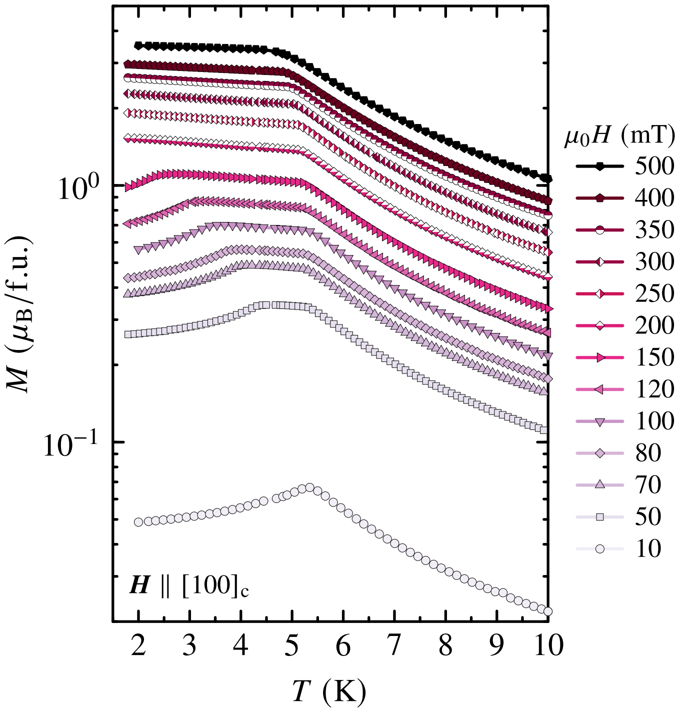

Figure 3.7: Low-temperature magnetization $M(T)$ of pristine $EuTiO_3$ in different magnetic fields. Enlarged view of $M(T)$ in semilog scale in the temperature range around T_N for magnetic fields $10\,\text{mT} \leq \mu_0 H \leq 500\,\text{mT}$ applied parallel to the cubic $[100]_c$ direction.

Publication	T_N (K)	θ_W (K)	J_1/k_B (mK)	J_2/k_B (mK)
This work	5.5	3.55	−15.5	35.9
Chien *et al.* [282]	5.5	3.8	−14	37
Akamatsu *et al.* [276]	5.5	3.6	−15	36
Guguchia *et al.* [250]	5.6	4.5	− 8.7	40.1
McGuire *et al.* [280]	5.3	3.8	−11.9 †	36.1 †
Mo *et al.* [283]	5.7	3.2	−19.8 †	35.3 †
Midya *et al.* [267]	5.6	3.1	−19.8 †	34.5 †
McGuire *et al.* [280]	5.3	3.8	−21	40
Midya *et al.* [267]	5.6	3.1	−40.7	82.8

Table 3.4: Magnetic transition temperatures and coupling constants in $EuTiO_3$. Néel temperature T_N, Weiss temperature θ_W and coupling constants J_1 and J_2 calculated within molecular field theory using Eqs. (3.1) and (3.2). † Calculated by the author of this thesis using T_N and θ_W from the respective reference. Mo *et al.* do not provide coupling constants. Midya *et al.* and McGuire *et al.* use other theoretical models that yield larger absolute values for J_1 and J_2 which are shown in the last two lines.

for C corresponds to a lower spin of $J = 3.43$. Figure 3.6 (c) shows the magnetization at 2 K as a function of magnetic field. The saturation value is $M_{\text{sat}} \approx 6.73\,\mu_{\text{B}}$ which is 96.2 % of the theoretically expected value of $M_{\text{sat}} = g_J J = 7\,\mu_{\text{B}}$, indicated as blue dashed line. Thus, both the Curie–Weiss analysis of the temperature-dependent measurement and the saturation magnetization yield values that are about 4 % lower than expected for a pure 7/2 system. This indicates the presence of 4 % Eu^{3+} ions meaning that the as-grown crystal is slightly oxygen excessive with $\delta = -0.04/2 = -0.02$ resulting in a nominal composition EuTiO$_{3.02}$. An enlarged view of the low-field range is seen in Fig. 3.6 (d), where $M(H)$ shows a kink at approximately 0.16 T.

Figure 3.7 (a) shows the low-temperature range ($T \leq 10$ K) of the magnetization $M(T)$ of pristine EuTiO$_3$ for different magnetic fields ($10\,\text{mT} \leq \mu_0 H \leq 500\,\text{mT}$) in semilogarithmic scales. At lowest field 10 mT a single peak appears at $T_{\text{N}} \approx 5.5$ K. Upon increasing field, this peak splits into two kinks, where the upper one slightly shifts to lower temperatures and arrives at 4.8 K for the highest field of 500 mT. The lower kink shifts more rapidly to lower temperatures and moves out of the measured temperature range for $\mu_0 H \geq 200$ mT. While the upper kink signals T_{N}, the lower kink indicates a spin-flop transition as discussed in Sec. 3.2.2. First indications for a spin-flop transition in EuTiO$_3$ are reported in Ref. [63] and investigated in detail in Ref. [72], where magnetic susceptibility curves are shown, having very similar anomalies as the $M(T)$ curves in Fig. 3.7 (a). Also the kink in $M(H)$ [see Fig. 3.6 (e)] resembles similar anomalies in $\chi(H)$ shown in Ref. [72].

Within the above discussed mean-field approach [Eqs. (3.1) and (3.2)] the coupling constants J_1 and J_2 for nearest-neighbor and next-nearest neighbor interaction, respectively, can be calculated using the experimental values for the Néel temperature T_{N} and the Weiss temperature θ_{W}. Inserting $T_{\text{N}} = 5.5$ K and $\theta_{\text{W}} = 3.55$ K gives $J_1/k_{\text{B}} = -15.5$ mK and $J_2/k_{\text{B}} = 35.9$ mK. Because both temperatures agree with literature data, the derived coupling constants agree likewise, as long as the same model is used [see Tab. 3.4].

Thermal expansion and magnetostriction Figure 3.8 (a) shows the uniaxial length change $\Delta L/L_0$ of EuTiO$_3$ along a cubic $[100]_{\text{c}}$ direction as a function of temperature in different magnetic fields $\mu_0 H/\text{T} = 0, 1, 5$ applied parallel to the same direction. The curves are adjusted according to $\Delta L(\mu_0 H)$ at lowest temperature shown in Fig. 3.8 (c). In the paramagnetic phase $T > 5.5$ K, the zero-field curve shows a minor contraction upon cooling. A spontaneous contraction is seen at $T_{\text{N}} = 5.5$ K where the crystal enters the antiferromagnetic phase. In a magnetic field of 1 T, the transition is shifted to lower temperature and the contraction in the AFM phase is less pronounced. In the 5 T curve, the anomaly is absent. The corresponding thermal-expansion coefficients α are seen in Fig. 3.8 (b).

Figure 3.8 (c) displays the field-dependent uniaxial length change $\Delta L/L_0$ along the cubic $[100]_{\text{c}}$ direction measured at different temperatures $0.26\,\text{K} \leq T \leq 6\,\text{K}$ and $\boldsymbol{H} \parallel [100]_{\text{c}}$. The curves are adjusted according to the zero-field length change $\Delta L(T)$ shown in Fig. 3.8 (a). At lowest temperature 0.26 K, the crystal expands upon increasing magnetic field up to

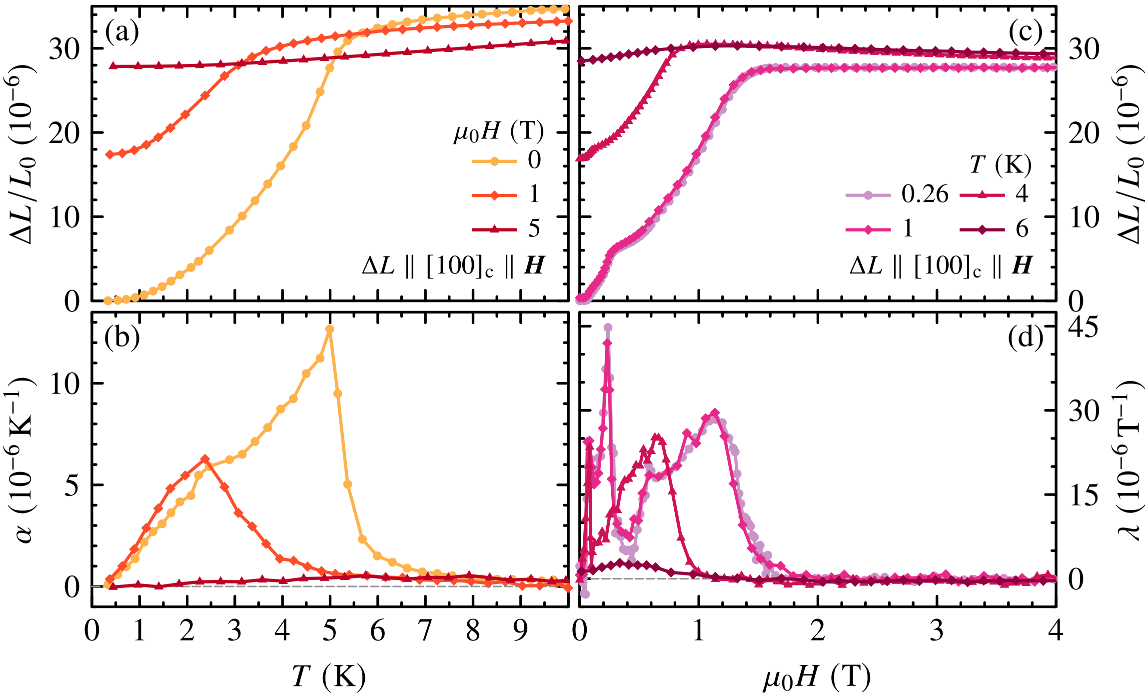

Figure 3.8: Thermal expansion and magnetostriction of pristine EuTiO$_3$. (a) Uniaxial length change $\Delta L/L_0$ of pristine EuTiO$_3$ as a function of temperature in different magnetic fields. (b) Corresponding thermal-expansion coefficient α. The dashed line indicates zero. (c) Uniaxial length change $\Delta L/L_0$ of pristine EuTiO$_3$ as a function of magnetic field $\mu_0 H$. (d) Corresponding magnetostriction coefficients λ. Dashed lines indicate zero.

approximately 1.2 T, whereas for higher fields the length remains almost constant. This behavior resembles the magnetization curve [see Fig. 3.6 (c)] by showing a saturation in the high-field regime above 1.2 K and a kink around 0.2 T that is related to the spin-flop transition. At higher temperatures, the expansion becomes smaller and the saturation plateau begins at smaller fields. At 6 K the field-induced length changes are only small. Figure 3.8 (d) shows the corresponding magnetostriction coefficients λ. The low-temperature curves for 0.26 K and 1 K reveal double-peaks below 0.2 T, whereas at 4 K only the lower peak survives.

Specific heat Figure 3.9 (a) shows the molar specific heat at constant pressure over temperature $c_p(T)/T$ of pristine EuTiO$_3$. While a huge anomaly appears at $T_N = 5.5$ K, the cubic-to-tetragonal transition in EuTiO$_3$ is not seen in this measurement, which is in contrast to other reports of the heat capacity of this material [66, 72, 267], where a kink appears around 282 K. Nevertheless, the absolute values of our measurement essentially agree with all three reports [see Tab. 3.5], including the position of the local minimum around 12 K. Figure 3.9 (b) displays an enlarged view of the temperature range around T_N, showing

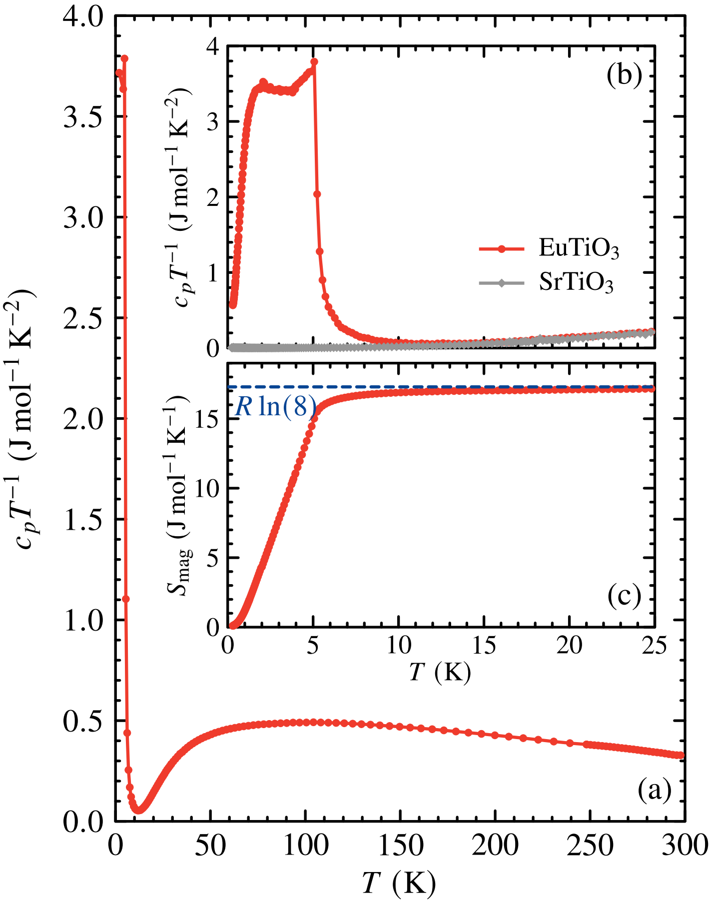

Figure 3.9: Specific heat and entropy of EuTiO$_3$. (a) Low-temperature specific heat c_p/T of pristine EuTiO$_3$ with pronounced anomaly at $T_N = 5.5$ K. Data of the non-magnetic SrTiO$_3$ with scaled temperature axis is used as phononic background. (b) Magnetic entropy S_{mag} compared to the theoretically expected value for a spin $S = 7/2$ system of $R\ln(8)$.

the specific heat $c_p(T)/T$ of EuTiO$_3$ in comparison to that of SrTiO$_3$. Because SrTiO$_3$ is nonmagnetic, its specific heat can be used as phononic background signal to extract the magnetic specific-heat contribution in EuTiO$_3$. In order to make the curves merge above the anomaly of the EuTiO$_3$ measurement, it is necessary to scale the temperature of the SrTiO$_3$ data by a factor 0.83. This can be done to take the unequal Debye temperatures of the different materials into account[7]. The magnetic entropy, calculated via

$$S_{\mathrm{mag}} = \int \frac{c_p^{\mathrm{ETO}} - c_p^{\mathrm{STO}}}{0.83 \cdot T} \, \mathrm{d}T \,,$$

is shown in Fig. 3.9 (c). The theoretically expected entropy of a spin $s = 7/2$ system is calculated via $S_{\mathrm{theor}} = R\ln(2s+1) = R\ln(8) \approx 17.3\,\mathrm{J\,mol^{-1}\,K^{-1}}$ and illustrated in Fig. 3.9 as blue dashed line.

Figure 3.10 (a) shows the specific heat c_p/T as a function of temperature for different magnetic fields up to 10 T applied parallel to the cubic $[100]_{\mathrm{c}}$ direction. With increasing

---

[7] The estimation $\theta_{\mathrm{D}}^{\mathrm{STO}}/\theta_{\mathrm{D}}^{\mathrm{ETO}} \propto \omega_{\mathrm{D}}^{\mathrm{STO}}/\omega_{\mathrm{D}}^{\mathrm{ETO}} \propto \sqrt{M^{\mathrm{STO}}/M^{\mathrm{ETO}}} \approx 0.86$ is close to the empirical value.

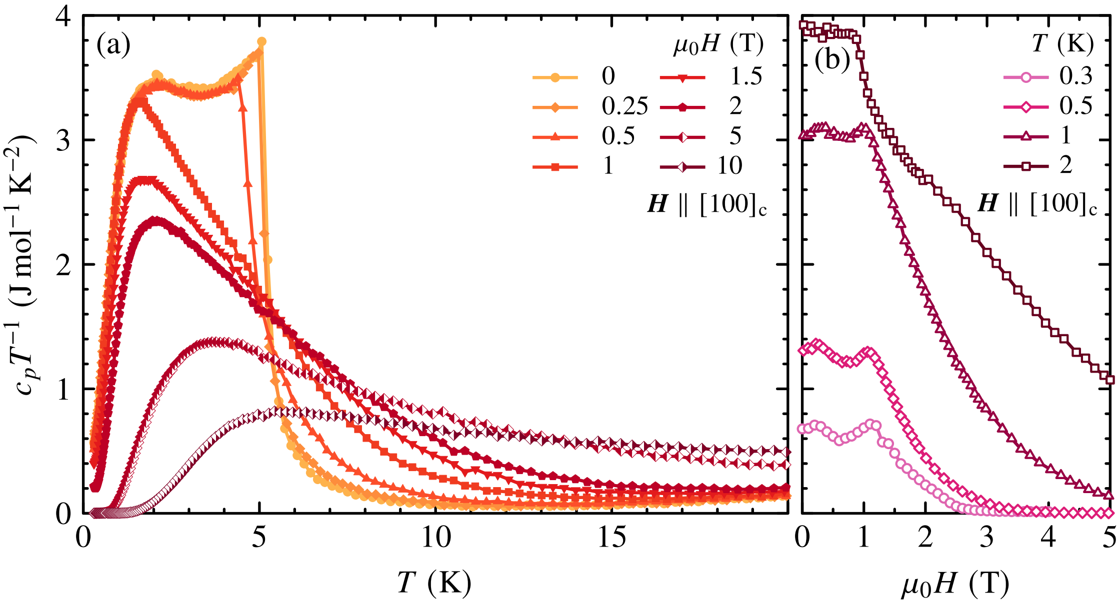

Figure 3.10: Specific heat of $\mathrm{EuTiO_3}$ in magnetic field. (a) Low-temperature specific heat c_p/T of pristine $\mathrm{EuTiO_3}$ as a function of temperature in different magnetic fields, with $\boldsymbol{H} \parallel [100]_c$. (b) c_p/T as a function of magnetic field at temperatures $0.3\,\mathrm{K} \leq T \leq 2\,\mathrm{K}$.

Table 3.5: Heat capacity of pristine $\mathrm{EuTiO_3}$: Literature values. Absolute values of c_p at room temperature and at T_N in comparison to literature values.

	c_p (J mol^{-1} K^{-1})	
Publication	300 K	T_N
This work	98	19
Bussmann-Holder *et al.* [66]	89	20
Petrovic *et al.* [72]	99	25
Midya *et al.* [267]	96	22

magnetic field, the sharp peak of the zero-field measurement at T_N shifts to lower temperatures and broadens rapidly, which is qualitatively in agreement with data of [72]. The field dependence of c_p/T is depicted in Fig. 3.10 (b). The curves show a kink, that shifts from 1.5 T at the lowest temperature 0.3 K to lower fields upon increasing temperature.

Figure 3.11 (a) compares the magnetic contributions of thermal-expansion coefficient and molar specific heat $\alpha^\mathrm{mag}(T)$ and $c_p^\mathrm{mag}(T)$, respectively. For $c_p^\mathrm{mag}(T)$, the specific heat of $\mathrm{SrTiO_3}$ $c_p^\mathrm{STO}(T)$ was taken as phononic background signal and subtracted from $c_p^\mathrm{ETO}(T)$ as has been done to determine S_mag [see Fig. 3.9]. However, this subtraction hardly changes $c_p^\mathrm{ETO}(T)$ below 10 K since $c_p^\mathrm{STO}(T)$ is almost zero in that temperature range. The thermal-expansion coefficient of $\mathrm{EuTiO_3}$ is even closer to zero at 10 K and does not change at all when subtracting a phononic background. Therefore, Fig. 3.11 (a) simply displays the original $\alpha(T)$ data as magnetic contribution. The anomaly shapes of both $c_p^\mathrm{mag}(T)$ and

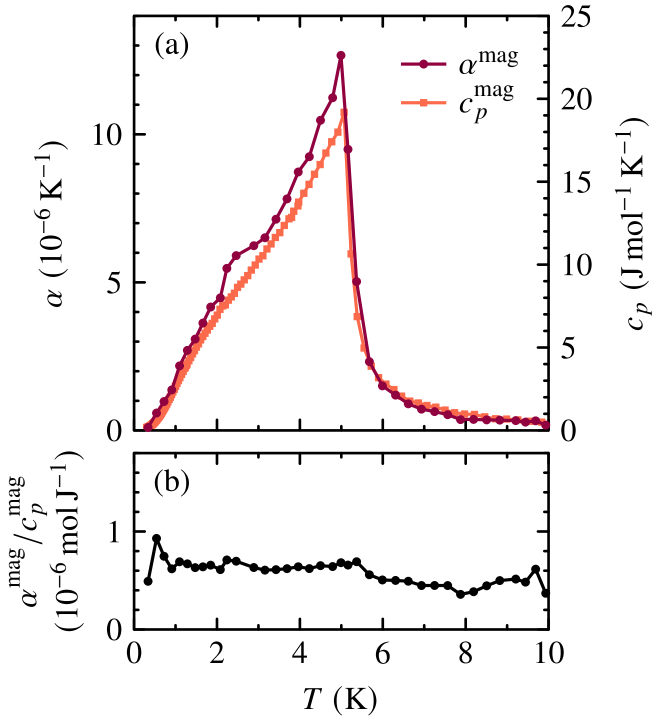

Figure 3.11: Comparison of α^{mag} and c_p^{mag} of pristine EuTiO$_3$. (a) Temperature dependence of the magnetic contributions of both the uniaxial thermal-expansion coefficient α (left axis) and the molar specific heat c_p (right axis) around T_N in zero magnetic field. (b) Ratio $\alpha^{\mathrm{mag}}/c_p^{\mathrm{mag}}$.

$\alpha^{\mathrm{mag}}(T)$ are very similar. This can be quantified by calculating the ratio $\alpha^{\mathrm{mag}}/c_p^{\mathrm{mag}}$ which is shown in Fig. 3.11 (b). It is almost constant over the whole temperature range of the anomaly, as is expected from a Grüneisen scaling.

This behavior is very similar to that of EuC$_2$, which is a ferromagnetic semiconductor with a Curie temperature of T_C = 14 K [289]. Despite of their different types of magnetic order (AFM vs. FM) and different magnetic transition temperatures (5.5 K vs 14 K) both materials strongly resemble the anomaly shapes of each other in both $c_p^{\mathrm{mag}}(T)$ and $\alpha^{\mathrm{mag}}(T)$. By using the Ehrenfest relation

$$\frac{\mathrm{d}T_\mathrm{N}}{\mathrm{d}p} = V_\mathrm{mol} T_\mathrm{N} \frac{\Delta\alpha}{\Delta c_p} \tag{3.5}$$

one can estimate the uniaxial pressure dependence of the transition temperature T_N. The molar volume is $V_\mathrm{mol} = N_\mathrm{A} V_\mathrm{uc}/N_\mathrm{uc} \simeq 3.6 \times 10^{-5}\,\mathrm{m^3\,mol^{-1}}$ with unit-cell volume $V_\mathrm{uc} = a^2c \simeq (5.51 \times 5.51 \times 7.8)\,\mathrm{\AA}^3$ and the number of formula units per unit cell $N_\mathrm{uc} = 4$. By extracting $\Delta\alpha \simeq 12.8 \times 10^{-6}\,\mathrm{K^{-1}}$ and $\Delta c_p \simeq 19\,\mathrm{J\,mol^{-1}\,K^{-1}}$ from Fig. 3.11 (a) one obtains $\mathrm{d}T_\mathrm{N}/\mathrm{d}p \approx 0.13\,\mathrm{K\,GPa^{-1}}$.

Resistivity Figure 3.12 (a) shows the dc resistivity $\rho(T)$ of pristine EuTiO$_3$ as dashed line. In contrast to the highly insulating SrTiO$_3$, the dc resistivity of EuTiO$_3$ is measurable down to $\simeq$ 80 K. This dc measurement is extended to lower temperatures by $\rho_\mathrm{ac}(T) = \sigma_\mathrm{ac}^{-1}(T)$ obtained from dielectric spectroscopy measurements (solid line), which are discussed in

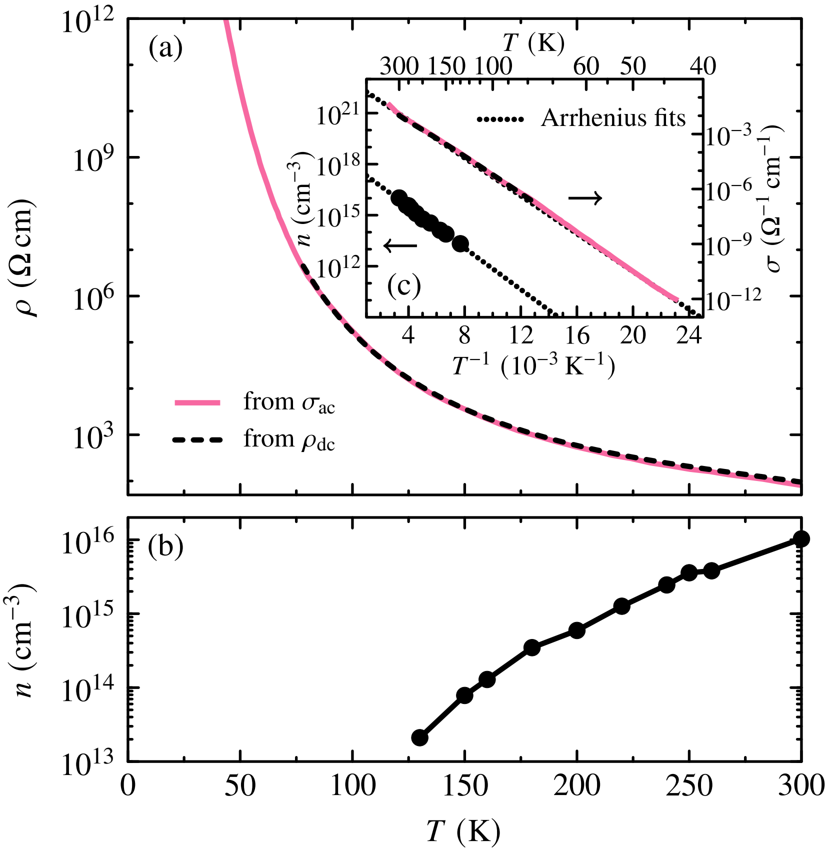

Figure 3.12: Resistivity and charge-carrier density of pristine EuTiO$_3$. (a) Resistivity of pristine EuTiO$_3$ as a function of temperature in semi-log scale, where ρ_{dc} is obtained by dc measurements and $\rho_{ac}(T) = \sigma_{ac}^{-1}(T)$ by dielectric measurements. (b) Charge-carrier density n versus temperature determined from Hall-effect measurements. (c) Arrhenius plot of $\sigma_{dc}(T) = \rho_{dc}^{-1}(T)$ and $\sigma_{ac}(T)$, as well as $n(T)$, both with linear fits (dotted lines).

detail in the following section [see Fig. 3.13]. Figure 3.12 (b) shows the charge-carrier density n as determined from Hall-effect measurements. As is expected for a semiconductor, n is temperature dependent since it represents the charge-carrier density of the conduction band. It ranges from $10^{16}\,\mathrm{cm}^{-3}$ at room temperature to $\simeq 10^{13}\,\mathrm{cm}^{-3}$ at 130 K, which is the lowest temperature accessible by Hall-effect measurements on this sample, due to the rapidly increasing resistivity.

The temperature-dependent behavior of both σ and n obey an Arrhenius law $\sigma \propto n \propto \exp(-\Delta/(k_B T))$ as is demonstrated in Fig. 3.12 (c). The Arrhenius plot displays both n (black circles, left axis) and σ (dashed and solid lines, right axis) as a function of T^{-1}. The corresponding fits (dotted lines) yield similar activation energies Δ of 100 meV from conductivity and 120 meV from charge-carrier density. This is about 10 % of the theoretically expected intrinsic band gap of 1 eV [83]. Due to the semiconducting behavior, the resistivity becomes unmeasurable at low temperatures, which is why the antiferromagnetic transition at 5.5 K is not accessible by dc resistivity measurements.

Permittivity The large low-temperature resistivity of pristine $EuTiO_3$ hinders an observation of a signature at T_N in $\rho(T)$ but simultaneously offers the opportunity to use dielectric measurements for an investigation of the highly insulating regime. Thus, dc resistivity and dielectric spectroscopy can be used as complementary methods to cover a large joint temperature range. Figure 3.13 (a) shows the permittivity $\varepsilon'(T)$ measured at different frequencies in the range $1\,\text{Hz} \leq \nu \leq 100\,\text{MHz}$. The high-frequency/low-temperature limit represents the intrinsic signal of the sample, whereas the steep increase of each curve above a ν-dependent temperature indicates the crossover to a contact-dominated signal caused by the Maxwell–Wagner effect [290, 291]. Schottky-type depletion layers emerge at the contact interfaces producing a capacitive contribution C_C. Since the contacts also have a resistance R_C they form an RC element which is in series with the intrinsic sample impedance. For frequencies $2\pi\nu > 1/R_C C_C$, the contacts are effectively short-circuited [292, 293]. Between 10 K and 20 K, the permittivity reaches its maximum of $\varepsilon'_{\text{max}} \approx 403$ which is in agreement with the largest reported value of 400 [21] [see Fig. 2.2]. Due to grain boundaries one expects lower values for ceramics compared to single crystals. However, Goian *et al.* [262] measured $\varepsilon'(T)$ on both ceramics and single crystals with very different results, where the single crystal had the lowest $\varepsilon'_{\text{max}}$. These variations may be explained by differences in the distribution of twin domains in the specific crystal. Nevertheless, ceramic samples measured by Kennedy *et al.* [64] show a rather large value of $\varepsilon'_{\text{max}} \approx 356$ that is almost as high as that of our single crystal.

The quantum paraelectric behavior is clearly seen in the intrinsic signal and can be modeled by the Barrett formula [132]

$$\varepsilon(T) = \frac{C}{(T_\Omega/2)\coth(T_\Omega/2T) - T_0} + \varepsilon_\infty\,, \tag{3.6}$$

where T_Ω describes the influence of quantum fluctuations and T_0 is the Curie–Weiss temperature of the paraelectric contribution. The Barrett fit is shown as dashed line in Fig. 3.13 (a) and yields $T_\Omega \simeq 160\,\text{K}$ and $T_0 \simeq -190\,\text{K}$. The first value agrees with T_Ω reported in Ref. [21] and is twice as large compared to $SrTiO_3$ [20, 294] indicating stronger quantum fluctuations in $EuTiO_3$. The value of T_0 is much lower than $T_0 = -25\,\text{K}$ from Ref. [21], but comparable to the value in Ref. [69] obtained from ceramics. Although the absolute value differs, all reports agree on a negative T_0 in $EuTiO_3$ indicating antiferroelectric correlations. A comparison of literature permittivity values for $EuTiO_3$ and $SrTiO_3$ is given in Tab. 3.6.

Figure 3.13 (b) shows an enlarged view of the low-temperature range, revealing both the plateau-like behavior being typical for a quantum paraelectric material and an additional drop below $T_N = 5.5\,\text{K}$ indicating the magnetoelectric coupling, which already has been observed [21] and theoretically explained [281]. Figure 3.13 (c) shows the corresponding ac

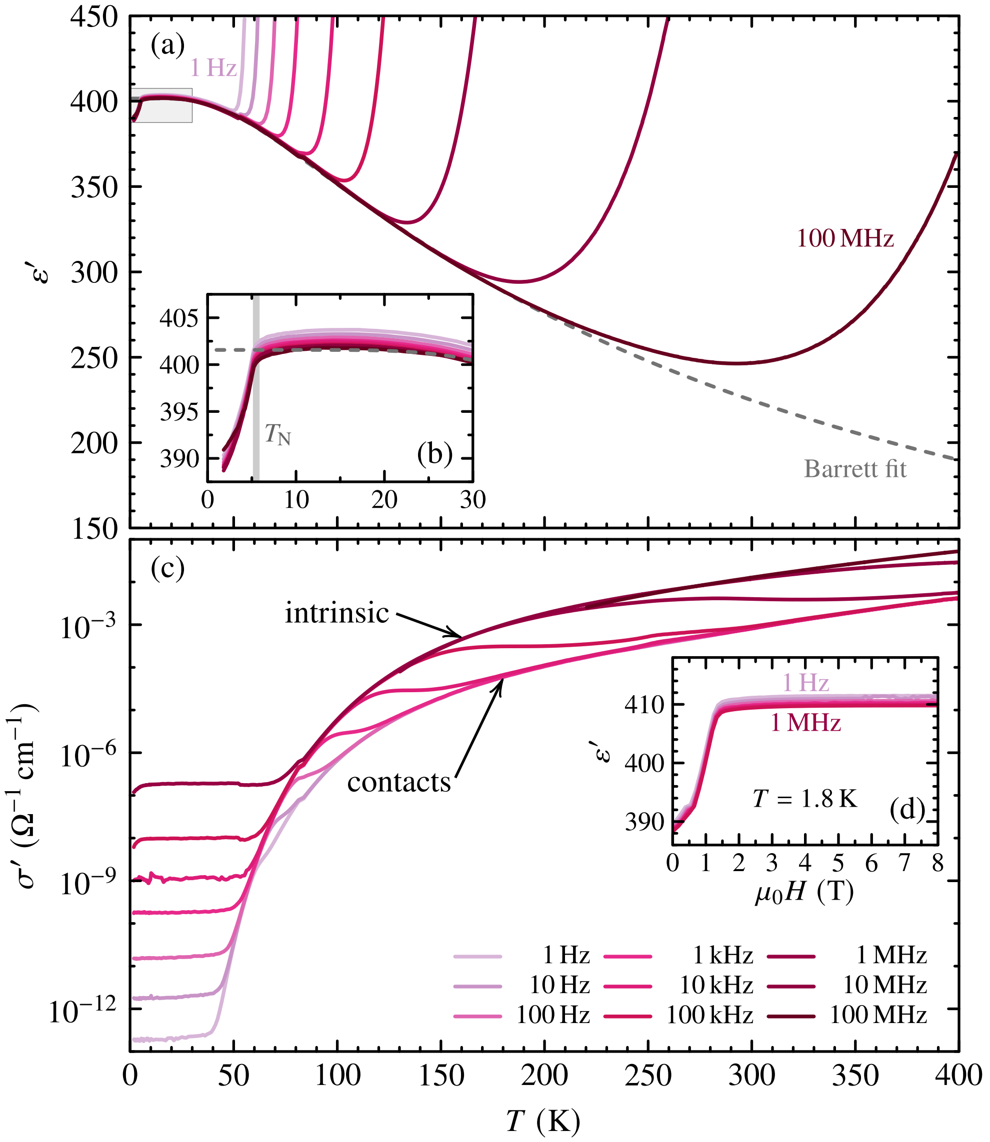

Figure 3.13: Dielectric measurements on EuTiO$_3$. (a) Permittivity ε' as a function of temperature measured at different frequencies $1\,\mathrm{Hz} \leq \nu \leq 100\,\mathrm{MHz}$ with Barrett fit (dashed line). Box indicates position of detail view. (b) Enlarged view of the low-temperature range with T_N indicated by vertical line. (c) Corresponding conductivity $\sigma'(T)$ in semi-log scale. (d) Permittivity ε' at 1.8 K as a function of magnetic field. All dielectric measurements were performed by Christoph P. Grams.

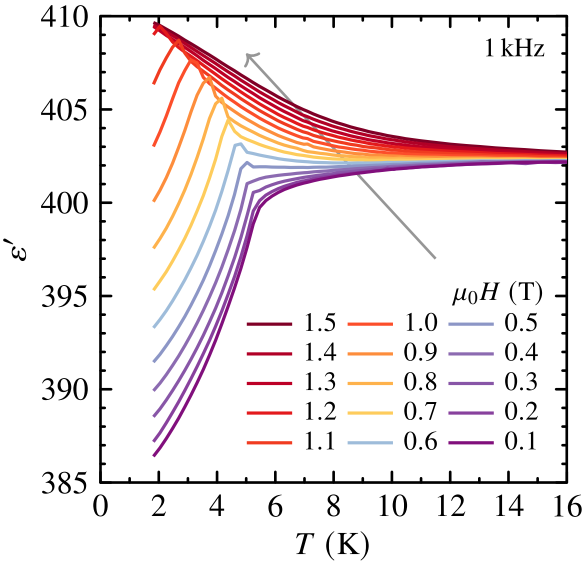

Figure 3.14: Low-temperature permittivity $\varepsilon'(T)$ of pristine EuTiO$_3$ in magnetic field. Permittivity in magnetic fields of $0.1\,\mathrm{T} \leq \mu_0 H \leq 1.5\,\mathrm{T}$ at a constant frequency of 1 kHz in the temperature range around T_N. Arrow indicates increasing field.

conductivity σ' as a function of temperature in semilogarithmic scales. The upper envelope represents the intrinsic conductivity, that is shown in Figs. 3.12 (a) and (c) as solid line, whereas the lower envelope is produced by contact effects.

Figure 3.13 (d) shows the permittivity ε' at 1.8 K as a function of magnetic field, with $\boldsymbol{E} \parallel [110]_\mathrm{c}$ and $\boldsymbol{H} \parallel [1\bar{2}1]_\mathrm{c}$. The curves are almost frequency independent and their behavior resembles that of the magnetization curves $M(H)$ [see Fig. 3.6]. The permittivity increases upon increasing field up to approximately 1.5 T by 5.7 % and saturates above. Furthermore, a kink is seen around 0.4 T which might be related to the spin-flop transition. However, it cannot be directly compared to the spin-flop features of the magnetostriction coefficient λ [see Fig. 3.8 (b)] because both quantities were measured with different field orientations. Figure 3.14 shows $\varepsilon'(T)$ around T_N in magnetic fields $0.1\,\mathrm{T} \leq \mu_0 H \leq 1.5\,\mathrm{T}$ measured at a fixed frequency 1 kHz. The transition shifts to lower temperatures as a function of magnetic field and the drop at T_N turns continuously into a sharp peak.

Phase diagram Figure 3.15 shows the magnetic phase diagram of EuTiO$_3$ including data from heat capacity, magnetization, thermal-expansion/magnetostriction, and permittivity measurements. The Néel temperature T_N decreases upon increasing field from its zero-field value 5.5 K down to lowest temperature at critical field of approximately 1.2 T. Above $T_\mathrm{N}(H)$, EuTiO$_3$ is a paramagnet (PM) that gets spin-polarized toward the high-field/low-temperature limit. Below the $T_\mathrm{N}(H)$ phase boundary, EuTiO$_3$ is an antiferromagnet showing a narrow multi-domain AFM phase in the small-field regime and a broad spin-flopped AFM phase. The data points from $\lambda(H)$ inside the multi-domain phase might indicate a further phase boundary arising from a transition from c-axis AFM to ab-plane AFM as is discussed in Ref. [72].

Publication	Material	Sample	$\varepsilon'_{\mathrm{max}}$	T_Ω (K)	T_0 (K)
This work	$EuTiO_3$	Single crystal	403	160	−190
Katsufuji, Takagi [21]	$EuTiO_3$	Single crystal	400	162	−25
Kamba *et al.* [69]	$EuTiO_3$	Ceramics	172	113	−221
Goian *et al.* [262]	$EuTiO_3$	Ceramics	200–400	-	-
Goian *et al.* [262]	$EuTiO_3$	Single crystal	140	-	-
Kennedy *et al.* [64]	$EuTiO_3$	Ceramics	356	-	-
Müller, Burkard [20]	$SrTiO_3$	Single crystal	24 000	80	35.5
Hemberger *et al.* [294]	$SrTiO_3$	Single crystal	12 000	84	34

Table 3.6: Literature values of ε' and Barrett-fit parameters for $EuTiO_3$ and $SrTiO_3$. Kamba *et al.* fitted the temperature-dependent soft-mode frequency $\omega_{\mathrm{sm}}(T)$ instead of $\varepsilon'(T)$. No Barrett fit is given by Goian *et al.* and Kennedy *et al.*

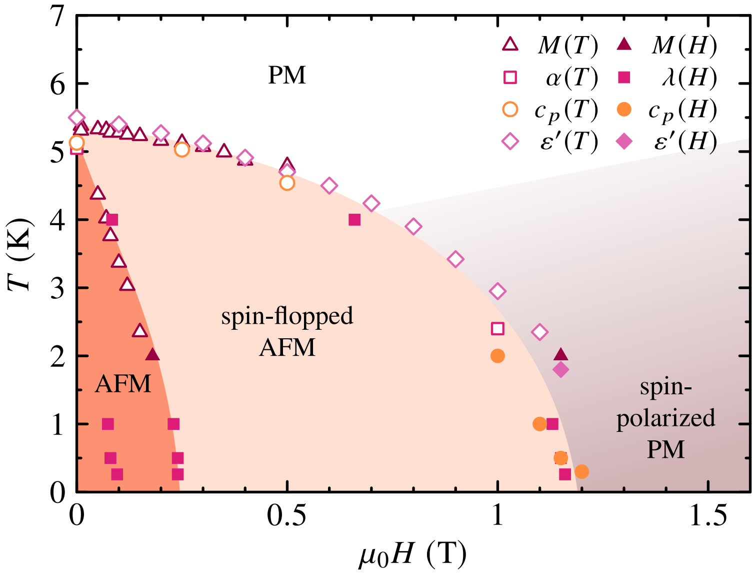

Figure 3.15: Phase diagram of pristine $EuTiO_3$. Transition temperatures collected from temperature-dependent (open symbols) and field-dependent (filled symbols) measurements. Temperatures of the low-field anomalies in $\lambda(H)$ are included.

3.5 Measurements on $EuTiO_{3-\delta}$

Only few publications on n-doped $EuTiO_3$ exist: One report deals with poly- and single-crystalline $EuTi_{1-x}Nb_xO_3$ with $x \leq 0.3$ [88] and another two with single-crystalline $Eu_{1-x}La_xTiO_3$ ($x \leq 0.1$ [70, 87]). Studies of oxygen-deficient $EuTiO_3$ are restricted to ceramics [64] and thin films [295]. None of these publications discusses a $\rho \propto T^2$ resistivity. This work is the first study of single-crystalline $EuTiO_{3-\delta}$ tuned from semiconducting to metallic via reduction. The electron mobility and its temperature dependence in comparison to that of $SrTiO_3$ is discussed and a AT^2 resistivity is found, where A systematically decreases with increasing charge-carrier content. The critical charge-carrier density of the MIT n_c as well as the n-dependent A factor is discussed in a larger context of charge transport in weakly doped perovskite oxides.

Resistivity and Hall effect Resistivity and charge-carrier concentration of pristine $EuTiO_3$ have been covered in the discussion of Fig. 3.12. In order to induce a metal–insulator transition, the above described annealing technique is used. A detailed discussion of this procedure is given in Sec. 1.5. Figure 3.16 (a) shows the resistivity ρ of these metallic samples; the corresponding charge-carrier density n as determined from Hall-effect measurements is seen in Fig. 3.16 (b), both as a function of temperature and in semilogarithmic scales. The right axis of Fig. 3.16 (b) shows the charge-carrier density translated to the number of electrons per unit cell, which is related to the nominal oxygen deficiency in $EuTiO_{3-\delta}$ by 2δ. As is expected for metals, the charge-carrier density of the individual crystals is temperature independent, which is why for some samples the Hall effect was measured only at few temperature set points. The carrier densities cover a range of $10^{20}\,\mathrm{cm}^{-3}$ to $10^{21}\,\mathrm{cm}^{-3}$, i.e., 5×10^{-3} to 5×10^{-2} charge carriers per formula unit. All resistivity curves $\rho(T)$ show a metallic behavior with decreasing ρ upon cooling. The transition to the antiferromagnetic state signals itself by a distinct kink at $T_N = 5.5\,\mathrm{K}$ [see Fig. 3.16 (c)], at least in the four curves with lowest n. For the two highest-doped samples, a kink is foreshadowing but not seen clearly, since they were not measured with the ^{3}He setup. The resistivity curves are ordered by carrier density at temperatures above 130 K, i.e., ρ decreases upon increasing n at a given temperature as indicated by a gray arrow. Below 130 K some of the $\rho(T)$ curves are crossing each other, which may partly arise from different residual resistivities and some uncertainty in determining the exact geometries. In order to cover a joint temperature range of $0.3\,\mathrm{K} \leq T \leq 300\,\mathrm{K}$, different setups were used for the high- and low-temperature regime. Figure 3.17 (a) shows the raw resistivity data of the four highest-doped samples. The high-temperature part is either measured with the transport dipstick ABE ($T \geq 7\,\mathrm{K}$) or the SCHNELLMESSSTAB setup ($T \geq 4.5\,\mathrm{K}$), whereas the low-temperature range ($0.3\,\mathrm{K} \leq T \leq 20\,\mathrm{K}$) is covered by the HELIOX system. It is seen that the absolute values of $\rho(T)$ curves of the same sample measured with different setups differ from each other by a constant factor. This deviations arise from uncertainties in the contact distance, since a setup change implied a renewal of the sample contacts. Figure 3.17 (b) shows the average of each pair of raw-data curves with the respective spread indicated as error bars.

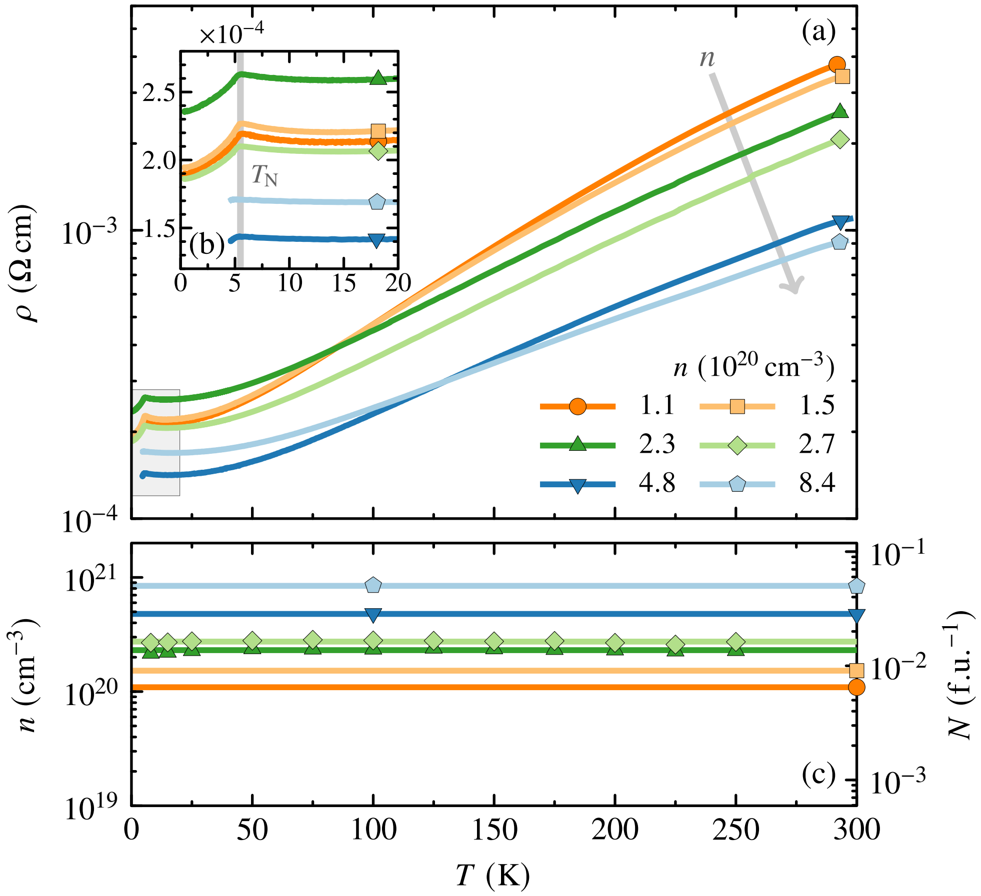

Figure 3.16: Resistivity and charge-carrier density of metallic $EuTiO_{3-\delta}$. (a) Resistivity of metallic $EuTiO_{3-\delta}$ in logarithmic scale as a function of temperature. Above 200 K the curves are ordered by n as indicated by the thick arrow. (b) Enlarged view of the temperature range around T_N. (c) Charge-carrier density n (left axis) and number of charge carrier per unit cell N (right axis).

These averaged curves are seen in Fig. 3.16 (a).

For annealing temperatures $600\,°C < T_{ann} < 750\,°C$, the simultaneously annealed samples of different thicknesses show large deviations in both $\rho(T)$ and n, indicating inhomogeneous charge carrier concentrations in these samples [see Figs. 1.8 and 1.10]. Thus, they are not taken into account here.

Bohr radius and Mott criterion An exact determination of the MIT is hindered by the absence of homogeneous samples between pristine and metallic $EuTiO_{3-\delta}$. The lowest carrier density $n = 10^{20}\,cm^{-3}$ of the metallic samples can be taken as an upper boundary for the critical carrier density n_c of the MIT. This is about four orders of magnitude larger than n_c of $SrTiO_3$ with $\approx 10^{16}\,cm^{-3}$ [89]. This difference can be understood by comparing

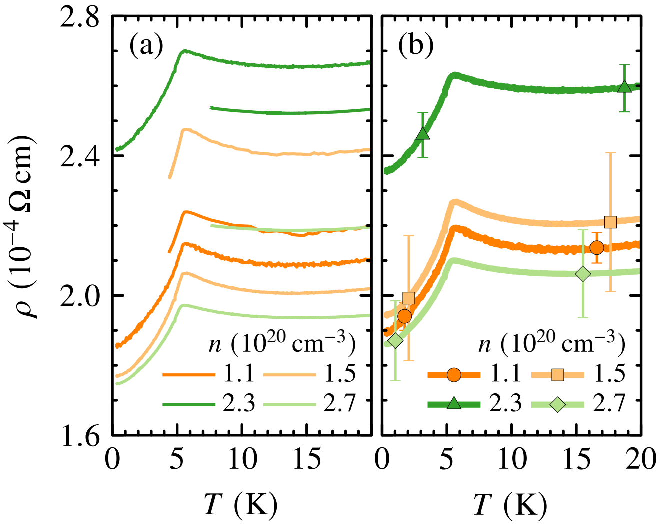

Figure 3.17: Resistivity of $EuTiO_{3-\delta}$: Raw data and uncertainty. (a) Resistivity $\rho(T)$ measured with different setups. High-temperature measurements were performed with the transport dipstick ABE ($T \geq 7$ K) or with the SCHNELLMESSSTAB setup ($T \geq 4.5$ K), whereas the low-temperature data is obtained using the HELIOX system ($0.3\,\text{K} \leq T \leq 20\,\text{K}$). (b) Averaged curves of high- and low-temperature data with error bars.

the permittivities ε of $EuTiO_3$ and $SrTiO_3$. While $SrTiO_3$ has an extremely large low-temperature ε of roughly 20 000 [20], that of $EuTiO_3$ is smaller by a factor of 50 [see Fig. 2.2]. The $EuTiO_3$ crystal grown within the scope of this thesis peaks at $\varepsilon = 403$ [see Fig. 3.13 (a)].

Of course, these are values obtained from pristine insulating $EuTiO_3$. For doped semiconductors, an effective Bohr radius $a_B^* = a_B \varepsilon m_e / m^*$ is defined that renormalizes the Bohr radius $a_B \approx 0.5$ Å of the hydrogen atom by taking the permittivity ε and the band mass m^* into account. The effective Bohr radius a_B^* is a measure for the overlap of the electronic wave functions of the donor atoms. The so-called Mott criterion [299] compares a_B^* to the average distance between two donor atoms that is given by the charge-carrier density via $n^{-1/3}$. The huge low-temperature ε of $SrTiO_3$ yields an effective Bohr radius of about 6700 Å, whereas for $EuTiO_3$ it is $a_B^* \approx 130$ Å. In this calculation, a band mass of $m^* = 1.5 m_e$ as determined for the lowest conduction band of $SrTiO_{3-\delta}$ [28] is used for both $SrTiO_3$ and $EuTiO_3$. The much smaller value of a_B^* explains immediately that the critical carrier density n_c for the MIT of $EuTiO_3$ is about four orders of magnitude larger than that of $SrTiO_3$. Furthermore, one should note that with increasing a_B^* the influence of the above-mentioned inhomogeneities in the oxygen-defect concentration becomes increasingly suppressed. Figure 3.18 shows a log–log plot of the effective Bohr radius a_B^* as a function of the critical charge-carrier density n_c of the MIT. The scaling behavior $n_c^{1/3} a_B^* = K$ for $K = 0.25$ and $K = 10$ is shown as dashed lines. For doped semiconductors, sharp MIT are obtained where the corresponding critical carrier densities n_c follow a scaling relation with $K = 0.25$ [297, 298]. This value is suggested by the original Mott criterion as a boundary separating metals and insulators [299]. In doped perovskite oxides there is no experimental data resolving a sharp MIT with a well-defined n_c, but metallic conductivity is observed in doped $EuTiO_3$, $SrTiO_3$ [89], and $KTaO_3$ [22, 296] at significantly larger charge-carrier densities than expected according to the Mott criterion with $K = 0.25$. Nevertheless, also these

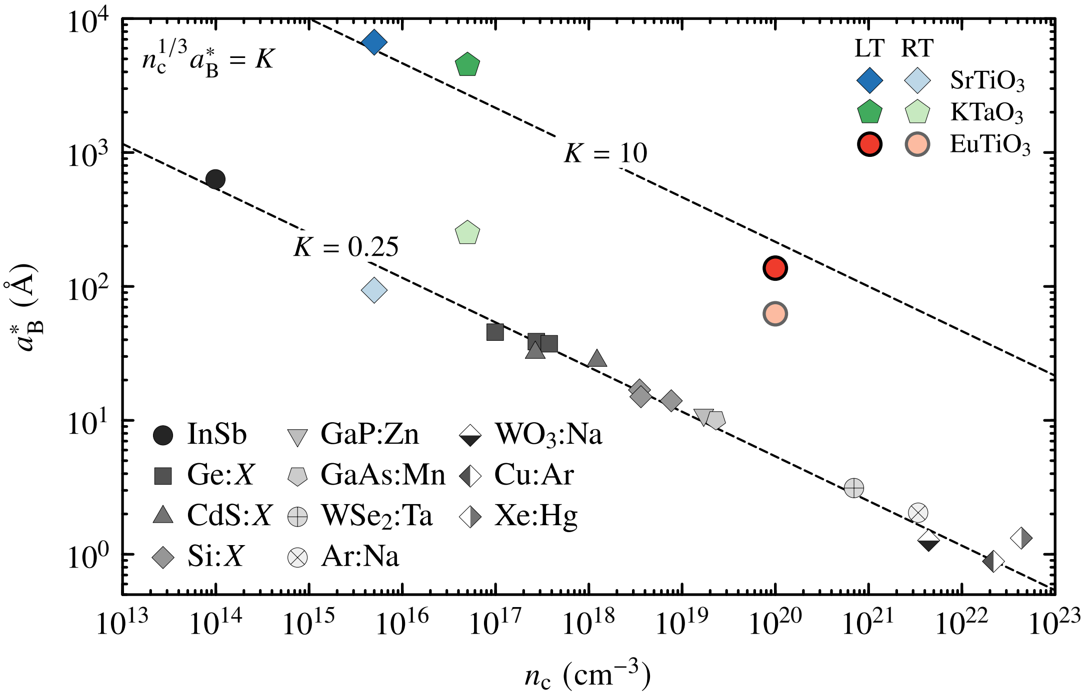

Figure 3.18: Bohr radii and Mott criterion. Effective Bohr radius a_B^* as a function of charge-carrier density n of $EuTiO_3$ in comparison to that of the perovskite materials $SrTiO_3$ [89] and $KTaO_3$ [22, 296], as well as selected doped semiconductors [297, 298]. Dashed lines represent the scaling behavior $n_c^{1/3} a_B^* = K$ for $K = 0.25, 10$. For the perovskite materials, low-temperature (LT) and room-temperature values (RT) of a_B^* are shown.

carrier densities obey the same scaling behavior $n_c^{1/3} a_B^* = K$ but with a larger $K = 10$. This result is obtained by using the low-temperature maximum values of ε, which are naturally large in quantum paraelectrics. If room-temperature values are used instead, the perovskite oxides $SrTiO_3$, $EuTiO_3$, and $KTaO_3$ move toward lower values of K. While $SrTiO_3$ joins the $K = 0.25$ scaling law, $KTaO_3$ remains clearly above this line, and $EuTiO_3$ does not change too much, due to the relatively weak temperature dependence of its permittivity [see Fig. 3.13 (a)].

Mobility Figure 3.19 displays a log–log plot of the electronic mobility $\mu = 1/(ne\rho)$ of metallic $EuTiO_{3-\delta}$ determined using the data of $\rho(T)$ and n as is shown in Fig. 3.16. With decreasing temperature, the $\mu(T)$ curves approach constant values below 40 K which are ordered by charge-carrier density, i.e., $\mu(n)$ decreases systematically at a given temperature. Because the mobility is essentially the conductivity $\sigma = 1/\rho$ scaled with the carrier density, the anomalies at $T_N = 5.5$ K in $\rho(T)$ [see Fig. 3.16 (a)] are preserved in $\mu(T)$. Toward high temperatures, all curves decrease and seem to approach an n-independent power law. A similar behavior has been found for doped $SrTiO_3$ [300]. The mobility data of four $SrTiO_{3-\delta}$

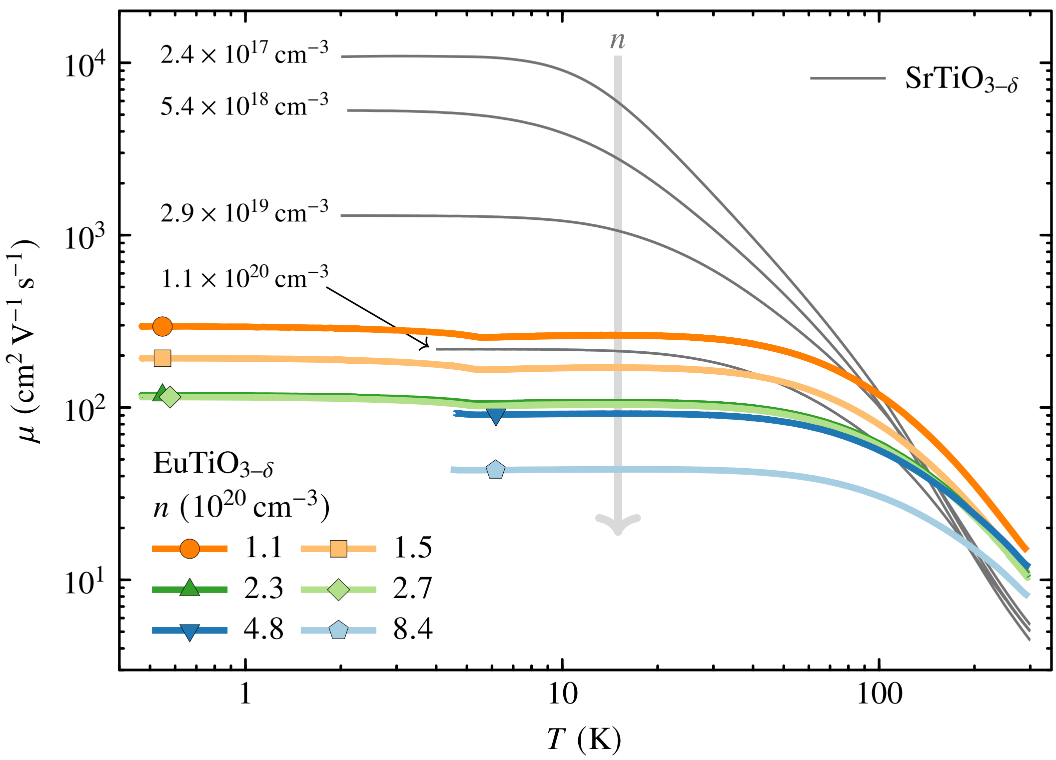

Figure 3.19: Mobility of EuTiO$_{3-\delta}$ and SrTiO$_{3-\delta}$. Mobility μ of metallic EuTiO$_{3-\delta}$ as a function of temperature in comparison to that of SrTiO$_{3-\delta}$ with four selected charge-carrier concentrations. The thick arrow indicates that curves are ordered by n across both compounds.

crystals covering a range 10^{17} cm^{-3} $\leq n \lesssim 10^{20}$ cm^{-3} are shown for comparison. Compared to EuTiO$_{3-\delta}$, the low-temperature mobility is much higher for SrTiO$_{3-\delta}$, because the latter material becomes metallic already for very low carrier concentrations. Nevertheless, all $\mu(T)$ curves remain ordered by n even across both compounds, as is indicated by the gray arrow. The mobility curves of SrTiO$_{3-\delta}$ merge toward room temperature and fall below those of EuTiO$_{3-\delta}$ at $T \gtrsim 200$ K. In this temperature range EuTiO$_3$ undergoes its structural phase transition [see Sec. 3.2.1], whereas in SrTiO$_3$ this transition appears at $T_s = 110$ K as is discussed in Sec. 2.2.2. For SrTiO$_{3-\delta}$, T_s decreases linearly with increasing charge-carrier density [241].

Surprisingly, neither SrTiO$_{3-\delta}$ nor EuTiO$_{3-\delta}$ show any anomalies in $\mu(T)$ that signal the structural transition. Since the investigated EuTiO$_3$ crystals also do not exhibit any anomalies at T_s in other macroscopic quantities like heat capacity, resistivity, or magnetization, single-crystal x-ray diffraction and Raman-scattering measurements were used to detect the cubic-to-tetragonal transition. Using this data, $T_s \simeq 260$ K is derived for pristine EuTiO$_3$ and $T_s \simeq 200$ K for the EuTiO$_{3-\delta}$ sample with the highest charge-carrier density of 8.4×10^{20} cm^{-3}. The absence of anomalies at T_s in the measured mobility data is in agreement with recent theoretical treatments of both the magnitude and temperature dependence of the mobility

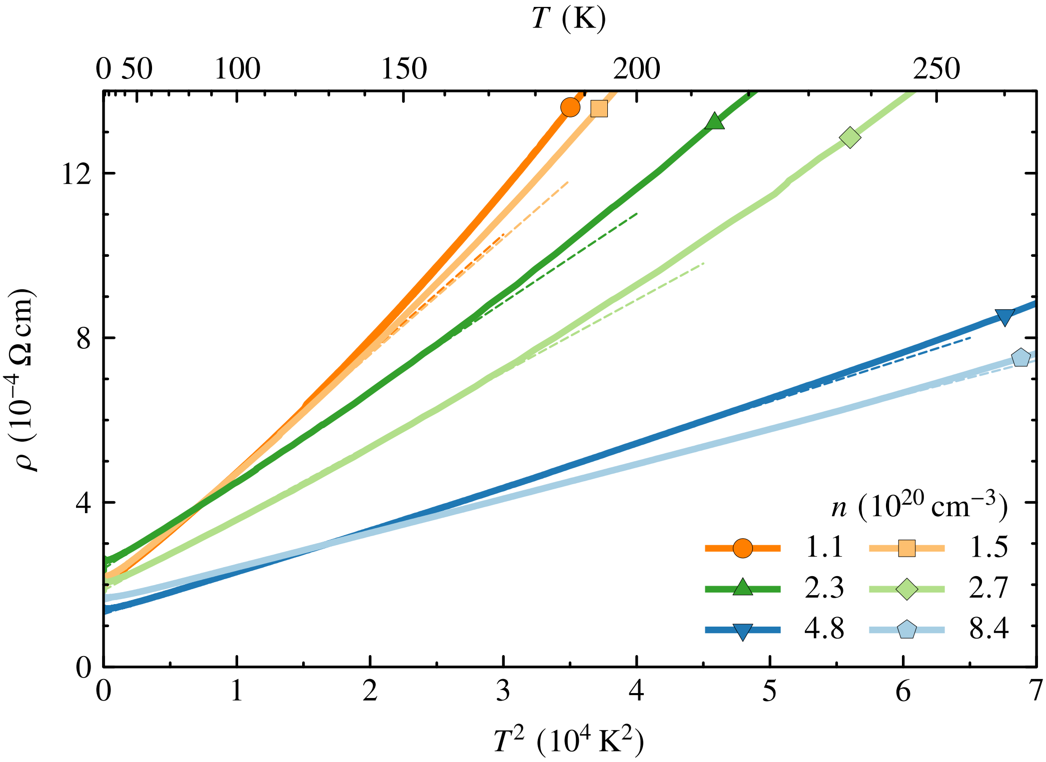

Figure 3.20: Resistivity of $\mathrm{EuTiO}_{3-\delta}$ as a function of T^2. Fits of the form $\rho(T) = \rho_0 + AT^2$ are shown by dashed lines. With increasing n the prefactor A decreases and the temperature range of the T^2 behavior extends toward higher temperature.

in $\mathrm{SrTiO}_{3-\delta}$ [301, 302], where the T_s-related antiferrodistortive soft mode does not play a key role for electron–phonon scattering.

***AT^2* resistivity and *$A(n)$* scaling** Figure 3.20 shows the resistivity ρ of all six metallic $\mathrm{EuTiO}_{3-\delta}$ samples as a function of T^2; the upper axis shows the corresponding temperature T. Fits of the form $\rho(T) = \rho_0 + AT^2$ for the respective curves are shown as dashed lines. Toward high temperatures, the fits deviate from the experimental data and the temperature range of the T^2 behavior systematically increases with increasing charge-carrier density n, what is in agreement with findings for $\mathrm{SrTiO}_{3-\delta}$ [31]. In $\mathrm{EuTiO}_{3-\delta}$, an additional deviation of the fit at low temperatures arises from the magnetic transition at $T_\mathrm{N} = 5.5\,\mathrm{K}$.

Figure 3.21 (a) shows a log–log plot of the prefactor A from these $\rho_0 + AT^2$ fits as a function of n. The $A(n)$ data for $\mathrm{EuTiO}_{3-\delta}$ (red circles) is compared to that of $\mathrm{SrTiO}_{3-\delta}$, $\mathrm{Sr}_{1-x}\mathrm{La}_x\mathrm{TiO}_3$, and $\mathrm{SrTi}_{1-x}\mathrm{Nb}_x\mathrm{O}_3$ [31, 254, 255]. Additionally, the $A(n)$ data of the non-titanate perovskite material $\mathrm{K}_{1-x}\mathrm{Ba}_x\mathrm{TaO}_3$ [303] is included. All of these doped perovskite materials have an insulating quantum-paraelectric parent compound as already discussed in Sec. 2.2.1. The titanate systems follow a generic trend as is indicated by dotted lines

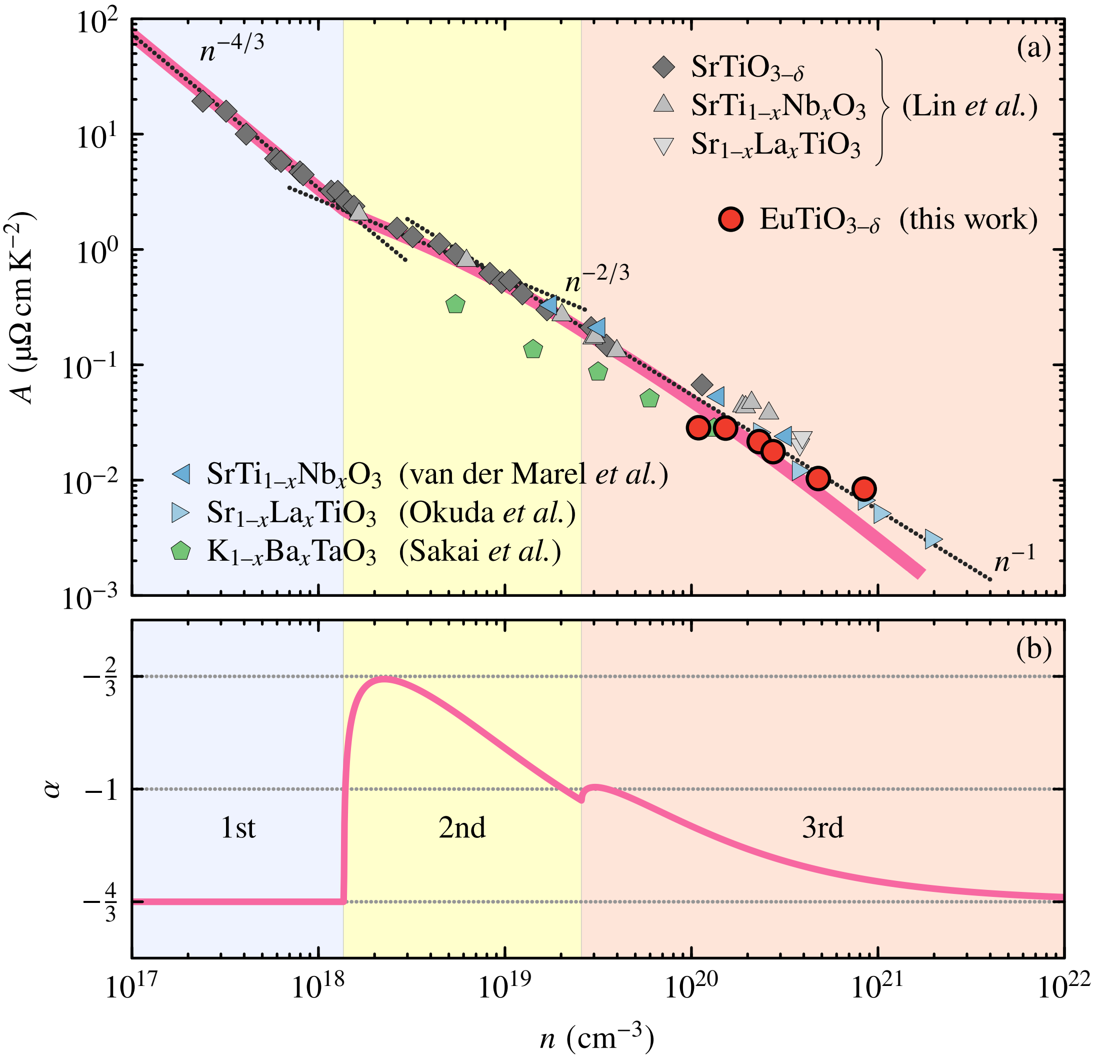

Figure 3.21: Prefactor of the AT^2 resistivity. (a) Prefactor A of $\rho(T) \propto AT^2$ as a function of charge-carrier density n in doped perovskite materials EuTiO$_3$, SrTiO$_3$ [31, 254, 255], and KTaO$_3$ [303]. Thick line represents $A(n)$ calculated for a three-band model. (b) Exponent α of $A(n) \propto n^{\alpha}$. Dotted lines represent values $\alpha = -4/3, -1, -2/3$ in both panels, color boundaries indicate band edges with $E_1 = 3$ meV and $E_2 = 10$ meV.

that represent power laws $A \propto n^{\alpha}$ with exponents $\alpha = -4/3, -2/3, -1$. Band-structure calculations for n-doped SrTiO_3 [253, 254] propose a model with three bands that are filled consecutively with increasing n. The band filling of the second and third band sets in at critical charge-carrier densities n_1 and n_2, respectively, which are known from measurements of Shubnikov–de Haas oscillations in $\mathrm{SrTiO}_{3-\delta}$ [28]. In Fig. 3.21, these critical carrier densities $n_1 \simeq 1.3 \times 10^{18}\,\mathrm{cm}^{-3}$ and $n_2 \simeq 2.6 \times 10^{19}\,\mathrm{cm}^{-3}$ are indicated as background-color boundaries.

For a single parabolic band, the 3d density of states $D(E)$ per volume V is given by

$$g(E) = \frac{D(E)}{V} = \frac{1}{2\pi^2}\left(\frac{2m}{\hbar^2}\right)^{3/2}\sqrt{E}\,, \tag{3.7}$$

where m is the band mass. If the electronic states are filled successively from 0 up to an energy level $E = E_\mathrm{F}$ that is the Fermi energy, the number of electrons N occupying these states are obtained by integrating the density of states. The electron density is then given by

$$n(E_\mathrm{F}) = \frac{N(E_\mathrm{F})}{V} = \frac{1}{2\pi^2}\left(\frac{2m}{\hbar^2}\right)^{3/2}\int_0^{E_\mathrm{F}}\sqrt{E}\,\mathrm{d}E = \frac{1}{2\pi^2}\left(\frac{2m}{\hbar^2}\right)^{3/2} E_\mathrm{F}^{3/2}\,. \tag{3.8}$$

Solving this equation for E_F yields the inverse function

$$E_\mathrm{F}(n) = \frac{\hbar^2}{2m}\left(3\pi^2 n\right)^{2/3}\,, \tag{3.9}$$

which is the famous textbook result for a single parabolic band [304, pp. 36–37]. As demonstrated in Ref. [31], the relation between E_F and the T^2 prefactor A is

$$A \propto E_\mathrm{F}^{-2}\,. \tag{3.10}$$

Using this relation and (3.9) one obtains the power law $A \propto n^{-4/3}$ that is shown as dotted line in the low-n regime in Fig. 3.21 (a). The experimental $\mathrm{SrTiO}_{3-\delta}$ data is well described by this power law in a range $n < n_1$, where only one band is filled (blue background color). Above n_1, the experimental data deviates significantly from $A \propto n^{-4/3}$ but shows an $A \propto n^{\alpha}$ dependence with much larger exponent α that finally approaches $\alpha = -1$.

This increase of α is the natural consequence of a three-band system. The most simple case is a model of three parabolic bands with band indices $i = 0, 1, 2$, band minima at energies E_i, and effective masses m_i [see Fig. 3.22 (a)]. Analogous to the single-band density of states [Eq. (3.7)], each band contributes a term

$$g_i(E) = \begin{cases} \dfrac{1}{2\pi^2}\left(\dfrac{2m_i}{\hbar^2}\right)^{3/2}\sqrt{E - E_i} & \text{for } E \geq E_i \\ 0 & \text{for } E < E_i \end{cases} \tag{3.11}$$

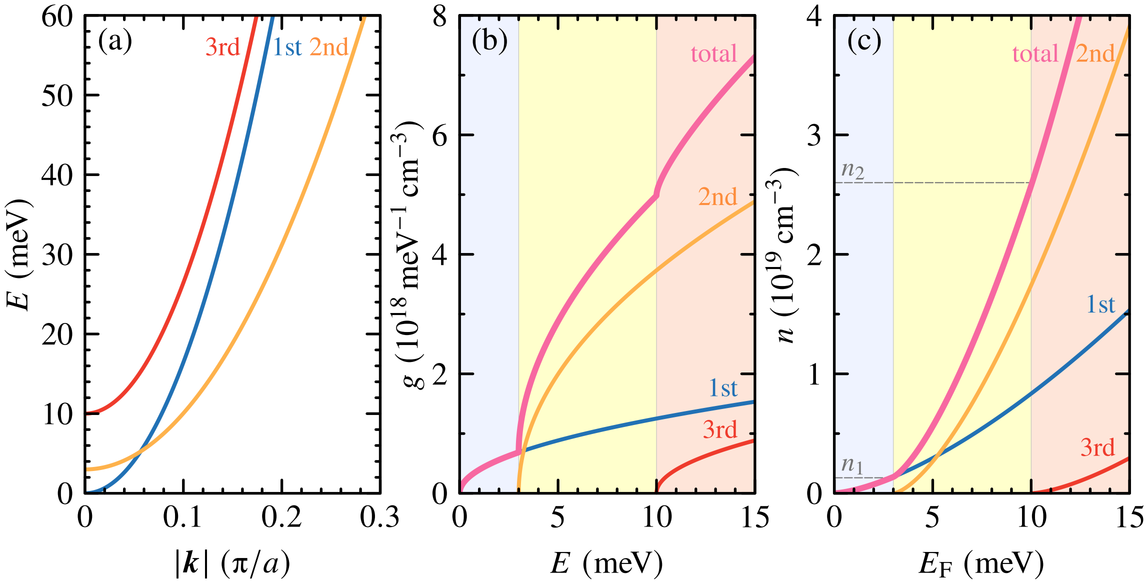

Figure 3.22: Three-band model of doped SrTiO$_3$. Three parabolic bands with band masses $m_{0,2} = 1.5m_e$, $m_1 = 3.5m_e$ and band edges $E_1 = 3\,\text{meV}$, $E_2 = 10\,\text{meV}$. (a) Band dispersion $E(\boldsymbol{k})$. (b) Total density of states $g(E) = D(E)/V$ and single-band contributions. (c) Total charge-carrier density $n(E_\text{F}) = \int_0^{E_\text{F}} g(E)\,\text{d}E$ and single-band contributions. Critical carrier densities $n_1 \simeq 1.3 \times 10^{18}\,\text{cm}^{-3}$ and $n_2 \simeq 2.6 \times 10^{19}\,\text{cm}^{-3}$ are indicated by dashed lines.

to the total density of states $g(E) = \sum_i g_i(E)$ [see Fig. 3.22 (b)] and, consequently, a term

$$n_i(E_\text{F}) = \begin{cases} \dfrac{1}{3\pi^2}\left(\dfrac{2m_i}{\hbar^2}\right)^{3/2}(E_\text{F} - E_i)^{3/2} & \text{for } E_\text{F} \geq E_i \\ 0 & \text{for } E_\text{F} < E_i \end{cases} \tag{3.12}$$

to the total charge-carrier density $n(E_\text{F}) = \sum_i n_i(E_\text{F})$ [see Fig. 3.22 (c)]. The inverse function $E_\text{F}(n)$ exists[8] but cannot be calculated analytically, since each term n_i contains a factor $(E_\text{F} - E_i)^{3/2}$ with different E_i. However, $E_\text{F}(n)$ can be obtained graphically by inverting the axes in Fig. 3.22 (c). Finally, one obtains the function $A(n) \propto E_\text{F}^{-2}(n)$, where a factor $20\,\mu\Omega\,\text{cm}\,\text{K}^{-2}(\text{meV})^2$ is needed to make the absolute values of $A(n)$ match the experimental data in the single-band regime. The meaning of this factor is discussed below. The resulting $A(n)$ function is shown as thick line in Fig. 3.21 (a) which describes the experimental data of doped titanates over almost the entire range of charge-carrier concentration n. For the calculation of $A(n)$, experimental values for m_i and E_i were used: band masses $m_0 = m_2 = 1.5m_e$ and $m_1 = 3.5m_e$ are from Shubnikov–de Haas measurements of SrTiO$_{3-\delta}$ [28] and the energies E_i were adjusted to $E_1 = 3\,\text{meV}$ and $E_2 =$

---

[8] The function $n(E_\text{F})$ is bijective and every bijective function has an inverse.

Figure 3.23: Electron–electron scattering in doped ATiO$_3$. Characteristic length scale ℓ for electron–electron scattering as a function of Fermi temperature $T_F = E_F/k_B$ with experimental values of doped $SrTiO_3$ [31] together with the calculated ℓ from the three-band model.

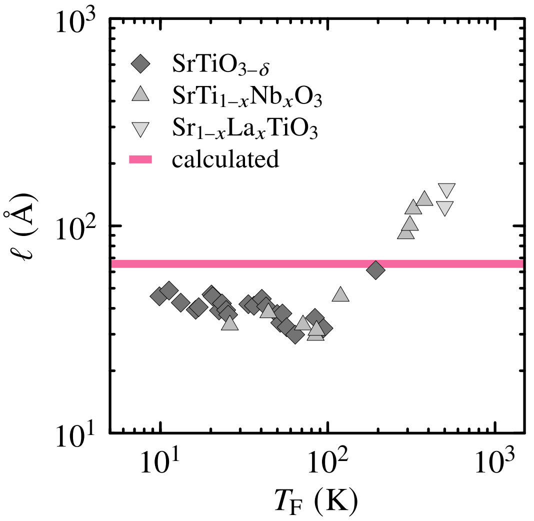

10 meV to match the experimental critical charge-carrier densities $n_1 \simeq 1.3 \times 10^{18}\,\mathrm{cm}^{-3}$ and $n_2 \simeq 2.6 \times 10^{19}\,\mathrm{cm}^{-3}$. In the three-band model of van der Marel *et al.* [254] the lowest band is heavy, while the others are light. In our much simpler model with purely parabolic bands, we neglect band repulsion. Therefore, the second band is the heavy one and crosses the lighter first band [see Fig. 3.22 (a)]. Figure 3.21 (b) shows the corresponding exponent α of $A \propto n^\alpha$ obtained from the derivative of $\log A$ vs $\log n$. The exponents $\alpha = -4/3, -2/3, -1$ are shown as dotted lines and correspond to the dotted lines in Fig. 3.21 (a). Although this simple model neglects the non-parabolic band shapes as well as their anisotropy, the agreement with the experimental data is remarkable. The available $A(n)$ data of the non-titanate perovskite $K_{1-x}Ba_xTaO_3$ [303] fit into this picture as well if we consider its lower effective masses ($0.55m_e$ to $0.8m_e$) [296]. Hence, at a given carrier concentration n, its Fermi energy is larger and A is lower compared to that of the titanate systems.

The applied scaling factor $20\,\mu\Omega\,\mathrm{cm}\,\mathrm{K}^{-2}(\mathrm{meV})^2$ defines the proportionality between the T^2 prefactor A and the Fermi energy via

$$A = 20\,\mu\Omega\,\mathrm{cm}\,\mathrm{K}^{-2}(\mathrm{meV})^2 \cdot E_F^{-2}\,. \tag{3.13}$$

According to Ref. [31], this factor is proportional to the characteristic length scale for the electron–electron scattering ℓ by

$$A = \frac{\hbar}{e^2}\left(\frac{k_B}{E_F}\right)^2 \ell\,, \tag{3.14}$$

with reduced Planck constant $\hbar$, elementary charge e, and Boltzmann constant k_B. By comparing Eqs. (3.13) and (3.14), one obtains

$$\ell = \frac{e^2}{\hbar k_B^2} \cdot 20\,\mu\Omega\,\mathrm{cm}\,\mathrm{K}^{-2}(\mathrm{meV})^2 \approx 66\,\text{Å}\,. \tag{3.15}$$

Figure 3.23 shows this theoretical value together with ℓ calculated from experimental values for A and E_F^2 of $SrTiO_{3-\delta}$, $SrTi_{1-x}Nb_xO_3$, and $Sr_{1-x}La_xTiO_3$ [31]. One should note that data points in Fig. 3.23 are available only for samples with A and E_F being determined independently from each other. Consequently, data points for $EuTiO_{3-\delta}$ do not exist, since there is no independent measurement of the Fermi energy of these samples.

3.6 Conclusion

Thanks to the given condition of Eu^{3+} to be nonmagnetic, it is possible to estimate a deviation δ from the nominal oxygen content in $EuTiO_{3-\delta}$ toward the oxygen excessive regime by studying the magnetic properties. The compared to a pure Eu^{2+} system reduced values for the Curie constant and the saturation magnetization prove the as-grown $EuTiO_3$ crystal to be oxygen excessive with $\delta = -0.02$ resulting in an actual composition of $EuTiO_{3.02}$. Apart from this fact, the experimental data of the pristine crystal agree well with literature data including Néel temperature, Weiss temperature, spin-flop transition, and the Barrett-type permittivity behavior. In oxygen-deficient $EuTiO_3$ a metal–insulator transition is observed that appears similar to the case of $SrTiO_3$ but sets in at much higher charge-carrier concentrations (factor 10^4). This results from the smaller permittivity of $EuTiO_3$, which implies a smaller effective Bohr radius a_B^*, i.e., a smaller overlap of the electronic wave functions. By plotting a_B^* versus the critical carrier density of the metal–insulator transition n_c, a scaling behavior of $n_c^{1/3} a_B^* = K$ is observed for doped perovskite oxides $EuTiO_3$, $SrTiO_3$, and $KTaO_3$ that resembles the original Mott criterion but with a significantly enhanced $K \approx 10$. The low-temperature mobility of metallic $EuTiO_3$ and $SrTiO_3$ systematically increases with decreasing n even across both materials. The resistivity of metallic $EuTiO_{3-\delta}$ shows a $\rho \propto AT^2$ behavior similar to that observed in doped $SrTiO_3$. The underlying scattering mechanism that is responsible for this behavior is unknown, but in contrast to doped $SrTiO_3$, the conventional theories predicting a T^2 resistivity cannot be ruled out for $EuTiO_3$ since the charge-carrier concentrations of the latter are much larger. Nevertheless, the prefactor $A(n)$ systematically decreases with increasing charge-carrier density n and even quantitatively agrees with the corresponding values observed in $SrTiO_{3-\delta}$, $SrTi_{1-x}Nb_xO_3$, and $Sr_{1-x}La_xTiO_3$. This general $A(n)$ behavior is well-described already by a simple three-band model with parabolic bands. The scaling factor that is used to make the theoretical $A(n)$ curve match the experimental data is proportional to the mean free path of the electrons and yields a value of $\ell \approx 66$ Å, which is close to the average of the experimental data.

4 Single-layered manganites

Doped Mott insulators are known to develop complex ordering patterns of charges, orbitals, and magnetic moments. This chapter covers the investigation of single-layered manganites $R_{1-x}A_{1+x}MnO_4$ beyond the well-known $La_{1-x}Sr_{1+x}MnO_4$, in particular $R_{1-x}Ca_{1+x}MnO_4$ (R = Pr, Nd, Sm, Tb) and $R_{1-x}Sr_{1+x}MnO_4$ (R = Pr, Nd) with doping levels $0.5 \leq x \leq 0.73$. Signatures of the charge and orbital order at T_{COO} are observed in resistivity, magnetization, and heat capacity. The evolution of T_{COO} with doping level x is investigated and the differences of this evolution between $R_{1-x}A_{1+x}MnO_4$ with different element combinations of R and A is discussed. The ion-size mismatch, expressed as variance σ^2, is found to be a key parameter for the explanation of the $T_{COO}(x)$ behavior in single-layered manganites.

Contents

4.1 Introduction

While the preceding chapters focus on two examples of doped band insulators, the single-layered manganites covered in this chapter, as well as their perovskite ancestors, are examples for doped Mott insulators. The first perovskite manganites $A\mathrm{MnO}_3$ were prepared in 1950 by G. H. Jonker and J. H. van Santen in polycrystalline form [305]. In these compounds, the nominal oxidation state of manganese was controlled by a defined mixture of aliovalent elements on the A site leading to a chemical formula $R_{1-x}A_x\mathrm{MnO}_3$, where R is a trivalent rare-earth element and A is a divalent alkaline earth element. The doping level x defines the oxidation state of manganese that is expressed as $R^{3+}_{1-x}A^{2+}_x\mathrm{Mn}^{3+}_{1-x}\mathrm{Mn}^{4+}_x\mathrm{O}_3$, where the average oxidation state is given by $\mathrm{Mn}^{(3+x)+}$. Jonker and van Santen observed a transition from a paramagnetic semiconducting to a ferromagnetic metallic state in these materials [306], which has been explained by double-exchange theory developed by C. Zener one year later [307]. Early neutron-scattering experiments from 1955 by E. O. Wollan and W. C. Koehler [268] revealed complex patterns of ferromagnetically and antiferromagnetically coupled moments in these mixed-valent manganites, which necessitated a new nomenclature for magnetic structures that is widely used nowadays [see Fig. 3.3]. In particular, half-doped manganites $R_{0.5}A_{0.5}\mathrm{MnO}_3$ show ferromagnetic zig-zag chains with antiferromagnetic interchain coupling, which is referred to as CE-type magnetic structure in the nomenclature of Wollan and Koehler [268]. A theoretical description of this structure is provided by the Goodenough model [308] [see Sec. 4.3.3].

The research on single-layered manganites having the $\mathrm{K}_2\mathrm{NiF}_4$ structure started with the first synthesis of polycrystalline $\mathrm{Sr}_2\mathrm{MnO}_4$ in 1955 [309]. For decades, studies on single-layered manganites were restricted to $\mathrm{Ca}_2\mathrm{MnO}_4$ [310–313] and $\mathrm{Sr}_2\mathrm{MnO}_4$ [314], where manganese appears exclusively tetravalent. An early investigation of a mixed-valent single-layered manganite was limited to $\mathrm{La}_{0.5}\mathrm{Sr}_{1.5}\mathrm{MnO}_4$ [315]. The discovery of high-T_c superconductivity in single-layered cuprates $\mathrm{La}_{2-x}A_x\mathrm{CuO}_4$ (A = Ca, Sr, Ba) in 1986 [11, 12]—which are also of the $\mathrm{K}_2\mathrm{NiF}_4$ type [316, 317]—stimulated the research on isostructural compounds. Thereupon, single-layered manganites were back in business and only one year after the discovery of high-T_c superconductivity in cuprates, the systematic research on manganites with $\mathrm{K}_2\mathrm{NiF}_4$ structure began with the study on $\mathrm{La}_{1-x}\mathrm{Sr}_{1+x}\mathrm{MnO}_4$ ($0.25 \leq x \leq 0.75$) by R. A. Mohan Ram [318]. Unlike their perovskite ancestors [305, 306], single-layered manganites do not exhibit a ferromagnetic metallic state. Instead they are semiconducting over the whole temperature range [318, 319], but, similar to perovskite manganites, the emerging ordering phenomena are governed by a competition between ferromagnetic double-exchange and antiferromagnetic superexchange interaction [320, 321].

Both the metal–insulator transition temperature T_MIT of perovskites $R_{1-x}A_x\mathrm{MnO}_3$ and the critical temperature of high-T_c cuprates $\mathrm{La}_{2-x}A_x\mathrm{CuO}_4$ show a scaling behavior as a function of x that strongly depends on structural parameters [322, 323]. As demonstrated by Attfield, the often used Goldschmidt tolerance factor [324] and the transition metal valency—which is directly related to the doping level x—are not sufficient to describe this scaling behavior. Instead, three parameters are relevant: doping level x, mean ionic radius of the cations on the A site, and the cation size variance σ^2 [322]. The latter can be interpreted as a measure for structural disorder provoked by the ion-size mismatch of R and A. Consequently, σ^2 vanishes if the ions R and A are of equal size. Mathieu *et al.* [325] demonstrated that the scaling behavior proposed by Attfield is also applicable to the charge and orbital order

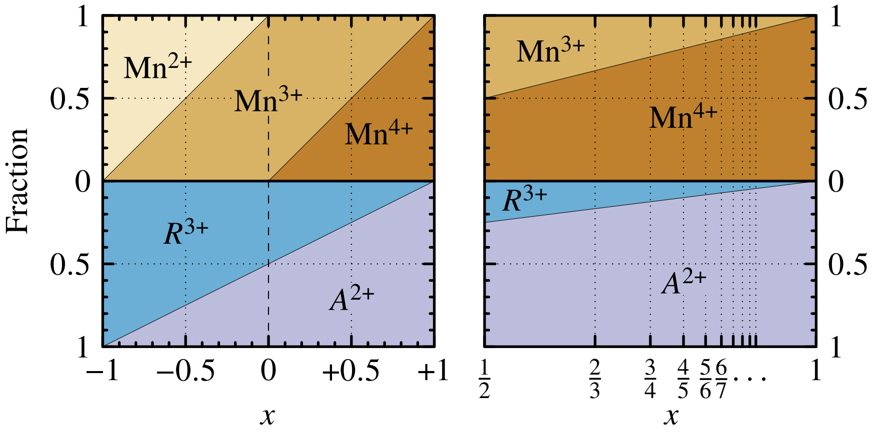

Figure 4.1: Oxidation states in $R_{1-x}A_{1+x}MnO_4$. Area plot of the nominal relative amounts of Mn^{2+} (🟨), Mn^{3+} (🟧), and Mn^{4+} (🟫) as well as R^{3+} (🟦) and A^{2+} (🟪) as a function of doping level x. Left: total, nominally accessible doping range $-1 \leq x \leq 1$. Right: Detail view of the doping range relevant for this work ($0.5 \leq x \leq 1$) with commensurate doping levels highlighted.

(COO) in single-layered manganites $R_{0.5}A_{1.5}MnO_4$.

Like in perovskite manganites, the nominal oxidation state of manganese in single-layered manganites $R_{1-x}A_{1+x}MnO_4$ can be controlled via a substitution of the divalent alkaline earth ion A^{2+} by a trivalent rare-earth ion R^{3+}, which implicates a substitution of Mn^{3+} by Mn^{4+} ions [see Fig. 4.1]. The chemical formula can be written as $R^{3+}_{1-x}A^{2+}_{1+x}Mn^{3+}_{1-x}Mn^{4+}_{x}O_4$, where the mixture of Mn^{3+} and Mn^{4+} defines the nominal oxidation state $Mn^{(3+x)+}$. If the number of Mn^{4+} ions is an integer multiple of the number of Mn^{3+} ions, which is the case for $x = 1/2$, $2/3$, $3/4$, . . . , the doping level x is referred to as commensurate [326]. These configurations are of special interest because they show stripe patterns which are in a sense fundamental since the incommensurate configurations can be seen as mixtures of commensurate ones. This is found in perovskite manganites like $La_{1-x}Ca_xMnO_3$ [326] as well as in single-layered manganites like $La_{0.42}Sr_{1.58}MnO_4$ [37].

Motivated by the possibility of a segregate investigation of the manganese magnetism, $La_{1-x}Sr_{1+x}MnO_4$ was in focus for a long time [315, 318, 327–334] because in this compound the ions besides manganese have noble-gas configuration and, thus, do not contribute to the magnetic properties. Unfortunately, for $La_{1-x}Sr_{1+x}MnO_4$ doping levels beyond $x = 0.6$ are difficult to synthesize. Studies on polycrystalline powders of $La_{1-x}Sr_{1+x}MnO_4$ show a chemical phase separation for $x \geq 0.62$ [335]. Unsuccessful attempts of growing high-quality single-crystals with $x > 0.7$ are reported [333], which matches the growth experiences made within the scope of this thesis [see Sec. 4.4]. Thus, publications on $La_{1-x}Sr_{1+x}MnO_4$ with $x > 0.6$ either only deal with polycrystalline samples or grapple with inhomogeneities [333, 335, 336]. Hence, the half-doped compound $La_{0.5}Sr_{1.5}MnO_4$ appears to be the only commensurate manganite with this combination of elements where high-quality single-crystals are available.

For a deeper understanding of the ordering phenomena in single-layered manganites, and in order to explore the scaling behavior of T_{COO} in the (σ^2, x) plane, higher doping levels are needed. To overcome the structural restrictions, La or Sr have to be substituted by smaller ions. A substitution of La by other rare-earth elements comes at the price of the introduction of further magnetic ions, which complicates the analysis of magnetic properties and possibly hinders investigations of the manganese magnetism. Studies of the charge and orbital ordered phase are, however, in essence unaffected because $T_{\mathrm{N}} \ll T_{\mathrm{COO}}$.

Literature reports of the $x = 1$ end members of the $R_{1-x}A_{1+x}\mathrm{MnO}_4$ series—$\mathrm{Ca}_2\mathrm{MnO}_4$ and $\mathrm{Sr}_2\mathrm{MnO}_4$—are predominantly restricted to polycrystalline samples [309–312, 314]. Although successful single-crystal growths of both end members are reported [313, 337], the growth of $R_{1-x}A_{1+x}\mathrm{MnO}_4$ in the high-doping range $0.5 \ll x < 1$ is prone to phase separations [337]. Therefore, the synthesis of high-quality single-crystals of $R_{1-x}\mathrm{Ca}_{1+x}\mathrm{MnO}_4$ is expected to be difficult for high doping levels, independent of the choice of R, but at least the achievement of higher doping levels than in $\mathrm{La}_{1-x}\mathrm{Sr}_{1+x}\mathrm{MnO}_4$ is possible. Only few publications on single-crystalline $\mathrm{Pr}_{1-x}\mathrm{Ca}_{1+x}\mathrm{MnO}_4$ (with $0.3 \leq x \leq 0.65$ [338] and $x = 0.67$ [35]) and $\mathrm{Nd}_{1-x}\mathrm{Sr}_{1+x}\mathrm{MnO}_4$ ($x = 0.67$ [35, 339], $0.75 \leq x < 0.8$ [337]) are available. The majority of publications on $R_{1-x}A_{1+x}\mathrm{MnO}_4$ with $R \neq \mathrm{La}$ deals with the half-doped case [325, 340, 341].

In principle, two approaches are conceivable: substituting the elements R and A while keeping the doping level x constant or changing the doping level while keeping the elements. The first implies structural changes at fixed charge carrier density, whereas the latter means a simultaneous variation of both structure and charge carrier density. Here, the behavior of the COO transition upon increasing doping level is investigated for different element combinations of R and A, in particular $R_{1-x}\mathrm{Ca}_{1+x}\mathrm{MnO}_4$ (R = Pr, Nd, Sm, Tb) and $R_{1-x}\mathrm{Sr}_{1+x}\mathrm{MnO}_4$ (R = Pr, Nd) with doping levels $0.5 \leq x \leq 0.73$.

Section 4.2 sums up the crystallographic characteristics of single-layered manganites and the structural differences between $R_{1-x}\mathrm{Ca}_{1+x}\mathrm{MnO}_4$ and $R_{1-x}\mathrm{Sr}_{1+x}\mathrm{MnO}_4$. Section 4.3 describes the origin of charge, orbital, and magnetic order in manganites. A short introduction of the Hubbard model is followed by the electronic configuration of the manganese ions in a crystal field and the role of Jahn–Teller distortion. The interplay between antiferromagnetic superexchange and ferromagnetic double-exchange interactions is explained, and the resulting stripe patterns are discussed in the context of the Goodenough model. In Sec. 4.5, the experimental results are presented, in particular measurements of resistivity, magnetization, and heat capacity on synthesized single crystals of $R_{1-x}\mathrm{Sr}_{1+x}\mathrm{MnO}_4$ (R = Pr, Nd) and $R_{1-x}\mathrm{Ca}_{1+x}\mathrm{MnO}_4$ (R = Nd, Sm, Tb) [for details of the crystal growth see Sec. 4.4.2]. Additionally, experimental results on $\mathrm{Pr}_{1-x}\mathrm{Ca}_{1+x}\mathrm{MnO}_4$ crystals grown by H. Ulbrich are included for comparison. The transition to the charge and orbital order at T_{COO} causes anomalies in resistivity, magnetization, and heat capacity. The extracted T_{COO} values are discussed as a function of both doping level x and ion-size variance σ^2.

n	Formula	Space group	f.u./u.c.	Examples
0	AX	$Fm\bar{3}m$ (225)	4	NaCl, LiF, SrO, TiO, EuO, MnO
1	A_2BX_4	$I4/mmm$ (139)	2	K_2NiF_4, Sr_2TiO_4, Eu_2TiO_4
2	$A_3B_2X_7$	$I4/mmm$ (139)	2	$Sr_3Ti_2O_7$, $Eu_3Ti_2O_7$
3	$A_4B_3X_{10}$	$I4/mmm$ (139)	2	$Sr_4Ti_3O_{10}$
⋮	⋮	⋮	⋮	
∞	ABX_3	$Pm\bar{3}m$ (221)	1	$SrTiO_3$, $EuTiO_3$, $BaTiO_3$, $LaMnO_3$

Table 4.1: Ruddlesden–Popper series $A_{n+1}B_nX_{3n+1}$. Space groups and examples are given for undistorted high-temperature phases. The fourth column (f.u./u.c.) shows the number of formula units per unit cell.

4.2 Crystal structure

In all perovskite materials with 113 stoichiometry—the ideal perovskites as well as the distorted ones—the BX_6 octahedra are corner-sharing with their six neighboring octahedra and form a three-dimensional network. These 113 systems can be seen as subspecies of a larger family of compounds, the so called Ruddlesden–Popper series [310, 342]. They have the general chemical formula

$$A_{n+1}B_nX_{3n+1}$$

with $n \in \mathbb{N}_0$. The two end members of this series are AX for $n = 0$, which has the rock-salt structure (space group $Fm\bar{3}m$ (No. 225)) and ABX_3 for $n \to \infty$, which has the aforementioned perovskite structure. Both end members are cubic, while all other Ruddlesden–Popper materials are tetragonal (space group $I4/mmm$ (No. 139)) and have layered structures that can be seen as intergrowths of the two end-member structures, the rock salt and perovskite structure.

For the tetragonal, layered Ruddlesden–Popper systems ($0 < n < \infty$), the crystallographic axes are chosen such that the fourfold rotation axis points into c direction. Then, the octahedra are corner-sharing within the ab plane. In c direction, blocks of n adjacent perovskite layers (ABX_3) are separated from each other by n rock-salt layers (AX). Systems with $n = 1$ have the formula A_2BX_4. They are called single-layered or 214 materials. Those with $n = 2$ ($A_3B_2X_7$) are called double-layered or 327 materials, etc. In the undistorted case, all of these layered systems are tetragonal with space group $I4/mmm$ (139) and have two formula units per unit cell. In this context the 113 Perowskite structure can be considered as the $n \to \infty$ limit of the Ruddlesden–Popper series. Sometimes, Ruddlesden–Popper materials are referred to as “layered perovskite”. An overview is given in Tab. 4.1.

The K_2NiF_4 structure [309] represents the undistorted prototype structure for single-layered manganites A_2MnO_4 with Mn–O–Mn bonds of 180°. The manganese ions are octahedrally surrounded by O^{2-} ions. These MnO_6 octahedra are corner-sharing within

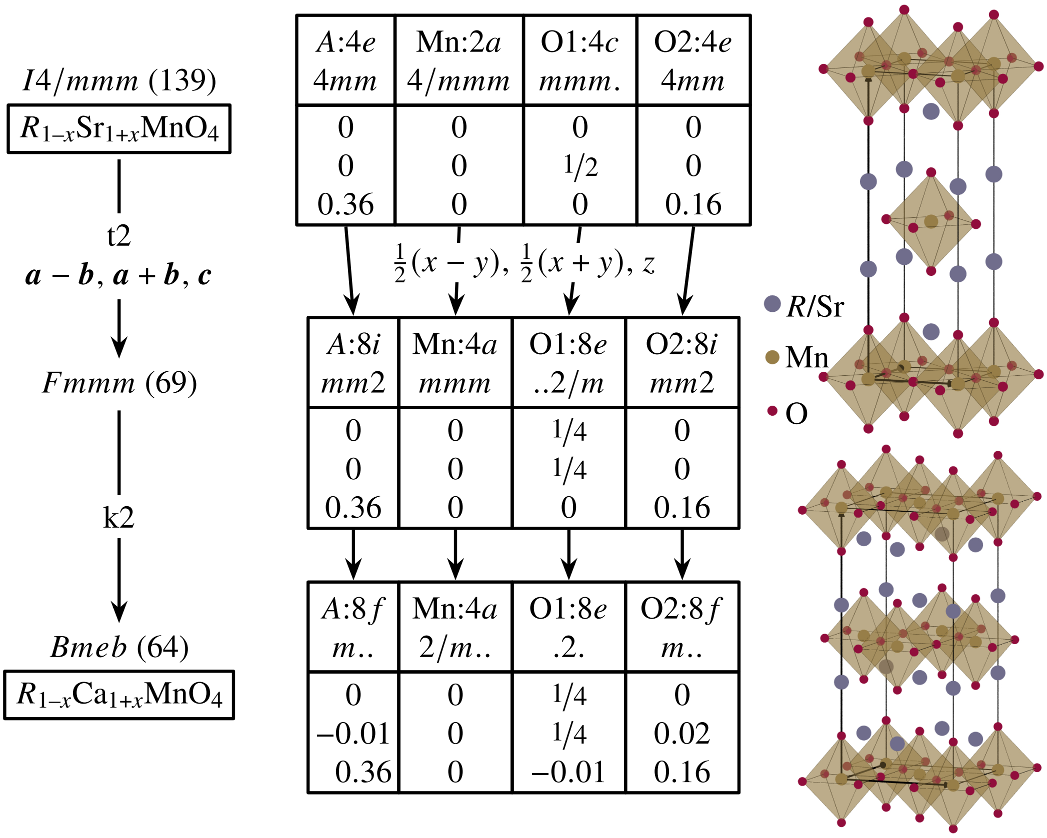

A:4e 4mm	Mn:2a 4/mmm	O1:4c mmm.	O2:4e 4mm
0	0	0	0
0	0	1/2	0
0.36	0	0	0.16

A:8i mm2	Mn:4a mmm	O1:8e ..2/m	O2:8i mm2
0	0	1/4	0
0	0	1/4	0
0.36	0	0	0.16

A:8f m..	Mn:4a 2/m..	O1:8e .2.	O2:8f m..
0	0	1/4	0
−0.01	0	1/4	0.02
0.36	0	−0.01	0.16

Figure 4.2: Group–subgroup relation for A_2MnO_4 (A = $R_{1-x}Sr_{1+x}$, $R_{1-x}Ca_{1+x}$). The space groups $I4/mmm$ of $R_{1-x}Sr_{1+x}MnO_4$ and $Bmeb$ of $R_{1-x}Ca_{1+x}MnO_4$ are linked via a group–subgroup relation, here represented as Bärnighausen tree. For a sequence of maximal subgroups, $Fmmm$ is needed as intermediate step. Tables show element symbols, Wyckoff positions, site symmetries, and atomic coordinates. The origin is set to the manganese ion. Integers and fractions are exact, decimals are approximate values from Refs. [346, 347].

the *ab* plane but separated in *c* direction by a single rock-salt layer. The *A* ion is 9-fold coordinated and forms an AO_9 polyhedron referred to as capped square antiprism [343–345]. The MnO_6 octahedra of adjacent planes are staggered by a half plane diagonal.

Depending on the elements *R* and *A*, the octahedra can be distorted, which lowers the symmetry from tetragonal to orthorhombic with a twice as large unit cell, where *a* and *b* axes are enlarged by a factor of $\sqrt{2}$ and rotated by 45°. The undistorted case is realized in strontium manganites $R_{1-x}Sr_{1+x}MnO_4$, whereas the calcium manganites $R_{1-x}Ca_{1+x}MnO_4$ are orthorhombic, most of them having space group $Bmeb$ (No. 64), which is a subgroup of $I4/mmm$. The group–subgroup relation between $I4/mmm$ and $Bmeb$ is illustrated in Fig. 4.2 as Bärnighausen tree [see also Sec. 2.2.2] with tables showing the respective atomic positions and site symmetries. For a sequence of maximal subgroups, the orthorhombic space group $Fmmm$ is needed as intermediate step. Wyckoff positions, site symmetries, and atomic coordinates with their transformation are taken from the *International Tables for Crystallography Vol. A* and *Vol. A1* [84, 168]. Atomic coordinates given as integer numbers or fractions are exact and required by symmetry, whereas the decimal numbers are approximate values of actual crystals, in particular of $La_{0.5}Sr_{1.5}MnO_4$ [346] for $I4/mmm$ and of $Nd_{0.33}Ca_{1.67}MnO_4$ [347] for $Bmeb$. These decimal coordinates are free parameters of the respective space group.

4.3 Ordering phenomena in manganites

The ordering phenomena observed in perovskite and layered manganites arise from the interplay between charge, orbital, and magnetic degrees of freedom, in particular from the interrelation of superexchange and double exchange mechanism. The origins of this mechanisms are described in the following.

4.3.1 Charge and orbital order

Hubbard model Solids with completely filled or empty bands are insulators, while systems with partially filled bands are usually expected to be metallic. However, insulating materials with partially filled bands are known since the 1930s [348, 349] and have widened to a large material class that nowadays is referred to as Mott insulators. The absence of metallicity in these systems can be understood within the theory developed by N. F. Mott [350] and J. Hubbard [351–353], where electronic delocalization is prevented by electron–electron interactions. This is described by the Hamiltonian

$$\hat{H} = -t \sum_{\langle i,j\rangle,\sigma} c^{\dagger}_{i\sigma} c_{j\sigma} + U \sum_{i} n_{i\uparrow} n_{i\downarrow}\,, \tag{4.1}$$

where $\sigma \in \{\uparrow, \downarrow\}$ and $n_{i\sigma} = c^{\dagger}_{i\sigma} c_{i\sigma}$. Here, $c^{\dagger}_{i\sigma}$ represents the creation of an electron with spin σ on site i and $c_{j\sigma}$ the annihilation of an electron with identical spin on site j. The term $n_{i\sigma} = c^{\dagger}_{i\sigma} c_{i\sigma}$ is the spin density operator for spin σ on site i and $n_{i\uparrow} n_{i\downarrow}$ represents the double occupation of site i with both spin states. The first term describes the hopping of electrons from site i to j without spin flip, the second term describes the electron–electron repulsion if site i is doubly occupied. The proportion between hopping t and repulsion U determines the conductivity of a solid. In the limit of $t \ll U$, the material is a metal, while for $t \gg U$ it is an insulator. If t and U are of comparable size, the behavior is more complicated.

Electronic configuration A free, neutral manganese atom has an electronic configuration of $[Ar]3d^5 4s^2$. In perovskite-type materials, manganese appears trivalent or tetravalent. The respective electronic configurations are $[Ar]3d^4$ for Mn^{3+} and $[Ar]3d^3$ for Mn^{4+}. Using Hund's rules [354–356] one obtains $\mu_J/\mu_B = 0$ for Mn^{3+} ($S = 2$, $L = 2$, $J = 0$, $g_J = 0$) and $\mu_J/\mu_B = 0.6$ for Mn^{4+} ($S = 3/2$, $L = 3$, $J = 3/2$, $g_J = 2/5$). However, if the ion is located in a

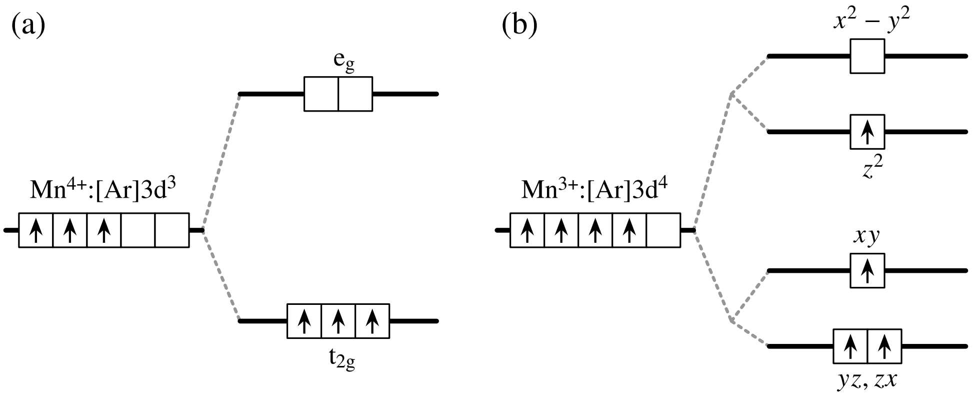

Figure 4.3: Crystal-field splitting for Mn^{4+} and Mn^{3+}. (a) Mn^{4+} ions in a regular MnO_6 octahedron see a cubic crystal field. The t_{2g} orbitals remain degenerate, while the e_g orbitals are empty. (b) Mn^{3+} ions see a tetragonal crystal field created by the Jahn–Teller-distorted MnO_6 octahedron.

crystal electric field of sufficient strength, Russel–Saunders coupling [357] is broken. This is the case for transition metal ions in an octahedral environment, since the extended 3d orbitals are sensitive to the crystal field. Then, the orbital angular momentum is quenched ($L = 0$) and consequently $J = S$. The impact on the magnetic moment is huge: for Mn^{3+} it is $\mu_J/\mu_B = 4$ instead of 0, for Mn^{4+} it is $\mu_J/\mu_B = 3$ instead of 0.6. The orbital angular momentum can be recovered by spin–orbit coupling (SOC), but for manganese this effect is negligible.

Crystal field The 3d energy levels of a free manganese ion are fivefold degenerate, whereas in a crystal electric field, this degeneracy is lifted. If the crystal field has a cubic symmetry (e.g., created by an ideal oxygen octahedron), the 3d level splits into two levels: one lower triply-degenerate t_{2g} level and a higher doubly-degenerate e_g level[1]. The t_{2g} level consists of the xy, yz, zx orbitals. In a real-space picture, the isosurface lobes of their spherical harmonics point to the centers of the octahedron faces, i.e., they have the largest possible distance to the oxygen ions. In contrast, the e_g level consists of the $x^2 - y^2$ and z^2 orbitals, whose isosurface lobes point directly onto the oxygen ions. In a crystal field with tetragonal symmetry (e.g., created by an elongated oxygen octahedron), the energy levels split further. If the fourfold rotation axis points into z direction, the triply-degenerate t_{2g} level splits into a yz, zx level and an xy level. The orbitals with z component are energetically favored, whereas the xy level has a higher energy.

As shown by H. A. Jahn and E. Teller, a system with orbital degeneracy is instable and it tends toward a symmetry reduction in order to lift its degeneracy [360]. Consequently, in manganite systems, the overall energy can be reduced by elongating the $Mn^{3+}O_6$ octahedra

---

[1] The symbols e_g and t_{2g} originate in a notation developed by R. S. Mulliken for a symmetry-based description of molecule spectra [358, 359].

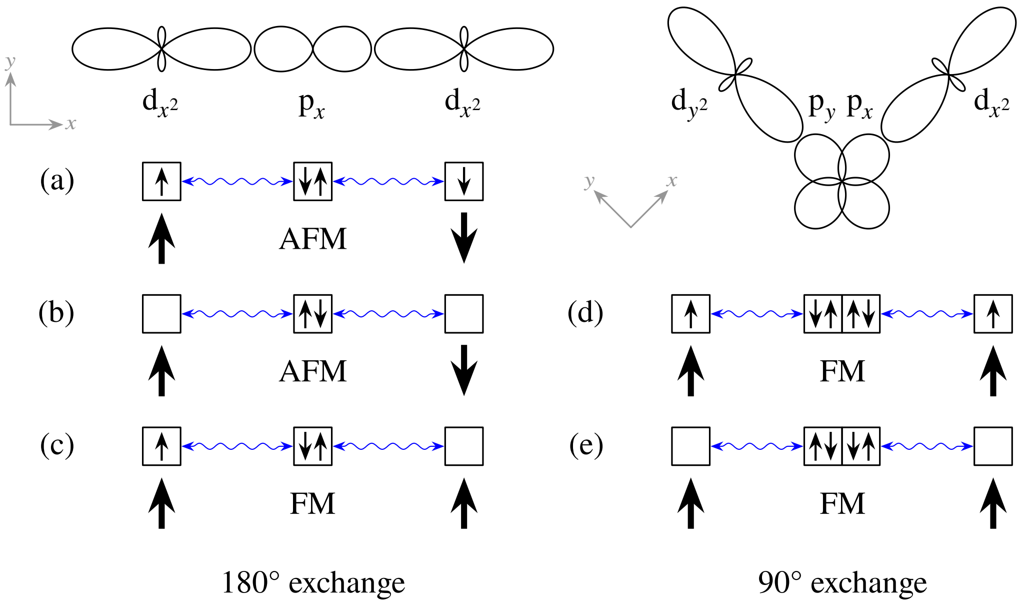

Figure 4.4: Superexchange (GKA rules). Illustration of the Goodenough–Kanamori–Anderson rules for different relative orientations of the orbitals. Large arrows represent the on-site spin, blue arrows indicate virtual hopping. A 180° exchange is AFM if neighboring x^2 orbitals are half-filled (a) or empty (b) and it is FM if one is half-filled and the other one is empty (c). A 90° exchange is FM in any case (d, e).

along z direction, which creates a crystal field with tetragonal symmetry around the Mn^{3+} ions. The energy gain results from a lowering of the singly occupied z^2 level, while the $x^2 - y^2$ orbital remains empty [see Fig. 4.3]. The elongation lifts the t_{2g} degeneracy as well, but this involves no energy gain since the xy orbital is singly occupied and the degenerate yz, zx orbital is doubly occupied. No Jahn–Teller distortion appears for $Mn^{4+}O_6$ octahedra because the empty e_g orbitals and the triply occupied t_{2g} orbital cannot reduce the total energy. Consequently, Mn^{4+} is called Jahn–Teller inactive, while Mn^{3+} is referred to as Jahn–Teller active.

4.3.2 Magnetic order

Superexchange In perovskite manganites with small distortion, the overlap between the 3d orbitals of two neighboring manganese ions is too small for direct exchange[2] since they are separated by an oxygen ion. However, the overlap of the Mn 3d orbitals and the 2p orbitals of the oxygen is large and the exchange between two neighboring Mn ions can be transmitted via the oxygen ion. This mechanism is called superexchange and has been developed by H. A. Kramers [363] and P. W. Anderson [364]. Superexchange can be ferromagnetic or

---

[2] This is the case for $RMnO_3$ with large rare-earth ions, e.g., R = La, Pr, Nd, Sm. However, in heavily distorted systems like $TbMnO_3$ or $HoMnO_3$, next-nearest-neighbor superexchange becomes important [361, 362].

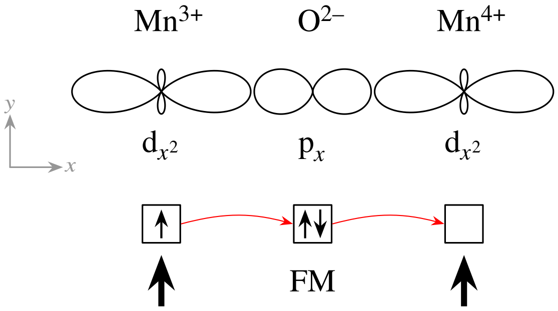

Figure 4.5: Double exchange between aliovalent ions. Illustration of double exchange between Mn^{3+} and Mn^{4+}. Charge transport (red arrows) is enabled if on-site spins are parallel.

antiferromagnetic depending on the relative orientation of the orbitals and their occupation. This is expressed in the so-called Goodenough–Kanamori–Anderson rules (GKA rules), named after J. B. Goodenough and J. Kanamori who extended Andersons superexchange theory [365, 366]:

- 180° exchange between two half-filled or two empty orbitals is antiferromagnetic,
- 180° exchange between a half-filled and an empty orbital is ferromagnetic,
- 90° exchange between two half-filled or two empty orbitals is ferromagnetic.

These rules are illustrated in Fig. 4.4.

Double exchange The simultaneous occurrence of ferromagnetism and metallic conductivity in perovskite manganites with mixed manganese valency was observed at first by G. H. Jonker and J. H. van Santen in 1950 [305, 306]. It can be understood by the so-called double-exchange model, a theoretical description developed by C. Zener [307] and extended by P. W. Anderson and H. Hasegawa [367] and P. G. de Gennes [368]. Double exchange emerges between aliovalent ions in general. In perovskite manganites, two neighboring manganese ions are bridged by an oxygen ion [see Fig. 4.5]. If they have different valencies (Mn^{3+} and Mn^{4+}), the electron in the z^2 orbital of Mn^{3+} can hop via the oxygen p_z orbital to the empty e_g orbitals of Mn^{4+}. The on-site Hund's rule exchange forces the t_{2g} and e_g spins to align parallel. Hopping without spin flip is only possible if the on-site t_{2g} spins of neighboring Mn^{3+} and Mn^{4+} ions are parallel. The overall energy of the system is minimized if hopping is enabled. Therefore, the double exchange provides ferromagnetic coupling and, simultaneously, a high mobility of the e_g electrons, which leads to metallic conductivity. One should note the difference to superexchange, which occurs between isovalent ions and involves only virtual hopping without charge transport.

4.3.3 Goodenough model

In 1955, J. B. Goodenough and A. L. Loeb developed the so-called semicovalent exchange model, based on superexchange and double-exchange theory, using the example of spinel-type structures [369]. Shortly after, this model has been applied to the perovskite manganites and predicted a particular ordering of ions, orbitals, and magnetic moments [308]. Neutron-scattering experiments by E. O. Wollan and W. C. Koehler [268] on the half-doped

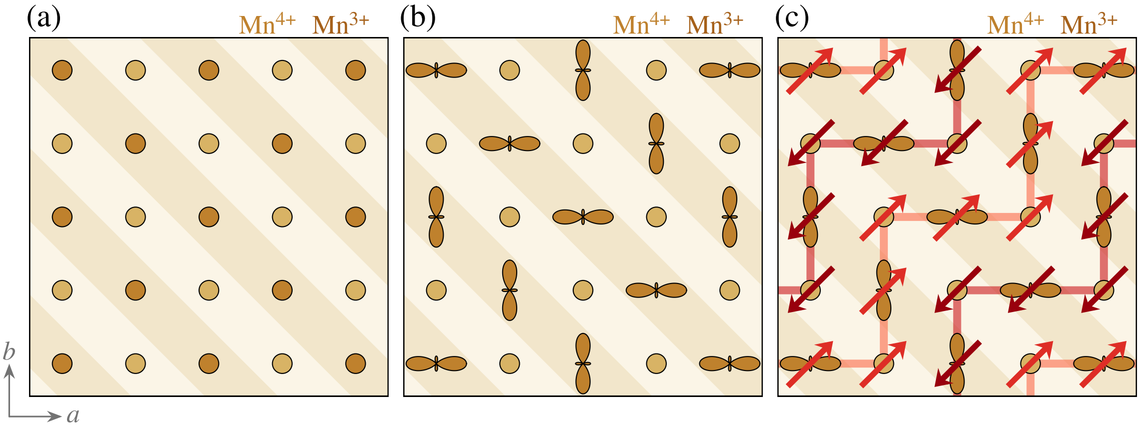

Figure 4.6: Goodenough model. Top view of the *ab* plane of half-doped, single-layered manganites. (a) Charge order of Mn^{3+} and Mn^{4+} forming a checkerboard pattern. (b) The charge order implies an orbital order with $3d_{z^2}$ orbitals of Mn^{3+} pointing in alternating perpendicular directions. (c) Below T_N, the magnetic moments arrange in ferromagnetic zig-zag chains with antiferromagnetic interchain coupling.

perovskite manganite $La_{0.5}Ca_{0.5}MnO_3$ in the very same year confirmed this model, which is nowadays known as Goodenough model. For perovskite manganites $R_{1-x}A_xMnO_3$, the Goodenough model predicts a charge ordering (CO) of aliovalent ions (e.g., Mn^{3+} and Mn^{4+}) that is accompanied by an orbital ordering (OO) emerging at the very same transition temperature T_{COO} [308]. The orbital order stamps the magnetic order that can be ferro- or antiferromagnetic (depending on x) and may arise at a temperature T_C or T_N lower than T_{COO}.

Half-doped manganites ($x = 1/2$) have an equal amount of Mn^{3+} and Mn^{4+} ions. Within the *ab* plane, the aliovalent ions alternate and form a checkerboard pattern [see Fig. 4.6 (a)]. Since the $3d_{z^2}$ orbital of Mn^{4+} is unoccupied, while that of Mn^{3+} is occupied, the charge ordering develops with a concomitant ordering of the $3d_{z^2}$ orbitals [Fig. 4.6 (b)]. Ions piled along the c direction are all isovalent meaning that also the orbitals are of the same type along the c axis. The magnetic order below T_N is formed by ferromagnetic zig-zag chains within the *ab* plane, which have an antiferromagnetic interchain coupling [Fig. 4.6 (c)]. In the zig-zag chain, three spins are aligned in one row. If the chain is considered as stairs, the step height is two. In c direction, zig-zag chains of adjacent *ab* planes couple antiferromagnetically. In the nomenclature of magnetic ordering developed by Wollan and Koehler [268] [for the complete scheme see Fig. 3.3], this is a so-called CE-type ordering [see Fig. 4.7]: within the *ab* plane, alternating C-type and E-type blocks are arranged in a checkerboard pattern, while blocks of the same type are stacked in c direction. The Goodenough model with site-centered COO has been confirmed, e.g., for $La_{0.5}Sr_{1.5}MnO_4$ [370] and outrivaled competing bond-centered COO models like the Zener-Polaron model [371]. However, the charge modulation is found to deviate from a Mn^{3+}-site centering [372] rendering the

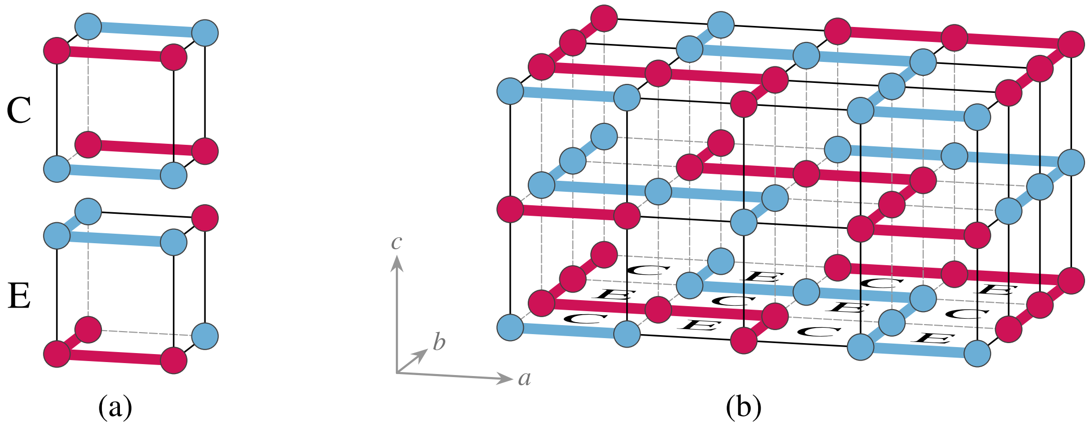

Figure 4.7: CE-type magnetic structure. (a) C-type and E-type magnetic structures. Circles illustrate magnetic moments. Same colors represent parallel moments, different colors represent antiparallel moments [for the complete nomenclature see Fig. 3.4]. (b) CE-type structure and generation of zig-zag chains (thick lines) by C-type and E-type building blocks.

Goodenough model to be only qualitatively correct.

For $x = 2/3$, the amount of Mn^{4+} ions is twice as large compared to that of Mn^{3+}. The charge order appears as stripe pattern with a double stripe of Mn^{4+} ions alternating with a single stripe of Mn^{3+} ions[3]. In the magnetically ordered phase, four spins are aligned in one row (in the stairs picture, the step height is three). Indeed, this pattern is confirmed experimentally for single-layered manganites $Pr_{0.33}Ca_{1.67}MnO_4$ and $Nd_{0.33}Sr_{1.67}MnO_4$ [35] but also for the perovskite manganite $La_{0.33}Ca_{0.67}MnO_3$ [326, 373, 374].

A generalized description of these stripe patterns can be framed as follows: If the doping level x is of the form $x = n/(n+1)$ with $n \in \mathbb{N}$, the number of Mn^{4+} ions is an integer multiple of the number of Mn^{3+} ions. This is the case for

$$x = \frac{1}{2}, \frac{2}{3}, \frac{3}{4}, \frac{4}{5}, \frac{5}{6} \dots . \tag{4.2}$$

Such a doping level is referred to as commensurate [326]. In the COO phase, this implies n adjacent stripes of Mn^{4+} alternating with one single stripe of Mn^{3+}. In the magnetically ordered phase, there are $n+3$ spins per row (or, translated to the stairs picture, a step height of $n+2$).

---

[3] The checkerboard pattern for $x = 1/2$ can also be seen as stripe pattern with alternating single Mn^{3+} and Mn^{4+} stripes as is hinted at by the diagonal background-color pattern in Fig. 4.6 (a).

Name	Formula	Appearance	Purity
Manganese(IV) oxide	MnO_2	brownish black	99.9 %
Lanthanum(III) oxide	La_2O_3	white	99.99 %
Praseodymium(III,IV) oxide	Pr_6O_{11}	black	99.99 %
Neodymium(III) oxide	Nd_2O_3	light blue	99.5 %
Samarium(III) oxide	Sm_2O_3	light yellow	99.99 %
Terbium(III,IV) oxide	Tb_4O_7	brown	99.9 %
Erbium(III) oxide	Er_2O_3	pink	99.99 %
Calcium carbonate	$CaCO_3$	white	99.95 %
Strontium carbonate	$SrCO_3$	white	99.8 %
Barium carbonate	$BaCO_3$	white	99.95 %

Table 4.2: Reactants for $R_{1-x}A_{1+x}MnO_4$. Polycrystalline powders used as reactants for the synthesis of $R_{1-x}A_{1+x}MnO_4$. All powders are from ALFA AESAR.

4.4 Preparation of single-layered manganites

4.4.1 Chemical aspects

Powders of MnO_2, the alkaline earth carbonates $CaCO_3$, $SrCO_3$, and $BaCO_3$ as well as of rare-earth oxides Pr_6O_{11}, Nd_2O_3, Sm_2O_3, Tb_4O_7, and Er_2O_3 were used as starting materials [see Tab. 4.2 for details]. The general chemical equation for a single-layered manganite $R_{1-x}A_{1+x}MnO_4$ with doping level x using the reactants R_aO_b, ACO_3 and MnO_2 is

$$\frac{1-x}{a}\,R_aO_b + (1+x)\,ACO_3 + MnO_2 \longrightarrow R_{1-x}A_{1+x}MnO_4 + (1+x)\,CO_2\uparrow + c\,O_2\uparrow$$

with

$$c = \frac{1}{2}\,(x-1)\left(1-\frac{b}{a}\right) .$$

4.4.2 Preparatory steps

The preparation of single-layered manganites follows essentially the procedure described in Sec. 1.2.2. A manganese excess of 3 % was weighed in, in order to compensate evaporation during the crystal growth. The excess amount is an empirical value based on preparation recipes in Ref. [375]. The starting materials were roughly mixed by hand, then further mixed and pestled in a planetary ball mill as described in Sec. 1.2.2. The mixing and grinding was repeated after each powder reaction. Powder reaction temperatures, dwell times, and repetitions are chosen similar to the recipe in Ref. [375], which itself is based on a detailed growth study on $La_{1-x}Sr_{1+x}MnO_4$ by Reutler *et al.* [331]. The generic procedure for manganites used within the scope of this thesis consists of two powder reactions and a final sintering of the pressed rod, each taking place in a muffle furnace under static air at

ID	t_1 (h)	T_1 (°C)	t_2 (h)	T_2 (°C)	t_3 (h)	T_3 (°C)	Atmosphere
R1	12	1200	6	1200	5	1500	Air
R2	12	1200	12	1350	5	1500	Air
R3	12	1200	12	1350	8	1500	Air
R4	12	1200	12	1350	7	1500	Air
R5	12	1200	12	1350	5	1400	Air

Table 4.3: Powder-reaction parameters for manganites $R_{1-x}A_{1+x}\mathrm{MnO}_4$. Powder-reaction procedures with plateau temperatures T_i and dwell times t_i, where $i = 1, 2$ denote first and second powder reaction and $i = 3$ designates the sintering of the pressed rod. Typical ramping times of 4 h to 6 h were used for heating and cooling.

ambient pressure. The presence of oxygen is desired since the intended product contains Mn^{3+} and Mn^{4+} with emphasis on the tetravalent species for doping levels $x > 0.5$. The powders were heated twice, at 1200 °C and 1350 °C, each for 12 h and followed by the described grinding procedure. The sintering was done at 1500 °C for 5 h. Platinum crucible and boat are used as containers for powders and pressed rod, respectively.

This sequence—with only small variations [see Tab. 4.3]—was used until sample JE19 [see Tabs. 4.5 and 4.6]. Measurements by energy dispersive x-ray spectroscopy (EDX) revealed platinum contaminations on the surface of the sintered rod. Therefore, the sintering temperature was reduced to 1400 °C and, in addition, the contact area between rod and platinum boat was minimized by deforming the boat such that the rod rests on the boat's edges. Further EDX measurements verified that these actions were sufficient to get rid of the platinum contaminations. This modified sequence was used for all manganites from JE20 onwards and is marked by R5 in Tabs. 4.3, 4.5, 4.6, and 4.7.

4.4.3 Single-crystal growth

Crystal-growth parameters for $R_{1-x}\mathrm{Ca}_{1+x}\mathrm{MnO}_4$, $R_{1-x}\mathrm{Sr}_{1+x}\mathrm{MnO}_4$, and $\mathrm{La}_{1-x}\mathrm{Ba}_{1+x}\mathrm{MnO}_4$ are given in Tabs. 4.5, 4.6, and 4.7, respectively. Samples JE27 to JE84 were grown within the scope of this thesis, whereas samples JE1 to JE26 were already grown during the author's diploma thesis [376] and are listed for the sake of completeness. All crystals are grown in pure oxygen atmosphere at (4–6) bar with a typical growth speed of 3 mm h^{-1} and a relative rotation of the rods of (20–40) rpm. Both floating-zone furnaces (CSI and CMI) are used and yield similar results. To reach the typical melting points of manganites, 4 × 1000 W lamps with a voltage of (75–85) % are needed using the CSI furnace and 2 × 2000 W lamps with a voltage of (55–65) V are needed for the CMI furnace. In the CSI furnace, the best results were achieved using 1000 W lamps with flat filaments (L2) [see Tab. 1.2]. 1500 W lamps (L3) and 1000 W lamps with helix filament (L4) were also tested but with poor results: The 1500 W lamps (used for sample JE7) need almost the same power as 1000 W lamps to melt the same sample, with the drawback of a larger melting zone. The 1000 W lamps with helix filament are used for sample JE84. They produce a larger melting zone and need a higher lamp power compared to the 1000 W flat-filament lamps to melt the same sample. Therefore, the growth of JE84 was aborted and then continued in the CMI furnace [see Tab. 4.5].

The main issue of manganite crystal growth is the porosity of the feed rod. It causes capillary action above the melting zone drawing the liquid material into the feed rod. This leads to a scarcity of liquid in the melting zone resulting in frequent disconnections and, simultaneously, a broadening of the soaked feed rod. The emergence of a cauliflower-shaped broadening above the melting zone is a typical sign of this scenario. This problem can be circumvented by sintering the rod in the mirror furnace. Compared to a sintering in a muffle furnace, this allows higher sintering temperatures without the risk of contaminations with crucible material. The associated higher densification of the feed rod leads to a diminution of the capillary action and an enormous improvement of the growth process. The sintering in a mirror furnace was first tested on sample JE20 and then used for all manganites from JE23 onwards, except JE42. Unfortunately, a mirror-furnace sintering is no proper replacement for a sintering in a muffle furnace. The softness of the merely pressed, unsintered rod does not allow a fixation in the mirror furnace. Therefore, a preceding sintering in a muffle furnace is necessary in addition.

Successful growth processes of single-layered manganites are often accompanied by the appearance of two facets—positioned opposing each other—indicating a crystal growth parallel to the *ab* plane. Sometimes, the nucleation process in manganites did not result in a single crystal, but two or more phases coexisted over a larger growth distance. Attempted applications of the necking technique failed regularly because the shrunken diameter of the melt boosted the probability of disconnections; an issue already described in Ref. [375].

Results The successfully grown single crystals of $R_{1-x}A_{1+x}$MnO$_4$ cover a doping range of $0.40 \leq x \leq 0.73$. An overview of all growth attempts is given in Tab. 4.4. Manganite single crystals with 20 different compositions were grown in total, including 8 compounds that were already synthesized in the scope of the author's diploma thesis. The successfully grown crystals include Nd$_{1-x}$Ca$_{1+x}$MnO$_4$ with $x = 0.40, 0.50, 0.60, 0.67$ as well as Sm$_{1-x}$Ca$_{1+x}$MnO$_4$ and Tb$_{1-x}$Ca$_{1+x}$MnO$_4$ each with $x = 0.50, 0.60, 0.67$. Higher doping levels are achieved with Sr manganites. The compound Pr$_{1-x}$Sr$_{1+x}$MnO$_4$ covers the broadest range of x (0.40, 0.50, 0.60, 0.67, 0.70, 0.73) including the highest doping level of all synthesized manganites. Nd$_{1-x}$Sr$_{1+x}$MnO$_4$ crystals were grown with $x = 0.60, 0.63, 0.67, 0.70$. Attempts to grow Er$_{1-x}Ca_{1+x}MnO_4$ (JE82, JE83, JE84) failed regardless of x. The initial goal to synthesize single-layered manganites with $x = 0.75$ could not be achieved with any element combination.

Properties of the as-grown manganite crystals All synthesized manganite crystals are opaque but differ slightly in color. The Sr-manganite crystals are black, whereas Ca manganites show a dark bluish coloring. The crystals have an easy cleavage parallel to

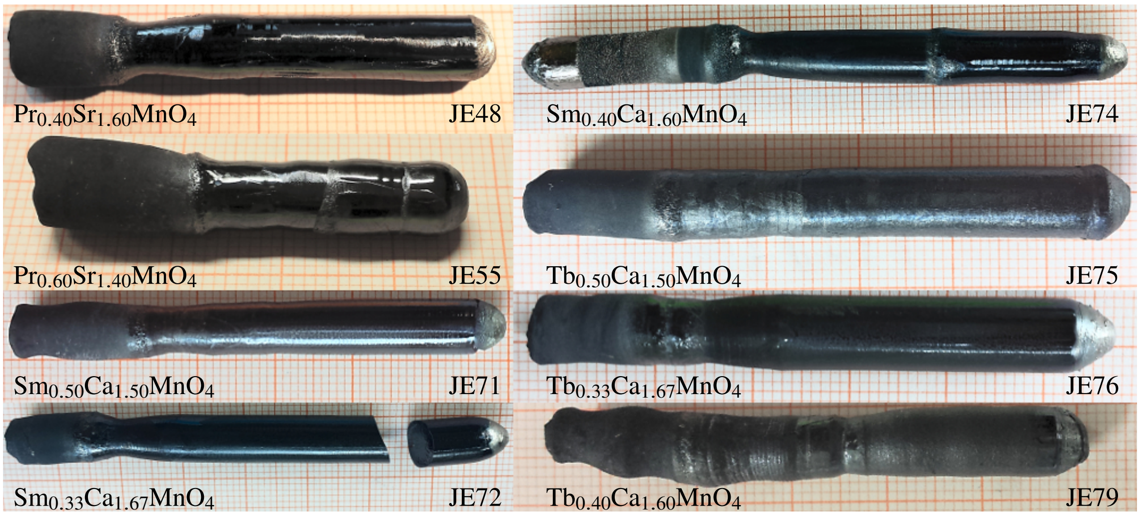

Figure 4.8: Single crystals of $R_{1-x}A_{1+x}MnO_4$. Representative single crystals of $R_{1-x}A_{1+x}MnO_4$ with R = Pr, Sm, Tb, and A = Ca, Sr. The growth direction is from left to right. For JE74 (top right), the feed-rod top of JE73 has been used as seed.

Compound	0.40	0.50	0.60	0.63	0.67	0.70	0.73	0.75
$Nd_{1-x}Ca_{1+x}MnO_4$	✓	✓	✓	○	✓	-	-	-
$Sm_{1-x}Ca_{1+x}MnO_4$	○	✓	✓	○	✓	○	○	-
$Tb_{1-x}Ca_{1+x}MnO_4$	○	✓	✓	○	✓	○	○	-
$Er_{1-x}Ca_{1+x}MnO_4$	○	-	○	○	-	○	○	○
$Pr_{1-x}Sr_{1+x}MnO_4$	✓	✓	✓	○	✓	✓	✓	-
$Nd_{1-x}Sr_{1+x}MnO_4$	○	-	✓	✓	✓	✓	○	-

Table 4.4: Growth attempts and success. Overview of growth attempts of $R_{1-x}A_{1+x}MnO_4$ single crystals: (✓) successful growth, (-) unsuccessful growth attempt, (○) not attempted.

the ab planes, which is also known from $La_{1-x}Sr_{1+x}MnO_4$ [319]. Generally, the cleavage is easier for manganite crystals with strontium, while the calcium-doped ones prove to be more robust. The growth direction is usually parallel to the ab plane. Discs of millimeter thickness cut perpendicular to this direction easily cleave into several pieces with already appropriate dimensions for measurements of resistivity, magnetization, and heat capacity. Therefore, further cutting was usually not necessary. Cleaved pieces exhibit specular (001) faces allowing a crystal orientation with the naked eye.

Samples of $Pr_{1-x}Sr_{1+x}MnO_4$ showed a degradation when stored under air for a couple of days. This was at first observed on sample JE2 that developed a grainy, light-colored coating on the non-specular surfaces parallel to the c direction, while the specular ab faces remained essentially intact. In contrast, the samples with calcium appeared to be more stable under air, which is in line with their higher resilience to cleavage. As a precaution, all manganite samples from JE3 onwards, regardless of their composition, were stored in the argon glovebox. Crystal orientation and preparatory steps for measurements were always done under air without any observable effect on the sample characteristics.

Sample			PR	Floating-zone furnace parameters							SC
ID	R	x		M/L	Sintering		Growth				
					U	v mm/h	U	v mm/h	r rpm	p bar	
JE1	Nd	0.67	R2	CSI/L2	-	-	77 %	3	20	5.5	-
JE3	Nd	0.67	R2	CSI/L2	-	-	80 %	3	29	5.2	-
JE4	Nd	0.67	R2	CSI/L2	-	-	84 %	3	28	5.5	-
JE21	Nd	0.67	R5	CMI/L5	-	-	60 V	3	22	5.5	✓✓
JE26	Nd	0.50	R5	CMI/L5	54 V	20	60 V	3	27	4–9	✓
JE35	Nd	0.70	R5	CMI/L5	56 V	20	60 V	3	32	7	-
JE37	Nd	0.75	R5	CMI/L5	55 V	15	62 V	3	32	8	-
JE39	Nd	0.73	R5	CMI/L5	54 V	15	56 V	3	34	6	-
JE58	Nd	0.60	R5	CSI/L2	70 %	15	76 %	3	34	3	✓✓
JE62	Nd	0.40	R5	CSI/L2	70 %	15	76 %	3	34	2.8	✓✓
JE71	Sm	0.50	R5	CSI/L2	65 %	15	74 %	3	36	4	✓✓
JE72	Sm	0.67	R5	CSI/L2	66 %	15	75 %	3	36	4	✓✓
JE73	Sm	0.75	R5	CSI/L2	65 %	15	75 %	3	36	4–8	-
JE74	Sm	0.60	R5	CSI/L2	63 %	15	75 %	3	36	4	✓✓
JE75	Tb	0.50	R5	CSI/L2	60 %	15	73 %	3	36	3–7	✓✓
JE76	Tb	0.67	R5	CSI/L2	62 %	15	75 %	3	36	7	✓✓
JE77	Tb	0.75	R5	CSI/L2	62 %	15	75 %	3	38	7–9	-
JE79	Tb	0.60	R5	CSI/L2	64 %	15	76 %	3	38	5	✓✓
JE81	Er	0.67	R5	CSI/L2	65 %	15	72 %	3	38	3–8	-
JE82	Er	0.50	R5	CSI/L2	59 %	15	-	-	-	-	-
JE84	Er	0.50	R5	CSI/L4	75 %	15	87 %	3	38	2–5	-
(continuation of JE84)				CMI/L5	-	-	60 V	3	38	3.5	-

Table 4.5: Synthesis of $R_{1-x}Ca_{1+x}MnO_4$: Parameters. All attempts to synthesize $R_{1-x}Ca_{1+x}MnO_4$ with sample identifier, rare-earth element R, doping level x, powder-reaction procedure PR [see Tab. 4.3], furnace model M and halogen lamps L [see Tab. 1.2], lamp voltage U (for CSI in %, for CMI in V) and pulling speed v in $\mathrm{mm\,h^{-1}}$ used for sintering and growth, relative rotation of the rods r in rpm, gas pressure p in bar, and success of single-crystal growth SC [see Tab. 1.8]. A pure O_2 atmosphere is used throughout.

Sample			PR	Floating-zone furnace parameters							SC
ID	R	x		M/L	Sintering		Growth				
					U	v mm/h	U	v mm/h	r rpm	p bar	
JE2	Nd	0.67	R1	CSI/L2	-	-	76 %	3–6	20	5.4	-
JE5	Nd	0.67	R2	CSI/L2	-	-	78 %	3	20	5	✓✓
JE6	Pr	0.67	R2	CSI/L2	-	-	78 %	3	20	6	-
JE7	Pr	0.67	R2	CSI/L3	-	-	75 %	3	20	5.5	-
JE8	Pr	0.67	R2	CSI/L2	-	-	77 %	3	20	5.5	-
JE9	Pr	0.75	R2	CSI/L2	-	-	75 %	3	12–20	5.7	-
JE10	Nd	0.75	R2	CSI/L2	-	-	78 %	3	16–20	5.5	-
JE11	Nd	0.60	R3	CSI/L2	-	-	78 %	3	14	5	✓✓
JE12	Pr	0.70	R3	CSI/L2	-	-	77 %	3	14	9	✓✓
JE13	Pr	0.75	R3	CSI/L2	-	-	79 %	3	20–43	9.5	-
JE14	Pr	0.73	R3	CSI/L2	-	-	75 %	3	14	5	✓✓
JE15	Pr	0.75	R3	CSI/L2	-	-	78 %	3	14–18	6–8	-
JE16	Pr	0.67	R3	CSI/L2	-	-	80 %	3	14	5.5	-
JE17	Pr	0.75	R4	CSI/L2	-	-	82 %	5–15	18	5.5	-
JE18	Pr	0.67	R4	CSI/L2	-	-	81 %	3	18	3.5	✓
JE19	Pr	0.75	R4	CSI/L2	-	-	79 %	7	20	6	-
JE20	Pr	0.75	R5	CMI/L5	50 V	40	60 V	3	28	5	-
JE22	Pr	0.75	R5	CMI/L5	-	-	63 V	3	22	6.5	-
JE23	Nd	0.75	R5	CMI/L5	55 V	20	60 V	3	22	6–8	-
JE24	Pr	0.50	R5	CMI/L5	54 V	20	63 V	3	22	5.5	✓
JE40	Nd	0.50	R5	CMI/L5	60 V	15	64 V	3	36	5.5	-
JE42	Nd	0.60	R5	CSI/L2	-	-	78 %	3	34	4.5	✓✓
JE43	Nd	0.70	R5	CSI/L2	76 %	10	79 %	3	34	5	-
JE44	Nd	0.75	R5	CSI/L2	72 %	12	78 %	3	34	5	-
JE45	Nd	0.70	R5	CSI/L2	72 %	8–12	79 %	3	34	5	✓
JE47	Nd	0.75	R5	CSI/L2	72 %	12	78 %	3	34	4.6	-
JE48	Pr	0.60	R5	CSI/L2	72 %	15	78 %	3	34	4	✓✓
JE55	Pr	0.40	R5	CSI/L2	73 %	15	80 %	3	34	3	✓✓
JE60	Pr	0.55	R5	CSI/L2	70 %	15	80 %	3	34	3.5	-
JE61	Nd	0.63	R5	CSI/L2	70 %	15	82 %	3	34	5	✓
JE80	Pr	0.70	R5	CSI/L2	67 %	15	80 %	3	38	3–6	-

Table 4.6: Synthesis of $R_{1-x}Sr_{1+x}MnO_4$: Parameters. All attempts to synthesize $R_{1-x}Sr_{1+x}MnO_4$ with sample identifier, rare-earth element R, doping level x, powder-reaction procedure PR [see Tab. 4.3], furnace model M and halogen lamps L [see Tab. 1.2], lamp voltage U (for CSI in %, for CMI in V) and pulling speed v in $\mathrm{mm\,h^{-1}}$ used for sintering and growth, relative rotation of the rods r in rpm, gas pressure p in bar, and success of single-crystal growth SC [see Tab. 1.8]. A pure O_2 atmosphere is used throughout.

Sample		PR	Floating-zone furnace parameters								SC
ID	x		M/L	Gas	Sintering		Growth				
					U V	v mm/h	U V	v mm/h	r rpm	p bar	
JE25	+0.50	R5	CMI/L5	O_2	38	20	48	3	38	5	-
JE27	−0.50	R5	CMI/L5	Ar/O_2	47	20	53	3	35	4–6	-
JE29	−0.25	R5	CMI/L5	Ar/O_2	48	20	50	3	35–45	3	-

Table 4.7: Synthesis of $La_{1-x}Ba_{1+x}MnO_4$: Parameters. All attempts to synthesize $La_{1-x}Ba_{1+x}MnO_4$ with sample identifier, doping level x, powder-reaction procedure PR [see Tab. 4.3], furnace model M and halogen lamps L [see Tab. 1.2], gas, lamp voltage U in V and pulling speed v in mm h^{-1} used for sintering and growth, relative rotation of the rods r in rpm, gas pressure p in bar, and success of single-crystal growth SC [see Tab. 1.8].

4.5 Measurements on $R_{1-x}A_{1+x}\mathrm{MnO}_4$

4.5.1 Methods

The chemical composition was verified using energy-dispersive x-ray spectroscopy (EDX), phase purity was checked using an x-ray powder diffractometer (BRUKER D5000MATIC) with Bragg–Brentano geometry and Cu x-ray tube supplying Cu $K\alpha_{1,2}$ radiation. Single crystallinity was checked with a Laue camera. For some of the samples, a crystal-structure determination has been performed by L. Weber using a single-crystal x-ray diffractometer (BRUKER X8-APEX) [377]. Resistivity was measured by a standard four-probe method using a home-built dipstick setup (SCHNELLMESSSTAB) and a commercial cryostat with resistivity option (PPMS, QUANTUM DESIGN INC.). Magnetization measurements were performed using a SQUID magnetometer (MPMS, QUANTUM DESIGN INC.), specific-heat measurements were done using the microcalorimeter option of the PPMS. SQUID measurements were partly performed by S. Heijligen. Single crystals of $\mathrm{Pr}_{1-x}\mathrm{Ca}_{1+x}\mathrm{MnO}_4$ were grown by H. Ulbrich and their respective resistivities were measured by G. Kolland.

4.5.2 Results

Crystal structure Detailed structural analyses using single-crystal x-ray diffraction have been performed by L. Weber [377] on $\mathrm{Pr}_{1-x}\mathrm{Sr}_{1+x}\mathrm{MnO}_4$ ($x = 0.6, 0.67$), $\mathrm{Nd}_{1-x}\mathrm{Sr}_{1+x}\mathrm{MnO}_4$ ($x = 0.6, 0.7$), $\mathrm{Sm}_{1-x}\mathrm{Ca}_{1+x}\mathrm{MnO}_4$ ($x = 0.5, 0.6, 0.67$), and $\mathrm{Tb}_{1-x}\mathrm{Ca}_{1+x}\mathrm{MnO}_4$ ($x = 0.5, 0.67$). This paragraph briefly summarizes the results of this investigation.

The room-temperature structures of $\mathrm{Pr}_{1-x}\mathrm{Sr}_{1+x}\mathrm{MnO}_4$ ($x = 0.6, 0.67$) and $\mathrm{Nd}_{1-x}\mathrm{Sr}_{1+x}\mathrm{MnO}_4$ ($x = 0.6, 0.7$) were determined to be tetragonal with space group $I4/mmm$ (No. 139) implying Mn–O–Mn bond angles of 180°. Hence, both compounds have the ideal $\mathrm{K}_2\mathrm{NiF}_4$ structure for all investigated x and are isostructural with $\mathrm{La}_{1-x}\mathrm{Sr}_{1+x}\mathrm{MnO}_4$. The structure of $\mathrm{Sm}_{1-x}\mathrm{Ca}_{1+x}\mathrm{MnO}_4$ ($x = 0.5, 0.6, 0.67$) was studied at 240 K and 160 K. The orthorhombic space group $Bmeb$ (No. 64) properly describes the crystal structure at 240 K for all x. This crystal symmetry allows a tilt of the octahedra around the a axis. At 160 K, the structure is better described using the space group $Pccn$ (No. 56) which allows tilts around both a and b axis. $\mathrm{Tb}_{1-x}\mathrm{Ca}_{1+x}\mathrm{MnO}_4$ ($x = 0.5, 0.67$) was measured at temperatures 300 K, 240 K, and 160 K. The compound with $x = 0.5$ has space group $Pccn$ at all investigated temperatures analogous to the low-temperature structure of $\mathrm{Sm}_{1-x}\mathrm{Ca}_{1+x}\mathrm{MnO}_4$. For $\mathrm{Tb}_{0.33}\mathrm{Ca}_{1.67}\mathrm{MnO}_4$, refinements using $Bmeb$ yield better results compared to $Pccn$.

For $R_{1-x}\mathrm{Ca}_{1+x}\mathrm{MnO}_4$ (R = Sm, Tb), also the charge and orbital order has been investigated by x-ray techniques. Below T_{COO}, the orbital ordering causes small modulations of the oxygen positions manifesting itself in superstructure reflexes visible in the precession images of the single crystal x-ray diffractometer. This superstructure appears as four satellite spots around each main reflex $(hk0)$ at positions $(h \pm 1/2, k \pm 1/2, 0)$ for the half-doped compounds and at $(h \pm 1/3, k \pm 1/3, 0)$ for $x = 2/3$. These additional spots are not visible in precession images of the $(h0l)$ or $(0kl)$ plane, reflecting the two-dimensional character of the COO state. For the half-doped compounds $Pr_{0.5}Ca_{1.5}MnO_4$ and $Sm_{0.5}Ca_{1.5}MnO_4$, a doubling of the a axis and a change to space group *Pmnb* (No. 62) is needed to include the superstructure into the crystallographic description, whereas for $x = 2/3$, a triplication of the a axis is required and a change of the space group to *Pcab* (No. 61).

Magnetization Figure 4.9 shows the magnetization of $R_{1-x}Ca_{1+x}MnO_4$ with R = Pr, Nd, Sm, Tb (left panels) and of $R_{1-x}Sr_{1+x}MnO_4$ with R = Pr, Nd (right panels), each one measured in a magnetic field of $\mu_0 H = 1\,\mathrm{T}$ applied in c direction (open symbols) and parallel to the ab plane (filled symbols). All curves represent field-cooled measurements. Arrows indicate transition temperatures T_{COO} as determined from peaks in the later discussed $\mathrm{d}(\ln(\rho/\rho_0))/\mathrm{d}(T^{-1})$ [see Fig. 4.10].

The Ca manganites show comparably sharp peaks at T_{COO}, which agrees with findings for $Nd_{1-x}Ca_{1+x}MnO_4$ [347] and $R_{0.5}Ca_{1.5}MnO_4$ (R = Pr, Nd, Sm, Eu) [347]. In contrast, the $M(T)$ anomalies of $R_{1-x}Sr_{1+x}MnO_4$ are rather broad, which is also reported for $R_{0.5}Sr_{1.5}MnO_4$ (R = La, Pr) [325]. Signatures in the magnetization at the COO transition are known from $La_{1-x}Sr_{1+x}MnO_4$ [36, 37, 319, 335] and $R_{0.5}A_{1.5}MnO_4$ [325]. In contrast to a previous report on $M(T)$ of $Nd_{0.33}Sr_{1.67}MnO_4$ [35] where no anomaly is observed, here a kink is clearly visible at $\approx 260\,\mathrm{K}$. By trend, the distinctness of the anomalies increases with T_{COO}. While a Curie–Weiss behavior is foreshadowing above T_{COO}, a distinct deviation from this law is seen below. Above their respective T_{COO}, in-plane and out-of-plane magnetization are (almost) identical for the individual compounds, whereas below T_{COO}, an anisotropy emerges and increases with decreasing temperature. Toward the low-temperature regime, the out-of-plane magnetization is larger than the in-plane magnetization for all $R_{1-x}A_{1+x}MnO_4$.

In the low-temperature regime, all curves show a more or less steep increase of the magnetization, which mainly stems from the rare-earth magnetism. By comparing the low-temperature rise with the magnetic moments of the respective rare-earth ion [see Tab. 4.8], one can easily see a correspondence. The ion with the smallest moment of approximately $0.7\mu_{\mathrm{B}}$ is Sm^{3+}. Consequently, the $M(T)$ curves of $Sm_{1-x}Ca_{1+x}MnO_4$ show a comparably weak increase at low temperatures. In contrast, Tb^{3+} has the largest moment of $9\mu_{\mathrm{B}}$ and the respective $M(T)$ curves show a monotonic increase upon cooling over the entire temperature range, even for large values of x implying a small terbium content.

For each compound $R_{1-x}A_{1+x}MnO_4$, the absolute values of the magnetization decrease with increasing doping level at a given temperature. This is understandable because with increasing x, the magnetic rare-earth ion R is successively replaced by a non-magnetic alkaline earth ion A and, simultaneously, Mn^{3+} with a magnetic moment of $\mu_J = 4\mu_{\mathrm{B}}$ is substituted by Mn^{4+} with a smaller $\mu_J = 3\mu_{\mathrm{B}}$.

Because some $M(T)$ curves show further anomalies at lower temperatures, e.g., that of $Nd_{0.33}Ca_{1.67}MnO_4$ around 120 K, one may assume that T_{N} is hinted there. However, in view of the fact that even in $La_{1-x}Sr_{1+x}MnO_4$ with nonmagnetic La^{3+}, no well-defined signature of T_{N} is seen in the magnetization [36, 37], it is highly unlikely to see fingerprints of the bare manganese magnetism in $R_{1-x}A_{1+x}MnO_4$ with magnetic rare-earth ions R. Instead,

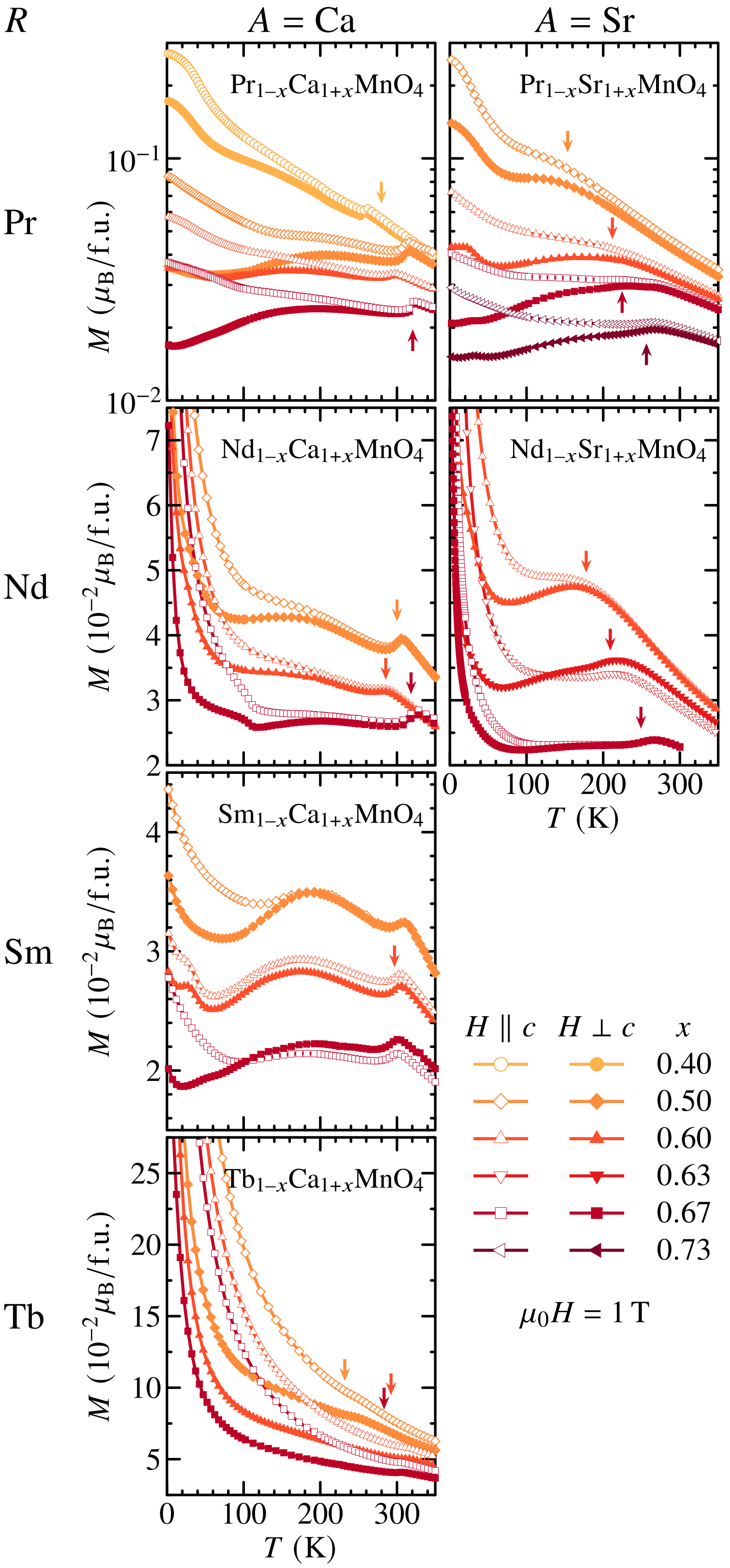

Figure 4.9: Magnetization of $R_{1-x}A_{1+x}\mathrm{MnO}_4$. In-plane (filled symbols) and out-of-plane (open symbols) magnetization $M(T)$ of $R_{1-x}\mathrm{Ca}_{1+x}\mathrm{MnO}_4$ with R = Pr, Nd, Sm, Tb (left panels) and $R_{1-x}\mathrm{Sr}_{1+x}\mathrm{MnO}_4$ with R = Pr, Nd with doping levels $0.40 \leq x \leq 0.73$. All measurements are field-cooled. Arrows indicate peak positions in $\mathrm{d}(\ln(\rho/\rho_0))/\mathrm{d}(T^{-1})$ [see Fig. 4.10].

Ion	Configuration	S	L	J	Symbol	g_J	μ_J/μ_B
Pr^{3+}	[Xe]$4f^2$	1	5	4	$^3H_4$	4/5	3.2
Nd^{3+}	[Xe]$4f^3$	3/2	6	9/2	$^4I_{9/2}$	5/7	3.273
Sm^{3+}	[Xe]$4f^5$	5/2	5	5/2	$^6H_{5/2}$	2/7	0.714
Tb^{3+}	[Xe]$4f^8$	3	3	6	$^7F_6$	3/2	9

Table 4.8: Free-ion configurations of rare-earth ions. Electronic configuration, spin quantum number S, orbital angular momentum quantum number L, total angular momentum quantum number J, term symbol $^{2S+1}L_J$, Landé factor g_J, and total magnetic moment μ_J according to Hund's rules.

the manganese magnetism is probably covered by the rare-earth magnetism or/and both magnetic subsystems interact with each other in a nontrivial way.

Resistivity The upper panels of Fig. 4.10 show the in-plane resistivity of $R_{1+x}A_{1+x}MnO_4$ in semilogarithmic scales as a function of temperature, in particular, $Pr_{1-x}Ca_{1+x}MnO_4$ [Fig. 4.10 (a)], $Nd_{1-x}Ca_{1+x}MnO_4$ [Fig. 4.10 (c)], $Pr_{1-x}Sr_{1+x}MnO_4$ [Fig. 4.10 (e)], and $Nd_{1-x}Sr_{1+x}MnO_4$ [Fig. 4.10 (g)]. The curves $\rho(T)$ are normalized to the resistivity at highest temperature ρ_0, which is 400 K for $R_{1-x}Ca_{1+x}MnO_4$ [Figs. 4.10 (a, c)] and 300 K for $R_{1-x}Sr_{1+x}MnO_4$ [Figs. 4.10 (e, g)]. Because up and down measurements revealed no difference, only one of them is shown in Fig. 4.10. In contrast, a thermal hysteresis is reported for the resistivity of $Pr_{0.5}Ca_{1.5}MnO_4$ [325]. All $\rho(T)$ curves in Fig. 4.10 exhibit an essentially semiconducting behavior with anomalies appearing in a temperature range between 150 K and 320 K where the resistivity increases steeply. Such a steep increase in $\rho(T)$ is known to occur at the transition to the charge and orbital ordered state and has been observed in $La_{1-x}Sr_{1+x}MnO_4$ [36, 37, 319, 335, 340] and $Pr_{0.5}Sr_{1.5}MnO_4$ [325]. Therefore, the anomalies in $\rho(T)$ in Fig. 4.10 are attributed to the COO transition. Figures 4.10 (b, d, f, h) show the derivatives of the Arrhenius plots $d(\ln(\rho/\rho_0))/d(T^{-1})$ for the corresponding resistivity curves in the upper panels. These derivatives correspond to the activation energy expressed in Kelvin and transform anomalies in $\rho(T)$ into clearly identifiable peaks defining the transition temperature to the COO state T_{COO}.

Ca manganites $R_{1-x}Ca_{1+x}MnO_4$ (R = Pr, Nd) [Figs. 4.10 (b, d)] show very sharp peaks in a narrow range around room temperature. Above T_{COO}, the derivative is roughly constant, which corresponds to the usual Arrhenius behavior. At least for $Nd_{1-x}Ca_{1+x}MnO_4$, the T_{COO} are not ordered by x since the peak of $x = 0.40$ is between those of 0.60 and 0.67. The peak sharpness increases with increasing T_{COO}. Sr manganites $R_{1-x}Sr_{1+x}MnO_4$ (R = Pr, Nd) show anomalies at much lower temperatures compared to Ca manganites, and they cover a larger temperature range of $150\,K \leq T \leq 250\,K$ [Figs. 4.10 (f, h)]. The peaks in the derivatives are much less pronounced than those of the Ca manganites. The largest peak of the Sr manganites ($Pr_{0.27}Sr_{1.73}MnO_4$) is one order of magnitude smaller than the maximum of the Ca manganites ($Pr_{0.33}Ca_{0.67}MnO_4$). Consequently, the signal-to-noise ratio

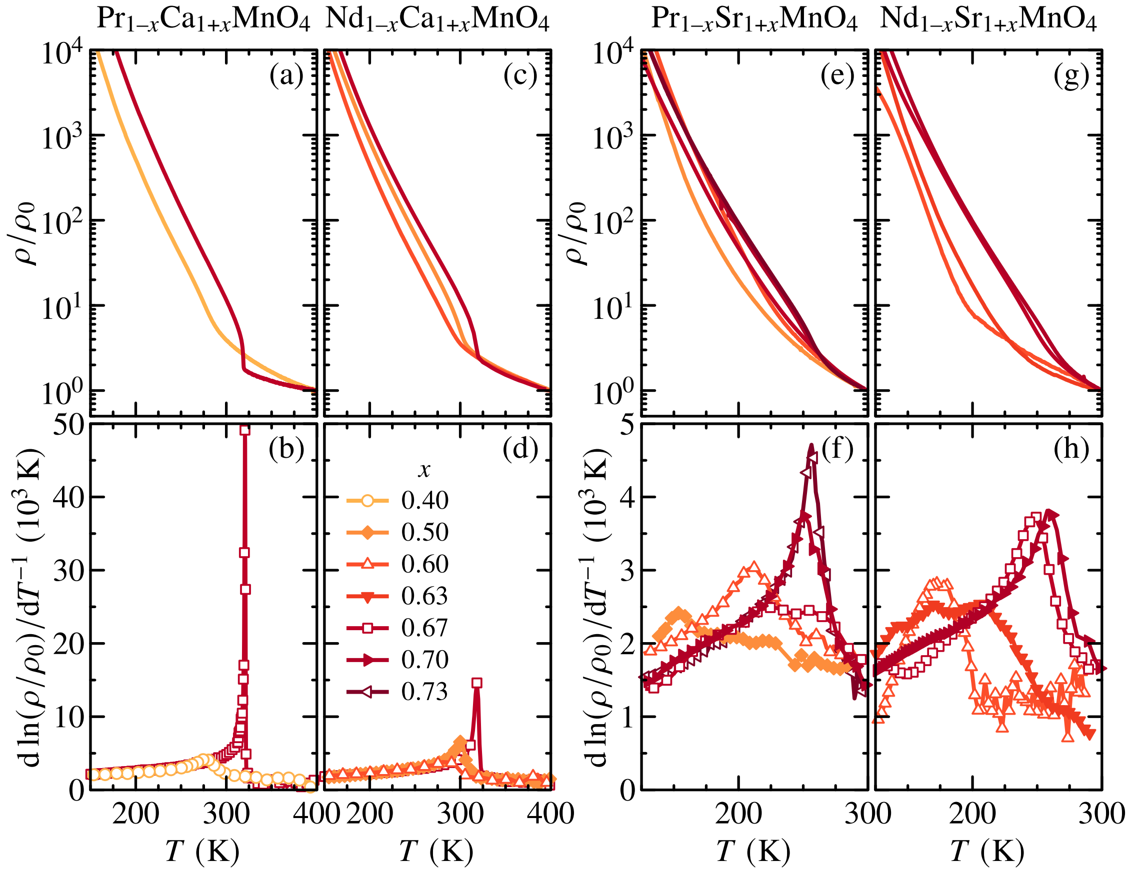

Figure 4.10: In-plane resistivity of $R_{1-x}A_{1+x}$MnO$_4$. In-plane resistivity ρ of Pr$_{1-x}A_{1+x}$MnO$_4$ and Nd$_{1-x}A_{1+x}$MnO$_4$ for A = Ca (left) and A = Sr (right). Top panels: $\rho(T)$ normalized to ρ at highest temperatures (400 K for A = Ca and 300 K for A = Sr) in semilogarithmic scales. The resistivity of Pr$_{1-x}$Ca$_{1+x}$MnO$_4$ was measured by G. Kolland. Lower panels: Derivative of the Arrhenius plot.

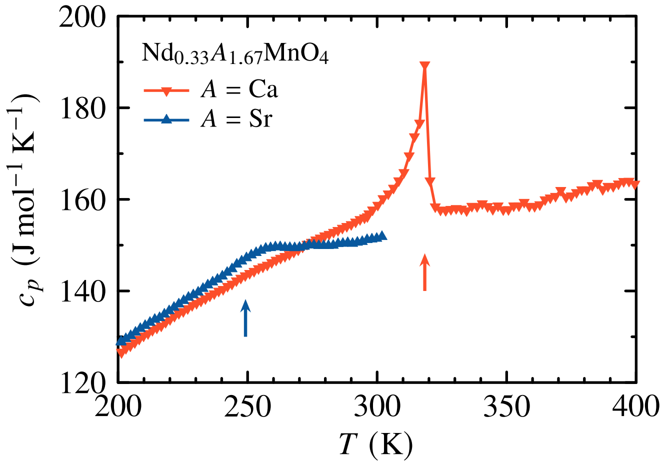

Figure 4.11: Specific heat of $Nd_{0.33}A_{1.67}MnO_4$. Comparison of $c_p(T)$ of two single-layered manganites with identical rare-earth element R = Nd and doping level x but different alkaline earth elements: $Nd_{0.33}Ca_{1.67}MnO_4$ and $Nd_{0.33}Sr_{1.67}MnO_4$. Arrows correspond to peak positions in $d(\ln(\rho/\rho_0))/d(T^{-1})$.

in Figs. 4.10 (f, h) is much smaller than in Figs. 4.10 (b, d). Nevertheless, one finds clearly identifiable peaks with the exceptions of $Pr_{0.33}Sr_{1.67}MnO_4$ and $Nd_{0.37}Sr_{1.63}MnO_4$, which show very broad humps. In contrast to Ca manganites, the maxima are ordered by x. Except for $Pr_{0.33}Sr_{1.67}MnO_4$ and $Nd_{0.37}Sr_{1.63}MnO_4$, the peak sharpness increases with increasing T_{COO}.

Heat capacity Figure 4.11 shows the high-temperature specific heat $c_p(T)$ of two samples $Nd_{0.33}A_{1.67}MnO_4$ with A = Ca, Sr. Although both compounds have the same doping level x and the same rare-earth element R = Nd, the T_{COO} anomaly of the Ca manganite is much more pronounced and appears at a higher temperature compared to the Sr manganite. This observation is in line with the above discussed findings for $d(\ln(\rho/\rho_0))/d(T^{-1})$ and $M(T)$, where $R_{1-x}Ca_{1+x}MnO_4$ shows much sharper peaks than $R_{1-x}Sr_{1+x}MnO_4$ independent of R.

4.5.3 Discussion

Figure 4.12 shows the COO transition temperatures of $R_{1-x}A_{1+x}MnO_4$, extracted from the measurements discussed in the previous sections, as a function of doping level x. In addition, the transition temperatures T_{COO} of $La_{1-x}Sr_{1+x}MnO_4$ taken from Refs. [36, 37, 375, 378] are depicted. This phase diagram allows to make three statements: First, one distinguishes two distinct regimes; one with low transition temperatures ($150\,K \leq T_{COO} \leq 260\,K$) containing the Sr manganites, and one regime with higher transition temperatures ($230\,K \leq T_{COO} \leq 320\,K$) containing the Ca manganites. Second, the variation of T_{COO} with doping level x is large for Sr manganites and small for Ca manganites. Third, for the Sr compounds, T_{COO} is monotonically increasing with x, whereas for Ca manganites this is not the case. Instead, $Pr_{1-x}Ca_{1+x}MnO_4$ and $Nd_{1-x}Ca_{1+x}MnO_4$ have the highest T_{COO} at commensurate doping levels $x = 1/2, 2/3$.

The first statement can be understood easily if one recalls the crystal structure of respective compounds. The Sr compounds are tetragonal with 180° Mn–O–Mn bonds, whereas Ca

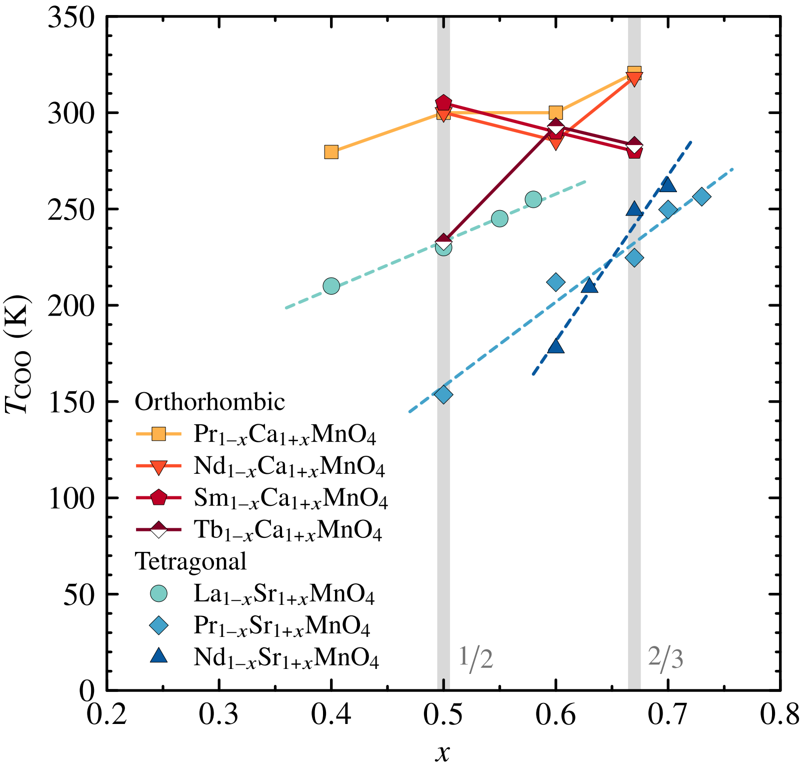

Figure 4.12: Phase diagram $T_{\mathrm{COO}}(x)$ of $R_{1-x}A_{1+x}\mathrm{MnO}_4$. T_{COO} as a function of doping level x for $R_{1-x}A_{1+x}\mathrm{MnO}_4$. Dashed lines are linear fits, solid lines are guides to the eye. Commensurate doping levels at $x = 1/2, 2/3$ are highlighted. Data points of $\mathrm{La}_{1-x}\mathrm{Sr}_{1+x}\mathrm{MnO}_4$ are compiled from Refs. [36, 37, 375, 378].

manganites are orthorhombic with tilted MnO_6 octahedra resulting in a smaller overlap of the electronic wave functions. Consequently, the hopping between Mn sites is reduced in Ca manganites, which stabilizes charge order. Therefore, the COO appears at higher temperatures in Ca manganites compared to the Sr compounds.

Furthermore, T_{COO} is governed by the ion-size disorder on the A site. In general, the average ion size is given by $\langle r\rangle = \sum_i y_i r_i$, where r_i is the ionic radius and y_i the fraction of the respective ion i, with normalization $\sum_i y_i = 1$. The disorder is then given by

$$\sigma^2 = \langle r^2\rangle - \langle r\rangle^2 = \sum_i y_i r_i^2 - \left(\sum_i y_i r_i\right)^2 . \tag{4.3}$$

In $R_{1-x}A_{1+x}\mathrm{MnO}_4$, the A site is shared by two different ions. Thus, this equation reduces to $\sigma^2 = y_1 y_2 (r_1 - r_2)^2$ and the average ion size becomes $\langle r\rangle = y_1 r_1 + y_2 r_2$. By inserting the ion radii $r_1 = r_R$, $r_2 = r_A$ and the fractional occupations $y_1 = (1-x)/2$, $y_2 = (1+x)/2$, one obtains the mean ion size on the A site

$$\langle r_{R,A}\rangle = \frac{1-x}{2} r_R + \frac{1+x}{2} r_A \tag{4.4}$$

and the disorder

$$\sigma^2(x, \langle r_{R,A}\rangle) = \frac{(1-x)(1+x)}{4}(r_R - r_A)^2 , \tag{4.5}$$

Site	Ion	Coordination	Eff. ion radius (Å)
X	O^{2-}	6 ‡	1.40
A	Ba^{2+}	9	1.47
A	Sr^{2+}	9	1.31
A	Ca^{2+}	9	1.18
A	La^{3+}	9	1.216
A	Pr^{3+}	9	1.179
A	Nd^{3+}	9	1.163
A	Sm^{3+}	9	1.132
A	Tb^{3+}	9	1.095
A	Er^{3+}	9	1.062
B	Mn^{3+}	6	0.645
B	Mn^{4+}	6	0.530

Table 4.9: Ionic radii in single-layered manganites. Rare earth elements and alkaline earth elements share the same 9-fold coordinated A site. Values are taken from Shannon [261]. ‡ As pointed out in Ref. [263, p. 54], the coordination of O^{2-} in perovskite materials is debatable. Often, it is assumed to be 6 (see, e.g., Refs. [264, 265] or [266, Suppl.]).

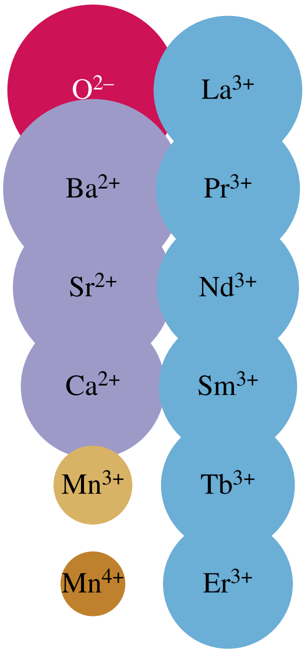

Figure 4.13: Illustration of ionic radii in single-layered manganites. Ionic radii for the respective coordinations in Tab. 4.9 drawn to scale.

which depends quadratically on x. By considering the projection of $\sigma^2(x, \langle r_{R,A}\rangle)$ on the (σ^2, x) plane, one can describe σ^2 as a family of functions in two dimensions with $\langle r_{R,A}\rangle$ as parameter. These functions are shown in Fig. 4.14. The lower, yellow regime contains $\sigma^2(x)$ for $\langle r_{R,\mathrm{Ca}}\rangle$, the upper bluish part includes $\langle r_{R,\mathrm{Sr}}\rangle$. Values for ionic radii are taken from Ref. [261] and are shown in Tab. 4.9 and illustrated in Fig. 4.13. The orthorhombic Ca manganites $Pr_{1-x}Ca_{1+x}MnO_4$ and $Nd_{1-x}Ca_{1+x}MnO_4$ have a comparably small structural disorder, independent of x, because Pr^{3+} and Nd^{3+} have almost the same size as Ca^{2+}) [see Fig. 4.13]. For the tetragonal Sr compounds (and, to some extent, also for $R_{1-x}Ca_{1+x}MnO_4$ with R = Tb, Sm), the disorder σ^2 is much larger. Furthermore, the disorder increases within each of the two regimes (yellow and blue) with decreasing ion size of R^{3+}, a correlation known as lanthanoid contraction, as indicated in Fig. 4.14 by black arrows. This explains the second statement: if R^{3+} and A^{2+} are of similar size, a variation of doping level x does not have much influence on T_{COO}, because the structural changes are small, while in the Sr manganites, a change of x has a huge impact on T_{COO} since a small rare-earth ion is replaced by a much larger Sr^{2+}.

The third statement can be understood if one considers commensurate configurations to be more stable in general and, thus, to have higher T_{COO}, but this is not visible in the manganite

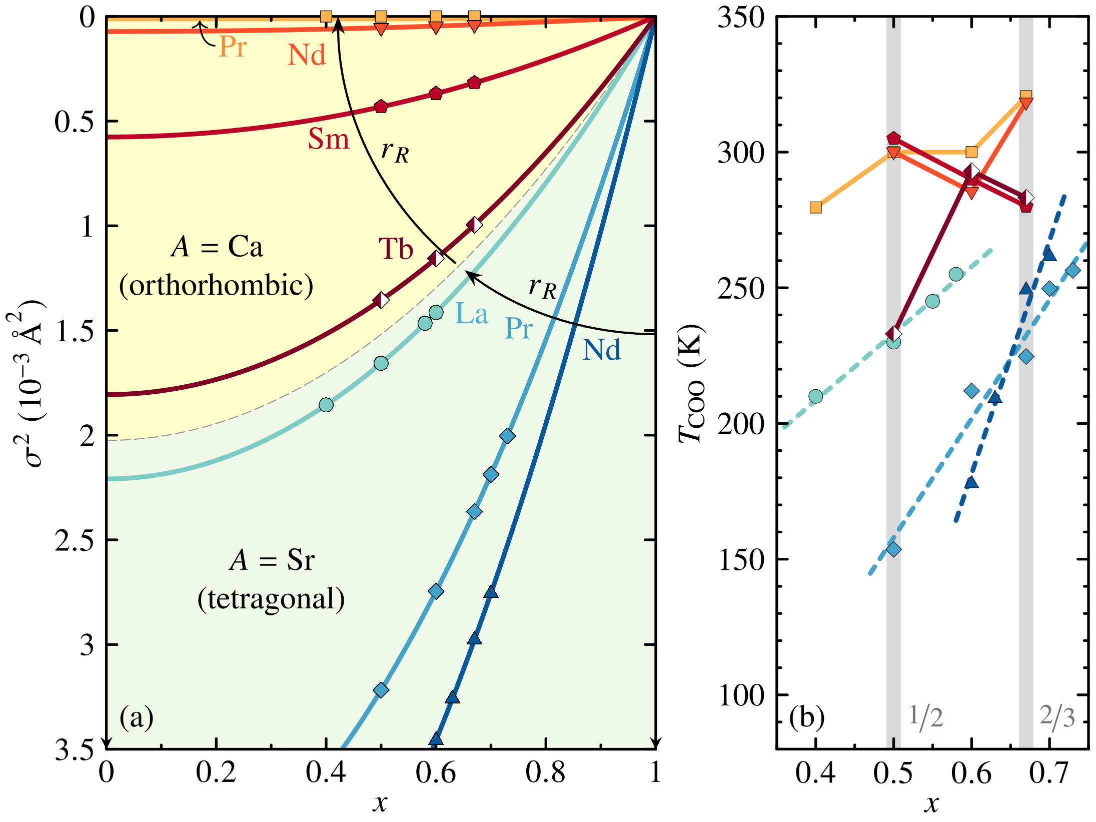

Figure 4.14: Variance versus doping level. (a) Calculated ion-size variance σ^2 in $R_{1-x}A_{1+x}$MnO$_4$ with A = Ca, Sr combined with different R = La, Pr, Nd, Sm, Tb as a function of doping level x using the ion radii listed in Tab. 4.9. Data points correspond to doping levels of investigated samples. Thick arrows indicate increasing R^{3+} ion radius. Please note the reversed axis of ordinates. (b) Detail view of Fig. 4.12.

systems with large disorder. Only the highly ordered manganites Pr$_{1-x}$Ca$_{1+x}$MnO$_4$ and Nd$_{1-x}$Ca$_{1+x}$MnO$_4$ reveal this effect. Fig. 4.14 also shows why Tb$_{1-x}$Ca$_{1+x}$MnO$_4$ is special and does not fit to the other Ca manganites: For $x = 0.5$, its T_{COO} is comparable to that of La$_{0.5}$Sr$_{1.5}$MnO$_4$, but, for higher doping, it approaches the high-T_{COO} regime of its sister compounds R_{1-x}Ca$_{1+x}$MnO$_4$ [see Fig. 4.12]. The disorder σ^2 of Tb$_{1-x}$Ca$_{1+x}$MnO$_4$ is the highest amongst the Ca manganites, being almost comparable to that of La$_{1-x}$Sr$_{1+x}$MnO$_4$, which has the smallest disorder of the Sr compounds.

There is another conclusion one can deduce from $\sigma^2(x)$: Increasing the doping level x means substituting rare-earth ions by alkaline earth ions, i.e., when approaching $x = 1$, structural disorder vanishes and the average ionic radius becomes identical with the radius of the alkaline earth ion ($x \longrightarrow 1 \Rightarrow \sigma^2 \longrightarrow 0$, $\langle r_{R,A} \rangle \longrightarrow r_A$). Therefore, one should expect a convergence of COO transition temperatures for $x \longrightarrow 1$ to two characteristic values, one for R_{1-x}Ca$_{1+x}$MnO$_4$ and one for R_{1-x}Sr$_{1+x}$MnO$_4$. This behavior is seen suggestively in the

$T_{\text{COO}}(x)$ phase diagram [see Fig. 4.12] but cannot be settled conclusively due to the lack of doping levels beyond $x = 0.73$. Of course, single-layered manganites with $x = 1$ cannot show COO at all due to the absence of Mn^{3+}. One should note that an additional ion-size disorder exists for Mn^{3+} and Mn^{4+}. Upon increasing x, Mn^{3+} is consecutively replaced by the smaller Mn^{4+}. Like the A-site disorder, the manganese disorder vanishes for $x = 1$, but, in contrast to the latter, it reaches its maximum at $x = 0.5$, while the A-site disorder peaks at $x = 0$.

4.6 Conclusion

New compounds of single-layered manganites $R_{1-x}A_{1+x}MnO_4$ beyond the well-known $La_{1-x}Sr_{1+x}MnO_4$ system were grown in single-crystalline form [see growth details in Sec. 4.4.2]. Different element combinations for R and A were used to reach higher doping levels x compared to $La_{1-x}Sr_{1+x}MnO_4$, which is limited to $x \lesssim 0.6$. The initial goal to grow single crystals with doping level $x = 0.75$, in order to enable a survey of the predicted stripe orders of charges and orbitals and possible 4-spin zig-zag chains, could not be achieved. The highest doping level of $x = 0.73$ has been accomplished for the composition $Pr_{1-x}Sr_{1+x}MnO_4$. The transition to the charge and orbital order (COO) causes characteristic fingerprints in resistivity, magnetization, and heat capacity. The evolution of T_{COO} with doping level x is summarized in a common phase diagram for all investigated $R_{1-x}A_{1+x}MnO_4$ compounds. The tetragonal $R_{1-x}Sr_{1+x}MnO_4$ systems are qualitatively different from the orthorhombic $R_{1-x}Ca_{1+x}MnO_4$ materials. In comparison to the latter, the Sr manganites show much lower transition temperatures in general and a much larger x dependence of T_{COO} due to the larger ion-size mismatch of their respective R and A ions. To some extent, this is also seen for $Sm_{1-x}Ca_{1+x}MnO_4$ and $Tb_{1-x}Ca_{1+x}MnO_4$, which have the largest A-ion size disorder of the Ca manganites. In contrast, $Pr_{1-x}Ca_{1+x}MnO_4$ and $Nd_{1-x}Ca_{1+x}MnO_4$, both having only a tiny ion-size mismatch, show the largest T_{COO} of all single-layered manganites. Only these two compounds exhibit a larger T_{COO} at commensurate doping levels $x = 1/2, 2/3$; an effect that is not seen in manganites with higher ion-size disorder like $R_{1-x}Sr_{1+x}MnO_4$ or $R_{1-x}Ca_{1+x}MnO_4$ with $R = \text{Sm, Tb}$.

5 Summary

In this thesis, different single-crystalline, perovskite-type transition metal oxides are studied, where the perovskite titanates $Sr_{1-x}Ca_xTiO_{3-\delta}$ and $EuTiO_{3-\delta}$ are doped band insulators with a quantum-paraelectric parent and the single-layered manganites $R_{1-x}A_{1+x}MnO_4$ are doped Mott insulators.

The competition of ferroelectric and metallic phase in $Sr_{1-x}Ca_xTiO_{3-\delta}$ has been hitherto investigated primarily by resistivity measurements [30], where the signatures of the ferroelectric(-like) transition were found to persist upon increasing charge-carrier density n and vanish at a critical n_c that depends on the calcium content x. In order to clarify the nature of this transition, an investigation by a thermodynamic probe was required. In this thesis, commercial $Sr_{1-x}Ca_xTiO_3$ single crystals with a calcium content of $x = 0.009$ and carrier densities tuned from the insulating, ferroelectric parent material up to $n \simeq 60 \times 10^{19}\,\mathrm{cm}^{-3}$ are studied by measurements of the thermal expansion α/T. Pronounced anomalies are observed, signaling the ferroelectric transition of pristine $Sr_{1-x}Ca_xTiO_3$, and persist in reduced $Sr_{1-x}Ca_xTiO_{3-\delta}$ upon increasing charge-carrier density n, which is in line with the resistivity findings. In contrast to the latter, the anomalies in α/T do not completely vanish as a function of n but are present over the entire studied doping range. However, these anomalies change in character at a certain threshold carrier density $n^* \approx 1.3 \times 10^{19}\,\mathrm{cm}^{-3}$ as is quantified by an analysis of the spontaneous strain. This might be an indication for a structural phase transition upon crossing n^*. Indeed, the requirement for a non-centrosymmetric space group of the ferroelectric parent $Sr_{1-x}Ca_xTiO_3$ is obsolete in the presence of mobile charge carriers in $Sr_{1-x}Ca_xTiO_{3-\delta}$. It is reasonable that this requirement is not immediately destroyed at very low carrier densities but requires a certain threshold concentration. A similar transition is known from the parent compound $Sr_{1-x}Ca_xTiO_3$ that changes from non-centrosymmetric ferroelectric to centrosymmetric antiferroelectric as a function of calcium content x. Temperature-dependent measurements like thermal-expansion can hardly detect (almost) vertical phase boundaries in a T_C versus n diagram. Therefore, detailed structural analyses of $Sr_{1-x}Ca_xTiO_{3-\delta}$ crystals with charge-carrier concentrations on both sides of n^* are required to resolve this puzzle. A sign change of α as a function of n, as is expected for a quantum phase transition where n is the control parameter, could not be observed in this material.

The large effective Bohr radius in doped $SrTiO_3$ allows the material to become metallic already at extremely dilute charge-carrier concentrations n and the observed T^2 resistivity challenges conventional theories for electron–electron scattering in view of the low n. Because $EuTiO_3$ is isostructural to $SrTiO_3$, it is the prime candidate to explore a similar behavior in another material. In this thesis, single crystals of $EuTiO_3$ are grown by the floating-zone method. Similar to $SrTiO_3$ and $Sr_{1-x}Ca_xTiO_3$, the physical properties of

$EuTiO_3$ strongly depend on the actual oxygen content. The material hosts a magnetic Eu^{2+} ion and the coincidence of Eu^{3+} to be nonmagnetic allows a determination of the nominal oxygen content toward the oxygen-excessive regime by analyzing the magnetic properties of $EuTiO_3$. The as-grown crystal is found to be oxygen-excessive by comparing its saturation magnetization to that of a pure Eu^{2+} system, resulting in a nominal composition $EuTiO_{3.02}$. Other key parameters as Néel temperature, Weiss temperature, and the Barrett-type permittivity agree with literature data.

Metallic $EuTiO_{3-\delta}$ samples are obtained by annealing pieces of the as-grown crystal. In order to have an indicator for the homogeneity of the oxygen-defect concentration, two samples of different thicknesses are annealed simultaneously. Samples annealed at temperatures below 750 °C exhibit very different resistivities indicating inhomogeneously distributed charge-carrier concentrations. Homogeneous samples are obtained for annealing temperatures $T \geq 750\,°\mathrm{C}$. The induced metal–insulator transition is qualitatively similar to that of $SrTiO_{3-\delta}$ but appears at a charge-carrier concentration n_c larger by a factor of 10^4. This is due to the smaller permittivity of $EuTiO_3$ implying a smaller effective Bohr radius of $a_B^* \approx 130\,\text{Å}$ compared to 6700 Å in $SrTiO_3$. The Mott criterion for the metal–insulator boundary compares a_B^* with the average distance of two donor atoms $n_c^{1/3}$. Many doped semiconductors obey the scaling law $n_c^{1/3} a_B^* = K$ with a constant $K = 0.25$, resembling the original Mott criterion. It is found that doped perovskite oxides $EuTiO_3$, $SrTiO_3$, and $KTaO_3$ obey the same behavior but with a significantly enhanced $K = 10$. At low temperature, the electronic mobility of metallic $EuTiO_{3-\delta}$ and $SrTiO_{3-\delta}$ increases systematically upon decreasing charge-carrier density across both materials. An AT^2 resistivity is observed in metallic $EuTiO_{3-\delta}$ that has not been reported previously. The prefactor A decreases with increasing n and, simultaneously, the temperature range of the T^2 behavior extends toward higher temperatures, very similar to the results for $SrTiO_{3-\delta}$. A simple three-band model is derived, which describes the $A(n)$ scaling of doped $EuTiO_3$ and $SrTiO_3$ over a large range of n.

Doped Mott insulators show complex patterns of charges, orbitals, and spins. The well-studied single-layered manganite $La_{1-x}Sr_{1+x}MnO_4$ exhibits stripe orders of charges and $3d_{z^2}$ orbitals, as well as ferromagnetic zig-zag chains with antiferromagnetic interchain coupling. Commensurate doping levels $x = 1/2, 2/3, 3/4$ are in a sense fundamental, since the stripe patterns of incommensurate configurations can be considered as combinations of the commensurate ones. However, the material $La_{1-x}Sr_{1+x}MnO_4$ is prone to chemical phase separation above $x \simeq 0.6$. Therefore, $x = 1/2$ is the only commensurate configuration of single-layered manganites with this element combination. In this thesis, single-layered manganites $R_{1-x}A_{1+x}MnO_4$ with different element combinations R/A were grown in single-crystalline form to overcome the structural restrictions in $La_{1-x}Sr_{1+x}MnO_4$ and push x to new levels. The synthesized crystals cover a doping range of $0.40 \leq x \leq 0.73$, where the maximum of $x = 0.73$ is achieved with $Pr_{1-x}Sr_{1+x}MnO_4$. The transition to the charge and orbital order at T_{COO} signals itself by characteristic features in resistivity, magnetization, and heat capacity. A common phase diagram for all investigated manganites $R_{1-x}A_{1+x}MnO_4$

is established, where the evolution of T_{COO} as a function of x resembles the disorder $\sigma^2(x)$ caused by the ion-size mismatch of R and A. This mismatch is large in the tetragonal manganites $R_{1-x}\mathrm{Sr}_{1+x}\mathrm{MnO}_4$. These compounds exhibit comparably low transition temperatures and their respective T_{COO} systematically increases as a function of x. In contrast, manganites with small ion-size mismatch like $\mathrm{Pr}_{1-x}\mathrm{Ca}_{1+x}\mathrm{MnO}_4$ and $\mathrm{Nd}_{1-x}\mathrm{Ca}_{1+x}\mathrm{MnO}_4$ show the highest transition temperatures T_{COO} of all investigated manganites. In these two compounds, the evolution of T_{COO} with x is not monotonic as is observed for strontium manganites. Instead, the highest transition temperatures appear at commensurate doping levels $x = 1/2, 2/3$.

Appendices

A Further growth processes

A.1 Pyrochlore systems

A.1.1 Introduction

The mineral pyrochlore, discovered in 1826 [379], is the ancestor of a large family of compounds with general chemical formula

$$A_2B_2X_7$$

and eponym of the pyrochlore structure. It has a cubic symmetry with space group $Fd\bar{3}m$ (No. 227), which is the same as for the diamond structure. Because the pyrochlore structure is rather complicated (e.g., compared to the perovskite structure), there are various approaches of description and each variant emphasizes different aspects. Often, A site or B site (or both) are occupied by magnetic ions. In order to emphasize the magnetic interaction, a popular point of view is to neglect the oxygen ions completely and focus on the two interpenetrating sublattices formed by A and B ions, respectively. Each of both species forms a network of corner-sharing tetrahedra. By omitting the oxygen ions, the A and B sublattices appear equivalent, which is misleading because the local environments of A and B ions are different. The A ions are surrounded by 8 oxygen ions forming a distorted cube, whereas the B ions are surrounded by 6 oxygen ions forming a distorted octahedron. The pyrochlore structure is tolerant in terms of chemical substitutions [380, 381]. One can distinguish pyrochlore oxides $A_2B_2O_7$ by the oxidation states of the A and B ions, which can be (3+, 4+) or (2+, 5+). Possible element combinations can be found as stability field maps in Refs. [380, 382]. The synthesized molybdates $R_2Mo_2O_7$ and the zirconate $Pr_2Zr_2O_7$ both belong to the (3+, 4+) class.

Pyrochlore systems represent a huge material family exhibiting a multitude of physical phenomena. Pyrochlore oxides include ferromagnetic metals ($Nd_2Mo_2O_7$, $Sm_2Mo_2O_7$, $Gd_2Mo_2O_7$ [383–385]), spin glasses ($Y_2Mo_2O_7$ [386, 387], $Tb_2Mo_2O_7$ [388]), spin-ice systems ($Dy_2Ti_2O_7$ [389], $Ho_2Ti_2O_7$ [390]), quantum spin-ice materials ($Pr_2Zr_2O_7$ [391]) and superconductors ($Cd_2Re_2O_7$ [392]). Because A site and B site ions form networks of corner-sharing tetrahedra, magnetic interactions in pyrochlore systems are often dominated by magnetic frustration. Prime examples for such frustrated systems are the spin-ice materials $Dy_2Ti_2O_7$ and $Ho_2Ti_2O_7$, where large magnetic moments reside on the A site, while the B-site sublattice is nonmagnetic.

The atomic positions of the pyrochlore structure have one free parameter which is the x coordinate of the oxygen ion on the $48f$ site [see Tab. A.1]. The physical properties of pyrochlore materials are very sensitive to this parameter. Nominally, it takes values of

Ion	Multiplicity	Wyckoff letter	Site symmetry	Coordinates
A	16	d	$.\bar{3}m$	1/2, 1/2, 1/2
B	16	c	$.\bar{3}m$	0, 0, 0
O	48	f	$2.mm$	x, 1/8, 1/8
O’	8	b	$\bar{4}3m$	3/8, 3/8, 3/8
V_O	8	a	$\bar{4}3m$	1/8, 1/8, 1/8

Table A.1: Atomic positions in pyrochlore oxides $A_2B_2O_7$. Standard setting of the cubic pyrochlore structure with space group $Fd\bar{3}m$ (No. 227) where B is placed at the origin (origin choice 2 in the *International Tables for Crystallography Vol. A* [84, pp. 700–703]). The structure has one single free parameter $x \approx 0.33$ in the $48f$ position [see also Fig. A.1]. The unit cell contains 8 formula units. Additionally, the oxygen vacancy position of the fluorite parent structure is given (V_O denotes an oxygen vacancy in Kröger–Vink notation [393]).

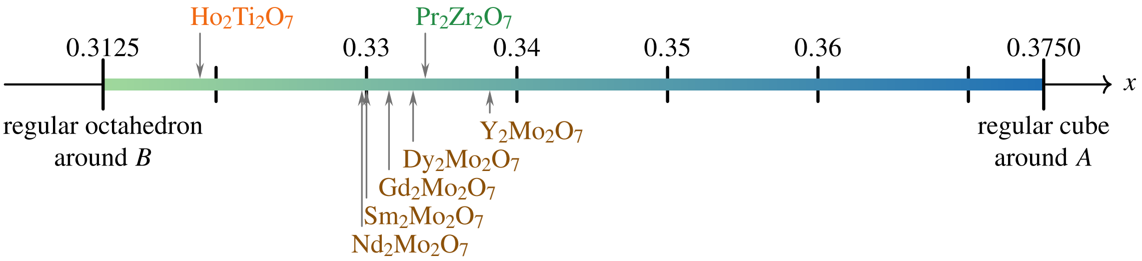

Figure A.1: Pyrochlore structure: Free parameter. In pyrochlore oxides $A_2B_2O_7$ the structural parameter x of the Wyckoff position $48f$ is limited to a range $x \in [0.3125, 0.375]$. For $x = 0.3125 = 5/16$, the local environment of B is a regular octahedron of O^{2-}, while simultaneously the cube around A is maximally distorted. For $x = 0.375 = 3/8$, the local environment of A is a regular cube of O^{2-}, while the octahedron around B is maximally distorted. The x values of real materials are marked with arrows [see Tab. A.2 for references].

$0.3125 \leq x \leq 0.3750$ and determines the degree of distortion of the cube around A and the octahedron around B, respectively. In the extreme case of $x = 0.3125$, the octahedron around B is regular, while the cube around A is maximally distorted. For $x = 0.3750$, the cube around A is regular and the octahedron around B is maximally distorted. In real materials, the free parameter appears in a more narrow range $x \leq 0.34$, where a regular octahedron around B is closer than a regular cube around A [see Fig. A.1].

A.1.2 $R_2Mo_2O_7$ (R = Nd, Sm, Gd, Dy)

Introduction

In molybdate pyrochlores $R_2Mo_2O_7$, magnetic ions occupy both A site and B site. The physical properties are governed by the Mo–O–Mo bond angle and the Mo–Mo distance

Table A.2: Pyrochlore structure: Literature parameters. Lattice parameter a and x position of the $48f$ oxygen atom.

Compound	a (Å)	x	Ref.
$Y_2Mo_2O_7$	10.230(1)	0.3382(1)	[387]
$Dy_2Mo_2O_7$	10.2728(1)	0.3331(6)	[394]
$Gd_2Mo_2O_7$	10.3356(1)	0.3315(8)	[394]
$Sm_2Mo_2O_7$	10.4196(1)	0.3300(5)	[394]
$Nd_2Mo_2O_7$	10.4836(2)	0.3297(7)	[394]
$Pr_2Zr_2O_7$	10.703 798(3)	0.333 91(15)	[395]
$Ho_2Ti_2O_7$	10.099 51(9)	0.321 64	[396]

Name	Formula	Appearance	Purity
Molybdenum(IV) oxide	MoO_2	black	99 %
Titanium(IV) oxide	TiO_2	white	99.99 %
Zirconium(IV) oxide	ZrO_2	white	99.978 %
Praseodymium(III,IV) oxide	Pr_6O_{11}	black	99.99 %
Neodymium(III) oxide	Nd_2O_3	light blue	99.99 %
Samarium(III) oxide	Sm_2O_3	light yellow	99.99 %
Gadolinium(III) oxide	Gd_2O_3	white	99.99 %
Dysprosium(III) oxide	Dy_2O_3	white	99.99 %

Table A.3: Reactants for $R_2Mo_2O_7$ and $Pr_2(Zr_{1-x}Ti_x)_2O_7$. Polycrystalline powders used as reactants for the synthesis of $R_2Mo_2O_7$ (R = Nd, Sm, Gd, Dy) and $Pr_2(Zr_{1-x}Ti_x)_2O_7$. All powders are from ALFA AESAR.

that both depend on the free parameter x of the pyrochlore crystal structure while x itself depends on the R ion radius $r(R)$ [397]. Upon decreasing $r(R)$, the material properties change from a ferromagnetic metallic state (R = Nd, Sm, Gd) to an insulating spin glass (R = Tb, Dy, Ho, Er, Tm, Yb) [381, 398]. The lanthanoid contraction can be utilized to tune the R ion size. Within the scope of this thesis, the crystal growth of three compounds from the ferromagnetic metallic regime (R = Nd, Sm, Gd) and one from the insulating regime (R = Dy) was attempted.

Preparation

Polycrystalline powders of MoO_2 and the rare-earth oxides Nd_2O_3, Sm_2O_3, Gd_2O_3, and Dy_2O_3 were used as starting materials [see Tab. A.3 for details]. The general chemical equation for a rare-earth molybdate $R_2Mo_2O_7$ using the reactants R_2O_3 and MoO_2 is

$$R_2O_3 + 2\,MoO_2 \longrightarrow R_2Mo_2O_7\,. \tag{A.1}$$

All elements have to keep their oxidation states during this reaction. Preparation recipes by J. Frielingsdorf [399] and the detailed growth study on $Sm_2Mo_2O_7$ by S. Singh *et al.* [57]

Figure A.2: Boat with titanium powder. Photograph of a boat with (partially) oxidized titanium powder after heating in a tube furnace with argon gas flow. The arrow indicates the temperature gradient in the furnace.

ID	t_1 (h)	T_1 (°C)	t_2 (h)	T_2 (°C)	t_3 (h)	T_3 (°C)	Atmosphere
R6	25	1450	25	1450	-	-	Ar
R7	12	1350	25	1450	5	1450	Ar
R8	8	1280	-	-	5	1280	Ar
R9	12	1350	12	1450	5	1450	Ar
R10	12	1400	-	-	5	1400	Ar
R11	12	1200	12	1300	5	1350	Ar
R12	12	1200	12	1300	5	1400	Ar

Table A.4: Powder-reaction parameters for molybdates $R_2Mo_2O_7$. Powder-reaction procedures with plateau temperatures T_i and dwell times t_i, where $i = 1, 2$ denote first and second powder reaction and $i = 3$ denotes the sintering of the pressed rod. Typical ramping times of 4 h to 5 h were used for heating and cooling. All powder reactions of $R_2Mo_2O_7$ took place in a tube furnace with argon gas flow and titanium metal powder as oxygen catcher.

were used as starting point. Both studies emphasize the need for a molybdenum excess to compensate evaporation and the importance of an inert atmosphere to stabilize the Mo^{4+} oxidation state and avoid the emergence of Mo^{6+}. Therefore, powder reactions and crystal growth were executed under argon atmosphere. In addition, the powder was pressed to a pellet before heating to minimize the surface area. Furthermore, a boat with titanium metal powder was placed nearby the sample to act as oxygen catcher during the powder reaction. Despite these precautions, it was difficult to avoid an oxidation of the powder. The most striking indicator for the presence of oxygen during the heating process is the titanium powder exhibiting various colors after heating. Figure A.2 shows a photograph of this powder and the temperature gradient of the tube furnace. While the titanium at the cold end is still pristine metallic, the different colors towards the hot end indicate increasing oxidation states up to TiO_2, which is white. Therefore, preliminary powder reactions were skipped in later synthesis attempts (samples JE59 and JE63–JE70).

The single-crystal growth of pyrochlore molybdates turned out to be extremely difficult not only due to the risk of oxygen capture but also because of the strong evaporation of molybdenum. To address this problem, an excess of MoO_2 was weighed in. For the first synthesis attempts, molybdenum-excess values of 1 % (JE31) and 2 % (JE30) were tested,

Sample		PR	Floating-zone furnace parameters								SC
ID	R		M/L	Gas	Sintering		Growth				
					U	v mm/h	U	v mm/h	r rpm	p bar	
JE30	Nd	R6	-	-	-	-	-	-	-	-	-
JE31	Gd	R7	CMI/L5	Ar	-	-	65 V	10	42	7.5	✓
JE32	Sm	R8	CMI/L5	Ar	-	-	(52–80) V	10	27	6	✓
JE33	Gd	R9	CMI/L5	-	-	-	-	-	-	-	-
JE34	Gd	R9	CMI/L5	Ar	-	-	(60–90) V	8	36	7.5	✓
JE36	Nd	-	CMI/L5	-	-	-	-	-	-	-	-
JE38	Nd	R10	CMI/L5	Ar	-	-	45 V	8–15	36	7.5	-
JE59	Nd	-	CMI/L5	Ar	42 V	20	47 V	10	34	3	-
JE63	Nd	-	CSI/L2	FG	50 %	27	80 %	8–20	34	0.5	-
JE64	Nd	-	CSI/L2	FG	-	-	(80–95) %	20	34	0.6	-
JE65	Nd	-	CSI/L2	Ar	45 %	20	49 %	10	34	1.5	-
JE66	Gd	-	CSI/L2	Ar	(50–98) %	20	-	-	-	2	-
(cont. of JE66)			CMI/L5	Ar	-	-	65 V	-	-	3	-
JE67	Gd	-	CMI/L5	Ar	55 V	20	-	-	-	-	-
JE68	Gd	-	CMI/L5	Ar	-	-	(50–90) V	10	38	3.8	-
JE69	Gd	-	CMI/L5	Ar	35 V	20	59 V	10	34	1.5	-
JE70	Sm	-	CMI/L5	Ar	46 V	10	55 V	10	36	3	-
JE78	Dy	R11	CMI/L5	Ar	-	-	(75–93) V	10	38	3	-
JE83	Dy	R12	CMI/L5	Ar	-	-	(80–93) V	10	38	3	-

Table A.5: Synthesis of $R_2Mo_2O_7$: Parameters. All attempts to synthesize $R_2Mo_2O_7$ with identifier, rare-earth element R, powder-reaction procedure PR [see Tab. A.4], floating-zone furnace model M and halogen lamps L [see Tab. 1.2], gas (FG = forming gas with 90 % N_2 + 10 % H_2), lamp voltage U (for CSI in %, for CMI in V) and pulling speed v in mm h^{-1} used for sintering and growth, relative rotation of the rods r in rpm, gas pressure p in bar, and success of single-crystal growth SC [see Tab. 1.8].

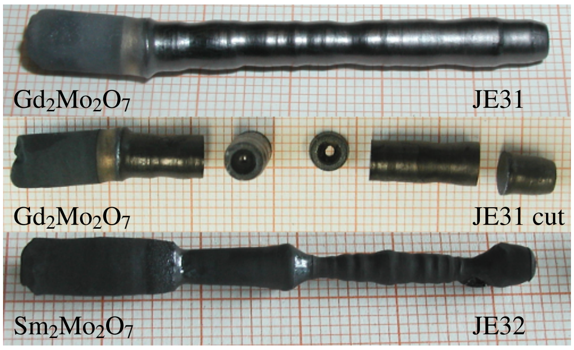

Figure A.3: Growth result for $R_2Mo_2O_7$. Crystals of $Gd_2Mo_2O_7$ appear to be large (top) but the emergence of bubbles during the growth leads to large holes (center). Growths of $Sm_2Mo_2O_7$ suffered from sudden changes of the melting point after few millimeters (bottom). Growth direction from left to right.

respectively, whereas from sample JE32 onwards, a larger excess of 5 % was used; for JE78 even 10 %. In addition, elevated pulling speeds of 8 to 10 mm h^{-1} were used to limit evaporation. Also higher speeds were tested, e.g., for JE38, JE63, and JE64, but without any improvement of the growth. Out of 18 growth attempts, only three were (partly) successful including one growth of $Sm_2Mo_2O_7$ (JE32) and two growths of $Gd_2Mo_2O_7$ (JE31, JE33). Further efforts to improve the crystal quality failed. Attempts to grow $Nd_2Mo_2O_7$ and $Dy_2Mo_2O_7$ failed throughout.

Only very small single crystals of $Gd_2Mo_2O_7$ and $Sm_2Mo_2O_7$ were obtained. Figure A.3 shows two results of partly successful growth attempts of $Gd_2Mo_2O_7$ and $Sm_2Mo_2O_7$. While $Gd_2Mo_2O_7$ appears like a huge single crystal, large holes were found inside after cutting arising from the emergence of bubbles during the growth process. Growths of $Sm_2Mo_2O_7$ stopped frequently after a few millimeters due to a sudden change of the melting point.

A.1.3 $Pr_2Zr_2O_7$

$Pr_2Zr_2O_7$ is a candidate material for quantum spin-ice behavior, where the dominant Ising interaction is between S_z spin components with additional interactions between S_x and S_y components [391]. Due to the very high melting point of $Pr_2Zr_2O_7$, floating-zone growths of this material in literature apply xenon lamps [395, 400]. Within this thesis, a growth of $Pr_2Zr_2O_7$ with halogen lamps was attempted because xenon lamps were not available. Using the reactants Pr_6O_{11} and ZrO_2 [see Tab. A.3 for details], the chemical equation is

$$Pr_6O_{11} + 6\,ZrO_2 \longrightarrow 3\,Pr_2Zr_2O_7 + O_2\uparrow\,. \tag{A.2}$$

Two preliminary powder reactions at 1300 °C and 1350 °C were performed, each for 12 h under air. The pressed rod was sintered for 5 h at 1400 °C. Details of the crystal growth are given in Tab. A.6. The maximum lamp voltage of the floating-zone furnace was needed to melt the powder. Two green, translucent crystals were obtained (samples JE99, JE100) both showing multiple cracks over the entire growth length [see Fig. A.4]. A partial substitution of zirconium by titanium $Pr_2(Zr_{1-x}Ti_x)_2O_7$ was tested via

$$\frac{1}{3}\,Pr_6O_{11} + (2-2x)\,ZrO_2 + 2x\,TiO_2 \longrightarrow Pr_2(Zr_{1-x}Ti_x)_2O_7 + \frac{1}{3}\,O_2\uparrow \tag{A.3}$$

for $x = 0.5$ without success.

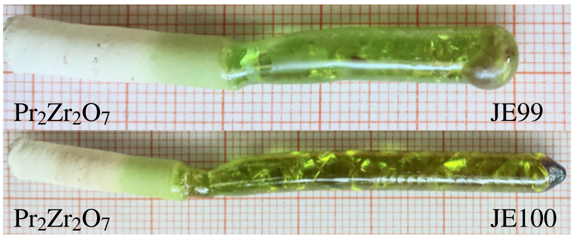

Figure A.4: Growth result for $Pr_2Zr_2O_7$. Crystals of $Pr_2Zr_2O_7$ developed multiple cracks during the floating-zone process.

Sample		Floating-zone furnace parameters								SC
ID	x	M/L	Gas	Sintering		Growth				
				U V	v mm/h	U V	v mm/h	r rpm	p bar	
(JE85, JE86, JE89, JE92, JE94, JE96 had an incorrect chemical equation.)										
JE99	0	CMI/L5	Ar	68	6	101	10	38	1.8	✓
JE100	0	CMI/L5	Ar	85	10	101.9	10	38	1.7	✓
JE101	0	CMI/L5	Ar	70	10	102.3	-	-	1.2	-
JE103	0.5	CMI/L5	Ar	60	10	67	10	34	1.5	-
JE104	0.5	CMI/L5	Ar	61	10	-	-	-	-	-
JE105	0.5	CMI/L5	Ar	60	15	90	10	38	1.5	-
JE106	0.5	CMI/L5	Ar	65	15	90	10	36	1.8	-

Table A.6: Synthesis of $Pr_2Zr_{1-x}Ti_xO_7$: Parameters. All attempts to synthesize $Pr_2(Zr_{1-x}Ti_x)_2O_7$ with identifier, titanium substitution x, floating-zone furnace model M and halogen lamps L [see Tab. 1.2], gas, lamp voltage U in V and pulling speed v in mm h^{-1} used for sintering and growth, relative rotation of the rods r in rpm, gas pressure p in bar, and success of single-crystal growth SC [see Tab. 1.8].

A.2 $Sr_{1-x}Eu_xTiO_3$

Single crystals of $SrTiO_3$ are commercially available even with calcium substitution $Sr_{1-x}Ca_xTiO_3$, whereas $Sr_{1-x}Eu_xTiO_3$ has to be home made. As proof of concept, one crystal of pure $SrTiO_3$ was grown beforehand since the desired mixed crystals of $Sr_{1-x}Eu_xTiO_3$ ($x \leq 5\,\%$) are basically $SrTiO_3$ with dilute europium. One should note that commercial $SrTiO_3$ crystals are synthesized by the Verneuil technique (also called flame-fusion growth) [401–403], whereas the home-made crystals are obtained by the floating-zone method. The feasibility of a $SrTiO_3$ growth via the floating-zone technique has been demonstrated earlier [46, 53, 54, 404].

The chemical equation for $SrTiO_3$ is straightforward when using strontium carbonate and the fully oxidized titanium(IV) oxide as reactants:

$$SrCO_3 + TiO_2 \longrightarrow SrTiO_3 + CO_2\uparrow . \tag{A.4}$$

However, for the mixed systems $Sr_{1-x}Eu_xTiO_3$, again two different titanium oxides are

Name	Formula	Appearance	Purity
Strontium carbonate	$SrCO_3$	white	99.8 %
Europium(III) oxide	Eu_2O_3	white	99.99 %
Yttrium(III) oxide	Y_2O_3	white	99.99 %
Titanium	Ti	metallic	99.99 %
Titanium(II) oxide	TiO	brown	99.5 %
Titanium(III) oxide	Ti_2O_3	dark violet	99.8 %
Titanium(IV) oxide	TiO_2	white	99.99 %

Table A.7: Reactants for $Sr_{1-x}Eu_xTiO_3$ and $YTiO_3$. Polycrystalline powders used as reactants for the synthesis of $Sr_{1-x}Eu_xTiO_3$ and $YTiO_3$. All powders are from ALFA AESAR.

Sample		Floating-zone furnace parameters								SC
ID	x	M/L	Gas	Sintering		Growth				
				U V	v mm/h	U V	v mm/h	r rpm	p bar	
JE112	0	CMI/L5	Ar	-	-	80	10	34	1.7	✓✓
JE113	0	CMI/L5	Ar	-	-	-	-	-	-	-
JE114	0.05	CMI/L5	Ar	70	10	78	10	34	1.6	✓
JE115	0.04	CMI/L5	Ar	65	10	77	5	34	1.7	✓
JE116	0.03	CMI/L5	Ar	60	10	78	5	34	1	✓✓✓
JE117	0.02	CMI/L5	Ar	60	10	78	6	34	2.1	✓✓

Table A.8: Synthesis of $Sr_{1-x}Eu_xTiO_3$: Parameters. All attempts to synthesize $Sr_{1-x}Eu_xTiO_3$ with sample identifier, nominal Eu content x, furnace model M and halogen lamps L [see Tab. 1.2], gas, lamp voltage U in V and pulling speed v in $\mathrm{mm\,h^{-1}}$ used for sintering and growth, relative rotation of the rods r in rpm, gas pressure p in bar, and success of single-crystal growth SC [see Tab. 1.8].

needed when using Eu_2O_3, for the same reason as described in Sec. 1.4.1. Because TiO and TiO_2 were found to be the best working combination of reactants to produce $EuTiO_3$ [see Sec. 1.4.2], the same titanium oxides were used for the mixed system $Sr_{1-x}Eu_xTiO_{3-\delta}$ [for details of the chemical reactants see Tab. A.7]. With these reactants the chemical equation is

$$(1-x)\,\mathrm{SrCO_3} + \frac{x}{2}\,\mathrm{Eu_2O_3} + m\,\mathrm{TiO} + n\,\mathrm{TiO_2} \longrightarrow \mathrm{Sr_{1-\mathit{x}}Eu_\mathit{x}TiO_\mathit{y}} + (1-x)\,\mathrm{CO_2}\uparrow\,, \tag{A.5}$$

with

$$m = \left(\frac{7}{2} - y - \frac{1-x}{2}\right), \qquad n = \left(y - \frac{5}{2} + \frac{1-x}{2}\right). \tag{A.6}$$

Apart from $SrTiO_3$, single crystals of $Sr_{1-x}Eu_xTiO_3$ were grown with europium contents $x = 0.02$, 0.03, 0.04, and 0.05. Details of the growth parameters are given in Tab. A.8.

Figure A.5: Growth result for $Sr_{1-x}Eu_xTiO_3$. Crystals of $Sr_{1-x}Eu_xTiO_3$ with europium contents $x = 0, 0.04, 0.03, 0.02$. Growth direction from left to right.

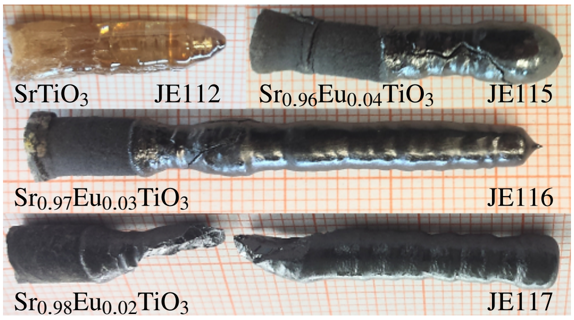

A.3 $YTiO_3$

The perovskite titanate $YTiO_3$ is a typical Mott insulator [92, 93, 405] belonging to the (3+, 3+) perovskites. In contrast to $SrTiO_3$ and $EuTiO_3$, the room-temperature structure of $YTiO_3$ is not cubic but orthorhombic with space group *Pbnm* (No. 62)[1] [406]. While Y^{3+} has the noble-gas configuration [Kr], Ti^{3+} has the configuration $[Ar]3d^1$ leading to a magnetic moment of $1.2\mu_B$ ($S = 1/2$, $L = 2$, $J = 3/2$, $g_J = 4/5$). The magnetic moments order ferromagnetically at a transition temperature of $T_C \approx 30\,K$ [407–409] or 35 K [410] depending on the exact oxygen content.

The chemical aspects of the synthesis of $YTiO_3$ are similar to that of $EuTiO_3$ concerning the choice of reactants [see Sec. 1.4.1]. While yttrium(III) oxide (Y_2O_3) is the only stable oxide of yttrium[2], titanium oxides exist in four different oxidation states ranging from elemental Ti over titanium(II) oxide (TiO), titanium(III) oxide (Ti_2O_3), to titanium(IV) oxide (TiO_2). Because titanium is trivalent in the desired product, one has to prevent the emergence of Ti^{4+} that will result in the pyrochlore phase $Y_2Ti_2O_7$. Using TiO_2 as single titanium reactant produces surplus oxygen via

$$\frac{1}{2}\,Y_2O_3 + TiO_2 \longrightarrow YTiO_3 + \frac{1}{4}\,O_2\uparrow . \tag{A.7}$$

If not counteracted by a reducing atmosphere, the reaction

$$Y_2O_3 + 2\,TiO_2 \longrightarrow Y_2Ti_2O_7 \tag{A.8}$$

will take place instead, as happened for sample JE50. It appears natural to use Ti_2O_3 since it contains already the desired trivalent titanium. The chemical reaction is then

$$\frac{1}{2}\,Y_2O_3 + \frac{1}{2}\,Ti_2O_3 \longrightarrow YTiO_3 . \tag{A.9}$$

This reaction path is used by Kovaleva *et al.* [409], Akimitsu *et al.* [407], and Roth [411]. Due to the risk of oxygen capture that would stabilize the pyrochlore phase, Kovaleva *et al.* and

---

[1] *Pbnm* is the ***cab*** setting of *Pnma*.

[2] See also footnote 3 on page 59.

Reactants	Pwd/SC	Atmosphere	Temperature	Dwell	Ref.
Y_2O_3, Ti_2O_3	powder	vacuum	950 °C, 1050 °C	12 h	[409]
Y_2O_3, Ti_2O_3	SC	50 %Ar/50 %H_2	-	(5–10) mm h^{-1}	[409]
Y_2O_3, Ti_2O_3	SC	Ar	-	6 mm h^{-1}	[411]
Y_2O_3, Ti_2O_3	SC	40 %Ar/60 %H_2	-	-	[407]
Y_2O_3, Ti, TiO_2	powder	vacuum	1500 °C	30 min	[412]
Y_2O_3, Ti, TiO_2	SC	60 %Ar/40 %H_2	-	5 mm h^{-1}	[412]

Table A.9: Preparation of $YTiO_3$ in literature. Single crystals (SC) were grown by the floating-zone method, where the temperature is unknown and pulling speeds are given instead of dwell times.

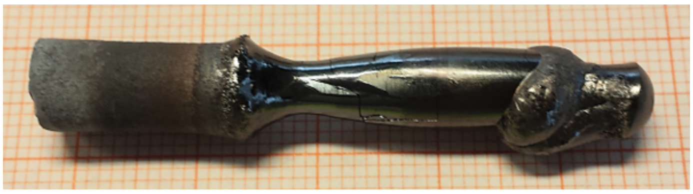

Figure A.6: Growth result for $YTiO_3$. Single crystal of $YTiO_3$ (JE57). Growth direction from left to right.

Akimitsu *et al.* performed the crystal growth in a reducing atmosphere of 50 % Ar/50 % H_2 and 40 % Ar/60 % H_2, respectively, whereas Roth succeeded with pure argon atmosphere. Within the scope of this thesis, path (A.9) is used for samples JE41 and JE46, path (A.7) is tested for samples JE49 and JE50 [see overview in Tab. A.10].

Another way to prevent the emergence of the pyrochlore phase is, to take oxygen capture into account and start with an oxygen-deficient composition $YTiO_{3-\delta}$. This is only possible by combining two different titanium oxides. The implications for the accessible oxygen content $y = 3 - \delta$ have been discussed already in the context of the $EuTiO_3$ growth [see Sec. 1.4.1]. Table 1.4 on page 19 shows an overview of all combinations of titanium oxides and the respective ranges of oxygen content y. Apart from the stoichiometric approaches (A.7) and (A.9), the following combinations have been performed within the scope of this thesis: The reaction path using Ti and TiO_2 implies the chemical equation

$$\frac{1}{2}\,Y_2O_3 + \left(\frac{7}{4} - \frac{y}{2}\right)Ti + \left(\frac{y}{2} - \frac{3}{4}\right)TiO_2 \longrightarrow YTiO_y\,, \tag{A.10}$$

which is used for sample JE51. It is also used by Taguchi *et al.* [412]. Using Ti and Ti_2O_3 leads to

$$\frac{1}{2}\,Y_2O_3 + \left(2 - \frac{2y}{3}\right)Ti + \left(\frac{y}{3} - \frac{1}{2}\right)Ti_2O_3 \longrightarrow YTiO_y\,, \tag{A.11}$$

which is tested for samples JE52 and JE53. With TiO and TiO_2, one obtains the chemical equation

$$\frac{1}{2}\,Y_2O_3 + \left(\frac{7}{2} - y\right)TiO + \left(y - \frac{5}{2}\right)TiO_2 \longrightarrow YTiO_y\,, \tag{A.12}$$

Sample		R	Floating-zone furnace parameters						SC
ID	y		M/L	Gas	Growth				
					U V	v mm/h	r rpm	p bar	
JE41	3	(A.9)	CMI/L5	Ar	55	6	38	1.5	✓
JE46	3	(A.9)	CMI/L5	Ar	55	6	38	2.5	-
JE49	3	(A.7)	-	-	-	-	-	-	-
JE50	3	(A.7)	CMI/L5	Ar	65	10	38	2.5	(✓)
JE51	2.95	(A.10)	CMI/L5	Ar	57	10	38	3	-
JE52	2.95	(A.11)	CMI/L5	Ar	58	10	34	2.8	-
JE53	2.97	(A.11)	CMI/L5	Ar	58	12	34	3.2	-
JE54	2.95	(A.12)	-	-	-	-	-	-	-
JE56	2.95	(A.12)	CMI/L5	Ar	59	12	34	3.2	-
JE57	2.95	(A.13)	CMI/L5	Ar	60	15	34	2.5	✓✓

Table A.10: Synthesis of $YTiO_3$: Parameters. All attempts to synthesize $YTiO_3$ with identifier, nominal oxygen content y, chemical reaction R, floating-zone furnace model M and halogen lamps L [see Tab. 1.2], gas, lamp voltage U in V and pulling speed v in $\mathrm{mm\,h^{-1}}$, relative rotation of the rods r in rpm, gas pressure p in bar, and success of single-crystal growth SC [see Tab. 1.8]. JE50 resulted in the pyrochlore phase $Y_2Ti_2O_7$. Powders of JE49 and JE54 were discarded because they became wet during pressing.

which is used for samples JE54 and JE56. By using TiO and Ti_2O_3, the chemical reaction is running via

$$\frac{1}{2}\,Y_2O_3 + (6 - 2y)\,TiO + \left(y - \frac{5}{2}\right)Ti_2O_3 \longrightarrow YTiO_y\,, \tag{A.13}$$

which resulted in the most successful growth attempt, sample JE57. The resulting crystal is shown in Fig. A.6. Details of the growth parameters of all attempts to grow $YTiO_3$ are given in Tab. A.10. Similar to the procedures in Refs. [407, 411], no preliminary powder reactions or sintering processes were applied. For details of the chemical reactants see Tab. A.7.

A.4 $CoNb_2O_6$

$CoNb_2O_6$ is an effective spin-1/2 system that shows geometric frustration and quantum critical dynamics [413–416]. In this compound, cobalt is divalent having an electron configuration $[Ar]3d^7$, while both Nb^{5+} and O^{2-} have noble-gas configuration. The material crystallizes in the columbite structure, which is orthorhombic having space group *Pbcn* (No. 60) and lattice parameters $a \approx 14.1$ Å, $b \approx 5.7$ Å, $c \approx 5.0$ Å [416]. Both Co^{2+} and Nb^{5+} ions are surrounded by distorted oxygen octahedra. Each of the two octahedra

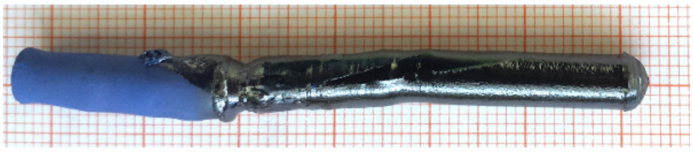

Figure A.7: Growth result for $CoNb_2O_6$. Single crystal of $CoNb_2O_6$ (JE98). Growth direction from left to right.

species CoO_6 and NbO_6 forms chains of edge-sharing octahedra along the *c* direction. Octahedra of different species are corner-sharing. The local environment of the magnetic Co^{2+} ions produces a strong easy-axis anisotropy via the crystal field, which renders the material an Ising model system [415].

The preparation recipe was chosen similar to that used by Prabhakaran *et al.* [417] and J. Frielingsdorf [399]. Using the reactants Co_3O_4 and Nb_2O_5, the chemical equation is

$$2\,Co_3O_4 + 6\,Nb_2O_5 \longrightarrow 6\,CoNb_2O_6 + O_2\uparrow\,. \tag{A.14}$$

Stoichiometric amounts of Co_3O_4 and Nb_2O_5 [see Tab. A.13 for details about the reactants]—15 mg in total—were mixed and pestled as described in Sec. 1.2.2. A corundum crucible was used for the powder reactions. The powder was heated in a muffle furnace and under air, at 1200 °C and 1250 °C, respectively, each for 12 h with ramping times of 4 h. Grinding and milling was applied between both heating procedures as described in Sec. 1.2.2. While the powder appears gray after mixing, it shows the typical cobalt blue [see seed rod in Fig. A.7] already after the first reaction. The pressed rod was placed in a corundum boat and sintered at 1275 °C for 12 h with a ramping time of 5 h. No additional sintering in the floating-zone furnace was undertaken. A single crystal of several centimeters was grown using the CMI furnace with 2000 W lamps at 41 V with a pulling speed of 3 mm h^{-1} and a relative rotation of the rods of 30 rpm. The growth took place in an atmosphere of 80 % O_2 and 20 % Ar at pressures between 1 bar and 2 bar. The single crystal appears black [see Fig. A.7] and shows no pronounced cleavage. The first growth attempt (sample JE98) was already successful and no further attempts were undertaken.

A.5 $LiFe(WO_4)_2$

In 2006, $MnWO_4$ was found to host a ferroelectric polarization coexisting with a spin spiral phase [418, 419] rendering the material a type-II multiferroic [420]. It was the first multiferroic tungstate [421]. $MnWO_4$ is known as mineral hübnerite [422] and is one end member of the wolframite group $(Fe,Mn)WO_4$ [423]. Like all members of this group, it is monoclinic with space group $P2/c$ (No. 13). In that structure, both the Mn^{2+} ions and the W^{6+} ions are surrounded by distorted oxygen octahedra. Each of the two octahedra species—MnO_6 and WO_6—is edge-sharing and forms zig-zag chains along the *c* direction. Octahedra of different species are corner-sharing and alternate along *a* and *b* direction.

A substitution of Mn^{2+} by a combination of a monovalent ion A^+ and a trivalent ion B^{3+} leads to the so-called double-tungstate compound family $AB(WO_4)_2$ [423]. While the distorted, edge-sharing WO_6 octahedra form zig-zag chains along the *c* axis like in

ID	t_1 (h)	T_1 (°C)	t_2 (h)	T_2 (°C)	t_3 (h)	T_3 (°C)	t_4 (h)	T_4 (°C)	Atmos.
R13	24	600	-	-	-	-	24	750	Air
R14	12	600	12	700	12	750	12	760	Air

Table A.11: Powder-reaction parameters for LiFe(WO$_4$)$_2$. Powder-reaction procedures with plateau temperatures T_i and dwell times t_i, where $i = 1, 2, 3$ denote first, second, and third powder reaction, respectively, and $i = 4$ denotes the sintering of the pressed rod. A ramping time of 3 h was used for heating and cooling. All powder reactions of LiFe(WO$_4$)$_2$ took place under static air at ambient pressure in a muffle furnace. Corundum was used as crucible/boat material.

Figure A.8: LiFe(WO$_4$)$_2$ powder. The appearance of LiFe(WO$_4$)$_2$ powder changes after each powder reaction. While the merely mixed starting materials appear dark violet, the powder turns red, orange, and greenish yellow after first, second, and third reaction, respectively (left to right).

MnWO$_4$, the cation ordering of A^+ and B^{3+} depends on the relative ion sizes [424, 425]. For NaFe(WO$_4$)$_2$, distorted, edge-sharing NaO$_6$ and FeO$_6$ octahedra form zig-zag chains along the c axis, while chains of both species alternate in a direction and chains of identical species form planes perpendicular to a. Neighboring chains of NaO$_6$ and FeO$_6$ octahedra are separated by a chain of WO$_6$ octahedra. Octahedra of WO$_6$ are corner-sharing with NaO$_6$ and FeO$_6$ octahedra, respectively [426]. The double-tungstate compound NaFe(WO$_4$)$_2$ has the same crystal symmetry as the wolframite parent structure but it is not multiferroic in contrast to MnWO$_4$ [426].

Crystal structure and physical properties change when replacing Na$^+$ by the smaller Li$^+$. While the chains of WO$_6$ octahedra remain identical to that in NaFe(WO$_4$)$_2$, the other chains of edge-sharing octahedra along the c axis do not consist of a single species anymore. In LiFe(WO$_4$)$_2$, LiO$_6$ and FeO$_6$ octahedra alternate along the c axis and along the b axis [427]. This changes the crystal symmetry to the monoclinic space group $C2/c$ (No. 15) and resembles the crystal structure of the mineral wodginite (MnSnTa$_2$O$_8$) [423]. LiFe(WO$_4$)$_2$ has lattice parameters $a \approx 9.3$ Å, $b \approx 11.4$ Å, $c \approx 4.9$ Å and a monoclinic angle β between 89° and 91° [424, 427–429]. Like MnWO$_4$ but in contrast to NaFe(WO$_4$)$_2$, LiFe(WO$_4$)$_2$ is found to be a type-II multiferroic [429]. It is the second multiferroic tungstate and the first multiferroic double tungstate.

Within the scope of this thesis, a single-crystal growth of LiFe(WO$_4$)$_2$ via the floating-zone technique was attempted. The initial recipe for the powder reaction follows essentially that of Liu *et al.* [429]. However, in that reference, only "oxides and carbonates" are mentioned as starting materials but not the exact compositions. The most natural choice for lithium and iron are Li$_2$CO$_3$ and Fe$_2$O$_3$, where both elements have already the desired oxidation states.

Sample ID	PR	Floating-zone furnace parameters								SC
		M/L	Gas	Sintering		Growth				
				U %	v mm/h	U %	v mm/h	r rpm	p bar	
JE118	R13	CSI/L1	Air	-	-	46	5	40	0	-
JE119	R14	CSI/L1	Air	42	5	45	5	32	0	-
JE123	R14	CSI/L1	O_2	40	10	50	5	36	4.7	-

Table A.12: Synthesis of LiFe(WO_4)$_2$: Parameters. All attempts to synthesize LiFe(WO_4)$_2$ with sample identifier, powder-reaction procedure PR [see Tab. A.11], floating-zone furnace model M and halogen lamps L (CSI furnace with 300 W lamps) [see Tab. 1.2], gas, lamp voltage U in % and pulling speed v in mm h^{-1} used for sintering and growth, relative rotation of the rods r in rpm, gas pressure p in bar, and success of single-crystal growth SC [see Tab. 1.8].

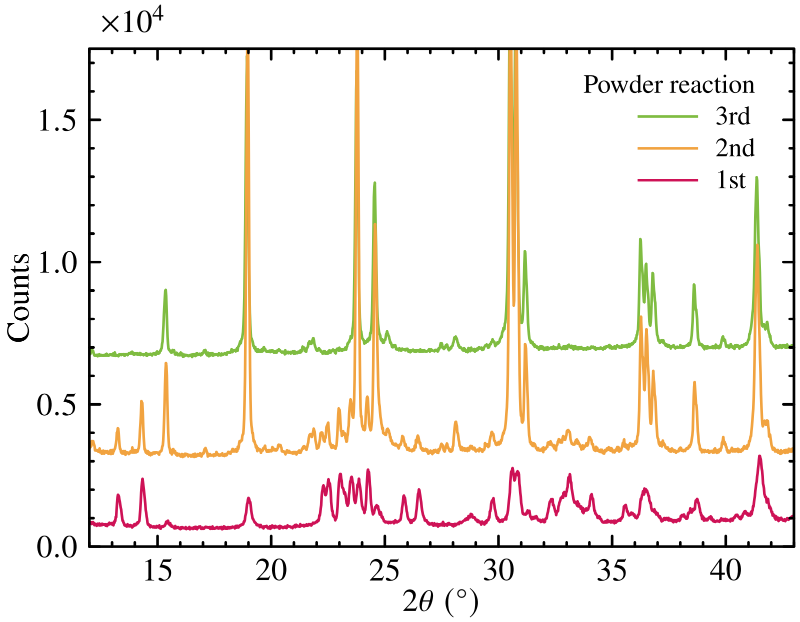

Figure A.9: Powder-pattern comparison of LiFe(WO_4)$_2$. Detail view of x-ray powder diffraction patterns of LiFe(WO_4)$_2$ (sample JE119) after first, second, and third powder reaction as specified in Tab. A.11. Curves are shifted with respect to each other. The corresponding powders are shown in Fig. A.8.

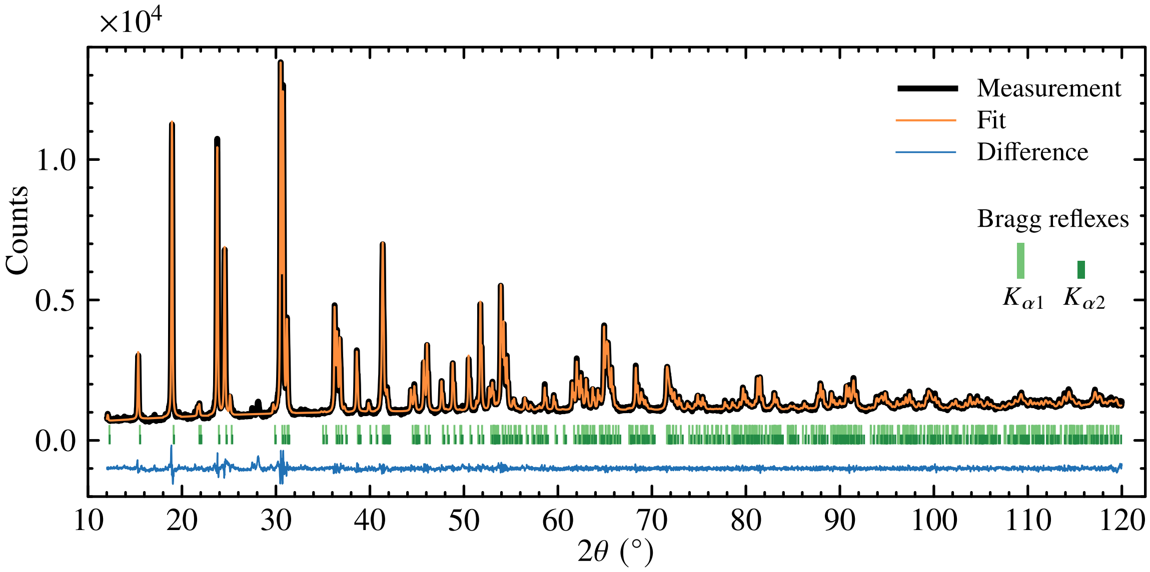

Figure A.10: XRD powder pattern of LiFe(WO$_4$)$_2$ and Le Bail fit. Powder x-ray diffraction pattern of LiFe(WO$_4$)$_2$ (sample JE119 after third reaction) with Le Bail fit. The difference curve is shifted by -0.1×10^4 for clarity. Locations of Bragg reflexes are indicated by bars.

Tungsten is available in form of various substoichiometric oxides, the so-called Magnéli phases [430, 431]. Using the tungsten oxide $WO_{2.9}$ (also written as $W_{20}O_{58}$), the chemical equation is

$$\frac{1}{2}\,Li_2CO_3 + \frac{1}{2}\,Fe_2O_3 + 2\,WO_{2.9} + \frac{1}{10}\,O_2 \longrightarrow LiFe(WO_4)_2 + \frac{1}{2}\,CO_2\uparrow\,, \qquad (A.15)$$

where the presence of oxygen is required to compensate the “oxygen deficiency” of the tungsten oxide [see Tab. A.13 for details about the reactants]. The powder reaction temperatures and dwell times follow closely the recipe of Liu *et al.* [429] with only one powder reaction at 600 °C for 24 h under air and, after pressing the rod, a subsequent sintering at 750 °C for 24 h again under air. Because no literature parameters were available, the growth parameters for the floating-zone procedure had to be figured out from scratch. The first growth attempt (sample JE118) failed totally. There was no chance to establish a stable melting zone, regardless of the choice of parameters. The powder patterns after the first reaction and after the sintering indicated further chemical reactions during the sintering. Therefore, additional powder reaction procedures were undertaken for the following attempts. While the dwell time was reduced from 24 h to 12 h, a second and third reaction was added with target temperatures of 700 °C and 750 °C, respectively [see Tab. A.11]. The sintering temperature was slightly increased to 760 °C. Figure A.8 shows the successive color change of the powder after each reaction indicating progressive changes in the chemical composition. This is in line with the evolution of the acquired powder diffraction data that progressively

Name	Formula	Appearance	Purity
Cobalt(II,III) oxide	Co_3O_4	black	99.9985 %
Niobium(V) oxide	Nb_2O_5	white	99.9985 %
Lithium carbonate	Li_2CO_3	white	99.998 %
Iron(III) oxide	Fe_2O_3	red	99.99 %
Tungsten oxide	$WO_{2.9}$	black	99.99 %
Rubidium chloride	RbCl	white	99 %
Cobalt(II) chloride hexahydrate	$CoCl_2 \cdot 6\,H_2O$	violet	99.9 %

Table A.13: Reactants for $CoNb_2O_6$, $LiFe(WO_4)_2$, and Rb_2CoCl_4. Polycrystalline powders used as reactants for the synthesis of $CoNb_2O_6$, $LiFe(WO_4)_2$, and Rb_2CoCl_4. All powders are from Alfa Aesar.

changes upon further heating procedures of the powder [see Fig. A.9].

Figure A.10 shows the x-ray powder pattern for sample JE119 after the third powder reaction measured with a Bruker D5000matic diffractometer with Bragg–Brentano geometry and Cu x-ray tube (for wavelengths see Ref. [432]). A Le Bail fit [433] was done using the software JANA2006 [85]. The measured data is well described by the fit with the exception of two small peaks around 28°. The resulting lattice parameters are $a = 9.2799(3)$ Å, $b = 11.4068(3)$ Å, $c = 4.8975(3)$ Å, $\beta = 90.606(2)°$ and are close to that determined by Liu *et al.* but do not agree within the specified uncertainty ranges [429].

Hence, the modified powder reaction procedure results in more thoroughly reacted powders and was applied for samples JE119 and JE123. For both samples, an additional sintering in the mirror furnace has been performed to minimize capillary action and maximize the density of the rod as explained in Sec. 1.2.2. Although these powders are thoroughly reacted, both growth procedures were unsuccessful. No further attempts were undertaken. All attempts to grow $LiFe(WO_4)_2$ and the respective furnace parameters are listed in Tab. A.12.

A.6 Rb_2CoCl_4

Cs_2CoCl_4 is an example of a spin-1/2 XXZ chain system [219, 434]. It has the potassium sulfate (K_2SO_4) structure implying the orthorhombic space group *Pnam* (No. 62)[3] [435]. In Cs_2CoCl_4, Co^{2+} ions are tetrahedrally surrounded by Cl^- ions and these $CsCl_4$ tetrahedra are separated by Cs^+ ions. Equally oriented tetrahedra form chains along the b axis. The dominating exchange path between neighboring cobalt ions is parallel to these chains, whereas the interchain coupling is partly frustrated. By replacing the Cs^+ ion by another alkaline metal, e.g., the smaller Rb^+ ion, one may expect changes in the coupling constants.

Based on a growth recipe for Cs_2CoCl_4 by R. Müller [219, 434], single crystals of

---

[3] *Pnam* is the $\boldsymbol{a\bar{c}b}$ setting of *Pnma*.

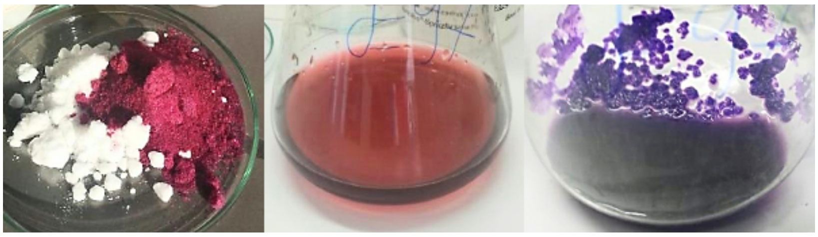

Figure A.11: Growth of Rb_2CoCl_4. Reactants (left), aqueous solution (center), and crystals (right) of Rb_2CoCl_4.

Rb_2CoCl_4 were grown from an aqueous solution of RbCl and $CoCl_2 \cdot 6\,H_2O$ by slow evaporation [see Tab. A.13 for details about the reactants]. The intended chemical reaction is

$$2\,RbCl + CoCl_2 \cdot 6\,H_2O \longrightarrow Rb_2CoCl_4 + 6\,H_2O\,. \tag{A.16}$$

A total amount of 20 g with a RbCl excess of 3 % was used. First crystals were visible after three weeks [see Fig. A.11].

B Sample list

Each synthesis attempt has an individual identifier. Following a widely-used practice (see PhD theses [378, 436–440] and diploma theses [399, 411, 441–448]), the identifier is composed of the initials of the sample preparator and a consecutive number (e.g., JE123). The following table is a complete list of all synthesis attempts undertaken within the scope of this thesis. The samples JE1 to JE26—already grown during the diploma thesis of the author [376]—are listed as well since they are part of the results in Ch. 4. This list is sorted by identifier (i.e., in chronological order) and includes information about the (intended) substance. Details of the growth parameters are given in the respective tables or sections specified in the rightmost column.

ID	Type	Structure	Stoich.	Chem. Formula	Abbrev.	See
JE1	Manganite	K_2NiF_4	214	$Nd_{0.33}Ca_{1.67}MnO_4$	NCMO	Tab. 4.5
JE2	Manganite	K_2NiF_4	214	$Pr_{0.33}Sr_{1.67}MnO_4$	PSMO	Tab. 4.6
JE3	Manganite	K_2NiF_4	214	$Nd_{0.33}Ca_{1.67}MnO_4$	NCMO	Tab. 4.5
JE4	Manganite	K_2NiF_4	214	$Nd_{0.33}Ca_{1.67}MnO_4$	NCMO	Tab. 4.5
JE5	Manganite	K_2NiF_4	214	$Nd_{0.33}Sr_{1.67}MnO_4$	NSMO	Tab. 4.6
JE6	Manganite	K_2NiF_4	214	$Pr_{0.33}Sr_{1.67}MnO_4$	PSMO	Tab. 4.6
JE7	Manganite	K_2NiF_4	214	$Pr_{0.33}Sr_{1.67}MnO_4$	PSMO	Tab. 4.6
JE8	Manganite	K_2NiF_4	214	$Pr_{0.33}Sr_{1.67}MnO_4$	PSMO	Tab. 4.6
JE9	Manganite	K_2NiF_4	214	$Pr_{0.25}Sr_{1.75}MnO_4$	PSMO	Tab. 4.6
JE10	Manganite	K_2NiF_4	214	$Nd_{0.25}Sr_{1.75}MnO_4$	NSMO	Tab. 4.6
JE11	Manganite	K_2NiF_4	214	$Nd_{0.40}Sr_{1.60}MnO_4$	NSMO	Tab. 4.6
JE12	Manganite	K_2NiF_4	214	$Pr_{0.30}Sr_{1.70}MnO_4$	PSMO	Tab. 4.6
JE13	Manganite	K_2NiF_4	214	$Pr_{0.25}Sr_{1.75}MnO_4$	PSMO	Tab. 4.6
JE14	Manganite	K_2NiF_4	214	$Pr_{0.27}Sr_{1.73}MnO_4$	PSMO	Tab. 4.6
JE15	Manganite	K_2NiF_4	214	$Pr_{0.25}Sr_{1.75}MnO_4$	PSMO	Tab. 4.6
JE16	Manganite	K_2NiF_4	214	$Pr_{0.33}Sr_{1.67}MnO_4$	PSMO	Tab. 4.6
JE17	Manganite	K_2NiF_4	214	$Pr_{0.25}Sr_{1.75}MnO_4$	PSMO	Tab. 4.6
JE18	Manganite	K_2NiF_4	214	$Pr_{0.33}Sr_{1.67}MnO_4$	PSMO	Tab. 4.6
JE19	Manganite	K_2NiF_4	214	$Pr_{0.25}Sr_{1.75}MnO_4$	PSMO	Tab. 4.6
JE20	Manganite	K_2NiF_4	214	$Pr_{0.25}Sr_{1.75}MnO_4$	PSMO	Tab. 4.6
JE21	Manganite	K_2NiF_4	214	$Nd_{0.33}Ca_{1.67}MnO_4$	NCMO	Tab. 4.5
JE22	Manganite	K_2NiF_4	214	$Pr_{0.25}Sr_{1.75}MnO_4$	PSMO	Tab. 4.6
JE23	Manganite	K_2NiF_4	214	$Nd_{0.25}Sr_{1.75}MnO_4$	NSMO	Tab. 4.6
JE24	Manganite	K_2NiF_4	214	$Pr_{0.50}Sr_{1.50}MnO_4$	PSMO	Tab. 4.6

Continued on next page...

ID	Type	Structure	Stoich.	Chem. Formula	Abbrev.	See
JE25	Manganite	K_2NiF_4	214	$La_{0.50}Ba_{1.50}MnO_4$	LBMO	Tab. 4.7
JE26	Manganite	K_2NiF_4	214	$Nd_{0.50}Ca_{1.50}MnO_4$	NCMO	Tab. 4.5
JE27	Manganite	K_2NiF_4	214	$La_{1.50}Ba_{0.50}MnO_4$	LBMO	Tab. 4.7
JE28	Manganite	K_2NiF_4	214	$LaBaMnO_4$	LBMO	Tab. 4.7
JE29	Manganite	K_2NiF_4	214	$La_{1.25}Ba_{0.75}MnO_4$	LBMO	Tab. 4.7
JE30	Molybdate	Pyrochlore	227	$Nd_2Mo_2O_7$	NMO	Tab. A.5
JE31	Molybdate	Pyrochlore	227	$Gd_2Mo_2O_7$	GMO	Tab. A.5
JE32	Molybdate	Pyrochlore	227	$Sm_2Mo_2O_7$	SMO	Tab. A.5
JE33	Molybdate	Pyrochlore	227	$Gd_2Mo_2O_7$	GMO	Tab. A.5
JE34	Molybdate	Pyrochlore	227	$Gd_2Mo_2O_7$	GMO	Tab. A.5
JE35	Manganite	K_2NiF_4	214	$Nd_{0.30}Ca_{1.70}MnO_4$	NCMO	Tab. 4.5
JE36	Molybdate	Pyrochlore	227	$Nd_2Mo_2O_7$	NMO	Tab. A.5
JE37	Manganite	K_2NiF_4	214	$Nd_{0.25}Ca_{1.75}MnO_4$	NCMO	Tab. 4.5
JE38	Molybdate	Pyrochlore	227	$Nd_2Mo_2O_7$	NMO	Tab. A.5
JE39	Manganite	K_2NiF_4	214	$Nd_{0.27}Ca_{1.73}MnO_4$	NCMO	Tab. 4.5
JE40	Manganite	K_2NiF_4	214	$Nd_{0.50}Sr_{1.50}MnO_4$	NSMO	Tab. 4.6
JE41	Titanate	Perovskite	113	$YTiO_3$	YTO	Tab. A.10
JE42	Manganite	K_2NiF_4	214	$Nd_{0.40}Sr_{1.60}MnO_4$	NSMO	Tab. 4.6
JE43	Manganite	K_2NiF_4	214	$Nd_{0.30}Sr_{1.70}MnO_4$	NSMO	Tab. 4.6
JE44	Manganite	K_2NiF_4	214	$Nd_{0.25}Sr_{1.75}MnO_4$	NSMO	Tab. 4.6
JE45	Manganite	K_2NiF_4	214	$Nd_{0.30}Sr_{1.70}MnO_4$	NSMO	Tab. 4.6
JE46	Titanate	Perovskite	113	$YTiO_3$	YTO	Tab. A.10
JE47	Manganite	K_2NiF_4	214	$Nd_{0.25}Sr_{1.75}MnO_4$	NSMO	Tab. 4.6
JE48	Manganite	K_2NiF_4	214	$Pr_{0.40}Sr_{1.60}MnO_4$	PSMO	Tab. 4.6
JE49	Titanate	Perovskite	113	$YTiO_3$	YTO	Tab. A.10
JE50	Titanate	Perovskite	113	$YTiO_3$	YTO	Tab. A.10
JE51	Titanate	Perovskite	113	$YTiO_{2.95}$	YTO	Tab. A.10
JE52	Titanate	Perovskite	113	$YTiO_3$	YTO	Tab. A.10
JE53	Titanate	Perovskite	113	$YTiO_3$	YTO	Tab. A.10
JE54	Titanate	Perovskite	113	$YTiO_3$	YTO	Tab. A.10
JE55	Manganite	K_2NiF_4	214	$Pr_{0.60}Sr_{1.40}MnO_4$	PSMO	Tab. 4.6
JE56	Titanate	Perovskite	113	$YTiO_3$	YTO	Tab. A.10
JE57	Titanate	Perovskite	113	$YTiO_3$	YTO	Tab. A.10
JE58	Manganite	K_2NiF_4	214	$Nd_{0.40}Ca_{1.60}MnO_4$	NCMO	Tab. 4.5
JE59	Molybdate	Pyrochlore	227	$Nd_2Mo_2O_7$	NMO	Tab. A.5
JE60	Manganite	K_2NiF_4	214	$Pr_{0.45}Sr_{1.55}MnO_4$	PSMO	Tab. 4.6
JE61	Manganite	K_2NiF_4	214	$Nd_{0.37}Sr_{1.63}MnO_4$	NSMO	Tab. 4.6
JE62	Manganite	K_2NiF_4	214	$Nd_{0.60}Ca_{1.40}MnO_4$	NCMO	Tab. 4.5
JE63	Molybdate	Pyrochlore	227	$Nd_2Mo_2O_7$	NMO	Tab. A.5

Continued on next page...

ID	Type	Structure	Stoich.	Chem. Formula	Abbrev.	See
JE64	Molybdate	Pyrochlore	227	$Nd_2Mo_2O_7$	NMO	Tab. A.5
JE65	Molybdate	Pyrochlore	227	$Nd_2Mo_2O_7$	NMO	Tab. A.5
JE66	Molybdate	Pyrochlore	227	$Gd_2Mo_2O_7$	GMO	Tab. A.5
JE67	Molybdate	Pyrochlore	227	$Gd_2Mo_2O_7$	GMO	Tab. A.5
JE68	Molybdate	Pyrochlore	227	$Gd_2Mo_2O_7$	GMO	Tab. A.5
JE69	Molybdate	Pyrochlore	227	$Gd_2Mo_2O_7$	GMO	Tab. A.5
JE70	Molybdate	Pyrochlore	227	$Sm_2Mo_2O_7$	SMO	Tab. A.5
JE71	Manganite	K_2NiF_4	214	$Sm_{0.50}Ca_{1.50}MnO_4$	SCMO	Tab. 4.5
JE72	Manganite	K_2NiF_4	214	$Sm_{0.33}Ca_{1.67}MnO_4$	SCMO	Tab. 4.5
JE73	Manganite	K_2NiF_4	214	$Sm_{0.25}Ca_{1.75}MnO_4$	SCMO	Tab. 4.5
JE74	Manganite	K_2NiF_4	214	$Sm_{0.40}Ca_{1.60}MnO_4$	SCMO	Tab. 4.5
JE75	Manganite	K_2NiF_4	214	$Tb_{0.50}Ca_{1.50}MnO_4$	TCMO	Tab. 4.5
JE76	Manganite	K_2NiF_4	214	$Tb_{0.33}Ca_{1.67}MnO_4$	TCMO	Tab. 4.5
JE77	Manganite	K_2NiF_4	214	$Tb_{0.25}Ca_{1.75}MnO_4$	TCMO	Tab. 4.5
JE78	Molybdate	Pyrochlore	227	$Dy_2Mo_2O_7$	DMO	Tab. A.5
JE79	Manganite	K_2NiF_4	214	$Tb_{0.40}Ca_{1.60}MnO_4$	TCMO	Tab. 4.5
JE80	Manganite	K_2NiF_4	214	$Pr_{0.30}Sr_{1.70}MnO_4$	PSMO	Tab. 4.6
JE81	Manganite	K_2NiF_4	214	$Er_{0.33}Ca_{1.67}MnO_4$	ECMO	Tab. 4.5
JE82	Manganite	K_2NiF_4	214	$Er_{0.50}Ca_{1.50}MnO_4$	ECMO	Tab. 4.5
JE83	Molybdate	Pyrochlore	227	$Dy_2Mo_2O_7$	DMO	Tab. A.5
JE84	Manganite	K_2NiF_4	214	$Er_{0.50}Ca_{1.50}MnO_4$	ECMO	Tab. 4.5
JE85	Zirconate	Pyrochlore	227	$Pr_2Zr_2O_7$	PZO	Tab. A.6
JE86	Zirconate	Pyrochlore	227	$Pr_2Zr_2O_7$	PZO	Tab. A.6
JE87	Titanate	Perovskite	113	$EuTiO_3$	ETO	Tab. 1.7
JE88	Titanate	Perovskite	113	$EuTiO_3$	ETO	Tab. 1.7
JE89	Zirconate	Pyrochlore	227	$Pr_2Zr_2O_7$	PZO	Tab. A.6
JE90	Titanate	Perovskite	113	$EuTiO_{2.95}$	ETO	Tab. 1.7
JE91	Titanate	Perovskite	113	$EuTiO_3$	ETO	Tab. 1.7
JE92	Zirconate	Pyrochlore	227	$Pr_2Zr_2O_7$	PZO	Tab. A.6
JE93	Titanate	Perovskite	113	$EuTiO_3$	ETO	Tab. 1.7
JE94	Zirconate	Pyrochlore	227	$Pr_2Zr_2O_7$	PZO	Tab. A.6
JE95	Titanate	Perovskite	113	$EuTiO_3$	ETO	Tab. 1.7
JE96	Zirconate	Pyrochlore	227	$Pr_2Zr_2O_7$	PZO	Tab. A.6
JE97	Chloride	K_2SO_4	214	Rb_2CoCl_4	RCC	Sec. A.6
JE98	Niobate	Columbite	126	$CoNb_2O_6$	CNO	Sec. A.4
JE99	Zirconate	Pyrochlore	227	$Pr_2Zr_2O_7$	PZO	Tab. A.6
JE100	Zirconate	Pyrochlore	227	$Pr_2Zr_2O_7$	PZO	Tab. A.6
JE101	Zirconate	Pyrochlore	227	$Pr_2Zr_2O_7$	PZO	Tab. A.6
JE102	Titanate	Perovskite	113	$EuTiO_3$	ETO	Tab. 1.7

Continued on next page...

ID	Type	Structure	Stoich.	Chem. Formula	Abbrev.	See
JE103	Zirconate	Pyrochlore	227	Pr_2TiZrO_7	PTZO	Tab. A.6
JE104	Zirconate	Pyrochlore	227	Pr_2TiZrO_7	PTZO	Tab. A.6
JE105	Zirconate	Pyrochlore	227	Pr_2TiZrO_7	PTZO	Tab. A.6
JE106	Zirconate	Pyrochlore	227	Pr_2TiZrO_7	PTZO	Tab. A.6
JE107	Titanate	Perovskite	113	$EuTiO_{2.95}$	ETO	Tab. 1.7
JE108	Titanate	Perovskite	113	$EuTiO_3$	ETO	Tab. 1.7
JE109	Titanate	Perovskite	113	$EuTiO_3$	ETO	Tab. 1.7
JE110	Titanate	Perovskite	113	$EuTiO_{2.99}$	ETO	Tab. 1.7
JE111	Titanate	Perovskite	113	$EuTiO_{2.98}$	ETO	Tab. 1.7
JE112	Titanate	Perovskite	113	$SrTiO_3$	STO	Tab. A.8
JE113	Titanate	Perovskite	113	$SrTiO_3$	STO	Tab. A.8
JE114	Titanate	Perovskite	113	$Sr_{0.95}Eu_{0.05}TiO_3$	SETO	Tab. A.8
JE115	Titanate	Perovskite	113	$Sr_{0.96}Eu_{0.04}TiO_3$	SETO	Tab. A.8
JE116	Titanate	Perovskite	113	$Sr_{0.97}Eu_{0.03}TiO_3$	SETO	Tab. A.8
JE117	Titanate	Perovskite	113	$Sr_{0.98}Eu_{0.02}TiO_3$	SETO	Tab. A.8
JE118	Tungstate	Wodginite	1128	$LiFe(WO_4)_2$	LFWO	Sec. A.5
JE119	Tungstate	Wodginite	1128	$LiFe(WO_4)_2$	LFWO	Sec. A.5
JE120	Titanate	Perovskite	113	$Eu_{0.999}La_{0.001}TiO_{2.97}$	ELTO	Tab. 1.11
JE121	Titanate	Perovskite	113	$Eu_{0.999}La_{0.001}TiO_{2.97}$	ELTO	Tab. 1.11
JE122	Titanate	Perovskite	113	$Eu_{0.999}La_{0.001}TiO_{2.96}$	ELTO	Tab. 1.11
JE123	Tungstate	Wodginite	1128	$LiFe(WO_4)_2$	LFWO	Sec. A.5
JE124	Titanate	Perovskite	113	$Eu_{0.99}La_{0.01}TiO_{2.96}$	ELTO	Tab. 1.11
JE125	Titanate	Perovskite	113	$Eu_{0.95}La_{0.05}TiO_{2.98}$	ELTO	Tab. 1.11
JE126	Titanate	Perovskite	113	$EuTi_{0.99}Nb_{0.01}O_{2.98}$	ETNO	Tab. 1.11
JE127	Titanate	Perovskite	113	$EuTi_{0.95}Nb_{0.05}O_{2.99}$	ETNO	Tab. 1.11
JE128	Titanate	Perovskite	113	$EuTi_{0.97}Nb_{0.03}O_{2.99}$	ETNO	Tab. 1.11
JE129	Titanate	Perovskite	113	$EuTi_{0.98}Nb_{0.02}O_3$	ETNO	Tab. 1.11

Table B.1: Complete sample list

C Symmetry conditions

	Crystal system	Crystal class	Space groups (No.)	Centro-symmetric	Piezo-electric	Pyro-electric
#	7	32	230	11	20	10
	Triclinic	1	1	-	✓	✓
		$\bar{1}$	2	✓	-	-
	Monoclinic	2	3–5	-	✓	✓
		m	6–9	-	✓	✓
		$2/m$	10–15	✓	-	-
	Orthorhombic	222	16–24	-	✓	-
		$mm2$	25–46	-	✓	✓
		mmm	47–74	✓	-	-
	Tetragonal	4	75–80	-	✓	✓
		$\bar{4}$	81–82	-	✓	-
		$4/m$	83–88	✓	-	-
		422	89–98	-	✓	-
		$4mm$	99–110	-	✓	✓
		$\bar{4}2m$	111–122	-	✓	-
		$4/mmm$	123–142	✓	-	-
	Trigonal	3	143–146	-	✓	✓
		$\bar{3}$	147–148	✓	-	-
		32	149–155	-	✓	-
		$3m$	156–161	-	✓	✓
		$\bar{3}m$	162–167	✓	-	-
	Hexagonal	6	168–173	-	✓	✓
		$\bar{6}$	174	-	✓	-
		$6/m$	175–176	✓	-	-
		622	177–182	-	✓	-
		$6mm$	183–186	-	✓	✓
		$\bar{6}2m$	187–190	-	✓	-
		$6/mmm$	191–194	✓	-	-
	Cubic	23	195–199	-	✓	-
		$m\bar{3}$	200–206	✓	-	-
		432	207–214	-	-	-
		$\bar{4}3m$	215–220	-	✓	-
		$m\bar{3}m$	221–230	✓	-	-

Table C.1: Restrictions of physical properties by symmetry. All 32 crystal classes with indicators (✓) for the existence of an inversion center and the occurrence of piezo- and pyroelectricity. Compiled from information given in [84, pp. 794, 805], inspired by [449, Appendix A].

List of Figures

List of Tables

Bibliography

[1] H. S. Wang, C. H. Lineweaver, and T. R. Ireland, “The elemental abundances (with uncertainties) of the most Earth-like planet”, Icarus **299**, 460–474 (2018).

[2] C. Allègre, G. Manhès, and É. Lewin, “Chemical composition of the Earth and the volatility control on planetary genetics”, Earth Planet. Sci. Lett. **185**, 49–69 (2001).

[3] J. W. Morgan and E. Anders, “Chemical composition of Earth, Venus, and Mercury”, Proc. Natl. Acad. Sci. USA **77**, 6973–6977 (1980).

[4] G. J. Taylor, “The bulk composition of Mars”, Chem. Erde **73**, 401–420 (2013).

[5] A. Khan, C. Liebske, A. Rozel, A. Rivoldini, F. Nimmo, J. A. D. Connolly, A.-C. Plesa, and D. Giardini, “A geophysical perspective on the bulk composition of Mars”, J. Geophys. Res. Planets **123**, 575–611 (2018).

[6] R. G. Prinn and B. Fegley, “The atmospheres of Venus, Earth, and Mars: a critical comparison”, Annu. Rev. Earth Planet. Sci. **15**, 171–212 (1987).

[7] L. Pauling, “The nature of the chemical bond. IV. The energy of single bonds and the relative electronegativity of atoms”, J. Am. Chem. Soc. **54**, 3570–3582 (1932).

[8] V. G. Krivovichev and M. V. Charykova, “Number of minerals of various chemical elements: statistics 2012 (a new approach to an old problem)”, Geol. Ore Deposits **56**, 553–559 (2014).

[9] O. Tschauner, C. Ma, J. R. Beckett, C. Prescher, V. B. Prakapenka, and G. R. Rossman, “Discovery of bridgmanite, the most abundant mineral in Earth, in a shocked meteorite”, Science **346**, 1100–1102 (2014).

[10] A. S. Bhalla, R. Guo, and R. Roy, “The perovskite structure – a review of its role in ceramic science and technology”, Mater. Res. Innovations **4**, 3–26 (2000).

[11] J. G. Bednorz and K. A. Müller, “Possible high T_c superconductivity in the Ba–La–Cu–O system”, Z. Phys. B **64**, 189–193 (1986).

[12] J. G. Bednorz, K. A. Müller, and M. Takashige, “Superconductivity in alkaline earth-substituted La_2CuO_{4-y}”, Science **236**, 73–75 (1987).

[13] R. von Helmolt, J. Wecker, B. Holzapfel, L. Schultz, and K. Samwer, “Giant negative magnetoresistance in perovskitelike $La_{2/3}Ba_{1/3}MnO_x$ ferromagnetic films”, Phys. Rev. Lett. **71**, 2331–2333 (1993).

[14] A. von Hippel, “Ferroelectricity, domain structure, and phase transitions of barium titanate”, Rev. Mod. Phys. **22**, 221–237 (1950).

[15] S. H. Wemple, M. Didomenico, and I. Camlibel, “Dielectric and optical properties of melt-grown $BaTiO_3$”, J. Phys. Chem. Solids **29**, 1797–1803 (1968).

[16] V. G. Bhide, K. G. Deshmukh, and M. S. Hegde, “Ferroelectric properties of $PbTiO_3$”, Physica **28**, 871–876 (1962).

[17] P.-H. Sun, T. Nakamura, Y. J. Shan, Y. Inaguma, and M. Itoh, “The study on the dielectric property and structure of perovskite titanate $CdTiO_3$”, Ferroelectrics **217**, 137–145 (1998).

[18] B. J. Kennedy, Q. Zhou, and M. Avdeev, “The ferroelectric phase of $CdTiO_3$: a powder neutron diffraction study”, J. Solid State Chem. **184**, 2987–2993 (2011).

[19] V. V. Lemanov, A. V. Sotnikov, E. P. Smirnova, M. Weihnacht, and R. Kunze, “Perovskite $CaTiO_3$ as an incipient ferroelectric”, Solid State Commun. **110**, 611–614 (1999).

[20] K. A. Müller and H. Burkard, “$SrTiO_3$: an intrinsic quantum paraelectric below 4 K”, Phys. Rev. B **19**, 3593–3602 (1979).

[21] T. Katsufuji and H. Takagi, “Coupling between magnetism and dielectric properties in quantum paraelectric $EuTiO_3$”, Phys. Rev. B **64**, 054415 (2001).

[22] S. H. Wemple, “Some transport properties of oxygen-deficient single-crystal potassium tantalate ($KTaO_3$)”, Phys. Rev. **137**, A1575–A1582 (1965).

[23] Y. I. Vorob’yev, A. A. Konev, Y. V. Malyshonok, G. F. Afonina, and A. N. Sapozhnikov, “Tausonite, $SrTiO_3$, a new mineral of the perovskite group”, Int. Geol. Rev. **26**, 462–465 (1984).

[24] C. Ma and G. R. Rossman, “Barioperovskite, $BaTiO_3$, a new mineral from the Benitoite mine, California”, Am. Mineral. **93**, 154–157 (2008).

[25] M. Imada, A. Fujimori, and Y. Tokura, “Metal–insulator transitions”, Rev. Mod. Phys. **70**, 1039–1263 (1998).

[26] J. G. Bednorz and K. A. Müller, “$Sr_{1-x}Ca_xTiO_3$: an XY quantum ferroelectric with transition to randomness”, Phys. Rev. Lett. **52**, 2289–2292 (1984).

[27] H. P. R. Frederikse, W. R. Thurber, and W. R. Hosler, “Electronic transport in strontium titanate”, Phys. Rev. **134**, A442–A445 (1964).

[28] X. Lin, G. Bridoux, A. Gourgout, G. Seyfarth, S. Krämer, M. Nardone, B. Fauqué, and K. Behnia, “Critical doping for the onset of a two-band superconducting ground state in $SrTiO_{3-\delta}$”, Phys. Rev. Lett. **112**, 207002 (2014).

[29] B. S. de Lima, M. S. da Luz, F. S. Oliveira, L. M. S. Alves, C. A. M. dos Santos, F. Jomard, Y. Sidis, P. Bourges, S. Harms, C. P. Grams, J. Hemberger, X. Lin, B. Fauqué, and K. Behnia, “Interplay between antiferrodistortive, ferroelectric, and superconducting instabilities in $Sr_{1-x}Ca_xTiO_{3-\delta}$”, Phys. Rev. B **91**, 045108 (2015).

[30] C. W. Rischau, X. Lin, C. P. Grams, D. Finck, S. Harms, J. Engelmayer, T. Lorenz, Y. Gallais, B. Fauqué, J. Hemberger, and K. Behnia, "A ferroelectric quantum phase transition inside the superconducting dome of $Sr_{1-x}Ca_xTiO_{3-\delta}$", Nat. Phys. **13**, 643–648 (2017).

[31] X. Lin, B. Fauqué, and K. Behnia, "Scalable T^2 resistivity in a small single-component Fermi surface", Science **349**, 945–948 (2015).

[32] J. M. Tranquada, B. J. Sternlieb, J. D. Axe, Y. Nakamura, and S. Uchida, "Evidence for stripe correlations of spins and holes in copper oxide superconductors", Nature **375**, 561–563 (1995).

[33] J. M. Tranquada, D. J. Buttrey, and V. Sachan, "Incommensurate stripe order in $La_{2-x}Sr_xNiO_4$ with $x = 0.225$", Phys. Rev. B **54**, 12318–12323 (1996).

[34] H. Ulbrich and M. Braden, "Neutron scattering studies on stripe phases in non-cuprate materials", Physica C **481**, 31–45 (2012).

[35] H. Ulbrich, P. Steffens, D. Lamago, Y. Sidis, and M. Braden, "Hourglass dispersion in overdoped single-layered manganites", Phys. Rev. Lett. **108**, 247209 (2012).

[36] D. Senff, O. Schumann, M. Benomar, M. Kriener, T. Lorenz, Y. Sidis, K. Habicht, P. Link, and M. Braden, "Melting of magnetic correlations in charge–orbital ordered $La_{1/2}Sr_{3/2}MnO_4$: competition of ferromagnetic and antiferromagnetic states", Phys. Rev. B **77**, 184413 (2008).

[37] H. Ulbrich, D. Senff, P. Steffens, O. J. Schumann, Y. Sidis, P. Reutler, A. Revcolevschi, and M. Braden, "Evidence for charge orbital and spin stripe order in an overdoped manganite", Phys. Rev. Lett. **106**, 157201 (2011).

[38] S. Jodlauk, P. Becker, J. A. Mydosh, D. I. Khomskii, T. Lorenz, S. V. Streltsov, D. C. Hezel, and L. Bohatý, "Pyroxenes: a new class of multiferroics", J. Phys.: Condens. Matter **19**, 432201 (2007).

[39] G. Rose, "Beschreibung einiger neuen Mineralien des Urals", Ann. Phys. (Leipzig) **124**, 551–573 (1839).

[40] G. Rose, "Ueber einige neue Mineralien des Urals", J. prakt. Chem. **19**, 459–468 (1840).

[41] É. G. Gravina, J. D. Ayala, and N. G. Fernandes, "Natural perovskite: $(Ca^{II}_{0.95(1)}Ce^{III}_{0.011(2)}Na^{I}_{0.010(4)})(Fe^{III}_{0.022(2)}Ti^{IV}_{0.98(1)})O_3$", Acta Crystallogr., Sect. E: Struct. Rep. Online **64**, i65–i65 (2008).

[42] D. Radusinović and C. Markov, "Macedonite-lead titanate: a new mineral", Am. Mineral. **56**, 387–394 (1971).

[43] R. H. Mitchell, M. D. Welch, and A. R. Chakhmouradian, "Nomenclature of the perovskite supergroup: a hierarchical system of classification based on crystal structure and composition", Mineral. Mag. **81**, 411–461 (2017).

[44] G. Dhanaraj, K. Byrappa, V. Prasad, and M. Dudley, eds., *Springer handbook of crystal growth* (Springer, Berlin, Heidelberg, 2010).

[45] P. Rudolph, ed., *Handbook of crystal growth Vol. II: Bulk crystal growth*, 2nd ed. (Elsevier, Boston, 2015).

[46] A. M. Balbashov and S. K. Egorov, “Apparatus for growth of single crystals of oxide compounds by floating zone melting with radiation heating”, J. Cryst. Growth **52**, 498–504 (1981).

[47] A. Possolo, A. M. H. van der Veen, J. Meija, and D. B. Hibbert, “Interpreting and propagating the uncertainty of the standard atomic weights (IUPAC technical report)”, Pure Appl. Chem. **90**, 395–424 (2018).

[48] J. Meija, T. B. Coplen, M. Berglund, W. A. Brand, P. D. Bièvre, M. Gröning, N. E. Holden, J. Irrgeher, R. D. Loss, T. Walczyk, and T. Prohaska, “Atomic weights of the elements 2013 (IUPAC technical report)”, Pure Appl. Chem. **88**, 265–291 (2016).

[49] Sartorius AG, *Operating Instructions – Sartorius Extend Series* (2005).

[50] S. Romm, “The person behind the name: Charles Bingham Penrose”, Plast. Reconstr. Surg. **70**, 397–399 (1982).

[51] J. V. Alemán, A. V. Chadwick, J. He, M. Hess, K. Horie, R. G. Jones, P. Kratochvíl, I. Meisel, I. Mita, G. Moad, S. Penczek, and R. F. T. Stepto, “Definitions of terms relating to the structure and processing of sols, gels, networks, and inorganic–organic hybrid materials (IUPAC recommendations 2007)”, Pure Appl. Chem. **79**, 1801–1829 (2007).

[52] T. Akashi, K. Matumi, T. Okada, and T. Mizutani, “Preparation of ferrite single crystals by new floating zone technique”, IEEE Trans. Magn. **5**, 285–289 (1969).

[53] J. G. Bednorz and H. Arend, “A 1 kW mirror furnace for growth of refractory oxide single crystals by a floating-zone technique”, J. Cryst. Growth **67**, 660–662 (1984).

[54] P. I. Nabokin, D. Souptel, and A. M. Balbashov, “Floating zone growth of high-quality $SrTiO_3$ single crystals”, J. Cryst. Growth **250**, 397–404 (2003).

[55] OMEGA Engineering GmbH, *Thermoelectric alloy property data*, Data sheet.

[56] S. Hara, Y. Yoshida, S.-I. Ikeda, N. Shirakawa, M. K. Crawford, K. Takase, Y. Takano, and K. Sekizawa, “Crystal growth of germanium-based oxide spinels by the float zone method”, J. Cryst. Growth **283**, 185–192 (2005).

[57] S. Singh, R. Suryanarayanan, R. S. Martin, G. Dhalenne, and A. Revcolevschi, “Single-crystal growth and magnetic properties of the metallic molybdate pyrochlore $Sm_2Mo_2O_7$”, J. Cryst. Growth **308**, 237–240 (2007).

[58] Crystal Systems Inc., *Optical Floating Zone System FZ-10000-H-VI-VP Instruction Manual* (1999).

[59] Canon Machinery Inc., *SC1-MDH11020-CE IR Image Furnace Instruction Manual* (2012).

[60] D. Rivas and R. Haya, "Analysis of secondary radiation (multiple reflections) in monoellipsoidal mirror furnaces", J. Cryst. Growth **241**, 249–260 (2002).

[61] J. Brous, I. Fankuchen, and E. Banks, "Rare earth titanates with a perovskite structure", Acta Crystallogr. **6**, 67–70 (1953).

[62] H. Holzapfel and J. Sieler, "Zur Darstellung und Struktur der Seltenen Erd-Titanate und des Europium(II)-zirkonats", Z. anorg. allg. Chem. **343**, 174–180 (1966).

[63] V. Scagnoli, M. Allieta, H. Walker, M. Scavini, T. Katsufuji, L. Sagarna, O. Zaharko, and C. Mazzoli, "$EuTiO_3$ magnetic structure studied by neutron powder diffraction and resonant x-ray scattering", Phys. Rev. B **86**, 094432 (2012).

[64] B. J. Kennedy, G. Murphy, E. Reynolds, M. Avdeev, H. E. R. Brand, and T. Kolodiazhnyi, "Studies of the antiferrodistortive transition in $EuTiO_3$", J. Phys.: Condens. Matter **26**, 495901 (2014).

[65] T. R. McGuire, B. E. Argyle, M. W. Shafer, and J. S. Smart, "Magnetic properties of some divalent europium compounds", J. Appl. Phys. **34**, 1345–1346 (1963).

[66] A. Bussmann-Holder, J. Köhler, R. K. Kremer, and J. M. Law, "Relation between structural instabilities in $EuTiO_3$ and $SrTiO_3$", Phys. Rev. B **83**, 212102 (2011).

[67] J. Köhler, R. Dinnebier, and A. Bussmann-Holder, "Structural instability of $EuTiO_3$ from x-ray powder diffraction", Phase Transit. **85**, 949–955 (2012).

[68] J. Schiemer, L. J. Spalek, S. S. Saxena, C. Panagopoulos, T. Katsufuji, A. Bussmann-Holder, J. Köhler, and M. A. Carpenter, "Magnetic field and in situ stress dependence of elastic behavior in $EuTiO_3$ from resonant ultrasound spectroscopy", Phys. Rev. B **93**, 054108 (2016).

[69] S. Kamba, D. Nuzhnyy, P. Vaněk, M. Savinov, K. Knížek, Z. Shen, E. Šantavá, K. Maca, M. Sadowski, and J. Petzelt, "Magnetodielectric effect and optic soft mode behaviour in quantum paraelectric $EuTiO_3$ ceramics", Europhys. Lett. **80**, 27002 (2007).

[70] T. Katsufuji and Y. Tokura, "Transport and magnetic properties of a ferromagnetic metal: $Eu_{1-x}R_xTiO_3$", Phys. Rev. B **60**, R15021–R15023 (1999).

[71] M. Allieta, M. Scavini, L. J. Spalek, V. Scagnoli, H. C. Walker, C. Panagopoulos, S. S. Saxena, T. Katsufuji, and C. Mazzoli, "Role of intrinsic disorder in the structural phase transition of magnetoelectric $EuTiO_3$", Phys. Rev. B **85**, 184107 (2012).

[72] A. P. Petrovic, Y. Kato, S. S. Sunku, T. Ito, P. Sengupta, L. Spalek, M. Shimuta, T. Katsufuji, C. D. Batista, S. S. Saxena, and C. Panagopoulos, "Electric field modulation of the tetragonal domain orientation revealed in the magnetic ground state of quantum paraelectric $EuTiO_3$", Phys. Rev. B **87**, 064103 (2013).

[73] L. J. Spalek, S. S. Saxena, C. Panagopoulos, T. Katsufuji, J. A. Schiemer, and M. A. Carpenter, “Elastic and anelastic relaxations associated with phase transitions in $EuTiO_3$”, Phys. Rev. B **90**, 054119 (2014).

[74] P. G. Wahlbeck and P. W. Gilles, “Reinvestigation of the phase diagram for the system titanium–oxygen”, J. Am. Ceram. Soc. **49**, 180–183 (1966).

[75] G. J. McCarthy, W. B. White, and R. Roy, “The system Eu–Ti–O: phase relations in a portion of the 1400 °C isotherm”, J. Inorg. Nucl. Chem. **31**, 329–339 (1969).

[76] R. Roy and W. B. White, “Growth of titanium oxide crystals of controlled stoichiometry and order”, J. Cryst. Growth **13-14**, 78–83 (1972).

[77] J. L. Murray and H. A. Wriedt, “The O–Ti (Oxygen–Titanium) system”, J. Phase Equilib. **8**, 148–165 (1987).

[78] G. Eriksson and A. D. Pelton, “Critical evaluation and optimization of the thermodynamic properties and phase diagrams of the MnO–TiO_2, MgO–TiO_2, FeO–TiO_2, Ti_2O_3–TiO_2, Na_2O–TiO_2, and K_2O–TiO_2 systems”, Metall. Trans. B **24**, 795–805 (1993).

[79] H. Bärnighausen, “Untersuchungen am system EuO–Eu_2O_3”, J. prakt. Chem. **34**, 1–14 (1966).

[80] N. L. Henderson, X. Ke, P. Schiffer, and R. E. Schaak, “Solution precursor synthesis and magnetic properties of $Eu_{1-x}Ca_xTiO_3$”, J. Solid State Chem. **183**, 631–635 (2010).

[81] L. Li, H. Zhou, J. Yan, D. Mandrus, and V. Keppens, “Research update: magnetic phase diagram of $EuTi_{1-x}B_xO_3$ (B = Zr, Nb)”, APL Mater. **2**, 110701 (2014).

[82] A. Bussmann-Holder and J. Köhler, “Revisiting the fascinating properties of $EuTiO_3$ and its mixed crystals with $SrTiO_3$: possible candidates for novel functionalities”, J. Phys. Chem. Solids **84**, 2–12 (2015).

[83] H. Akamatsu, Y. Kumagai, F. Oba, K. Fujita, H. Murakami, K. Tanaka, and I. Tanaka, “Antiferromagnetic superexchange via 3d states of titanium in $EuTiO_3$ as seen from hybrid Hartree–Fock density functional calculations”, Phys. Rev. B **83**, 214421 (2011).

[84] T. Hahn, ed., *International Tables for Crystallography, Volume A, Space-group symmetry*, 5th edition, corrected reprint (International Union of Crystallography, 2005).

[85] V. Petříček, M. Dušek, and L. Palatinus, “Crystallographic computing system JANA2006: general features”, Z. Kristallogr. **229**, 345–352 (2014).

[86] M. W. Shafer, “Preparation and crystal chemistry of divalent europium compounds”, J. Appl. Phys. **36**, 1145–1152 (1965).

[87] Y. Tomioka, T. Ito, and A. Sawa, "Magnetotransport properties of $Eu_{1-x}La_xTiO_3$ ($0 \leq x \leq 0.07$) single crystals", J. Phys. Soc. Jpn. **87**, 094716 (2018).

[88] L. Li, J. R. Morris, M. R. Koehler, Z. Dun, H. Zhou, J. Yan, D. Mandrus, and V. Keppens, "Structural and magnetic phase transitions in $EuTi_{1-x}Nb_xO_3$", Phys. Rev. B **92**, 024109 (2015).

[89] A. Spinelli, M. A. Torija, C. Liu, C. Jan, and C. Leighton, "Electronic transport in doped $SrTiO_3$: conduction mechanisms and potential applications", Phys. Rev. B **81**, 155110 (2010).

[90] J. Engelmayer, X. Lin, F. Koç, C. P. Grams, J. Hemberger, K. Behnia, and T. Lorenz, "Ferroelectric order versus metallicity in $Sr_{1-x}Ca_xTiO_{3-\delta}$ ($x = 0.009$)", Phys. Rev. B **100**, 195121 (2019).

[91] Y. Okada, T. Arima, Y. Tokura, C. Murayama, and N. Môri, "Doping- and pressure-induced change of electrical and magnetic properties in the Mott–Hubbard insulator $LaTiO_3$", Phys. Rev. B **48**, 9677–9683 (1993).

[92] Y. Tokura, Y. Taguchi, Y. Moritomo, K. Kumagai, T. Suzuki, and Y. Iye, "Barely metallic states with enhanced carrier mass in $Y_{1-x}Ca_xTiO_3$", Phys. Rev. B **48**, 14063–14066 (1993).

[93] T. Katsufuji, Y. Taguchi, and Y. Tokura, "Transport and magnetic properties of a Mott–Hubbard system whose bandwidth and band filling are both controllable: $R_{1-x}Ca_xTiO_{3+y/2}$", Phys. Rev. B **56**, 10145–10153 (1997).

[94] T. Nakamura, P.-H. Sun, Y. J. Shan, Y. Inaguma, M. Itoh, I.-S. Kim, J.-H. Sohn, M. Ikeda, T. Kitamura, and H. Konagaya, "On the perovskite-related materials of high dielectric permittivity with small temperature dependence and low dielectric loss", Ferroelectrics **196**, 205–209 (1997).

[95] I.-S. Kim, M. Itoh, and T. Nakamura, "Electrical conductivity and metal–nonmetal transition in the perovskite-related layered system $Ca_{n+1}Ti_nO_{3n+1-\delta}$ ($n = 2, 3, \infty$)", J. Solid State Chem. **101**, 77–86 (1992).

[96] G. A. Samara and P. S. Peercy, "Pressure and temperature dependence of the static dielectric constants and raman spectra of TiO_2 (rutile)", Phys. Rev. B **7**, 1131–1148 (1973).

[97] W. Schmidt, "Bestimmung der Dielektricitätsconstanten von Krystallen mit elektrischen Wellen", Ann. Phys. **314**, 919–937 (1902).

[98] W. Schmidt, "Bestimmung der Dielekrizitätskonstanten von Kristallen mit elektrischen Wellen", Ann. Phys. **316**, 114–126 (1903).

[99] A. Eucken and A. Büchner, "Die Dielektrizitätskonstante schwach polarer Kristalle und ihre Temperaturabhängigkeit", Z. Phys. Chem. **27B**, 321–349 (1934).

[100] B. Wul, "Dielectric constants of some titanates", Nature **156**, 480–480 (1945).

[101] E. Wainer, “High titania dielectrics”, Trans. Electrochem. Soc. **89**, 331–356 (1946).

[102] A. von Hippel, R. G. Breckenridge, F. G. Chesley, and L. Tisza, “High dielectric constant ceramics”, Industr. Engng. Chem. **38**, 1097–1109 (1946).

[103] J. Valasek, “Piezoelectric and allied phenomena in Rochelle salt, Minutes of the Washington Meeting, April 23 and 24, 1920”, in Proceedings of the American Physical Society, Vol. XV. 6 (Apr. 1920), pp. 537–538.

[104] J. Valasek, “Piezo-electric and allied phenomena in Rochelle salt”, Phys. Rev. **17**, 475–481 (1921).

[105] H. Mueller, “Properties of Rochelle salt”, Phys. Rev. **47**, 175–191 (1935).

[106] G. Busch and P. Scherrer, “Eine neue seignette-elektrische Substanz”, Naturwissenschaften **23**, 737–737 (1935).

[107] G. Busch, “Early history of ferroelectricity”, Ferroelectrics **74**, 267–284 (1987).

[108] B. Wul, “Barium titanate: a new ferro-electric”, Nature **157**, 808–808 (1946).

[109] J. H. van Santen and G. H. Jonker, “Effect of temperature on the permittivity of barium titanate”, Nature **159**, 333–334 (1947).

[110] H. D. Megaw, “Temperature changes in the crystal structure of barium titanium oxide”, Proc. Royal Soc. Lond. A **189**, 261–283 (1947).

[111] M. G. Harwood, P. Popper, and D. F. Rushman, “Curie point of barium titanate”, Nature **160**, 58–59 (1947).

[112] H. F. Kay and R. G. Rhodes, “Barium titanate crystals”, Nature **160**, 126–127 (1947).

[113] J. K. Hulm, “Dielectric properties of single crystals of barium titanate”, Nature **160**, 127–128 (1947).

[114] W. P. Mason and B. T. Matthias, “Theoretical model for explaining the ferroelectric effect in barium titanate”, Phys. Rev. **74**, 1622–1636 (1948).

[115] S. Roberts, “Dielectric constant of barium titanate at high temperatures”, Phys. Rev. **75**, 989–990 (1949).

[116] P. W. Forsbergh, “Domain structures and phase transitions in barium titanate”, Phys. Rev. **76**, 1187–1201 (1949).

[117] H. D. Megaw, “Origin of ferroelectricity in barium titanate and other perovskite-type crystals”, Acta Crystallogr. **5**, 739–749 (1952).

[118] H. D. Megaw, “Ferroelectricity and crystal structure. II”, Acta Crystallogr. **7**, 187–194 (1954).

[119] B. T. Matthias and J. P. Remeika, “Ferroelectricity in the ilmenite structure”, Phys. Rev. **76**, 1886–1887 (1949).

[120] R. S. Weis and T. K. Gaylord, “Lithium niobate: summary of physical properties and crystal structure”, Appl. Phys. A **37**, 191–203 (1985).

[121] I. Inbar and R. E. Cohen, “Origin of ferroelectricity in $LiNbO_3$ and $LiTaO_3$”, Ferroelectrics **194**, 83–95 (1997).

[122] G. Rayner-Canham and Z. Zheng, “Naming elements after scientists: an account of a controversy”, Found. Chem. **10**, 13–18 (2007).

[123] B. T. Matthias, “New ferroelectric crystals”, Phys. Rev. **75**, 1771–1771 (1949).

[124] B. T. Matthias and J. P. Remeika, “Dielectric properties of sodium and potassium niobates”, Phys. Rev. **82**, 727–729 (1951).

[125] S. L. Skjærvø, K. Høydalsvik, A. B. Blichfeld, M.-A. Einarsrud, and T. Grande, “Thermal evolution of the crystal structure and phase transitions of $KNbO_3$”, R. Soc. Open Sci. **5**, 180368 (2018).

[126] G. Shirane, S. Hoshino, and K. Suzuki, “X-ray study of the phase transition in lead titanate”, Phys. Rev. **80**, 1105–1106 (1950).

[127] J. K. Hulm, “The dielectric properties of some alkaline earth titanates at low temperatures”, Proc. Phys. Soc. London, Sect. A **63**, 1184–1185 (1950).

[128] H. Gränicher, “Induzierte Ferroelektrizität von $SrTiO_3$ bei sehr tiefen Temperaturen und über die Kälteerzeugung durch adiabatische Entpolarisierung”, Helv. Phys. Acta **29**, 210–212 (1956).

[129] A. F. Devonshire, “XCVI. Theory of barium titanate”, Phil. Mag. **40**, 1040–1063 (1949).

[130] A. F. Devonshire, “CIX. Theory of barium titanate – Part II”, Phil. Mag. **42**, 1065–1079 (1951).

[131] J. C. Slater, “The Lorentz correction in barium titanate”, Phys. Rev. **78**, 748–761 (1950).

[132] J. H. Barrett, “Dielectric constant in perovskite type crystals”, Phys. Rev. **86**, 118–120 (1952).

[133] R. A. Parker, “Static dielectric constant of rutile (TiO_2), 1.6–1060 °K”, Phys. Rev. **124**, 1719–1722 (1961).

[134] F. Gervais and W. Kress, “Lattice dynamics of incipient ferroelectric rutile TiO_2”, Phys. Rev. B **28**, 2962–2968 (1983).

[135] C. Lee, P. Ghosez, and X. Gonze, “Lattice dynamics and dielectric properties of incipient ferroelectric TiO_2 rutile”, Phys. Rev. B **50**, 13379–13387 (1994).

[136] S.-P. Shen, Y.-S. Chai, J.-Z. Cong, P.-J. Sun, J. Lu, L.-Q. Yan, S.-G. Wang, and Y. Sun, “Magnetic-ion-induced displacive electric polarization in FeO_5 bipyramidal units of $(Ba,Sr)Fe_{12}O_{19}$ hexaferrites”, Phys. Rev. B **90**, 180404(R) (2014).

[137] S.-P. Shen, J.-C. Wu, J.-D. Song, X.-F. Sun, Y.-F. Yang, Y.-S. Chai, D.-S. Shang, S.-G. Wang, J. F. Scott, and Y. Sun, "Quantum electric-dipole liquid on a triangular lattice", Nat. Commun. **7**, 10569 (2016).

[138] L. H. Yin, L. Hu, J. Yang, P. Teng, W. H. Song, J. M. Dai, X. B. Zhu, and Y. P. Sun, "Negative and positive photodielectric effects in quantum paraelectric $BaFe_{12}O_{19}$ single crystals", J. Mater. Chem. C **6**, 12707–12713 (2018).

[139] W. J. Burke and R. J. Pressley, "Stress induced ferroelectricity in $SrTiO_3$", Solid State Commun. **9**, 191–195 (1971).

[140] H. Uwe and T. Sakudo, "Stress-induced ferroelectricity and soft phonon modes in $SrTiO_3$", Phys. Rev. B **13**, 271–286 (1976).

[141] E. Hegenbarth, "Die Feldstärkeabhängigkeit der Dielektrizitätskonstanten von $SrTiO_3$-Einkristallen im Temperaturbereich von 15 bis 80 °K", phys. stat. sol. (b) **6**, 333–337 (1964).

[142] M. A. Saifi and L. E. Cross, "Dielectric properties of strontium titanate at low temperature", Phys. Rev. B **2**, 677–684 (1970).

[143] J. Hemberger, P. Lunkenheimer, R. Viana, R. Böhmer, and A. Loidl, "Electric-field-dependent dielectric constant and nonlinear susceptibility in $SrTiO_3$", Phys. Rev. B **52**, 13159–13162 (1995).

[144] H. Uwe, H. Unoki, Y. Fujii, and T. Sakudo, "Stress induced ferroelectricity in $KTaO_3$", Solid State Commun. **13**, 737–739 (1973).

[145] H. Uwe and T. Sakudo, "Electrostriction and stress-induced ferroelectricity in $KTaO_3$", J. Phys. Soc. Jpn. **38**, 183–189 (1975).

[146] U. T. Höchli, H. E. Weibel, and L. A. Boatner, "Quantum limit of ferroelectric phase transitions in $KTa_{1-x}Nb_xO_3$", Phys. Rev. Lett. **39**, 1158–1161 (1977).

[147] U. T. Höchli and L. A. Boatner, "Quantum ferroelectricity in $K_{1-x}Na_xTaO_3$ and $KTa_{1-y}Nb_yO_3$", Phys. Rev. B **20**, 266–275 (1979).

[148] U. T. Höchli, "Experimental studies on quantum ferroelectrics", Ferroelectrics **35**, 17–30 (1981).

[149] K. A. Müller, "Electron paramagnetic resonance of manganese IV in $SrTiO_3$", Phys. Rev. Lett. **2**, 341–343 (1959).

[150] W. I. Dobrov, R. F. Vieth, and M. E. Browne, "Electron paramagnetic resonance in $SrTiO_3$", Phys. Rev. **115**, 79–80 (1959).

[151] L. Rimai and G. A. deMars, "Electron paramagnetic resonance of trivalent gadolinium ions in strontium and barium titanates", Phys. Rev. **127**, 702–710 (1962).

[152] F. W. Lytle, "X-ray diffractometry of low-temperature phase transformations in strontium titanate", J. Appl. Phys. **35**, 2212–2215 (1964).

[153] H. Unoki and T. Sakudo, “Electron spin resonance of Fe^{3+} in $SrTiO_3$ with special reference to the 110 °K phase transition”, J. Phys. Soc. Jpn. **23**, 546–552 (1967).

[154] J. M. Kiat and T. Roisnel, “Rietveld analysis of strontium titanate in the Müller state”, J. Phys.: Condens. Matter **8**, 3471–3475 (1996).

[155] A. Hachemi, H. Hachemi, A. Ferhat-Hamida, and L. Louail, “Elasticity of $SrTiO_3$ perovskite under high pressure in cubic, tetragonal and orthorhombic phases”, Phys. Scr. **82**, 025602 (2010).

[156] P. A. Fleury, J. F. Scott, and J. M. Worlock, “Soft phonon modes and the 110 °K phase transition in $SrTiO_3$”, Phys. Rev. Lett. **21**, 16–19 (1968).

[157] G. Shirane and Y. Yamada, “Lattice-dynamical study of the 110 °K phase transition in $SrTiO_3$”, Phys. Rev. **177**, 858–863 (1969).

[158] H. Fujishita, Y. Shiozaki, and E. Sawaguchi, “X-ray crystal structure analysis of low temperature phase of $SrTiO_3$”, J. Phys. Soc. Jpn. **46**, 581–586 (1979).

[159] A. M. Glazer, “The classification of tilted octahedra in perovskites”, Acta Crystallogr. Sect. B **28**, 3384–3392 (1972).

[160] A. M. Glazer, “Simple ways of determining perovskite structures”, Acta Crystallogr. Sect. A **31**, 756–762 (1975).

[161] K. S. Aleksandrov, “The sequences of structural phase transitions in perovskites”, Ferroelectrics **14**, 801–805 (1976).

[162] H. Bärnighausen, “Group–subgroup relations between space groups: a useful tool in crystal chemistry”, Commun. Math. Chem. **9**, 139–175 (1980).

[163] O. Bock and U. Müller, “Symmetrieverwandtschaften bei Varianten des Perowskit-Typs”, Acta Crystallogr. Sect B **58**, 594–606 (2002).

[164] U. Müller, “Kristallographische Gruppe-Untergruppe-Beziehungen und ihre Anwendung in der Kristallchemie”, Z. anorg. allg. Chem. **630**, 1519–1537 (2004).

[165] A. Authier, ed., *International Tables for Crystallography, Volume D, Physical properties of crystals*, 1st edition (International Union of Crystallography, Oct. 2003).

[166] H. Wondratschek and W. Jeitschko, “Twin domains and antiphase domains”, Acta Crystallogr. Sect. A **32**, 664–666 (1976).

[167] U. Müller, *Symmetry relationships between crystal structures* (Oxford University Press, Apr. 2013).

[168] H. Wondratschek and U. Müller, eds., *International Tables for Crystallography, Volume A1, Symmetry relations between space groups*, 1st edition (International Union of Crystallography, 2004).

[169] K. Tsuda and M. Tanaka, “Refinement of crystal structure parameters using convergent-beam electron diffraction: the low-temperature phase of $SrTiO_3$”, Acta Crystallogr. Sect. A **51**, 7–19 (1995).

[170] R. Ranjan, D. Pandey, and N. P. Lalla, “Novel features of $Sr_{1-x}Ca_xTiO_3$ phase diagram: evidence for competing antiferroelectric and ferroelectric interactions”, Phys. Rev. Lett. **84**, 3726–3729 (2000).

[171] R. Ranjan and D. Pandey, “Antiferroelectric phase transition in $(Sr_{1-x}Ca_x)TiO_3$: II. X-ray diffraction studies”, J. Phys.: Condens. Matter **13**, 4251–4266 (2001).

[172] M. A. Carpenter, C. J. Howard, K. S. Knight, and Z. Zhang, “Structural relationships and a phase diagram for $(Ca,Sr)TiO_3$ perovskites”, J. Phys.: Condens. Matter **18**, 10725–10749 (2006).

[173] W. Jackson and W. Reddish, “High permittivity crystalline aggregates”, Nature **156**, 717–717 (1945).

[174] D. F. Rushman and M. A. Strivens, “The permittivity of polycrystals of the perovskite type”, Trans. Faraday Soc. **42**, A231–A238 (1946).

[175] P. R. Coursey and K. G. Brand, “Dielectric constants of some titanates”, Nature **157**, 297–298 (1946).

[176] G. Durst, M. Grotenhuis, and A. G. Barkow, “Solid solubility study of barium, strontium, and calcium titanates”, J. Am. Ceram. Soc. **33**, 133–139 (1950).

[177] H. Gränicher and O. Jakits, “Über die dielektrischen Eigenschaften und Phasenumwandlungen bei Mischkristallsystemen vom Perowskittyp”, Nuovo Cim. **11**, 480–520 (1954).

[178] M. McQuarrie and F. W. Behnke, “Structural and dielectric studies in the system $(Ba,Ca)(Ti,Zr)O_3$”, J. Am. Ceram. Soc. **37**, 539–543 (1954).

[179] M. McQuarrie, “Structural behavior in the system $(Ba,Ca,Sr)TiO_3$ and its relation to certain dielectric characteristics”, J. Am. Ceram. Soc. **38**, 444–449 (1955).

[180] R. C. DeVries and R. Roy, “Phase equilibria in the system $BaTiO_3$–$CaTiO_3$”, J. Am. Ceram. Soc. **38**, 142–146 (1955).

[181] T. Mitsui and W. B. Westphal, “Dielectric and x-ray studies of $Ca_xBa_{1-x}TiO_3$ and $Ca_xSr_{1-x}TiO_3$”, Phys. Rev. **124**, 1354–1359 (1961).

[182] R. Ouillon, J.-P. Pinan-Lucarre, P. Ranson, P. Pruzan, S. K. Mishra, R. Ranjan, and D. Pandey, “A Raman scattering study of the phase transitions in $SrTiO_3$ and in the mixed system $(Sr_{1-x}Ca_x)TiO_3$ at ambient pressure from $T = 300$ K down to 8 K”, J. Phys.: Condens. Matter **14**, 2079–2092 (2002).

[183] P. Ranson, R. Ouillon, J.-P. Pinan-Lucarre, P. Pruzan, S. K. Mishra, R. Ranjan, and D. Pandey, “The various phases of the system $Sr_{1-x}Ca_xTiO_3$—a Raman scattering study”, J. Raman Spectrosc. **36**, 898–911 (2005).

[184] R. Ranjan and D. Pandey, “Antiferroelectric phase transition in $(Sr_{1-x}Ca_x)TiO_3$ $(0.12 < x \leq 0.40)$: I. Dielectric studies”, J. Phys.: Condens. Matter **13**, 4239–4249 (2001).

[185] S. K. Mishra, R. Ranjan, D. Pandey, and B. J. Kennedy, “Powder neutron diffraction study of the antiferroelectric phase transition in $Sr_{0.75}Ca_{0.25}TiO_3$”, J. Appl. Phys. **91**, 4447–4452 (2002).

[186] U. Bianchi, W. Kleemann, and J. G. Bednorz, “Raman scattering of ferroelectric $Sr_{1-x}Ca_xTiO_3$, $x = 0.007$”, J. Phys.: Condens. Matter **6**, 1229–1238 (1994).

[187] W. Kleemann, A. Albertini, M. Kuss, and R. Lindner, “Optical detection of symmetry breaking on a nanoscale in $SrTiO_3$:Ca”, Ferroelectrics **203**, 57–74 (1997).

[188] S. K. Mishra and D. Pandey, “Low temperature x-ray diffraction study of the phase transitions in $Sr_{1-x}Ca_xTiO_3$ ($x = 0.02, 0.04$): evidence for ferrielectric ordering”, Appl. Phys. Lett. **95**, 232910 (2009).

[189] D. Bäuerle, W. Braun, V. Saile, G. Sprüssel, and E. E. Koch, “Vacuum ultraviolet reflectivity and band structure of $SrTiO_3$ and $BaTiO_3$”, Z. Phys. B **29**, 179–184 (1978).

[190] K. van Benthem, C. Elsässer, and R. H. French, “Bulk electronic structure of $SrTiO_3$: experiment and theory”, J. Appl. Phys. **90**, 6156–6164 (2001).

[191] J. F. Schooley, W. R. Hosler, and M. L. Cohen, “Superconductivity in semiconducting $SrTiO_3$”, Phys. Rev. Lett. **12**, 474–475 (1964).

[192] O. N. Tufte and E. L. Stelzer, “Piezoresistive properties of reduced strontium titanate”, Phys. Rev. **141**, 675–680 (1966).

[193] O. N. Tufte and P. W. Chapman, “Electron mobility in semiconducting strontium titanate”, Phys. Rev. **155**, 796–802 (1967).

[194] C. S. Koonce, M. L. Cohen, J. F. Schooley, W. R. Hosler, and E. R. Pfeiffer, “Superconducting transition temperatures of semiconducting $SrTiO_3$”, Phys. Rev. **163**, 380–390 (1967).

[195] D. Parker and J. Yahia, “ac Hall measurements in crystals of strontium titanate from 190 to 500 °K: dependence of Hall mobility on charge-carrier density”, Phys. Rev. **169**, 605–609 (1968).

[196] C. Lee, J. Yahia, and J. L. Brebner, “Electronic conduction in slightly reduced strontium titanate at low temperatures”, Phys. Rev. B **3**, 2525–2533 (1971).

[197] C. Lee, J. Destry, and J. L. Brebner, “Optical absorption and transport in semiconducting $SrTiO_3$”, Phys. Rev. B **11**, 2299–2310 (1975).

[198] D. Bäuerle and W. Rehwald, “Structural phase transitions in semiconducting $SrTiO_3$”, Solid State Commun. **27**, 1343–1346 (1978).

[199] D. Wagner, D. Bäuerle, F. Schwabl, B. Dorner, and H. Kraxenberger, “Soft modes in semiconducting $SrTiO_3$ – I. The zone boundary mode”, Z. Phys. B **37**, 317–320 (1980).

[200] D. Bäuerle, D. Wagner, M. Wöhlecke, B. Dorner, and H. Kraxenberger, “Soft modes in semiconducting $SrTiO_3$: II. The ferroelectric mode”, Z. Phys. B **38**, 335–339 (1980).

[201] H. P. R. Frederikse and W. R. Hosler, “Hall mobility in $SrTiO_3$”, Phys. Rev. **161**, 822–827 (1967).

[202] G. Binnig, A. Baratoff, H. E. Hoenig, and J. G. Bednorz, “Two-band superconductivity in Nb-doped $SrTiO_3$”, Phys. Rev. Lett. **45**, 1352–1355 (1980).

[203] S. Ohta, T. Nomura, H. Ohta, and K. Koumoto, “High-temperature carrier transport and thermoelectric properties of heavily La- or Nb-doped $SrTiO_3$ single crystals”, J. Appl. Phys. **97**, 034106 (2005).

[204] U. Balachandran, “Electrical conductivity in lanthanum-doped strontium titanate”, J. Electrochem. Soc. **129**, 1021–1026 (1982).

[205] K. Uematsu, O. Sakurai, N. Mizutani, and M. Kato, “Electrical properties of La-doped $SrTiO_3$ (La: 0.1 to 2.0 at %) single crystals grown by xenon-arc image floating zone method”, J. Mater. Sci. **19**, 3671–3679 (1984).

[206] H. Suzuki, H. Bando, Y. Ootuka, I. H. Inoue, T. Yamamoto, K. Takahashi, and Y. Nishihara, “Superconductivity in single-crystalline $Sr_{1-x}La_xTiO_3$”, J. Phys. Soc. Jpn. **65**, 1529–1532 (1996).

[207] C. Q. Tang, Z. Xia, S. Yao, and S. Chen, “Dependence of the electric properties and the positron lifetimes on the dopant content in La-doped $SrTiO_3$”, Cryst. Res. Technol. **31**, 821–826 (1996).

[208] M. D. Glinchuk and I. V. Kondakova, “Ruderman–Kittel-like interaction of electric dipoles in systems with carriers”, phys. stat. sol. (b) **174**, 193–197 (1992).

[209] M. D. Glinchuk, I. V. Kondakova, and R. O. Kuzian, “The possibility of Kondo-like effect in systems with non-tunneling off-center ions”, Ferroelectrics **153**, 97–102 (1994).

[210] S. E. Rowley, L. J. Spalek, R. P. Smith, M. P. M. Dean, M. Itoh, J. F. Scott, G. G. Lonzarich, and S. S. Saxena, “Ferroelectric quantum criticality”, Nat. Phys. **10**, 367–372 (2014).

[211] M. Itoh, R. Wang, Y. Inaguma, T. Yamaguchi, Y.-J. Shan, and T. Nakamura, “Ferroelectricity induced by oxygen isotope exchange in strontium titanate perovskite”, Phys. Rev. Lett. **82**, 3540–3543 (1999).

[212] L. Zhu, M. Garst, A. Rosch, and Q. Si, “Universally diverging Grüneisen prameter and the magnetocaloric effect close to quantum critical points”, Phys. Rev. Lett. **91**, 066404 (2003).

[213] M. Garst and A. Rosch, “Sign change of the Grüneisen parameter and magnetocaloric effect near quantum critical points”, Phys. Rev. B **72**, 205129 (2005).

[214] R. Küchler, N. Oeschler, P. Gegenwart, T. Cichorek, K. Neumaier, O. Tegus, C. Geibel, J. A. Mydosh, F. Steglich, L. Zhu, and Q. Si, "Divergence of the Grüneisen ratio at quantum critical points in heavy fermion metals", Phys. Rev. Lett. **91**, 066405 (2003).

[215] P. Gegenwart, F. Weickert, M. Garst, R. S. Perry, and Y. Maeno, "Metamagnetic quantum criticality in $Sr_3Ru_2O_7$ studied by thermal expansion", Phys. Rev. Lett. **96**, 136402 (2006).

[216] J. Baier, P. Steffens, O. Schumann, M. Kriener, S. Stark, H. Hartmann, O. Friedt, A. Revcolevschi, P. G. Radaelli, S. Nakatsuji, Y. Maeno, J. A. Mydosh, T. Lorenz, and M. Braden, "Magnetoelastic coupling across the metamagnetic transition in $Ca_{2-x}Sr_xRuO_4$ $(0.2 \leq x \leq 0.5)$", J. Low Temp. Phys. **147**, 405–420 (2007).

[217] T. Lorenz, S. Stark, O. Heyer, N. Hollmann, A. Vasiliev, A. Oosawa, and H. Tanaka, "Thermodynamics of the coupled spin-dimer system $TlCuCl_3$ close to a quantum phase transition", J. Magn. Magn. Mater. **316**, 291–297 (2007).

[218] T. Lorenz, O. Heyer, M. Garst, F. Anfuso, A. Rosch, C. Rüegg, and K. Krämer, "Diverging thermal expansion of the spin-ladder system $(C_5H_{12}N)_2CuBr_4$", Phys. Rev. Lett. **100**, 067208 (2008).

[219] O. Breunig, M. Garst, E. Sela, B. Buldmann, P. Becker, L. Bohatý, R. Müller, and T. Lorenz, "Spin-$\frac{1}{2}$ XXZ chain system Cs_2CoCl_4 in a transverse magnetic field", Phys. Rev. Lett. **111**, 187202 (2013).

[220] S. K. Niesen, G. Kolland, M. Seher, O. Breunig, M. Valldor, M. Braden, B. Grenier, and T. Lorenz, "Magnetic phase diagrams, domain switching, and quantum phase transition of the quasi-one-dimensional Ising-like antiferromagnet $BaCo_2V_2O_8$", Phys. Rev. B **87**, 224413 (2013).

[221] O. Breunig, M. Garst, A. Klümper, J. Rohrkamp, M. M. Turnbull, and T. Lorenz, "Quantum criticality in the spin-1/2 Heisenberg chain system copper pyrazine dinitrate", Sci. Adv. **3**, eaao3773 (2017).

[222] K. Grube, L. Pintschovius, F. Weber, J.-P. Castellan, S. Zaum, S. Kuntz, P. Schweiss, O. Stockert, S. Bachus, Y. Shimura, V. Fritsch, and H. v. Löhneysen, "Magnetic and structural quantum phase transitions in $CeCu_{6-x}Au_x$ are independent", Phys. Rev. Lett. **121**, 087203 (2018).

[223] C. Meingast, F. Hardy, R. Heid, P. Adelmann, A. Böhmer, P. Burger, D. Ernst, R. Fromknecht, P. Schweiss, and T. Wolf, "Thermal expansion and Grüneisen parameters of $Ba(Fe_{1-x}Co_x)_2As_2$: a thermodynamic quest for quantum criticality", Phys. Rev. Lett. **108**, 177004 (2012).

[224] R. Pott and R. Schefzyk, "Apparatus for measuring the thermal expansion of solids between 1.5 and 380 K", J. Phys. E: Sci. Instrum. **16**, 444–449 (1983).

[225] E. McCalla, J. Walter, and C. Leighton, "A unified view of the substitution-dependent antiferrodistortive phase transition in $SrTiO_3$", Chem. Mater. **28**, 7973–7981 (2016).

[226] E. K. H. Salje, M. C. Gallardo, J. Jiménez, F. J. Romero, and J. del Cerro, "The cubic–tetragonal phase transition in strontium titanate: excess specific heat measurements and evidence for a near-tricritical, mean field type transition mechanism", J. Phys.: Condens. Matter **10**, 5535–5543 (1998).

[227] A. Okazaki and M. Kawaminami, "Lattice constant of strontium titanate at low temperatures", Mater. Res. Bull. **8**, 545–550 (1973).

[228] S. K. Mishra, R. Ranjan, D. Pandey, P. Ranson, R. Ouillon, J.-P. Pinan-Lucarre, and P. Pruzan, "A combined x-ray diffraction and Raman scattering study of the phase transitions in $Sr_{1-x}Ca_xTiO_3$ ($x = 0.04, 0.06$, and 0.12)", J. Solid State Chem. **178**, 2846–2857 (2005).

[229] N. Ohama, H. Sakashita, and A. Okazaki, "The temperature dependence of the lattice constant of $SrTiO_3$ around the 105 K transition", Phase Transit. **4**, 81–90 (1984).

[230] M. Sato, Y. Soejima, N. Ohama, A. Okazaki, H. J. Scheel, and K. A. Müller, "The lattice constant vs. temperature relation around the 105 K transition of a flux-grown $SrTiO_3$ crystal", Phase Transit. **5**, 207–218 (1985).

[231] S. A. T. Redfern, "High-temperature structural phase transitions in perovskite ($CaTiO_3$)", J. Phys.: Condens. Matter **8**, 8267–8275 (1996).

[232] B. J. Kennedy, C. J. Howard, and B. C. Chakoumakos, "Phase transitions in perovskite at elevated temperatures—a powder neutron diffraction study", J. Phys.: Condens. Matter **11**, 1479–1488 (1999).

[233] R. Ali and M. Yashima, "Space group and crystal structure of the perovskite $CaTiO_3$ from 296 to 1720 K", J. Solid State Chem. **178**, 2867–2872 (2005).

[234] V. V. Lemanov, "Phase transitions in $SrTiO_3$-based solid solutions", Phys. Solid State **39**, 1468–1473 (1997).

[235] R. W. Cahn, "Twinned crystals", Adv. Phys. **3**, 363–445 (1954).

[236] S. K. Niesen, O. Breunig, S. Salm, M. Seher, M. Valldor, P. Warzanowski, and T. Lorenz, "Substitution effects on the temperature versus magnetic field phase diagrams of the quasi-one-dimensional effective Ising spin-$\frac{1}{2}$ chain system $BaCo_2V_2O_8$", Phys. Rev. B **90**, 104419 (2014).

[237] S. Kunkemöller, D. Brüning, A. Stunault, A. A. Nugroho, T. Lorenz, and M. Braden, "Magnetic shape-memory effect in $SrRuO_3$", Phys. Rev. B **96**, 220406(R) (2017).

[238] A. Okazaki and N. Ohama, "Improvement of high-angle double-crystal x-ray diffractometry (HADOX) for measuring temperature dependence of lattice constants. I. Theory", J. Appl. Crystallogr. **12**, 450–454 (1979).

[239] N. Ohama, H. Sakashita, and A. Okazaki, “Improvement of high-angle double-crystal x-ray diffractometry (HADOX) for measuring temperature dependence of lattice constants. II. Practice”, J. Appl. Crystallogr. **12**, 455–459 (1979).

[240] W. Kleemann, F. J. Schäfer, K. A. Müller, and J. G. Bednorz, “Domain state properties of the random-field xy-model system $Sr_{1-x}Ca_xTiO_3$”, Ferroelectrics **80**, 297–300 (1988).

[241] Q. Tao, B. Loret, B. Xu, X. Yang, C. W. Rischau, X. Lin, B. Fauqué, M. J. Verstraete, and K. Behnia, “Nonmonotonic anisotropy in charge conduction induced by antiferrodistortive transition in metallic $SrTiO_3$”, Phys. Rev. B **94**, 035111 (2016).

[242] J. Engelmayer, X. Lin, C. P. Grams, R. German, T. Fröhlich, J. Hemberger, K. Behnia, and T. Lorenz, “Charge transport in oxygen-deficient $EuTiO_3$: the emerging picture of dilute metallicity in quantum-paraelectric perovskite oxides”, Phys. Rev. Materials **3**, 051401(R) (2019).

[243] S. Tsunekawa, H. F. J. Watanabe, and H. Takei, “Linear thermal expansion of $SrTiO_3$”, phys. stat. sol. (a) **83**, 467–472 (1984).

[244] P. W. Anderson and E. I. Blount, “Symmetry considerations on martensitic transformations: "ferroelectric" metals?”, Phys. Rev. Lett. **14**, 217–219 (1965).

[245] Y. Shi, Y. Guo, X. Wang, A. J. Princep, D. Khalyavin, P. Manuel, Y. Michiue, A. Sato, K. Tsuda, S. Yu, M. Arai, Y. Shirako, M. Akaogi, N. Wang, K. Yamaura, and A. T. Boothroyd, “A ferroelectric-like structural transition in a metal”, Nat. Mater. **12**, 1024–1027 (2013).

[246] A. Filippetti, V. Fiorentini, F. Ricci, P. Delugas, and J. Íñiguez, “Prediction of a native ferroelectric metal”, Nat. Commun. **7**, 11211 (2016).

[247] A. Fajardo-Peralta, F. Noriega Romero-Vargas, J. C. Rosas-Bonilla, J. L. Torres-Mayorga, J. Mata, and J. M. Siqueiros, “Characterization of polycrystals of STO doped with europium: $Sr_{1-x}Eu_xTiO_3$”, Integr. Ferroelectr. **101**, 114–120 (2008).

[248] Z. Guguchia, A. Shengelaya, H. Keller, J. Köhler, and A. Bussmann-Holder, “Tuning the structural instability of $SrTiO_3$ by Eu doping: the phase diagram of $Sr_{1-x}Eu_xTiO_3$”, Phys. Rev. B **85**, 134113 (2012).

[249] D. S. Keeble and P. A. Thomas, “On the tetragonality of the room-temperature ferroelectric phase of barium titanate, $BaTiO_3$”, J. Appl. Crystallogr. **42**, 480–484 (2009).

[250] Z. Guguchia, H. Keller, A. Bussmann-Holder, J. Köhler, and R. K. Kremer, “The low temperature magnetic phase diagram of $Eu_xSr_{1-x}TiO_3$”, Eur. Phys. J. B **86**, 409 (2013).

[251] O. Prakash, A. Kumar, A. Thamizhavel, and S. Ramakrishnan, “Evidence for bulk superconductivity in pure bismuth single crystals at ambient pressure”, Science **355**, 52–55 (2017).

[252] X. Lin, Z. Zhu, B. Fauqué, and K. Behnia, “Fermi surface of the most dilute superconductor”, Phys. Rev. X **3**, 021002 (2013).

[253] L. P. Gor’kov, “Phonon mechanism in the most dilute superconductor n-type $SrTiO_3$”, Proc. Natl. Acad. Sci. U.S.A. **113**, 4646–4651 (2016).

[254] D. van der Marel, J. L. M. van Mechelen, and I. I. Mazin, “Common Fermi-liquid origin of T^2 resistivity and superconductivity in $SrTiO_3$”, Phys. Rev. B **84**, 205111 (2011).

[255] T. Okuda, K. Nakanishi, S. Miyasaka, and Y. Tokura, “Large thermoelectric response of metallic perovskites: $Sr_{1-x}La_xTiO_3$ $(0 \leq x \leq 0.1)$”, Phys. Rev. B **63**, 113104 (2001).

[256] W. G. Baber, “The contribution to the electrical resistance of metals from collisions between electrons”, Proc. R. Soc. London, Ser. A **158**, 383–396 (1937).

[257] W. J. de Haas and J. de Boer, “The electrical resistance of platinum at low temperatures”, Physica **1**, 609–616 (1934).

[258] K. Yamada and K. Yosida, “Fermi liquid theory on the basis of the periodic Anderson Hamiltonian”, Prog. Theor. Phys. **76**, 621–638 (1986).

[259] H. Maebashi and H. Fukuyama, “Electrical conductivity of interacting fermions. II. Effects of normal scattering processes in the presence of Umklapp scattering processes”, J. Phys. Soc. Jpn. **67**, 242–251 (1998).

[260] K. Kadowaki and S. B. Woods, “Universal relationship of the resistivity and specific heat in heavy-fermion compounds”, Solid State Commun. **58**, 507–509 (1986).

[261] R. D. Shannon, “Revised effective ionic radii and systematic studies of interatomic distances in halides and chalcogenides”, Acta Crystallogr. Sect. A **32**, 751–767 (1976).

[262] V. Goian, S. Kamba, O. Pacherová, J. Drahokoupil, L. Palatinus, M. Dušek, J. Rohlíček, M. Savinov, F. Laufek, W. Schranz, A. Fuith, M. Kachlík, K. Maca, A. Shkabko, L. Sagarna, A. Weidenkaff, and A. A. Belik, “Antiferrodistortive phase transition in $EuTiO_3$”, Phys. Rev. B **86**, 054112 (2012).

[263] A. R. West, *Solid state chemistry and its applications, student edition*, 2nd ed. (John Wiley & Sons, 2014).

[264] O. Fukunaga and T. Fujita, “The relation between ionic radii and cell volumes in the perovskite compounds”, J. Solid State Chem. **8**, 331–338 (1973).

[265] C. Chatzichristodoulou, P. Norby, P. V. Hendriksen, and M. B. Mogensen, “Size of oxide vacancies in fluorite and perovskite structured oxides”, J. Electroceram. **34**, 100–107 (2015).

[266] C. J. Bartel, C. Sutton, B. R. Goldsmith, R. Ouyang, C. B. Musgrave, L. M. Ghiringhelli, and M. Scheffler, “New tolerance factor to predict the stability of perovskite oxides and halides”, Sci. Adv. **5**, eaav0693 (2019).

[267] A. Midya, P. Mandal, Km. Rubi, R. Chen, J.-S. Wang, R. Mahendiran, G. Lorusso, and M. Evangelisti, “Large adiabatic temperature and magnetic entropy changes in $EuTiO_3$”, Phys. Rev. B **93**, 094422 (2016).

[268] E. O. Wollan and W. C. Koehler, “Neutron diffraction study of the magnetic properties of the series of perovskite-type compounds $[(1-x)La,xCa]MnO_3$”, Phys. Rev. **100**, 545–563 (1955).

[269] K. Kaminaga, R. Sei, K. Hayashi, N. Happo, H. Tajiri, D. Oka, T. Fukumura, and T. Hasegawa, “A divalent rare earth oxide semiconductor: yttrium monoxide”, Appl. Phys. Lett. **108**, 122102 (2016).

[270] H. A. Eick, N. C. Baenziger, and L. Eyring, “Lower oxides of samarium and europium. The preparation and crystal structure of $SmO_{0.4-0.6}$, SmO and EuO”, J. Am. Chem. Soc. **78**, 5147–5149 (1956).

[271] G. Brauer, H. Bärnighausen, and N. Schultz, “Versuche zur Darstellung niederer Oxide von Neodym, Samarium und Ytterbium”, Z. anorg. allg. Chem. **356**, 46–55 (1967).

[272] G. J. McCarthy and W. B. White, “On the stabilities of the lower oxides of the rare earths”, J. Less-Common Metals **22**, 409–417 (1970).

[273] J. M. Leger, N. Yacoubi, and J. Loriers, “Synthesis of rare earth monoxides”, J. Solid State Chem. **36**, 261–270 (1981).

[274] M. Dulick, E. Murad, and R. F. Barrow, “Thermochemical properties of the rare earth monoxides”, J. Chem. Phys. **85**, 385–390 (1986).

[275] V. Narayanamurti, A. Jayaraman, and E. Bucher, “Optical absorption in ytterbium monochalcogenides under pressure”, Phys. Rev. B **9**, 2521–2523 (1974).

[276] H. Akamatsu, K. Fujita, H. Hayashi, T. Kawamoto, Y. Kumagai, Y. Zong, K. Iwata, F. Oba, I. Tanaka, and K. Tanaka, “Crystal and electronic structure and magnetic properties of divalent europium perovskite oxides $EuMO_3$ (M = Ti, Zr, and Hf): experimental and first-principles approaches”, Inorg. Chem. **51**, 4560–4567 (2012).

[277] T. R. McGuire and M. W. Shafer, “Ferromagnetic europium compounds”, J. Appl. Phys. **35**, 984–988 (1964).

[278] G. J. McCarthy, “Divalent europium compounds in the systems Eu–Mo–O and Eu–W–O”, Mater. Res. Bull. **6**, 31–39 (1971).

[279] J. E. Greedan, G. J. McCarthy, and C. Sipe, “Complex oxides containing divalent europium. II. ($Eu(M, M')O_3$) phases”, Inorg. Chem. **14**, 775–779 (1975).

[280] T. R. McGuire, M. W. Shafer, R. J. Joenk, H. A. Alperin, and S. J. Pickart, “Magnetic structure of $EuTiO_3$”, J. Appl. Phys. **37**, 981–982 (1966).

[281] V. V. Shvartsman, P. Borisov, W. Kleemann, S. Kamba, and T. Katsufuji, “Large off-diagonal magnetoelectric coupling in the quantum paraelectric antiferromagnet $EuTiO_3$”, Phys. Rev. B **81**, 064426 (2010).

[282] C.-L. Chien, S. DeBenedetti, and F. De S. Barros, “Magnetic properties of $EuTiO_3$, Eu_2TiO_4, and $Eu_3Ti_2O_7$”, Phys. Rev. B **10**, 3913–3922 (1974).

[283] Z.-J. Mo, J. Shen, L. Li, Y. Liu, C.-C. Tang, F.-X. Hu, J.-R. Sun, and B.-G. Shen, “Observation of giant magnetocaloric effect in $EuTiO_3$”, Mater. Lett. **158**, 282–284 (2015).

[284] K. Caslin, R. K. Kremer, Z. Guguchia, H. Keller, J. Köhler, and A. Bussmann-Holder, “Lattice and polarizability mediated spin activity in $EuTiO_3$”, J. Phys.: Condens. Matter **26**, 022202 (2013).

[285] D. I. Khomskii, *Basic aspects of the quantum theory of solids* (Cambridge University Press, 2010).

[286] L. Adamowicz, “Les surstructures antiferromagnétiques dans les réseaux cubiques simples par la methode du champ moleculaire”, Acta Phys. Pol. **22**, 195–198 (1962).

[287] R. Ranjan, H. S. Nabi, and R. Pentcheva, “Electronic structure and magnetism of $EuTiO_3$: a first-principles study”, J. Phys.: Condens. Matter **19**, 406217 (2007).

[288] R. Ranjan, H. S. Nabi, and R. Pentcheva, “First principles study of magnetism in divalent Eu perovskites”, J. Appl. Phys. **105**, 053905 (2009).

[289] O. Heyer, P. Link, D. Wandner, U. Ruschewitz, and T. Lorenz, “Thermodynamic properties and resistivity of the ferromagnetic semiconductor EuC_2”, New J. Phys. **13**, 113041 (2011).

[290] J. C. Maxwell, *A treatise on electricity and magnetism*, 3rd ed. (Dover Publications, New York, 1954).

[291] M. Iwamoto, “Maxwell–Wagner effect”, in *Encyclopedia of nanotechnology* (Springer Netherlands, 2015), pp. 1–13.

[292] P. Lunkenheimer, V. Bobnar, A. V. Pronin, A. I. Ritus, A. A. Volkov, and A. Loidl, “Origin of apparent colossal dielectric constants”, Phys. Rev. B **66**, 052105 (2002).

[293] D. Niermann, F. Waschkowski, J. de Groot, M. Angst, and J. Hemberger, “Dielectric properties of charge-ordered $LuFe_2O_4$ revisited: the apparent influence of contacts”, Phys. Rev. Lett. **109**, 016405 (2012).

[294] J. Hemberger, M. Nicklas, R. Viana, P. Lunkenheimer, A. Loidl, and R. Böhmer, “Quantum paraelectric and induced ferroelectric states in $SrTiO_3$”, J. Phys.: Condens. Matter **8**, 4673–4690 (1996).

[295] K. Kugimiya, K. Fujita, K. Tanaka, and K. Hirao, “Preparation and magnetic properties of oxygen deficient $EuTiO_{3-\delta}$ thin films”, J. Magn. Magn. Mater. **310**, 2268–2270 (2007).

[296] H. Uwe, J. Kinoshita, K. Yoshihiro, C. Yamanouchi, and T. Sakudo, “Evidence for light and heavy conduction electrons at the zone center in $KTaO_3$”, Phys. Rev. B **19**, 3041–3044 (1979).

[297] P. P. Edwards and M. J. Sienko, “Universality aspects of the metal–nonmetal transition in condensed media”, Phys. Rev. B **17**, 2575–2581 (1978).

[298] P. P. Edwards, T. V. Ramakrishnan, and C. N. R. Rao, “The metal–nonmetal transition: a global perspective”, J. Phys. Chem. **99**, 5228–5239 (1995).

[299] N. F. Mott, “The transition to the metallic state”, Philos. Mag. **6**, 287–309 (1961).

[300] X. Lin, C. W. Rischau, L. Buchauer, A. Jaoui, B. Fauqué, and K. Behnia, “Metallicity without quasi-particles in room-temperature strontium titanate”, npj Quantum Mater. **2**, 41 (2017).

[301] J.-J. Zhou, O. Hellman, and M. Bernardi, “Electron–phonon scattering in the presence of soft modes and electron mobility in $SrTiO_3$ perovskite from first principles”, Phys. Rev. Lett. **121**, 226603 (2018).

[302] A. S. Mishchenko, L. Pollet, N. V. Prokof’ev, A. Kumar, D. L. Maslov, and N. Nagaosa, “Polaron mobility in the "beyond quasiparticles" regime”, Phys. Rev. Lett. **123**, 076601 (2019).

[303] A. Sakai, T. Kanno, S. Yotsuhashi, H. Adachi, and Y. Tokura, “Thermoelectric properties of electron-doped $KTaO_3$”, Jpn. J. Appl. Phys. **48**, 097002 (2009).

[304] N. W. Ashcroft and N. D. Mermin, *Solid state physics* (Cengage Learning, Inc, 1976).

[305] G. H. Jonker and J. H. van Santen, “Ferromagnetic compounds of manganese with perovskite structure”, Physica **16**, 337–349 (1950).

[306] J. H. van Santen and G. H. Jonker, “Electrical conductivity of ferromagnetic compounds of manganese with perovskite structure”, Physica **16**, 599–600 (1950).

[307] C. Zener, “Interaction between the d-shells in the transition metals. II. Ferromagnetic compounds of manganese with perovskite structure”, Phys. Rev. **82**, 403–405 (1951).

[308] J. B. Goodenough, “Theory of the role of covalence in the perovskite-type manganites [La,M(II)]MnO_3”, Phys. Rev. **100**, 564–573 (1955).

[309] D. Balz and K. Plieth, “Die Struktur des Kaliumnickelfluorids, K_2NiF_4”, Z. Elektrochem. Ber. Bunsenges. Phys. Chem. **59**, 545–551 (1955).

[310] S. N. Ruddlesden and P. Popper, “New compounds of the K_2NiF_4 type”, Acta Crystallogr. **10**, 538–539 (1957).

[311] J. B. MacChesney, H. J. Williams, J. F. Potter, and R. C. Sherwood, “Magnetic study of the manganate phases: $CaMnO_3$, $Ca_4Mn_3O_{10}$, $Ca_3Mn_2O_7$, Ca_2MnO_4”, Phys. Rev. **164**, 779–785 (1967).

[312] D. E. Cox, G. Shirane, R. J. Birgeneau, and J. B. MacChesney, “Neutron-diffraction study of magnetic ordering in Ca_2MnO_4”, Phys. Rev. **188**, 930–932 (1969).

[313] M. E. Leonowicz, K. R. Poeppelmeier, and J. M. Longo, “Structure determination of Ca_2MnO_4 and $Ca_2MnO_{3.5}$ by x-ray and neutron methods”, J. Solid State Chem. **59**, 71–80 (1985).

[314] J.-C. Bouloux, J.-L. Soubeyroux, G. Le Flem, and P. Hagenguller, “Bidimensional magnetic properties of β-Sr_2MnO_4”, J. Solid State Chem. **38**, 34–39 (1981).

[315] J.-C. Bouloux, J.-L. Soubeyroux, A. Daoudi, and G. Le Flem, “Proprietes magnetiques de la phase $Sr_{1,50}La_{0,50}MnO_4$”, Mater. Res. Bull. **16**, 855–860 (1981).

[316] B. Grande, H. Müller-Buschbaum, and M. Schweizer, “Über Oxocuprate. XV Zur Kristallstruktur von Seltenerdmetalloxocupraten: La_2CuO_4, Gd_2CuO_4”, Z. anorg. allg. Chem. **428**, 120–124 (1977).

[317] B. Keimer, N. Belk, R. J. Birgeneau, A. Cassanho, C. Y. Chen, M. Greven, M. A. Kastner, A. Aharony, Y. Endoh, R. W. Erwin, and G. Shirane, “Magnetic excitations in pure, lightly doped, and weakly metallic La_2CuO_4”, Phys. Rev. B **46**, 14034–14053 (1992).

[318] R. A. Mohan Ram, P. Ganguly, and C. N. R. Rao, “Magnetic properties of quasi-two-dimensional $La_{1-x}Sr_{1+x}MnO_4$ and the evolution of itinerant electron ferromagnetism in the $SrO\cdot(La_{1-x}Sr_xMnO_3)_n$ system”, J. Solid State Chem. **70**, 82–87 (1987).

[319] Y. Moritomo, Y. Tomioka, A. Asamitsu, Y. Tokura, and Y. Matsui, “Magnetic and electronic properties in hole-doped manganese oxides with layered structures: $La_{1-x}Sr_{1+x}MnO_4$”, Phys. Rev. B **51**, 3297–3300 (1995).

[320] K. I. Kugel and D. I. Khomskii, “The Jahn–Teller effect and magnetism: transition metal compounds”, Sov. Phys. Usp. **25**, 231–256 (1982).

[321] J. van den Brink, G. Khaliullin, and D. Khomskii, “Charge and orbital order in half-doped manganites”, Phys. Rev. Lett. **83**, 5118–5121 (1999).

[322] J. P. Attfield, “A simple approach to lattice effects in conducting perovskite-type oxides”, Chem. Mater. **10**, 3239–3248 (1998).

[323] J. P. Attfield, A. L. Kharlanov, and J. A. McAllister, “Cation effects in doped La_2CuO_4 superconductors”, Nature **394**, 157–159 (1998).

[324] V. M. Goldschmidt, “Die Gesetze der Krystallochemie”, Naturwissenschaften **14**, 477–485 (1926).

[325] R. Mathieu, M. Uchida, Y. Kaneko, J. P. He, X. Z. Yu, R. Kumai, T. Arima, Y. Tomioka, A. Asamitsu, Y. Matsui, and Y. Tokura, “Bandwidth–disorder phase diagram of half-doped layered manganites”, Phys. Rev. B **74**, 020404(R) (2006).

[326] S. Mori, C. H. Chen, and S.-W. Cheong, “Pairing of charge-ordered stripes in $(La,Ca)MnO_3$”, Nature **392**, 473–476 (1998).

[327] B. J. Sternlieb, J. P. Hill, U. C. Wildgruber, G. M. Luke, B. Nachumi, Y. Moritomo, and Y. Tokura, “Charge and magnetic order in $La_{0.5}Sr_{1.5}MnO_4$”, Phys. Rev. Lett. **76**, 2169–2172 (1996).

[328] Y. Murakami, H. Kawada, H. Kawata, M. Tanaka, T. Arima, Y. Moritomo, and Y. Tokura, “Direct observation of charge and orbital ordering in $La_{0.5}Sr_{1.5}MnO_4$”, Phys. Rev. Lett. **80**, 1932–1935 (1998).

[329] T. Ishikawa, K. Ookura, and Y. Tokura, “Optical response to orbital and charge ordering in a layered manganite: $La_{1/2}Sr_{3/2}MnO_4$”, Phys. Rev. B **59**, 8367–8370 (1999).

[330] P. Mahadevan, K. Terakura, and D. D. Sarma, “Spin, charge, and orbital ordering in $La_{0.5}Sr_{1.5}MnO_4$”, Phys. Rev. Lett. **87**, 066404 (2001).

[331] P. Reutler, O. Friedt, B. Büchner, M. Braden, and A. Revcolevschi, “Growth of $La_{1-x}Sr_{1+x}MnO_4$ single crystals and characterization by scattering techniques”, J. Cryst. Growth **249**, 222–229 (2003).

[332] S. S. Dhesi, A. Mirone, C. D. Nadaï, P. Ohresser, P. Bencok, N. B. Brookes, P. Reutler, A. Revcolevschi, A. Tagliaferri, O. Toulemonde, and G. van der Laan, “Unraveling orbital ordering in $La_{0.5}Sr_{1.5}MnO_4$”, Phys. Rev. Lett. **92**, 056403 (2004).

[333] S. Larochelle, A. Mehta, L. Lu, P. K. Mang, O. P. Vajk, N. Kaneko, J. W. Lynn, L. Zhou, and M. Greven, “Structural and magnetic properties of the single-layer manganese oxide $La_{1-x}Sr_{1+x}MnO_4$”, Phys. Rev. B **71**, 024435 (2005).

[334] A. Gössling, M. W. Haverkort, M. Benomar, H. Wu, D. Senff, T. Möller, M. Braden, J. A. Mydosh, and M. Grüninger, “Mott–Hubbard versus charge-transfer behavior in $LaSrMnO_4$ studied via optical conductivity”, Phys. Rev. B **77**, 035109 (2008).

[335] W. Bao, C. H. Chen, S. A. Carter, and S.-W. Cheong, “Electronic phase separation and charge ordering in $(Sr,La)_2MnO_4$: indication of triplet bipolarons”, Solid State Commun. **98**, 55–59 (1996).

[336] W. Norimatsu and Y. Koyama, “Evolution of orthorhombic domain structures during the tetragonal-to-orthorhombic phase transition in the layered perovskite $Sr_{2-x}La_xMnO_4$”, Phys. Rev. B **74**, 085113 (2006).

[337] T. Kimura, K. Hatsuda, Y. Ueno, R. Kajimoto, H. Mochizuki, H. Yoshizawa, T. Nagai, Y. Matsui, A. Yamazaki, and Y. Tokura, “Charge–orbital ordering and ferromagnetic chains in single-layered manganite crystals”, Phys. Rev. B **65**, 020407 (2001).

[338] X. Z. Yu, R. Mathieu, T. Arima, Y. Kaneko, J. P. He, M. Uchida, T. Asaka, T. Nagai, K. Kimoto, A. Asamitsu, Y. Matsui, and Y. Tokura, “Variation of charge/orbital ordering in layered manganite $Pr_{1-x}Ca_{1+x}MnO_4$ investigated by transmission electron microscopy”, Phys. Rev. B **75**, 174441 (2007).

[339] T. Nagai, T. Kimura, A. Yamazaki, T. Asaka, K. Kimoto, Y. Tokura, and Y. Matsui, “Transversely modulated crystal structure of charge–orbital ordered manganites $Nd_{1-x}Sr_{1+x}MnO_4$ ($x = 2/3, 3/4$)”, Phys. Rev. B **65**, 060405 (2002).

[340] Y. Moritomo, A. Nakamura, S. Mori, N. Yamamoto, K. Ohoyama, and M. Ohashi, "Lattice effects on the charge-ordering transition in $R_{0.5}Sr_{1.5}MnO_4$", Phys. Rev. B **56**, 14879–14882 (1997).

[341] C. S. Hong, E. O. Chi, W. S. Kim, N. H. Hur, K. W. Lee, and C. H. Lee, "Magnetic properties and structural evolution in $Nd_{0.5}Sr_{1.5}MnO_4$", Chem. Mater. **13**, 945–951 (2001).

[342] S. N. Ruddlesden and P. Popper, "The compound $Sr_3Ti_2O_7$ and its structure", Acta Crystallogr. **11**, 54–55 (1958).

[343] R. King, "The topology of coordination polyhedra and their rearrangements", Polyhedron **13**, 2005–2016 (1994).

[344] R. B. King, "The shapes of coordination polyhedra", J. Chem. Educ. **73**, 993 (1996).

[345] R. B. King, "Atomic orbitals, symmetry, and coordination polyhedra", Coord. Chem. Rev. **197**, 141–168 (2000).

[346] D. Senff, P. Reutler, M. Braden, O. Friedt, D. Bruns, A. Cousson, F. Bourée, M. Merz, B. Büchner, and A. Revcolevschi, "Crystal and magnetic structure of $La_{1-x}Sr_{1+x}MnO_4$: role of the orbital degree of freedom", Phys. Rev. B **71**, 024425 (2005).

[347] T. Nagai, A. Yamazaki, K. Kimoto, and Y. Matsui, "Synthesis and structural properties of $n = 1$ Ruddlesden–Popper manganites $Nd_{1-x}Ca_{1+x}MnO_4$", J. Alloys Compd. **453**, 247–252 (2008).

[348] J. H. de Boer and E. J. W. Verwey, "Semi-conductors with partially and with completely filled 3d-lattice bands", Proc. Phys. Soc. **49**, 59–71 (1937).

[349] N. F. Mott and R. Peierls, "Discussion of the paper by de Boer and Verwey", Proc. Phys. Soc. **49**, 72–73 (1937).

[350] N. F. Mott, "The basis of the electron theory of metals, with special reference to the transition metals", Proc. Phys. Soc. London, Sect. A **62**, 416–422 (1949).

[351] J. Hubbard, "Electron correlations in narrow energy bands", Proc. Royal Soc. Lond. A **276**, 238–257 (1963).

[352] J. Hubbard, "Electron correlations in narrow energy bands. II. The degenerate band case", Proc. Royal Soc. Lond. A **277**, 237–259 (1964).

[353] J. Hubbard, "Electron correlations in narrow energy bands. III. An improved solution", Proc. Royal Soc. Lond. A **281**, 401–419 (1964).

[354] F. Hund, "Zur Deutung verwickelter Spektren, insbesondere der Elemente Scandium bis Nickel", Z. Phys. **33**, 345–371 (1925).

[355] F. Hund, "Atomtheoretische Deutung des Magnetismus der seltenen Erden", Z. Phys. **33**, 855–859 (1925).

[356] W. Kutzelnigg and J. D. Morgan, “Hund’s rules”, Z. Phys. D **36**, 197–214 (1996).

[357] H. N. Russell and F. A. Saunders, “New regularities in the spectra of the alkaline earths”, Astrophys. J. **61**, 38–69 (1925).

[358] R. S. Mulliken, “Report on notation for the spectra of polyatomic molecules”, J. Chem. Phys. **23**, 1997–2011 (1955).

[359] R. S. Mulliken, “Erratum: Report on notation for the spectra of polyatomic molecules”, J. Chem. Phys. **24**, 1118–1118 (1956).

[360] H. A. Jahn and E. Teller, “Stability of polyatomic molecules in degenerate electronic states. I. Orbital degeneracy”, Proc. R. Soc. A **161**, 220–235 (1937).

[361] T. Kimura, S. Ishihara, H. Shintani, T. Arima, K. T. Takahashi, K. Ishizaka, and Y. Tokura, “Distorted perovskite with e_g^1 configuration as a frustrated spin system”, Phys. Rev. B **68**, 060403(R) (2003).

[362] R. Kajimoto, H. Mochizuki, H. Yoshizawa, H. Shintani, T. Kimura, and Y. Tokura, “R-dependence of spin exchange interactions in $R\mathrm{MnO}_3$ (R = rare-earth ions)”, J. Phys. Soc. Jpn. **74**, 2430–2433 (2005).

[363] H. A. Kramers, “L’interaction entre les atomes magnétogènes dans un cristal paramagnétique”, Physica **1**, 182–192 (1934).

[364] P. W. Anderson, “Antiferromagnetism. Theory of superexchange interaction”, Phys. Rev. **79**, 350–356 (1950).

[365] J. B. Goodenough, A. Wold, R. J. Arnott, and N. Menyuk, “Relationship between crystal symmetry and magnetic properties of ionic compounds containing Mn^{3+}”, Phys. Rev. **124**, 373–384 (1961).

[366] J. Kanamori, “Superexchange interaction and symmetry properties of electron orbitals”, J. Phys. Chem. Solids **10**, 87–98 (1959).

[367] P. W. Anderson and H. Hasegawa, “Considerations on double exchange”, Phys. Rev. **100**, 675–681 (1955).

[368] P.-G. de Gennes, “Effects of double exchange in magnetic crystals”, Phys. Rev. **118**, 141–154 (1960).

[369] J. B. Goodenough and A. L. Loeb, “Theory of ionic ordering, crystal distortion, and magnetic exchange due to covalent forces in spinels”, Phys. Rev. **98**, 391–408 (1955).

[370] D. Senff, F. Krüger, S. Scheidl, M. Benomar, Y. Sidis, F. Demmel, and M. Braden, “Spin-wave dispersion in orbitally ordered $\mathrm{La}_{1/2}\mathrm{Sr}_{3/2}\mathrm{MnO}_4$”, Phys. Rev. Lett. **96**, 257201 (2006).

[371] A. Daoud-Aladine, J. Rodríguez-Carvajal, L. Pinsard-Gaudart, M. T. Fernández-Díaz, and A. Revcolevschi, “Zener polaron ordering in half-doped manganites”, Phys. Rev. Lett. **89**, 097205 (2002).

[372] H. Wu, C. F. Chang, O. Schumann, Z. Hu, J. C. Cezar, T. Burnus, N. Hollmann, N. B. Brookes, A. Tanaka, M. Braden, L. H. Tjeng, and D. I. Khomskii, “Orbital order in $La_{0.5}Sr_{1.5}MnO_4$: beyond a common local Jahn–Teller picture”, Phys. Rev. B **84**, 155126 (2011).

[373] A. P. Ramirez, P. Schiffer, S.-W. Cheong, C. H. Chen, W. Bao, T. T. M. Palstra, P. L. Gammel, D. J. Bishop, and B. Zegarski, “Thermodynamic and electron diffraction signatures of charge and spin ordering in $La_{1-x}Ca_xMnO_3$”, Phys. Rev. Lett. **76**, 3188–3191 (1996).

[374] C. H. Chen, S.-W. Cheong, and H. Y. Hwang, “Charge-ordered stripes in $La_{1-x}Ca_x$ MnO_3 with $x > 0.5$ (invited)”, J. Appl. Phys. **81**, 4326–4330 (1997).

[375] H. Ulbrich, “Interplay between charge, orbital and magnetic ordering in manganites”, Dissertation (Universität zu Köln, 2012).

[376] J. Engelmayer, “Einkristallsynthese und Charakterisierung von dotierten Seltenerdmanganaten $R_{1-x}A_{1+x}MnO_4$”, Diploma thesis (Universität zu Köln, Feb. 2013).

[377] L. Weber, “Strukturbestimmungen an Schichtsystemen vom (214)-Typ”, MA thesis (Universität zu Köln, Apr. 2015).

[378] O. Schumann, “Structural investigations on layered manganites and ruthenates”, PhD thesis (Universität zu Köln, 2010).

[379] F. Wöhler, “Ueber den Pyrochlor, eine neue Mineralspecies”, Ann. Phys. **83**, 417–428 (1826).

[380] E. Aleshin and R. Roy, “Crystal chemistry of pyrochlore”, J. Am. Ceram. Soc. **45**, 18–25 (1962).

[381] J. S. Gardner, M. J. P. Gingras, and J. E. Greedan, “Magnetic pyrochlore oxides”, Rev. Mod. Phys. **82**, 53–107 (2010).

[382] M. A. Subramanian, G. Aravamudan, and G. V. S. Rao, “Oxide pyrochlores — a review”, Prog. Solid State Chem. **15**, 55–143 (1983).

[383] A. Manthiram and J. Gopalakrishnan, “Fluorite-related $Ln_2Mo_2O_7$ oxides in the Ln_2O_3–MoO_2 system”, Indian J. Chem. **19A**, 1042–1045 (1980).

[384] M. Sato, X. Yan, and J. E. Greedan, “Magnetic properties and magnetic ordering in the rare earth molybdenum(IV) pyrochlores: $R_2Mo_2O_7$”, Z. anorg. allg. Chem. **540**, 177–190 (1986).

[385] J. E. Greedan, M. Sato, N. Ali, and W. R. Datars, “Electrical resistivity of pyrochlore compounds $R_2Mo_2O_7$ (R = Nd, Sm, Gd, Tb, Y)”, J. Solid State Chem. **68**, 300–306 (1987).

[386] J. E. Greedan, M. Sato, X. Yan, and F. S. Razavi, “Spin-glass-like behavior in $Y_2Mo_2O_7$, a concentrated, crystalline system with negligible apparent disorder”, Solid State Commun. **59**, 895–897 (1986).

[387] J. N. Reimers, J. E. Greedan, and M. Sato, “The crystal structure of the spin-glass pyrochlore, $Y_2Mo_2O_7$”, J. Solid State Chem. **72**, 390–394 (1988).

[388] G. Ehlers, J. E. Greedan, J. R. Stewart, K. C. Rule, P. Fouquet, A. L. Cornelius, C. Adriano, P. G. Pagliuso, Y. Qiu, and J. S. Gardner, “High-resolution neutron scattering study of $Tb_2Mo_2O_7$: a geometrically frustrated spin glass”, Phys. Rev. B **81**, 224405 (2010).

[389] D. J. P. Morris, D. A. Tennant, S. A. Grigera, B. Klemke, C. Castelnovo, R. Moessner, C. Czternasty, M. Meissner, K. C. Rule, J.-U. Hoffmann, K. Kiefer, S. Gerischer, D. Slobinsky, and R. S. Perry, “Dirac strings and magnetic monopoles in the spin ice $Dy_2Ti_2O_7$”, Science **326**, 411–414 (2009).

[390] S. T. Bramwell, M. J. Harris, B. C. den Hertog, M. J. P. Gingras, J. S. Gardner, D. F. McMorrow, A. R. Wildes, A. L. Cornelius, J. D. M. Champion, R. G. Melko, and T. Fennell, “Spin correlations in $Ho_2Ti_2O_7$: a dipolar spin ice system”, Phys. Rev. Lett. **87**, 047205 (2001).

[391] K. Kimura, S. Nakatsuji, J.-J. Wen, C. Broholm, M. B. Stone, E. Nishibori, and H. Sawa, “Quantum fluctuations in spin-ice-like $Pr_2Zr_2O_7$”, Nat. Commun. **4**, 1934 (2013).

[392] H. Sakai, K. Yoshimura, H. Ohno, H. Kato, S. Kambe, R. E. Walstedt, T. D. Matsuda, Y. Haga, and Y. Onuki, “Superconductivity in a pyrochlore oxide, $Cd_2Re_2O_7$”, J. Phys.: Condens. Matter **13**, L785–L790 (2001).

[393] F. A. Kröger and H. J. Vink, “Relations between the concentrations of imperfections in crystalline solids”, in *Solid State Physics*, Vol. 3 (Elsevier, 1956), pp. 307–435.

[394] Y. Moritomo, S. Xu, A. Machida, T. Katsufuji, E. Nishibori, M. Takata, M. Sakata, and S.-W. Cheong, “Chemical pressure control of exchange interaction in Mo pyrochlore”, Phys. Rev. B **63**, 144425 (2001).

[395] S. M. Koohpayeh, J.-J. Wen, B. A. Trump, C. L. Broholm, and T. M. McQueen, “Synthesis, floating zone crystal growth and characterization of the quantum spin ice $Pr_2Zr_2O_7$ pyrochlore”, J. Cryst. Growth **402**, 291–298 (2014).

[396] A. Ghasemi, A. Scheie, J. Kindervater, and S. M. Koohpayeh, “The pyrochlore $Ho_2Ti_2O_7$: synthesis, crystal growth, and stoichiometry”, J. Cryst. Growth **500**, 38–43 (2018).

[397] I. V. Solovyev, “Effects of crystal structure and on-site Coulomb interactions on the electronic and magnetic structure of $A_2Mo_2O_7$ (A = Y, Gd, and Nd) pyrochlores”, Phys. Rev. B **67**, 174406 (2003).

[398] N. Ali, M. P. Hill, S. Labroo, and J. E. Greedan, “Magnetic and electrical properties of $R_2Mo_2O_7$ pyrochlore compounds”, J. Solid State Chem. **83**, 178–187 (1989).

[399] J. Frielingsdorf, “Präparation und Charakterisierung von Übergangsmetalloxiden in Pyrochlor-Struktur”, Diploma thesis (Universität zu Köln, May 2011).

[400] K. Matsuhira, C. Sekine, C. Paulsen, M. Wakeshima, Y. Hinatsu, T. Kitazawa, Y. Kiuchi, Z. Hiroi, and S. Takagi, “Spin freezing in the pyrochlore antiferromagnet $Pr_2Zr_2O_7$”, J. Phys. Conf. Ser. **145**, 012031 (2009).

[401] L. Merker, “Synthesis and properties of large single crystals of strontium titanate”, Trans. AIME Mining Eng. **7**, 645–648 (1955).

[402] J. G. Bednorz and H. J. Scheel, “Flame-fusion growth of $SrTiO_3$”, J. Cryst. Growth **41**, 5–12 (1977).

[403] M. Ueltzen, “The Verneuil flame fusion process: substances”, J. Cryst. Growth **132**, 315–328 (1993).

[404] J. Kawanabe, H. Minami, K. Oka, R. Oishi, and H. Uwe, “Floating zone growth of $SrTiO_3$ single crystals and characterization by electronic transport property”, Ferroelectrics **348**, 89–93 (2007).

[405] A. E. Bocquet, T. Mizokawa, K. Morikawa, A. Fujimori, S. R. Barman, K. Maiti, D. D. Sarma, Y. Tokura, and M. Onoda, “Electronic structure of early 3d-transition-metal oxides by analysis of the 2p core-level photoemission spectra”, Phys. Rev. B **53**, 1161–1170 (1996).

[406] D. A. MacLean, H.-N. Ng, and J. E. Greedan, “Crystal structures and crystal chemistry of the RETiO$_3$ perovskites: RE = La, Nd, Sm, Gd, Y”, J. Solid State Chem. **30**, 35–44 (1979).

[407] J. Akimitsu, H. Ichikawa, N. Eguchi, T. Miyano, M. Nishi, and K. Kakurai, “Direct observation of orbital ordering in $YTiO_3$ by means of the polarized neutron diffraction technique”, J. Phys. Soc. Jpn. **70**, 3475–3478 (2001).

[408] C. Ulrich, G. Khaliullin, S. Okamoto, M. Reehuis, A. Ivanov, H. He, Y. Taguchi, Y. Tokura, and B. Keimer, “Magnetic order and dynamics in an orbitally degenerate ferromagnetic insulator”, Phys. Rev. Lett. **89**, 167202 (2002).

[409] N. N. Kovaleva, A. V. Boris, P. Yordanov, A. Maljuk, E. Brücher, J. Strempfer, M. Konuma, I. Zegkinoglou, C. Bernhard, A. M. Stoneham, and B. Keimer, “Optical response of ferromagnetic $YTiO_3$ studied by spectral ellipsometry”, Phys. Rev. B **76**, 155125 (2007).

[410] M. Itoh, M. Tsuchiya, H. Tanaka, and K. Motoya, “Orbital ordering and local magnetic properties of Mott–Hubbard insulators $YTiO_3$ and $LaTiO_3$: NMR study”, J. Phys. Soc. Jpn. **68**, 2783–2789 (1999).

[411] H. Roth, “Präparation und Charakterisierung von Titanaten”, Diploma thesis (Universität zu Köln, Aug. 2003).

[412] Y. Taguchi, Y. Tokura, T. Arima, and F. Inaba, “Change of electronic structures with carrier doping in the highly correlated electron system $Y_{1-x}Ca_xTiO_3$”, Phys. Rev. B **48**, 511–518 (1993).

[413] I. Maartense, I. Yaeger, and B. M. Wanklyn, “Field-induced magnetic transitions of $CoNb_2O_6$ in the ordered state”, Solid State Commun. **21**, 93–96 (1977).

[414] S. Lee, R. K. Kaul, and L. Balents, “Interplay of quantum criticality and geometric frustration in columbite”, Nat. Phys. **6**, 702–706 (2010).

[415] R. Coldea, D. A. Tennant, E. M. Wheeler, E. Wawrzynska, D. Prabhakaran, M. Telling, K. Habicht, P. Smeibidl, and K. Kiefer, “Quantum criticality in an Ising chain: experimental evidence for emergent E_8 symmetry”, Science **327**, 177–180 (2010).

[416] P. W. C. Sarvezuk, E. J. Kinast, C. V. Colin, M. A. Gusmão, J. B. M. da Cunha, and O. Isnard, “New investigation of the magnetic structure of $CoNb_2O_6$ columbite”, J. Appl. Phys. **109**, 07E160 (2011).

[417] D. Prabhakaran, F. R. Wondre, and A. T. Boothroyd, “Preparation of large single crystals of ANb_2O_6 (A = Ni, Co, Fe, Mn) by the floating-zone method”, J. Cryst. Growth **250**, 72–76 (2003).

[418] K. Taniguchi, N. Abe, T. Takenobu, Y. Iwasa, and T. Arima, “Ferroelectric polarization flop in a frustrated magnet $MnWO_4$ induced by a magnetic field”, Phys. Rev. Lett. **97**, 097203 (2006).

[419] O. Heyer, N. Hollmann, I. Klassen, S. Jodlauk, L. Bohatý, P. Becker, J. A. Mydosh, T. Lorenz, and D. Khomskii, “A new multiferroic material: $MnWO_4$”, J. Phys.: Condens. Matter **18**, L471–L475 (2006).

[420] D. Khomskii, “Classifying multiferroics: mechanisms and effects”, Physics **2**, 20 (2009).

[421] J. Peng, Y. Zhang, L.-F. Lin, L. Lin, M. Liu, J.-M. Liu, and S. Dong, “New iron-based multiferroics with improper ferroelectricity”, J. Phys. D: Appl. Phys. **51**, 243002 (2018).

[422] H. Dachs, E. Stoll, and H. Weitzel, “Kristallstruktur und magnetische Ordnung des Hübnerits, $MnWO_4$”, Z. Kristallogr. **125**, 120–129 (1967).

[423] S. N. Britvin, I. V. Pekov, M. G. Krzhizhanovskaya, A. A. Agakhanov, B. Ternes, W. Schüller, and N. V. Chukanov, “Redefinition and crystal chemistry of samarskite-(Y), $YFe^{3+}Nb_2O_8$: cation-ordered niobate structurally related to layered double tungstates”, Phys. Chem. Miner. **46**, 727–741 (2019).

[424] G. Le Flem, R. Salmon, and P. Hagenmuller, “Sur quelques nouveaux tungstates doubles de structure wolframite”, C. R. Acad. Sc. Paris, Ser. C **268**, 1431–1434 (1969).

[425] R. Salmon, A. Casalot, G. Le Flem, and P. Hagenmuller, “Distribution cationique dans les tungstates $A^+B^{3+}(WO_4)_2$ de type wolframite”, Mater. Res. Bull. **5**, 341–351 (1970).

[426] S. Holbein, M. Ackermann, L. Chapon, P. Steffens, A. Gukasov, A. Sazonov, O. Breunig, Y. Sanders, P. Becker, L. Bohatý, T. Lorenz, and M. Braden, “Strong magnetoelastic coupling at the transition from harmonic to anharmonic order in $NaFe(WO_4)_2$ with $3d^5$ configuration”, Phys. Rev. B **94**, 104423 (2016).

[427] M. Albino, S. Pechev, P. Veber, M. Velazquez, and M. Josse, “Cation ordering in the double tungstate $LiFe(WO_4)_2$”, Acta Crystallogr. **C68**, i7–i8 (2012).

[428] G. E. Spinnler and L. L. Y. Chang, “Phase relations in the systems A_2O–metal oxide–WO_3 (A = Li, Na; metal = Fe, Cr, Sn, Zr, Th, V)”, J. Am. Ceram. Soc. **64**, 553–555 (1981).

[429] M. Liu, L. Lin, Y. Zhang, S. Li, Q. Huang, V. O. Garlea, T. Zou, Y. Xie, Y. Wang, C. Lu, L. Yang, Z. Yan, X. Wang, S. Dong, and J.-M. Liu, “Cycloidal magnetism driven ferroelectricity in double tungstate $LiFe(WO_4)_2$”, Phys. Rev. B **95**, 195134 (2017).

[430] A. Magnéli, “Structure of β-tungsten oxide”, Nature **165**, 356–357 (1950).

[431] A. Magnéli, “Structures of the ReO_3-type with recurrent dislocations of atoms: ‘homologous series’ of molybdenum and tungsten oxides”, Acta Crystallogr. **6**, 495–500 (1953).

[432] G. Hölzer, M. Fritsch, M. Deutsch, J. Härtwig, and E. Förster, “$K\alpha_{1,2}$ and $K\beta_{1,3}$ x-ray emission lines of the 3d transition metals”, Phys. Rev. A **56**, 4554–4568 (1997).

[433] A. Le Bail, “Whole powder pattern decomposition methods and applications: a retrospection”, Powder Diffr. **20**, 316–326 (2005).

[434] O. Breunig, “Thermodynamics of the spin-chain compounds Cs_2CoCl_4 and $Cu(C_4H_4N_2)(NO_3)_2$”, PhD thesis (Universität zu Köln, 2015).

[435] M. A. Porai-Koshits, “Structure of cesium-tetrachlorocobaltate crystals Cs_2CoCl_4”, Sov. Phys. – Crystallogr. **1**, 224–230 (1956).

[436] C. Zobel, “Einkristallpräparation, Magnetismus und Transporteigenschaften von $La_{1-x}Sr_xCoO_3$”, PhD thesis (Universität zu Köln, 2002).

[437] M. Benomar, “Einkristall-Präparation und Charakterisierung von dotiertem La_2MO_4 mit M = Co, Mn und Ni”, PhD thesis (Universität zu Köln, 2007).

[438] H. Roth, “Single crystal growth and electron spectroscopy of d^1-systems”, PhD thesis (Universität zu Köln, 2008).

[439] A. C. Komarek, “Complex ordering phenomena in transition metal oxides and oxyhalides”, PhD thesis (Universität zu Köln, 2009).

[440] S. Niesen, “Synthesis and characterization of spin-chain compounds of the $AM_2V_2O_8$ type”, PhD thesis (Universität zu Köln, 2015).

[441] M. Reuther, “Züchtung und Charakterisierung von Spinleiter- und *SE*CoO_3-Einkristallen”, Diploma thesis (Universität zu Köln, Dec. 2004).

[442] K. Binder, “Herstellung und Charakterisierung von $Y_{1-x}Ca_xTiO_3$ und $RMnO_3$”, Diploma thesis (Universität zu Köln, Jan. 2012).

[443] A. Reichl, “Präparation und Charakterisierung von iso- und heterovalent dotierten $LaCoO_3$-Einkristallen”, Diploma thesis (Universität zu Köln, Mar. 2012).

[444] C. Tölzer, “Strukturbestimmung von Übergangsmetallen mit nicht ganz gefüllter d-Schale”, Diploma thesis (Universität zu Köln, Sept. 2012).

[445] S. Kunkemöller, “Einkristallzüchtung und Charakterisierung von Ruthenaten”, Diploma thesis (Universität zu Köln, Aug. 2013).

[446] P. Laschitzky, “Präparation und Charakterisierung von dotierten Spin-Eis Systemen”, Diploma thesis (Universität zu Köln, Dec. 2013).

[447] V. Cho, “Präparation und Charakterisierung von magnetisch frustrierten Spin-Systemen”, Diploma thesis (Universität zu Köln, July 2014).

[448] J.-F. Welter, “Präparation und Charakterisierung von Seltenerdtitanaten in Pyrochlor-Struktur”, Diploma thesis (Universität zu Köln, May 2015).

[449] M. E. Lines and A. M. Glass, *Principles and applications of ferroelectrics and related materials* (Oxford University Press, Feb. 2001).

[450] Z. Wang, M. Schmidt, A. Loidl, J. Wu, H. Zou, W. Yang, C. Dong, Y. Kohama, K. Kindo, D. I. Gorbunov, S. Niesen, O. Breunig, J. Engelmayer, and T. Lorenz, “Quantum critical dynamics of a Heisenberg–Ising chain in a longitudinal field: many-body strings versus fractional excitations”, Phys. Rev. Lett. **123**, 067202 (2019).

[451] L. Wysocki, R. Mirzaaghayev, M. Ziese, L. Yang, J. Schöpf, R. B. Versteeg, A. Bliesener, J. Engelmayer, A. Kovács, L. Jin, F. Gunkel, R. Dittmann, P. H. M. van Loosdrecht, and I. Lindfors-Vrejoiu, “Magnetic coupling of ferromagnetic $SrRuO_3$ epitaxial layers separated by ultrathin non-magnetic $SrZrO_3/SrIrO_3$”, Appl. Phys. Lett. **113**, 192402 (2018).

[452] Z. Wang, T. Lorenz, D. I. Gorbunov, P. T. Cong, Y. Kohama, S. Niesen, O. Breunig, J. Engelmayer, A. Herman, J. Wu, K. Kindo, J. Wosnitza, S. Zherlitsyn, and A. Loidl, “Quantum criticality of an Ising-like spin-1/2 antiferromagnetic chain in a transverse magnetic field”, Phys. Rev. Lett. **120**, 207205 (2018).

[453] I. Lindfors-Vrejoiu, L. Jin, C. Himcinschi, J. Engelmayer, F. Hensling, C.-L. Jia, R. Waser, R. Dittmann, and P. H. M. van Loosdrecht, “Structure and orbital ordering of ultrathin $LaVO_3$ probed by atomic resolution electron microscopy and Raman spectroscopy”, Phys. Status Solidi RRL **11**, 1600350 (2017).

[454] I. Vrejoiu, C. Himcinschi, L. Jin, C.-L. Jia, N. Raab, J. Engelmayer, R. Waser, R. Dittmann, and P. H. M. van Loosdrecht, “Probing orbital ordering in $LaVO_3$ epitaxial films by Raman scattering”, APL Mater. **4**, 046103 (2016).

Danksagung

Zunächst danke ich Prof. Dr. Thomas Lorenz für die Möglichkeit zur Promotion, sowie Prof. Dr. Markus Braden für seine Bereitschaft als Gutachter zu fungieren. Prof. Dr. Simon Trebst danke ich, daß er trotz seines dichten Zeitplans den Vorsitz der Prüfungskommission übernommen hat. Für die Protokollführung bei meiner Disputation bedanke ich mich bei Dr. Christoph Grams.

Mein besonderer Dank gilt den Coautoren der beiden Titanat-Paper, ohne deren Unterstützung und Rat diese Arbeit nicht möglich gewesen wäre. Ich danke Christoph Grams für die dielektrischen Messungen an meinen Kristallen, Xiao Lin für die Einführung in die Abschmelzanlage und die Kunst des Temperns, Raphael German für die Ramanmessung, Tobias Fröhlich für die Apex-Messung, Fulya Koç für die Unterstützung bei Messungen der thermischen Ausdehnung und, nicht zuletzt, Joachim Hemberger und Kamran Behnia für die fruchtbaren Diskussionen.

Die Kristallzüchtung bildet das Fundament dieser Arbeit und wäre ohne den reichen Erfahrungsschatz anderer Züchter nicht möglich gewesen. Zugriff auf diesen Schatz gewährten mir Agung Nugroho, Martin Valldor, Sandra Niesen, Holger Ulbrich, Navid Qureshi und Karsten Binder, wofür ich mich herzlich bedanken möchte. Meinen Mitzüchtern Stefan Kunkemöller und Kevin Jenni danke ich für den regen Austausch und die Unterstützung bei spiegelofenspezifischen Problemen.

Der erste Schritt zur Beurteilung der gezüchteten Kristalle ist die Überprüfung der Einkristallinität und Phasenreinheit der Proben. Für die Einweisung in die dafür erforderlichen Röntgenapparaturen und Hilfestellung bei auftretenden Problemen bedanke ich mich bei Max Baum, Johanna Brand, Christine Tölzer, Jonas Stein, Florian Waßer und Kevin Jenni.

Dank der Luftempfindlichkeit meiner zahlreichen Manganatkristalle war ich ein reger Nutzer der Argonboxen. Für die Einführung in deren Bedienung danke ich Oliver Heyer und Gerhard Kolland. Als langjähriger Argonboxverantwortlicher bedanke ich mich auch für die Unterstützung meiner Co-Verantwortlichen Johanna Brand und Florian Waßer.

Für die Einführung in die Bedienung diverser Magnetkryostaten und in die Geheimnisse der Probenkontaktierung danke ich Gerhard Kolland und Oliver Breunig. Für die Einführung in die Nutzung des PPMS, sowie die Unterstützung bei den zahlreichen Problemen mit diesem Gerät, danke ich Christoph Grams und Daniel Niermann.

Meinem Mitdoktoranden Daniel Brüning danke ich für die Unterstützung bei Problemen aller Art, die sich in der täglichen Laborarbeit ergeben und besonders für seine Bereitschaft, mich in den letzten Tagen der Fertigstellung meiner Dissertation zu entlasten.

Tobias Fröhlich und Lionel Andersen danke ich für ihren kristallographischen Rat, die moralische Unterstützung und den inspirierenden Gedankenaustausch.

Jonas Stein, Tobias Fröhlich, Christoph Grams und Andrea Bliesener danke ich für die zahlreichen Tips bei LaTeX-Problemen, die bei der Erstellung einer solchen Arbeit unvermeidlich auftreten.

Ich danke Susanne Heijligen für die SQUID-Messungen an meinen Proben und die Einweisung in die Bedienung des MPMS. Inge Simons danke ich für die EDX-Messungen, welche die Platinkontamination der ersten Manganatkristalle aufdeckten.

Bei Ralf Müller bedanke ich mich für seinen Rat bei allen Fragen der Chemie und für die Beschaffung der Substanzen, die für die Kristallzüchtung erforderlich waren.

Andreas Freimut, Timur Zent und allen Mitarbeitern der Mechanikwerkstatt danke ich für die Fertigung und Reparatur diverser Laborutensilien.

Ich danke den Mitarbeitern der Elektronikwerkstatt, allen voran Klaus Lehmann, Harald Lüttgen und Christian Honerlage, für die Reparaturen zahlreicher Laborgeräte.

Norbert Henn, Lucie Hamdan und Pascal Hurth danke ich für ihre Hilfe bei diversen technischen Problemen.

Bei Dorothea Hochscheid, Ute Graffenberger und Anja Becker-Haumann bedanke ich mich für die Beschaffung zahlreicher, schwer erreichbarer Veröffentlichungen.

Nicht zuletzt danke ich Oliver Breunig, Christoph Grams, Daniel Brüning, Jakob Schluck, Sebastian Biesenkamp und Tobias Fröhlich für das Korrekturlesen von Teilen dieser Arbeit.

Abstract

In this thesis, different single-crystalline perovskite-type transition metal oxides are studied. Two of these materials are doped perovskite titanates with an insulating parent compound. Commercial $Sr_{1-x}Ca_xTiO_3$ single crystals with a calcium content of $x = 0.009$ and charge-carrier densities tuned from the insulating, ferroelectric parent material to $n \simeq 60 \times 10^{19}\,\mathrm{cm}^{-3}$ are investigated by thermal-expansion measurements. Pronounced α/T anomalies, signaling the ferroelectric transition of pristine $Sr_{1-x}Ca_xTiO_3$, persist upon increasing charge-carrier density n in reduced $Sr_{1-x}Ca_xTiO_{3-\delta}$, confirming earlier findings from resistivity measurements. Though, in contrast to the latter, the anomalies in α/T do not completely vanish as a function of n but change in character at a certain threshold carrier density $n^* \approx 1.3 \times 10^{19}\,\mathrm{cm}^{-3}$. This might indicate a structural phase transition when crossing n^*, analogously to the parent compound $Sr_{1-x}Ca_xTiO_3$ that changes from non-centrosymmetric ferroelectric to antiferroelectric as a function of x involving the recovery of an inversion center. However, an almost vertical phase boundary in a $T_C(n)$ diagram is not easily detectable by temperature-dependent measurements like thermal expansion. This puzzle can only be resolved by structural analyses of $Sr_{1-x}Ca_xTiO_{3-\delta}$ crystals with carrier concentrations on both sides of n^*. A sign change of α as a function of n, as is expected for a quantum phase transition where n is the control parameter, could not be observed.

Single crystals of $EuTiO_3$ are grown by the floating-zone method and characterized. Similar to $Sr_{1-x}Ca_xTiO_3$, the material's properties strongly depend on the actual oxygen content. The as-grown crystal is found to be oxygen-excessive by comparing its saturation magnetization to that of a pure Eu^{2+} system. Other key parameters as Néel temperature, Weiss temperature, and the Barrett behavior of the permittivity agree with literature values. To induce metallic conductivity, pieces of the as-grown $EuTiO_3$ crystal were reduced by annealing. The metallic $EuTiO_{3-\delta}$ samples show the full saturation magnetization of $7\,\mu_B$. A metal–insulator transition is induced being similar to that in $SrTiO_{3-\delta}$ but appearing at a charge-carrier concentration n_c larger by a factor of 10^4 due to the smaller permittivity of $EuTiO_3$ implying a smaller effective Bohr radius a_B^*. Doped crystals of $EuTiO_3$, $SrTiO_3$, and $KTaO_3$ obey a scaling behavior $n_c^{1/3} a_B^* = K$ resembling the original Mott criterion for a metal–insulator transition but at a much larger $K \approx 10$. At low temperature, the electronic mobility of metallic $EuTiO_{3-\delta}$ and $SrTiO_{3-\delta}$ systematically increases upon decreasing n across both materials. For the first time, an AT^2 resistivity is observed in metallic $EuTiO_{3-\delta}$, which is similar to that reported for doped $SrTiO_3$. The T^2 prefactor A scales with the charge-carrier density n and its absolute values match that of doped $SrTiO_3$ with the same n. A simple three-band model is used to describe the $A(n)$ scaling of both materials over a large range of n.

Several single-layered manganites $R_{1-x}A_{1+x}MnO_4$ with various element combinations

R/A and doping levels x were grown in single-crystalline form to outperform the doping range of the parent compound $La_{1-x}Sr_{1+x}MnO_4$ and shift the limit for x to new heights, where a maximum of $x = 0.73$ is achieved in $Pr_{1-x}Sr_{1+x}MnO_4$. The transition to the charge and orbital order at T_{COO} signals itself by characteristic features in resistivity, magnetization, and heat capacity. The tetragonal $R_{1-x}Sr_{1+x}MnO_4$ systems with a large ion-size mismatch exhibit comparably low transition temperatures, but their respective T_{COO} systematically increases as a function of x. In contrast, systems with small ion-size disorder like $Pr_{1-x}Ca_{1+x}MnO_4$ and $Nd_{1-x}Ca_{1+x}MnO_4$ show the highest transition temperatures T_{COO} of all investigated manganites. In these two compounds, the evolution of T_{COO} with x is not monotonic as it is observed for Sr manganites. Instead, the highest transition temperatures are reached at commensurate doping levels $x = 1/2, 2/3$.

Kurzzusammenfassung

In dieser Arbeit wurden verschiedene Übergangsmetalloxide vom Perowskittyp in einkristalliner Form untersucht. Zwei dieser Materialien sind dotierte Perowskittitanate, die jeweils von einer isolierenden Ausgangsverbindung abstammen. Handelsübliche $Sr_{1-x}Ca_xTiO_3$-Einkristalle mit einem Calciumgehalt von $x = 0.009$ und Ladungsträgerdichten bis zu $n \simeq 60 \times 10^{19}\,cm^{-3}$ wurden mittels Messungen der thermischen Ausdehnung untersucht. Ausgeprägte Anomalien im thermischen Ausdehnungskoeffizienten α/T, welche den ferroelektrischen Übergang im undotierten $Sr_{1-x}Ca_xTiO_3$ kennzeichnen, bleiben in dotiertem $Sr_{1-x}Ca_xTiO_{3-\delta}$ mit ansteigender Ladungsträgerdichte n erhalten, was frühere Ergebnisse bestätigt, die aus Widerstandsmessungen gewonnen wurden. Die Anomalien in α/T verschwinden jedoch nicht als Funktion von n, was bei den Widerstandsanomalien der Fall war, aber sie verändern sich qualitativ bei einem Schwellwert $n^* \approx 1.3 \times 10^{19}\,cm^{-3}$. Dies kann ein Indiz für einen strukturellen Phasenübergang sein, der beim Überschreiten von n^* auftritt. Ein analoges Verhalten zeigt das undotierte $Sr_{1-x}Ca_xTiO_3$, welches mit steigendem x von einer nicht-zentrosymmetrischen, ferroelektrischen Phase in eine zentrosymmetrische, antiferroelektrische Phase übergeht. Allerdings lässt sich eine vertikale Phasengrenze im $T_C(n)$-Phasendiagramm nur schwer mit temperaturabhängigen Messungen wie der thermischen Ausdehnung detektieren. Nur eine Analyse der Kristallstruktur von $Sr_{1-x}Ca_xTiO_{3-\delta}$-Kristallen mit Ladungsträgerdichten auf beiden Seiten von n^* könnte dieses Rätsel lösen. Ein Vorzeichenwechsel von α als Funktion von n, wie er für einen Quantenphasenübergang mit n als Kontrollparameter zu erwarten ist, konnte nicht beobachtet werden.

$EuTiO_3$-Einkristalle wurden mittels des Zonenschmelzverfahrens gezüchtet und charakterisiert. Ebenso wie bei $Sr_{1-x}Ca_xTiO_3$ hängen die Materialeigenschaften von $EuTiO_3$ empfindlich vom tatsächlichen Sauerstoffgehalt ab. Durch Vergleich der Sättigungsmagnetisierung der gezüchteten Proben mit der eines reinen Eu^{2+}-Systems konnte nachgewiesen werden, dass der gezüchtete Kristall einen nominellen Sauerstoffüberschuss aufweist. Andere Kennzahlen wie Néel- und Weiss-Temperatur, sowie das Barrett-Verhalten der Permittivität, stimmen mit Literaturwerten überein. Um metallische Leitfähigkeit in den Proben hervorzurufen, wurden Stücke des ursprünglichen Kristalls durch Tempern reduziert. Die metallischen $EuTiO_{3-\delta}$-Proben zeigen die volle Sättigungsmagnetisierung von $7\,\mu_B$. Der induzierte Metall-Isolator-Übergang gleicht qualitativ dem in $SrTiO_{3-\delta}$, tritt aber erst bei einer deutlich höheren kritischen Ladungsträgerdichte n_c auf. Verglichen mit $SrTiO_{3-\delta}$ ist sie um einen Faktor 10^4 größer, was sich mit der deutlich kleineren Permittivität in $EuTiO_3$ erklären lässt, die einen kleineren effektiven Bohrschen Radius a_B^* impliziert. Dotierte Kristalle aus $EuTiO_3$, $SrTiO_3$ und $KTaO_3$ zeigen ein Skalierungsverhalten $n_c^{1/3} a_B^* = K$, welches qualitativ dem Mott-Kriterium für Metall-Isolator-Übergänge entspricht, jedoch mit einem deutlich höheren $K \approx 10$. Die elektronische Beweglichkeit in metallischem

$EuTiO_{3-\delta}$ und $SrTiO_{3-\delta}$ steigt im Tieftemperaturbereich über beide Materialien hinweg systematisch mit steigendem n. Ein AT^2-Verhalten des elektrischen Widerstandes, welches für $SrTiO_{3-\delta}$ bereits bekannt war, ließ sich erstmals auch in $EuTiO_{3-\delta}$ beobachten. Der Vorfaktor A skaliert mit der Ladungsträgerdichte und seine Absolutwerte entsprechen denen von $SrTiO_{3-\delta}$ bei gleichem n. Das $A(n)$-Verhalten beider Materialien lässt sich über einen großen Bereich von n durch ein einfaches Drei-Bänder-Modell beschreiben.

Einfach geschichtete Manganate $R_{1-x}A_{1+x}MnO_4$ wurden in einkristalliner Form mit verschiedenen Elementkombinationen R/A und Dotierungsgraden x gezüchtet, um den Dotierungsbereich des gut untersuchten, aber auf $x \leq 0.6$ beschränkten $La_{1-x}Sr_{1+x}MnO_4$ zu erweitern. Durch die Elementkombination $Pr_{1-x}Sr_{1+x}MnO_4$ konnte eine maximale Dotierung von $x = 0.73$ erreicht werden. Der Übergang zur Ladungs- und orbitalen Ordnung bei T_{COO} ist durch charakteristische Anomalien im Widerstand, in der Magnetisierung und der Wärmekapazität gekennzeichnet. In den tetragonalen Verbindungen $R_{1-x}Sr_{1+x}MnO_4$ ist der Unterschied der Ionenradien von R und Sr groß. Diese Verbindungen zeigen relativ niedrige Übergangstemperaturen für die Ladungs- und orbitale Ordnung, die aber systematisch mit steigendem x ansteigen. Im Gegensatz dazu zeigen die Verbindungen $Pr_{1-x}Ca_{1+x}MnO_4$ und $Nd_{1-x}Ca_{1+x}MnO_4$ nur geringe strukturelle Unordnung und haben daher auch die höchsten Übergangstemperaturen aller Manganate. In diesen Verbindungen steigt T_{COO} nicht monoton mit x, wie es bei den Strontiummanganaten der Fall ist, sondern T_{COO} erreicht die höchsten Werte bei kommensurablen Dotierungen $x = 1/2, 2/3$.

Publikationen

Teilpublikationen

- J. Engelmayer, X. Lin, F. Koç, C. P. Grams, J. Hemberger, K. Behnia, and T. Lorenz, "Ferroelectric order versus metallicity in $Sr_{1-x}Ca_xTiO_{3-\delta}$ (x = 0.009)", Phys. Rev. B **100**, 195121 (2019)

- J. Engelmayer, X. Lin, C. P. Grams, R. German, T. Fröhlich, J. Hemberger, K. Behnia, and T. Lorenz, "Charge transport in oxygen-deficient $EuTiO_3$: the emerging picture of dilute metallicity in quantum-paraelectric perovskite oxides", Phys. Rev. Materials **3**, 051401(R) (2019)

- C. W. Rischau, X. Lin, C. P. Grams, D. Finck, S. Harms, J. Engelmayer, T. Lorenz, Y. Gallais, B. Fauqué, J. Hemberger, and K. Behnia, "A ferroelectric quantum phase transition inside the superconducting dome of $Sr_{1-x}Ca_xTiO_{3-\delta}$", Nat. Phys. **13**, 643–648 (2017)

Weitere Publikationen

- Z. Wang, M. Schmidt, A. Loidl, J. Wu, H. Zou, W. Yang, C. Dong, Y. Kohama, K. Kindo, D. I. Gorbunov, S. Niesen, O. Breunig, J. Engelmayer, and T. Lorenz, "Quantum critical dynamics of a Heisenberg–Ising chain in a longitudinal field: many-body strings versus fractional excitations", Phys. Rev. Lett. **123**, 067202 (2019)

- L. Wysocki, R. Mirzaaghayev, M. Ziese, L. Yang, J. Schöpf, R. B. Versteeg, A. Bliesener, J. Engelmayer, A. Kovács, L. Jin, F. Gunkel, R. Dittmann, P. H. M. van Loosdrecht, and I. Lindfors-Vrejoiu, "Magnetic coupling of ferromagnetic $SrRuO_3$ epitaxial layers separated by ultrathin non-magnetic $SrZrO_3/SrIrO_3$", Appl. Phys. Lett. **113**, 192402 (2018)

- Z. Wang, T. Lorenz, D. I. Gorbunov, P. T. Cong, Y. Kohama, S. Niesen, O. Breunig, J. Engelmayer, A. Herman, J. Wu, K. Kindo, J. Wosnitza, S. Zherlitsyn, and A. Loidl, "Quantum criticality of an Ising-like spin-1/2 antiferromagnetic chain in a transverse magnetic field", Phys. Rev. Lett. **120**, 207205 (2018)

- I. Lindfors-Vrejoiu, L. Jin, C. Himcinschi, J. Engelmayer, F. Hensling, C.-L. Jia, R. Waser, R. Dittmann, and P. H. M. van Loosdrecht, "Structure and orbital ordering of ultrathin $LaVO_3$ probed by atomic resolution electron microscopy and Raman spectroscopy", Phys. Status Solidi RRL **11**, 1600350 (2017)

- I. Vrejoiu, C. Himcinschi, L. Jin, C.-L. Jia, N. Raab, J. Engelmayer, R. Waser, R. Dittmann, and P. H. M. van Loosdrecht, “Probing orbital ordering in $LaVO_3$ epitaxial films by Raman scattering”, APL Mater. **4**, 046103 (2016)

Offizielle Erklärung

Ich versichere, dass ich die von mir vorgelegte Dissertation selbständig angefertigt, die benutzten Quellen und Hilfsmittel vollständig angegeben und die Stellen der Arbeit – einschließlich Tabellen, Karten und Abbildungen –, die anderen Werken im Wortlaut oder dem Sinn nach entnommen sind, in jedem Einzelfall als Entlehnung kenntlich gemacht habe; dass diese Dissertation noch keiner anderen Fakultät oder Universität zur Prüfung vorgelegen hat; dass sie – abgesehen von unten angegebenen Teilpublikationen – noch nicht veröffentlicht worden ist, sowie, dass ich eine solche Veröffentlichung vor Abschluss des Promotionsverfahrens nicht vornehmen werde. Die Bestimmungen der Promotionsordnung sind mir bekannt. Die von mir vorgelegte Dissertation ist von Prof. Dr. Thomas Lorenz betreut worden.

Köln, den ____________________ ____
Johannes Engelmayer

Teilpublikationen

- J. Engelmayer, X. Lin, F. Koç, C. P. Grams, J. Hemberger, K. Behnia, and T. Lorenz, "Ferroelectric order versus metallicity in $Sr_{1-x}Ca_xTiO_{3-\delta}$ ($x = 0.009$)", Phys. Rev. B **100**, 195121 (2019)
- J. Engelmayer, X. Lin, C. P. Grams, R. German, T. Fröhlich, J. Hemberger, K. Behnia, and T. Lorenz, "Charge transport in oxygen-deficient $EuTiO_3$: the emerging picture of dilute metallicity in quantum-paraelectric perovskite oxides", Phys. Rev. Materials **3**, 051401(R) (2019)
- C. W. Rischau, X. Lin, C. P. Grams, D. Finck, S. Harms, J. Engelmayer, T. Lorenz, Y. Gallais, B. Fauqué, J. Hemberger, and K. Behnia, "A ferroelectric quantum phase transition inside the superconducting dome of $Sr_{1-x}Ca_xTiO_{3-\delta}$", Nat. Phys. **13**, 643–648 (2017)